



SDC

The university partnership
Denmark – China

PhD thesis

Jens Broe Rix

Nonequilibrium Effects in Nanoscale Systems

Thermoelectrically driven ring currents

Coupled spins out of equilibrium

Supervisor: Per Hedegård

Handed in: 18 August 2019

Abstract

The field of thermoelectricity has gained increasing interest during the last decades, partly due to the advances in nanoscience. In the first part of this thesis, different aspects of the Seebeck effect in nanoscale systems are studied. We derive a mathematical tool to calculate local electric currents in single molecule junctions and use it to analyze thermoelectrically driven ring currents. Additionally, the expression is used to study the connection between ring currents and destructive interference in both electrically and thermoelectrically driven junctions. The Seebeck coefficient of single molecules is rather small, but when organic molecules are put together to form organic semiconductors, the Seebeck coefficient increases significantly. We will show that the thickness dependent Seebeck coefficient of a layered organic crystal can be described by band bending at the crystal-metal interfaces.

Recent research has shown that a spin-polarized current can flip a magnetic moment so that it points antiparallel to the magnetic field. In the second part of this thesis, we will show that even an ordinary charge current can flip magnetic moments, when at least two moments are present. An equation of motion is derived for two spins that couple to a current carrying metal and the explicit expressions and length dependence of the nonequilibrium torques are presented. We show that the nonequilibrium torques can drive the spin system into several unexpected configurations such as pointing antiparallel to the magnetic field.

Dansk resume

Forskningen inden for termoelektricitet har i de sidste årtier oplevet en stigende interesse, hvilket blandt andet skyldes de store fremskridt inden for nanoscience. Den første del af denne afhandling undersøger forskellige aspekter af Seebeck effekten på nanoskala. Vi udleder et matematisk udtryk til at beregne lokale elektriske strømme i molekulære kontakter og bruger det til at analysere termoelektrisk drevne ringstrømme. Udtrykket bliver yderligere brugt til at undersøge sammenhængen mellem ringstrømme og destruktiv interferens i både elektrisk og termoelektrisk drevne systemer. Seebeck koefficienten af enkelte molekyler er forholdsvis lille, men når organiske molekyler sættes sammen til organiske halvledere, så stiger Seebeck koefficienten betragteligt. Vi viser, at den tykkelsesafhængige Seebeck koefficient af en organisk krystal kan beskrives ved hjælp af "band bending" i området tæt på metalkontakterne.

Nyere forskning har vist, at en spin-polariseret strøm kan vende et magnetisk moment, så det peger i modsatte retning af det magnetiske felt. I den anden del af denne afhandling viser vi, at selv en upolariseret strøm kan vende magnetiske momenter, så længe der er mere end to af dem. Vi udleder en bevægelsesligning for to magnetiske momenter, der er koblet via et strømførende metal, og vi beregner de eksplicitte udtryk for ikke-ligevægts drejningsmomenterne. Vi demonstrerer, at de nye drejningsmomenter kan tvinge spinsystemet ind i uventede konfigurationer, for eksempel så de begge peger i modsatte retning end det magnetiske felt.

Acknowledgements

First of all, I want to thank Per Hedegård for giving me the opportunity to do this PhD project. Thank you for giving me the freedom to work in whichever direction I wanted and for inspiring me with your positive and optimistic approach to research.

I am grateful to professor Xiaohui Qiu for hosting me for more than half a year at the Nanoscience Center at University of Chinese Academy of Sciences, Beijing. I thank Xiaoxian, Qibin, Juan, and Jie for good discussions during my time in Beijing. Also many thanks to professor Jingtao Lü for hosting me for three months at Huazhong University of Science and Technology in Wuhan.

It has been a good experience to be part of the Condensed Matter Theory group at the University of Copenhagen. I would like to thank the lunch club for “hyggelige” breaks during, at times, hard days at the office. Thank you for the good chess and climbing experiences, and special thanks to Sakse Dalum for good company during our stays in China (and in Copenhagen as well).

Finally, I am grateful to my family and friends for the moral support during my PhD project. In particular, thanks to Nora and Anne for their love and patience.

Thanks also to the Sino-Danish Center for Education and Research (SDC) for the financial support and for making it possible for me to spend almost a year in China.

Contents

Abstract	i
Dansk resume	ii
Acknowledgements	iii
Contents	iv
Thesis overview	1
I Thermoelectricity	3
1 Introduction to thermoelectricity	4
1.1 The Seebeck coefficient	5
1.1.1 Seebeck coefficient in mesoscopic systems	6
1.1.2 Seebeck coefficient in bulk materials	8
1.1.3 Seebeck coefficient in parallel and series	9
1.2 Local currents	9
2 Local currents in single molecule junctions	12
2.1 Introduction to NEGF	12
2.2 Local currents	14
2.2.1 Local currents in single molecule junctions	15
2.3 Analysis of local currents in single molecule junctions	17
2.3.1 Qualitative prediction of currents	18
2.3.2 Alternant molecules	18
2.3.3 Interference and local currents	19
2.4 Conclusions	21
3 Thermoelectrically driven ring currents	22
3.1 Thermoelectrically driven ring currents in single molecules	22
3.1.1 Low temperature approximations	24
3.1.2 Thermoelectrically driven currents close to destructive interferences	26
3.2 Ring currents in graphene nanoribbons	29
3.3 Conclusions	29
4 Thickness dependent Seebeck coefficient in BDT crystals	31
4.1 BDT and experiments	32
4.1.1 Band bending	33
4.2 Band bending and Seebeck coefficient	35
4.2.1 Theoretical explanation: 1D model	36
4.2.2 Theoretical explanation: 3D calculations	38
4.3 The challenge of knowing the temperature drop	41
4.4 Discussion	44

II	Spins out of equilibrium	45
5	Introduction	46
5.1	Coupled spins in equilibrium	47
5.1.1	The RKKY interaction	47
5.1.2	Equation of motion	48
5.2	Spins in nonequilibrium conditions	49
6	Coupled spins out of equilibrium	51
6.1	Introduction to coherent states	51
6.1.1	Spin coherent states	51
6.1.2	Fermionic coherent states	53
6.2	Feynman-Vernon theory	53
6.2.1	The reduced density matrix	54
6.2.2	The spin action	56
6.2.3	The influence functional	57
6.2.4	Slow spin approximation	60
6.2.5	The final result	62
6.2.6	Estimating the nonequilibrium coefficients	63
6.3	Conclusions and outlook	64
7	Study of the spin equations of motion	65
7.1	Analytic considerations	65
7.2	Linear stability analysis	67
7.2.1	Fixed points	68
7.2.2	Linearization of the EOM around ferromagnetic and antiferromagnetic configurations	68
7.2.3	General linearization	70
7.2.4	Stability diagrams	71
7.3	Numerical calculations	75
7.4	Conclusion	76
	Appendices	79
A	Appendix to Chapters 2 and 3	80
A.1	Nonequilibrium density matrix in the single particle picture	80
A.2	Derivation of $\text{Tr} [G_M \Gamma G_M^\dagger A] = 0$	81
A.3	Derivation of single channel expression	81
A.4	Symmetry of γ for Alternant Molecules	83
A.5	Self-energy for semi-infinite leads	84
A.5.1	1D chain	84
A.5.2	Graphene nanoribbons	85
B	Appendix to Chapter 4	88
B.1	BDT experiment: Heat conduction through air	88
C	BDT paper draft	91

D	Appendix to Chapter 6	104
D.1	Equations of motion	104
D.2	Constructing the functional integral	105
D.3	Rewriting $\text{Tr} [G_0 \tilde{V} G_0 \tilde{V}]$	108
D.3.1	Fourier transforming	110
D.4	Integrals	111
D.4.1	$J, \mathcal{H} \{ \text{Re } \Lambda \} (0)$	113
D.4.2	$\eta, \frac{\partial}{\partial \omega} \Lambda_{nm}(\omega, 0) _{\omega=0}$	114
D.4.3	$\sigma, \text{Im } \Lambda(0, \Delta \mathbf{k})$	114
D.4.4	$\chi, \frac{\partial}{\partial \omega} \mathcal{H} \{ \text{Im } \Lambda_{21} \} (\omega) _{\omega=0}$	115
D.4.5	Additional integrals	116
E	Appendix to Chapter 7	118
E.1	Analytic considerations	118
E.2	Canted spin configuration	119
E.3	General linearization of the EOMs	120
F	Spin paper draft	123
	Bibliography	145

Thesis overview

This thesis is divided into two parts. The first part studies different aspects of Seebeck coefficient measurements in nanoscale junctions. The second part studies a two-spin system connected to a current carrying metal. To give an overview of the thesis, we will here go through the content and important findings in the different chapters.

After an introduction to some important theory and concepts regarding thermoelectricity in Chapter 1, local electric currents in single molecule junctions are studied in Chapter 2. The developed theory can be used to calculate local currents driven by either an electric potential difference, a temperature difference, or both. We will derive an analytic expression for the bond transmission in single molecule junctions in Sec. 2.2.1. The analytic expression can be used to explain different features of the local currents: it is used to predict the current patterns in symmetric junctions (Sec. 2.3.1) and to explain the symmetry in energy in alternant molecules (Sec. 2.3.2). Finally, in Sec. 2.3.3, the analytic expression is used to get a better understanding of why local ring currents change direction in some cases, when the energy passes through a point of destructive interference.

Chapter 3 builds on the theory developed in Chapter 2. We will consider the specific case in which a temperature and an electric potential difference are applied so that the net current cancels. This is the Seebeck measurement condition in which local currents can still flow. We will consider different molecular junctions to see that a variety of ring current patterns can appear. A low-temperature approximation for the ring currents is derived in Sec. 3.1.1 and the feature that the ring currents cancel twice around some destructive interference points is explained mathematically in Sec. 3.1.2. Finally, in Sec. 3.2, we will study gated graphene nanoribbons and show that thermoelectrically driven ring currents exist here as well.

In Chapter 4, the thickness dependence of Seebeck coefficients is studied in organic crystals. In Sec. 4.1, we present the experimental results of BDT crystals, which show that the Seebeck coefficient increases with thickness and saturates with a characteristic length of around 30 nm. This length is comparable to the length of the band bending at the metal-BDT interface and in Sec. 4.2, we set up two theoretical models that connect these effects. A 1D and 3D model are used, which both fit the experimental data well. The 3D model in Sec. 4.2.2 shows the existence of thermoelectrically driven ring currents in the setup. Finally, we will discuss some challenges regarding the temperature drop in the experimental setup in Sec. 4.3.

In the second part of the thesis, we will study two spins which are in contact with a nonequilibrium electronic environment. After an introduction in Chapter 5, we will use the Feynman-Vernon influence functional approach to derive the equations of motion for two spins in Chapter 6. The derivation is quite technical and an overview of the procedure is found in the beginning of Sec. 6.2. The nonequilibrium conditions give rise to two “new” torques and we present the explicit expressions for the torques for the particular model in Sec. 6.2.5.

In Chapter 7, we will study the derived equations of motion in a more general sense in order to understand how the new torques affect the dynamics of a two-spin system. In Sec. 7.2, we will do a linear stability analysis, which shows that

the nonequilibrium torques can drive the spin system into unexpected configurations. Numerical simulations of the spin trajectories are presented for some of the interesting cases in Sec. [7.3](#).

Part I

Thermoelectricity

Chapter 1

Introduction to thermoelectricity

This chapter is partially based on the author's master's thesis. The thesis is cited as Ref. [1].

In 1820, the Danish scientist Hans Christian Ørsted did his famous experiment in which he observed the deflection of a magnetic needle close to a current carrying wire. Together with e.g. Michael Faraday's discovery of electromagnetic induction, this demonstrated the connection between electricity and magnetism [2]. Inspired by Ørsted, the Estonian-German scientist Thomas Johann Seebeck did a similar experiment; he formed a loop by connecting two different materials, heated the loop at one of the material junctions, and he observed the deflection of a magnetic compass needle in the center of the loop [3, 4]. Seebeck wrongly concluded that his observation was due to a thermomagnetic effect. A few years later, he was corrected by Ørsted, who wrote "Seebeck ... has discovered that one can establish an electric circuit in metals without the interposition of any liquid. One establishes the current in this circuit by disturbing the equilibrium of temperature" [5]. Ørsted therefore understood that a temperature difference can drive an electric current, and he suggested the name *thermoelectric*¹ for circuits driven by temperature differences.²

Seebeck's observations mark the beginning of the field of thermoelectricity. In the 1830s, the French physicist Peltier discovered that an electric current can transfer heat [6, 7]; an effect now known as the Peltier effect. The Seebeck and Peltier effects are closely related and in the decades after the observations, it was shown that both effects can be described by the so-called Seebeck coefficient, S .³ To linear order, the electric and heat current densities in a material can be written as [6, 9]

$$\mathbf{j}_e = -\sigma \nabla V - \sigma S \nabla T \quad (1.1)$$

$$\mathbf{j}_q = -\kappa \nabla T - T \sigma S \nabla V \quad (1.2)$$

where σ is the electrical conductivity, S is the Seebeck coefficient (also known as thermopower), and κ is the thermal conductivity.⁴ The coefficients in front of the gradients are generally tensors, but we will here consider the materials to be isotropic. The first terms in Eqs. (1.1) and (1.2) are the ordinary Ohm's and Fourier's laws, while the second terms are the thermoelectric contributions. The Seebeck coefficient and the measurement hereof is the focus in this thesis, and we will return to it shortly.

¹In Ørsted's own words: "It will from now on doubtless be necessary to distinguish this new class of electric circuits by an appropriate term; and as such I propose the expression thermoelectric circuits ..." [5].

²This paragraph is similar to the introduction given in Ref. [1].

³A relation known as the *first Thomson relation* [6]. The connection between the two effects is a result of the more general symmetry in thermodynamic systems known as *Onsager's reciprocal relations* [8].

⁴ $\kappa = \lambda \left(1 + \frac{\sigma S^2 T}{\lambda}\right)$, where λ is the thermal conductivity in the case of $\mathbf{j}_e = 0$. See e.g. Refs. [1, 9].

It is obvious from the above, that the Seebeck effect can be used to turn thermal energy into electric energy. A device with this property is known as a thermoelectric generator. A closely related application is the thermoelectric cooler, which can use electrical energy to transfer heat. The efficiency of a thermoelectric material in either of these devices depends on the material properties via the so-called *figure of merit*, $ZT = S^2 T \sigma / \kappa$ [10]. The efficiency increases with ZT , and to obtain large efficiencies, both the electrical conductivity and Seebeck coefficient have to be large, while the thermal conductivity is small. During the first half of the 20th century, a lot of effort was put into improving the efficiency, but the progression stagnated [11]. With the new tools from nanoscience and an increasing interest in green technologies, the field of thermoelectrics has received more interest in the last two decades. A lot of different systems have been investigated in order to obtain large ZT -values. Some examples are nanostructured composites [12, 13], thin films [14], silicon nanowires [15], carbon nanotubes [16], and single molecule junctions [17]. The largest ZT value to date has been observed in SnSe single crystals, which have a layered crystal structure [18].

In addition to the possible applications, the material property provided by thermoelectrics, the Seebeck coefficient, can be used to study the fundamental transport mechanism in materials and nanoscopic systems. In this thesis, we will focus on this fundamental research branch in the field of thermoelectrics. We will start by studying the Seebeck coefficient in Sec. 1.1 and then move on to the concept of electric ring currents in Seebeck coefficient measurements in Sec. 1.2.

1.1 The Seebeck coefficient

The Seebeck coefficient can be measured in the following way: A temperature difference is applied across a system of interest, which drives an electric current (as well as a thermal current). An electric potential difference builds up and it will drive an electric current in the opposite direction. Eventually, a steady-state situation is reached in which the opposing currents cancel each other, and the Seebeck coefficient is obtained from the measured temperature and electric potential differences⁵

$$S = -\frac{\Delta V}{\Delta T}. \quad (1.3)$$

If the system is a homogeneous and isotropic material, the measured Seebeck coefficient is the same as the S in Eqs. (1.1) and (1.2). When the measurement is performed on a system composed of multiple materials, the measured value will be some combination of the Seebeck coefficients of the individual materials. In Sec. 1.1.3, we will consider some simple cases with multiple components.

The magnitude of the Seebeck coefficient varies strongly between different classes of materials. In metals, it is small and typically below $10 \mu\text{V}/\text{K}$ [6, 19]. In semiconductors, on the other hand, it is typically hundreds of $\mu\text{V}/\text{K}$ and can reach values above $1000 \mu\text{V}/\text{K}$ [19]. These facts have been known for a long time, but since our research group was puzzled about large Seebeck coefficients in organic crystals (see Chapter 4), we will here go through the theoretical description of the large differences. To do so, we will make a little detour and start out by considering the Seebeck coefficient in a mesoscopic system, i.e. a system in which the coherence length is longer than the sample size [20]. The general expression for the Seebeck coefficient is similar in both cases, and we will return to the bulk materials in Sec. 1.1.2.

⁵With the sign convention in Eq. (1.3), the Seebeck coefficient is positive (negative) in a p-type (n-type) semiconductor.

1.1.1 Seebeck coefficient in mesoscopic systems

A general way to describe coherent transport of charges is by using the Landauer formula [21]. Here a sample is placed between two contacts (denoted the left and right contact), and the electric current through the sample is

$$I = \frac{2e}{h} \int dE \mathcal{T}(E) [n_F^L(E) - n_F^R(E)], \quad (1.4)$$

where $\mathcal{T}(E)$ is the so-called transmission function, which describes the quantum mechanical probability for a charge to travel through the sample. The contacts are considered to be independent electron reservoirs so that $n_F^\alpha = [1 + \exp(\beta_\alpha(E - \mu_\alpha))]^{-1}$ is the Fermi function for contact α with chemical potential μ_α and inverse temperature $\beta_\alpha = (k_B T_\alpha)^{-1}$. If the temperature and potential differences between the contacts are small, the current can be taken to linear order in ΔV and ΔT . We can expand the Fermi functions around the temperature $T = (T_L + T_R)/2$ and chemical potential $\mu = (\mu_L + \mu_R)/2$ so that

$$n_F^L(E) - n_F^R(E) \approx -n'_F(E)[-e\Delta V + \beta(E - \mu)k_B\Delta T], \quad (1.5)$$

where $\beta = (k_B T)^{-1}$ and $n'_F(E)$ is the derivative of the Fermi function at T and μ . By inserting this into Eq. (1.4), we get the linear expression for the current. As mentioned earlier, the Seebeck coefficient is measured by applying both a potential and temperature difference so the the electric current cancels. By using $I = 0$ in the equations above, we arrive at the general expression for the Seebeck coefficient, $S = -\frac{\Delta V}{\Delta T}$,

$$S = -\frac{k_B}{e} \frac{\int_{-\infty}^{\infty} dE \mathcal{T}(E) \frac{E-\mu}{k_B T} [-n'_F(E)]}{\int_{-\infty}^{\infty} dE \mathcal{T}(E) [-n'_F(E)]}, \quad (1.6)$$

where $k_B/e = 86 \mu\text{V/K}$ is a useful quantity to remember. This expression has very different behaviors in different regimes. We will start by considering the low temperature case, which is e.g. used in single molecule studies [22, 23]. The derivative of the Fermi function is a symmetrically peaked function with a center at $E = \mu$ and a width of around $2k_B T$. At low temperatures, it becomes narrow and for $T \rightarrow 0$, it turns into a Dirac delta function, $-n'_F(E) = \delta(E - \mu)$. In this low-temperature limit, it is therefore the interval close to μ that dominates the integrals. If the transmission function is a slowly varying functions on the scale of $k_B T$, we can do a Sommerfeld expansion of both the numerator and denominator in Eq. (1.6). For a general function $g(E)$, $\int_{-\infty}^{\infty} dE g(E) [-n'_F(E)] \approx g(\mu) + \frac{\pi^2 k_B^2 T^2}{6} g''(\mu)$, so that

$$S_{\text{SM}} \approx -\frac{k_B}{e} \frac{\pi^2 k_B T}{3} \left. \frac{d \ln[\mathcal{T}(E)]}{dE} \right|_{E=\mu}, \quad (1.7)$$

where the subfix ‘‘SM’’ indicates that it is an approximation used in single molecules. We see that the Seebeck coefficient is proportional to the temperature, and it depends on the slope of the transmission function, $\mathcal{T}'(\mu)/\mathcal{T}(\mu)$. To demonstrate the validity of the approximation, consider the transmission function shown in Fig. 1.1a. It is constructed of two Lorentzian-like functions $L = a^2/((E - E_0)^2 + a^2)$ placed at $E_0 = -1 \text{ eV}$ and $E_0 = 1 \text{ eV}$ for $a = 0.1 \text{ eV}$. The Seebeck coefficient for this transmission function is shown in Fig. 1.1b at $T = 100 \text{ K}$, where the solid line is calculated using Eq. (1.6) and the dashed line is calculated using Eq. (1.7). As seen, there is a good

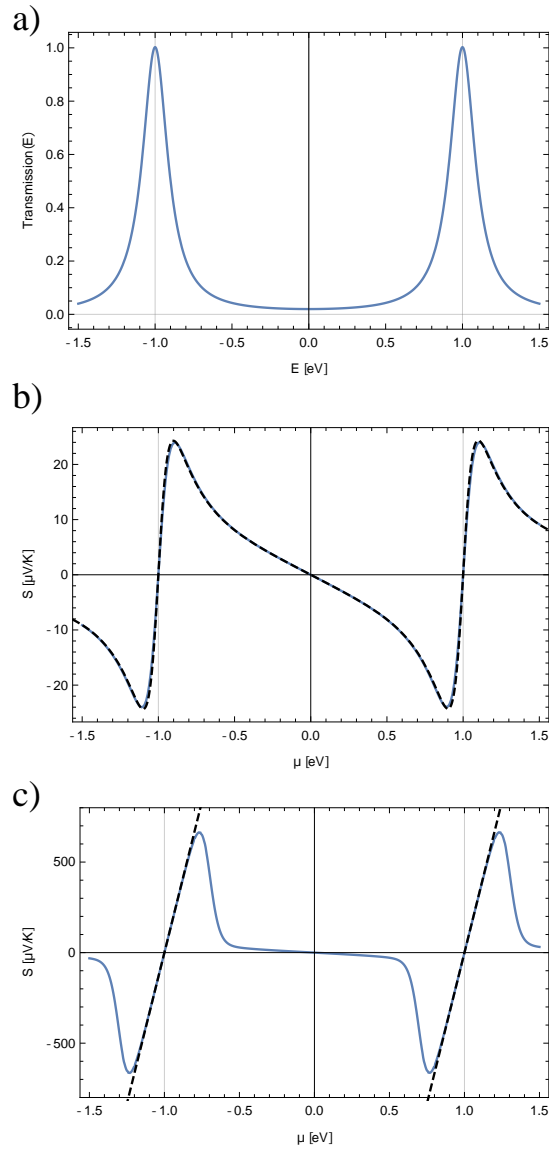


FIGURE 1.1: a) Transmission function constructed as the sum of two Lorentzian-like functions, $L = a^2/((E - E_0)^2 + a^2)$, with $E_0 = -1$ eV and $E_0 = 1$ eV. The plotted $\mathcal{T}(E)$ is for $a = 0.1$ eV. b) The Seebeck coefficient for the transmission function in (a) at temperature $T = 100$ K. The solid line is calculated using Eq. (1.6), while the dashed line is from the approximation in Eq. (1.7). c) The Seebeck coefficient in the case of narrow Lorentzian-like functions, $a = 10^{-5}$ eV, at $T = 300$ K. The dashed lines are obtained from Eq. (1.8).

agreement between the general and the approximate calculations.

The above approximation is not always true. If the transmission function is zero at $E = \mu$, the dominant contribution to the integrals does not come from the interval around μ . Consider for example a transmission function that has a very narrow single peak at E_0 .⁶ In this case, Eq. (1.6) reduces to

$$S_{\text{delta}} = \frac{k_B}{e} \frac{\mu - E_0}{k_B T}. \quad (1.8)$$

⁶Think of it as a delta function. However, the transmission function represents a probability and can therefore not take values above 1.

This model has e.g. been studied in the search for the optimal thermoelectric material [24–26]. We see that the Seebeck coefficient is proportional to the energy difference between the transport level, E_0 , and the chemical potential. It is obviously only the point $E = E_0$ that contributes to the integrals in Eq. (1.6). If we use a transmission function with a finite width, there will be a crossover between the two approximations. As an example, consider the double-Lorentzian transmission function in Fig. 1.1a, but now with narrow peaks compared to the thermal energy, $a = 10^{-5}$ eV. For this transmission function, the Seebeck coefficient at $T = 300$ K is as shown in Fig. 1.1c. Close to the transmission peaks, we see that Eq. (1.8) (dashed lines) is a good approximation. In these regions, it is the intervals close to the transmission peaks that dominate the integrals. When moving μ away from the E_0 's, there is a cross-over and in the interval -0.5 eV $< \mu < 0.5$ eV, Eq. (1.7) is again a good approximation.

From the above description, we see that small Seebeck coefficients are obtained when the transport takes place at the chemical potential. This is typically the case in single molecule junctions, where the experimentally obtained Seebeck coefficients are a few tens of $\mu\text{V/K}$ [27–29]. It is also the case in metals, which we will now consider.

1.1.2 Seebeck coefficient in bulk materials

In bulk materials, the general expression for the Seebeck coefficient is very similar to the one presented in Eq. (1.6) [30]. It can be derived from the Boltzmann equation using the relaxation time approximation to be [31]

$$S = -\frac{k_B}{e} \frac{\int_{-\infty}^{\infty} dE \sigma(E) \frac{E-\mu}{k_B T} [-n'_F(E)]}{\int_{-\infty}^{\infty} dE \sigma(E) [-n'_F(E)]}. \quad (1.9)$$

Here $\sigma(E)$ is a measure of how well electric charge is conducted in the material,⁷ and it is proportional to the density of states and the relaxation time. Eq. (1.9) is the same as Eq. (1.6), but with $\sigma(E)$ instead of $\mathcal{T}(E)$, and we can therefore use the same approximation as before. For metals, the conduction takes place at the Fermi level, and the Seebeck coefficient is therefore given by Eq. (1.7) with $\mathcal{T}(E) \rightarrow \sigma(E)$. This expression is known as Mott's formula [32, 34].

In non-degenerate semiconductors, the Fermi level is in the band gap in which $\sigma(E)$ is zero. The transport is dominated by carriers in either the valence or conduction band and the transport properties depend on the energy difference between the chemical potential and the transport band edge. Consider a p-type semiconductor in which holes in the valence are the charge carriers. If we consider the band edge to be sharp, so that $\sigma(E)$ is only non-zero for $E < E_v$, we can rewrite equation (1.9) as

$$S_{\text{SC}} = \frac{k_B}{e} \left[\frac{\mu - E_v}{k_B T} + A_v \right], \quad (1.10)$$

where

$$A_v = \frac{\int_{-\infty}^{E_v} dE \sigma(E) \frac{E_v - E}{k_B T} [-n'_F(E)]}{\int_{-\infty}^{E_v} dE \sigma(E) [-n'_F(E)]}. \quad (1.11)$$

The Seebeck coefficient of a non-degenerate semiconductor is therefore directly proportional to the energy difference between the chemical potential and the band edge [30, 33–37]. For n-type semiconductors, the transport takes place in the conduction

⁷The actual conductivity of the material is given by $\sigma = \int dE \sigma(E) [-n'_F(E)]$. For more details about $\sigma(E)$, see e.g. Refs. [31, 32]. In the literature, $-n'_F(E)\sigma(E)$ is sometimes expressed as $\sigma(E)$ and referred to as the differential conductivity [27, 33].

band, and the Seebeck coefficient is $S_{SC,c} = \frac{k_B}{e} \left[\frac{\mu - E_v}{k_B T} - A_c \right]$ [34]. The positive and dimensionless constant A_v depends on the shape of $\sigma(E)$ close to the valence band edge. In both conventional and organic semiconductors, A_v is typically between 2 and 4 [33, 38]. The expression for the Seebeck coefficient in semiconductors in Eq. (1.10) will be useful in Chapter 4, where we will analyze measured Seebeck coefficients of organic semiconductors.

1.1.3 Seebeck coefficient in parallel and series

As described in the beginning of Sec. 1.1, the measured Seebeck coefficient in Eq. (1.3) is the same as S 's in Eqs. (1.1) and (1.2), when the system is a single homogeneous material. However, if the setup is composed of different materials, the measured Seebeck coefficient is a combination of the Seebeck coefficients in the setup. Consider the macroscopic version of the transport equation in Eq. (1.1), $I = G\Delta V + GS\Delta T$, where G is the electrical conductance. If two components are connected in parallel, as shown in Fig. 1.2, and the Seebeck measurement condition $I = 0$ is used, we get the effective Seebeck coefficient of the setup [39]

$$S_{\text{parallel}} = \frac{G_1 S_1 + G_2 S_2}{G_1 + G_2}. \quad (1.12)$$

The effective Seebeck coefficient is therefore the sum of the components weighted by their electrical conductances. If the components are connected in series, the effective Seebeck coefficient is

$$S_{\text{series}} = \frac{S_1 R_{q1} + S_2 R_{q2}}{R_{q1} + R_{q2}}, \quad (1.13)$$

where R_{q2} is the thermal resistance. We can also formulate Eq. (1.13) as $S_{\text{series}} = (S_1 \Delta T_1 + S_2 \Delta T_2) / \Delta T$, where ΔT_i is the temperature drop across sample i , while $\Delta T = \Delta T_1 + \Delta T_2$. In series, the measured Seebeck coefficient is therefore the sum weighted by the temperature drop. Despite the simplicity of Eqs. (1.12) and (1.13), these expressions will be very useful in Chapter 4.

1.2 Local currents

Since the Seebeck coefficient is measured under the zero-net-current-condition, $I = 0$, it is usually assumed that local electric currents cancel as well. However, this is not necessarily true. A simple case in which a local current exists is when two thermoelectric elements are connected in parallel as shown in Fig. 1.2. Even though no electric current flows through the parallel setup, a ring current

$$I_{\text{ring}} = \frac{S_2 - S_1}{R_1 + R_2} \Delta T \quad (1.14)$$

flows in the loop [1, 39]. This might seem surprising at first sight, but it is basically the same as Thomas Seebeck observed in his original experiment. As explained, he connected two different materials in a loop and heated one of the material junctions, which drove an electric current in the loop. No electric current was flowing through his system, and it can therefore be thought of as the setup in Fig. 1.2.

Internal electric currents can also exist in a bulk material if it is either anisotropic [41, 42] or inhomogeneous [43, 44]. Their existence in an inhomogeneous isotropic setup can easily be shown by rewriting Eq. (1.1). If we divide it by σ and take the curl, we get $\nabla \times (\mathbf{j}_e / \sigma) = -\nabla S \times \nabla T$. If the gradient of the Seebeck coefficient has

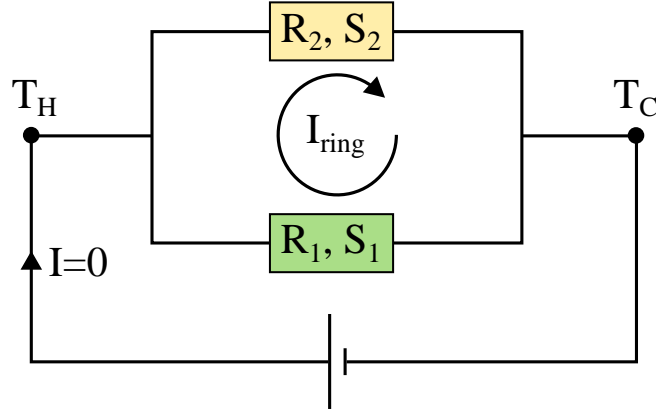


FIGURE 1.2: Schematic illustration of two thermoelectric elements connected in parallel. The electric ring current I_{ring} flows in the loop even though no net current is flowing. The figure is from Ref. [40].

a component perpendicular to the temperature gradient, $\nabla S \times \nabla T \neq 0$, somewhere inside the sample, local electric currents consequently have to exist.

An example of an inhomogeneous system is shown in Fig. 1.3a, where a small cylinder of one material is placed in the center of a larger cylinder of another material (a thought example presented in Ref. [1]). When a temperature difference is applied between the top and bottom, and the Seebeck measurement condition, $I = 0$, is reached, the question is how the effective Seebeck coefficient is calculated. If we could neglect the local currents, the approach would be to solve the steady-state heat equation to obtain the temperature distribution, from which the potential distribution could be calculated, $\mathbf{E} = S\nabla T$. However, the thermoelectric terms in \mathbf{j}_e and \mathbf{j}_q in Eqs. (1.1) and (1.2) affect the temperature distribution and due to the possible existence of local electric currents, Eq. (1.1) cannot simply be rewritten as $\mathbf{E} = S\nabla T$. The proposed solution in Ref. [1] was to solve the coupled continuity equations

$$\begin{aligned}\nabla \cdot \mathbf{j}_e &= 0 \\ \nabla \cdot \mathbf{j}_q &= 0\end{aligned}\tag{1.15}$$

with fixed boundary conditions, ΔT and ΔV , so that the electric current through the setup vanished. This procedure allows internal electric currents to exist even though the net current cancels. In the case of the setup in Fig. 1.3a, the local electric currents in a cross section of the cylinder are shown in Fig. 1.3b. We see that ring currents flow around the material boundary, which is (almost) parallel to the temperature gradient. Even though current passes through the top and bottom surfaces locally, the total current through the surfaces is zero. Internal ring currents like the ones shown in Fig. 1.3b are sometimes referred to as thermoelectric Eddy currents in the literature [42, 43, 45].

Thermoelectrically driven ring currents also exist in single molecule junctions, where the calculation is fully quantum mechanical [1, 40]. This was one of the main results in Ref. [1], and an example is shown for a meta-coupled benzene molecule in Fig. 1.3c. Again, the electric ring current exists even though no net current flows through the junction. We will study these thermoelectrically driven currents in depth in Chapter 3. But first, we will develop the theory to describe local electric currents in single molecule junctions in general.

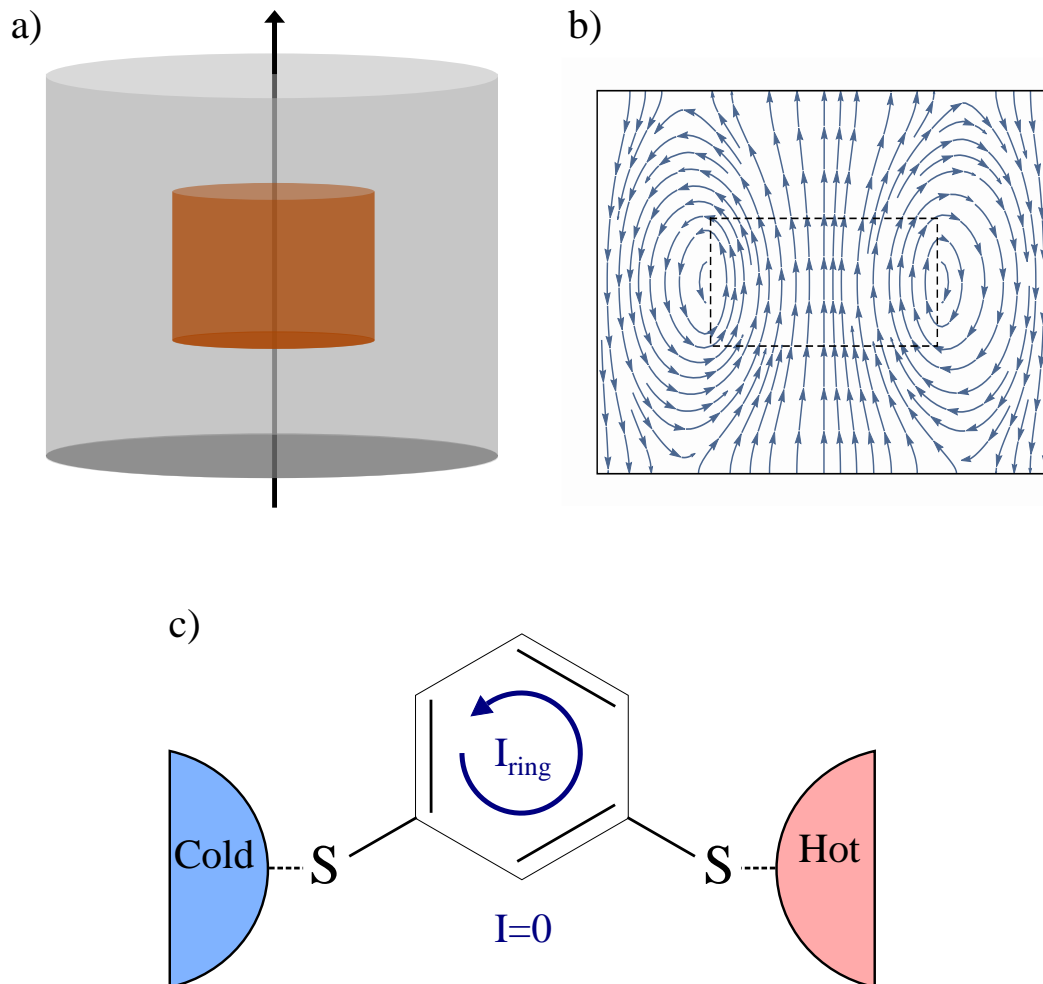


FIGURE 1.3: Internal electric current loops in Seebeck measurements. a) An inhomogeneous cylinder setup in which the grey and brown regions have different material properties. b) Electric current densities in a cross section of the cylinder setup in a Seebeck measurement with $I = 0$. Here, a temperature difference is applied between the bottom and top surfaces, while the sides are considered to be thermally and electrically insulated. c) A molecular junction with meta-coupled benzene. In a Seebeck measurement, a ring current exists in the benzene molecule. (a) and (b) are from Ref. [1] and (c) is from Ref. [40].

Chapter 2

Local currents in single molecule junctions

*This chapter is based on the paper 'J. Phys. Chem. C 2019, **123**, 6, 3817-3822' and its supporting information written by the author and Per Hedegård. The paper is referred to as Ref. [40] in this thesis. In this chapter, we will consider the results that are applicable to nanoscale junctions in general, i.e. the transport can for example be driven by a potential difference alone. We will return to the specific case of thermoelectrically driven ring currents in Chapter 3.*

Around 20 years ago, the first conductance measurements were done on single molecule junctions (SMJ) [46–48]. A SMJ is a metal-molecule-metal configuration, which can be formed by for example using mechanical break junctions or scanning tunneling microscopy. These experimental techniques allow researchers to study properties of individual molecules, and their discovery marks the beginning of the field of molecular electronics [49]. The field is interesting from a fundamental research perspective, but it has also gained a lot of interest because molecules might be important components in future electronic devices [50].

In this chapter, we will study local electric currents in nanoscale setups and in particular in single molecule junctions. Our motivation for the study was to understand thermoelectrically driven currents, which will be the topic of Chapter 3. Many groups have investigated the pathways of an electric current through single molecule junctions [51–56]. When only a potential difference is driving the current, the local currents in ring structured molecules can be split up into ring and transverse components [57]. The interplay between such ring currents and interference features has been studied by Ernzerhof et al. and Solomon et al. [51, 58]. They showed that when the energy passes through a point of destructive interference,¹ there can be a change in the direction of the ring currents. In Sec. 2.2.1, we will derive an analytic expression, which can explain this observation. Our analytic expression can also be used to do a qualitative prediction of the current patterns in symmetric junctions.

2.1 Introduction to NEGF

A useful tool to study quantum transport in nanoscale systems is the non-equilibrium Greens function method (NEGF). We will here go through the basics of NEGF, but more detailed descriptions can be found elsewhere [21, 59]. We will consider the electrons to be non-interacting, so that we can operate in the single particle picture.

¹A molecule is said to have destructive interference at the energy E_0 if $\mathcal{T}(E_0) = 0$.

The Hamiltonian of the system, H , is split into the following components

$$H = H_L + H_M + H_R + H_{LM} + H_{ML} + H_{RM} + H_{MR} \quad (2.1)$$

where H_L (H_R) is the Hamiltonian for the left (right) lead, H_M is the Hamiltonian describing the molecule, and $H_{\alpha\beta}$ describes the coupling between α and β . This can be done by using $(L+M+R)H(L+M+R)$, where L , M , and R are projection operators that project onto the left lead, molecular, and right lead subspaces respectively. It is assumed that the left and right leads are not directly connected. The different elements of the Hamiltonian are illustrated schematically in Fig. 2.1a.

We are interested in the retarded Greens function defined by $(E - H + i\eta)G = 1$, where η is a positive infinitesimal. By using the projection operators, we can get the full Greens function of the molecule²

$$G_M = \frac{1}{E - H_M + \Sigma_L + \Sigma_R}, \quad (2.2)$$

where

$$\Sigma_\alpha = H_{M\alpha}G_\alpha^0 H_{\alpha M} \quad (2.3)$$

is the self-energy from lead α , while $G_\alpha^0(E) = (E - H_\alpha + i\eta)^{-1}$ is the free propagator in lead α . The Greens function G_M is important when we want to calculate different properties of the junction. The transmission through a junction is e.g. given by

$$\mathcal{T}(E) = \text{Tr} \left[\Gamma_L G_M^\dagger \Gamma_R G_M \right], \quad (2.4)$$

where $\text{Tr}[A]$ denotes the trace of the matrix A , while $\Gamma_\alpha = -2 \text{Im} \Sigma_\alpha$. This expression is sometimes referred to as the Caroli formula [60, 61]. As explained in the beginning of Sec. 1.1.1, the transmission function can be used to calculate the electric current through a junction by using the Landauer formula in Eq. (1.4).

In the following, we want to calculate the local currents in molecular junctions. We are therefore interested in calculating the expectation value of an observable in the molecular subspace, $A = MAM$. To do so, the contributions from all the scattering states incoming from both the left and right leads need to be summed up. This can be done in a neat way in NEGF by using the single particle nonequilibrium density matrix [21, 59, 62, 63]

$$\rho_M = 2 \sum_{\alpha, k} n_F^\alpha(E_k) M |\psi_{\alpha k}\rangle \langle \psi_{\alpha k}| M \quad (2.5)$$

$$= \frac{1}{\pi} \sum_{\alpha} \int dE n_F^\alpha(E) G_M \Gamma_\alpha G_M^\dagger, \quad (2.6)$$

where $|\psi_{\alpha k}\rangle$ is the scattering state incoming from lead α with the quantum number k . The derivation from Eq. (2.5) to Eq. (2.6) is shown in Appendix A.1. With this, the nonequilibrium expectation value is just $\langle A \rangle = \text{Tr}[\rho_M A]$ [63], which will be useful in the following section.

²This can be done by rewriting the three equations $L(E - H + i\eta)GM = 0$, $M(E - H + i\eta)GM = 1$, and $R(E - H + i\eta)GM = 0$ as done in e.g. Ref. [59] in matrix form. The molecular Greens function is $G_M = MGM$.

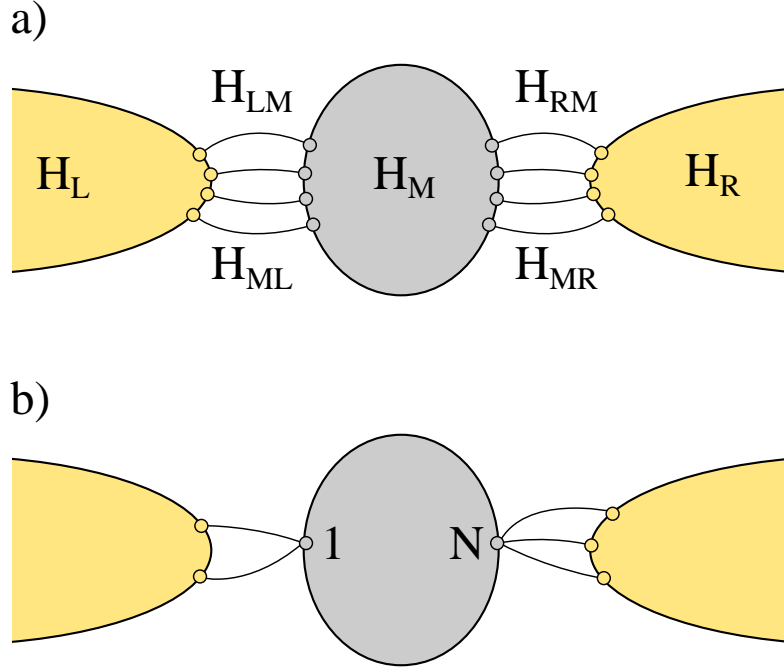


FIGURE 2.1: Schematic illustration of a single molecule junction. The grey oval represents the molecule, which is connected to the left and right contacts. a) A general junction in which multiple elements couple the molecule to the contacts. b) A situation in which the left lead couples to site 1 on the molecule, while the right lead couples to site N .

2.2 Local currents

We now want to calculate the local electric currents in a junction. We will work with tight-binding Hamiltonians

$$H = \sum_i \varepsilon_i |i\rangle\langle i| - \sum_{\langle ij \rangle} t_{ij} (|i\rangle\langle j| + |j\rangle\langle i|), \quad (2.7)$$

where $|i\rangle\langle i|$ is the atomic orbital for atom i , ε_i is the onsite energy, and t_{ij} is the real and positive hopping matrix element between atoms i and j . With this Hamiltonian, the local current operator is³

$$\hat{I}_{ij} = \frac{ie}{\hbar} t_{ij} (|i\rangle\langle j| - |j\rangle\langle i|), \quad (2.8)$$

which describes the electric current between the local orbitals i and j . To get the actual local current, we need to take into account the contributions from all the scattering states. Adding up all these contributions by using $I_{ij} = \langle \hat{I}_{ij} \rangle$, as described in the previous section, we get [62]

$$I_{ij} = \frac{2e}{h} \int dE \mathcal{T}_{ij}(E) [n_F^L(E) - n_F^R(E)], \quad (2.9)$$

³For the derivation, see e.g. Ref. [62].

where the bond transmission is given by

$$\mathcal{T}_{ij}(E) = \frac{\hbar}{e} \text{Tr}[\Gamma_L G_M^\dagger \hat{I}_{ij} G_M]. \quad (2.10)$$

To obtain this result, we used that $\text{Tr}[G_M \Gamma_L G_M^\dagger \hat{I}_{ij}] = -\text{Tr}[G_M \Gamma_R G_M^\dagger \hat{I}_{ij}]$. This is physically intuitive, since it implies that the local currents vanish for $\Delta V = \Delta T = 0$. In Appendix A.2, it is shown that the relation is true for any observable that reverses under time-reversal. With Eqs. (2.9) and (2.10), it is possible to calculate the local electric currents for any junction under the applied temperature and potential differences $\Delta T = T_L - T_R$ and $\Delta V = -(\mu_L - \mu_R)/e$. If the current is driven by a small potential difference, we can expand the Fermi functions to first order in the μ 's, and at low temperatures

$$I_{ij}^V \approx \frac{2e^2}{h} \mathcal{T}_{ij}(\mu) \Delta V. \quad (2.11)$$

Though the bond transmission in Eq. (2.10) is easy to calculate, the compact expression is not easy to interpret. In the following section, we will see that the expression for the bond transmission can be put on a simpler form in most single molecule junctions.

2.2.1 Local currents in single molecule junctions

In this section, we will see that the bond transmission in Eq. (2.10) can be put on a simpler form, when the self-energies can be written as

$$\begin{aligned} \Sigma_L &= a_L |1\rangle\langle 1| \\ \Sigma_R &= a_R |N\rangle\langle N|, \end{aligned} \quad (2.12)$$

where $|1\rangle$ and $|N\rangle$ are some orbitals on the molecule. This is the case when the leads only couple to the molecule at single atomic sites as illustrated schematically in Fig. 2.1b. This is usually a good assumption in single molecule junctions, since the molecule is often connected to the contacts via molecular anchor groups such as the thiol group in Fig. 1.3c, and it is widely used in theoretical studies [55, 57, 64, 65]. If the contact is modeled as a 1D tight-binding chain, the self-energies can also be written as in Eq. (2.12), where $|1\rangle$ and $|N\rangle$ can be any linear combination of atomic orbitals.⁴

For a junction with the self-energies in Eq. (2.12), the bond transmission in Eq. (2.10) can be put on a simpler form. This discovery was initially made by the author by using the transfer matrix method,⁵ but it is easier to get a general result with the NEGF method. In Appendix A.3, we derive that

$$\mathcal{T}_{ij}(E) = \gamma_{ij}(E) \mathcal{T}(E) \quad (2.13)$$

⁴Take the example where the left 1D chain couples to two sites, $H_{ML} = -t_{c1} |1\rangle\langle a| - t_{c2} |2\rangle\langle a| = -t_c |L\rangle\langle a|$, where $|a\rangle$ is the outermost orbital of the 1D chain and $|L\rangle = \frac{t_{c1}}{t_c} |1\rangle + \frac{t_{c2}}{t_c} |2\rangle$. In this case, the left self-energy can be written as $\Sigma_L = H_{ML} G_L^0 H_{LM} = t_c^2 \langle a| G_L^0 |a\rangle |L\rangle\langle L|$.

⁵Using the transfer matrix method, we first modeled the leads as semi-infinite chains of atoms for which the result in Eqs. (2.13) and (2.14) is true. We studied different concrete models for the leads just as in chapter 3 in Ref. [66]. However, we switched to the NEGF method in which the information about the leads is kept in the self-energies.

where $\gamma_{ij}(E)$ only depends on the isolated molecule

$$\gamma_{ij}(E) = t_{ij} \frac{G_{1i}^0 G_{jN}^0 - G_{1j}^0 G_{iN}^0}{G_{1N}^0}. \quad (2.14)$$

Here $G_{ij}^0 = \langle i | (E - H_M)^{-1} | j \rangle$ is an element of the Greens function of the isolated molecule. It is intuitive, that the bond transmissions go to zero with the transmission. However, the above factorization of the bond transmission is interesting since all the information about the leads is contained in the transmission function, \mathcal{T} , while the local information is found in $\gamma_{ij}(E)$. The analytic expression in Eqs. (2.13) and (2.14) is one of the main results of this chapter, and we will use it to analyze local currents in the following sections. It has previously been found by Tsai et al.,⁶ that the local transmission is proportional to $(G_{1i}^0 G_{jN}^0 - G_{1j}^0 G_{iN}^0)$, and that it is the only factor that depends on the sites i and j [67]. However, Tsai et al. did not realize that it could be put on the simple form in Eqs. (2.13) and (2.14).

In Fig. 2.2, the local transmissions are plotted for an anthracene and a biphenyl junction. The tight-binding setup and parameters are the same as in Chapter 3, but the numbers are not relevant for the discussion in this chapter. We see that some paths in the molecules are described by the same bond transmission, and these are marked with the same colors. Additionally, we observe that the bond transmissions are symmetric around $E = 0$. In the following sections, we will use our derived analytic tool in Eqs. (2.13) and (2.14) to describe these observations. Both of the junctions in Fig. 2.2 have been investigated by Rai et al. [57], but they did not explain these features.

The current patterns in Fig. 2.2 can in principle be modified by a magnetic field, which itself induces ring currents in the molecule. In this way, some of the bond currents could be turned off and a variety of current patterns could be obtained. However, it has been studied theoretically whether the local currents can be controlled by a magnetic field and unrealistically large fields are required to do so [68, 69].

The simplification in Eq. (2.13) is only true in the single channel case, i.e. when only one transport channel carries the current. In the case of multiple channels, the self-energies cannot be put on the simple form in Eq. (2.12). We have put a lot of effort into deriving an expression similar to Eq. (2.13), which is applicable in the multi-channel case, but we were not able to do so. A natural way to express the local currents, though, is to use the basis of transmission eigenchannels. A transmission eigenchannel $|p\rangle$ is an eigenvector of $\mathbf{t}^\dagger \mathbf{t}$, where \mathbf{t} is the transmission matrix [20, 70, 71],

$$\mathbf{t}^\dagger \mathbf{t} |p\rangle = \mathcal{T}^p |p\rangle. \quad (2.15)$$

Here \mathcal{T}^p is the transmission probability of eigenchannel p . The full transmission function is $\mathcal{T} = \text{Tr}[\mathbf{t}^\dagger \mathbf{t}]$ and by comparing this expression to the Caroli formula in Eq. (2.4), we see that NEGF analogue is obtained by defining $\mathbf{t} \equiv \Gamma_R^{1/2} G_M \Gamma_L^{1/2}$ [72]. In other words, $|p\rangle$ is an eigenvector of $\Gamma_L^{1/2} G_M^\dagger \Gamma_R G_M \Gamma_L^{1/2}$. Using this basis, the bond transmission in Eq. (2.10) can be written as

$$\mathcal{T}_{ij} = \sum_p \mathcal{T}_{ij}^p, \quad (2.16)$$

where the \mathcal{T}_{ij}^p 's are eigenvalues of the matrix $\frac{\hbar}{e} \Gamma_L G_M^\dagger \hat{I}_{ij} G_M$. This choice of basis has the advantage, that only a few eigenchannels carry the current in narrow junctions

⁶The author realized this while writing the thesis.

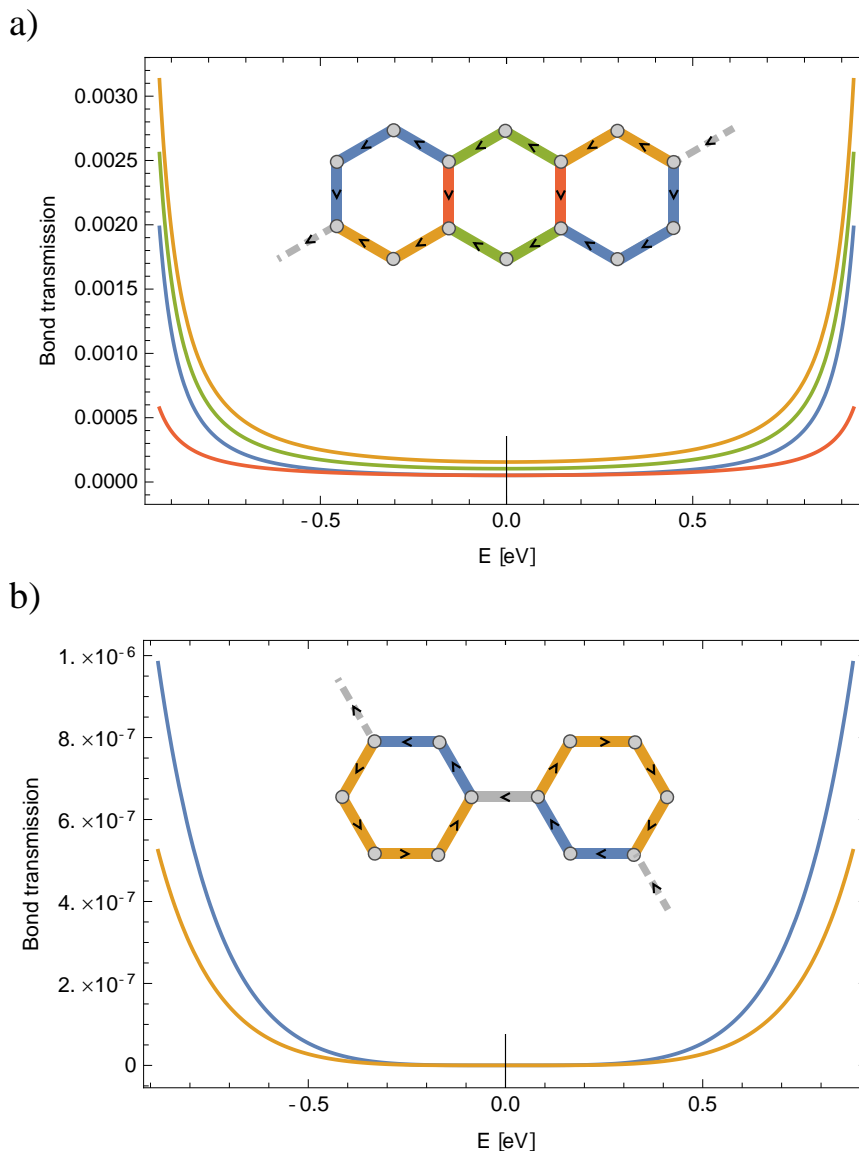


FIGURE 2.2: Bond transmissions for an anthracene junction in (a) and a biphenyl junction in (b). The directions of positive transmission are indicated with arrows on top of the bonds and the colors relate the different bonds to the graphs. The tight-binding parameters used in the calculation are the same as in Chapter 3. The HOMO/LUMO energies are ± 1.04 eV for anthracene and ± 1.76 eV for biphenyl.

[70]. Consequently, most of the eigenchannels are “closed”, $\mathcal{T}^p = 0$, and the same goes for most of the local current contributions, $\mathcal{T}_{ij}^p = 0$.

2.3 Analysis of local currents in single molecule junctions

With the analytic tool derived in the previous section, we can now analyze different types of molecular junctions. In Sec. 2.3.1, we develop a tool to predict current patterns in symmetric junctions. In Sec. 2.3.2, we show that the bond transmissions in alternant molecules is symmetric in energy, and finally we build some mathematical

understanding about the connection between local currents and destructive interference in Sec. 2.3.3.

2.3.1 Qualitative prediction of currents

The current patterns shown in Fig. 2.2 can be predicted qualitatively from a symmetry argument which follows from Eq. (2.14). The prediction rule is illustrated graphically in Fig 2.3 and it is based on the following argument: Consider a molecule that is invariant under a rotation O_R , which interchanges site 1 and site N

$$O_R^\dagger H_M O_R = H_M. \quad (2.17)$$

The rotation will take site i into site i' , $O_R |i\rangle = |i'\rangle$. Using this symmetry, we can rewrite the numerator in Eq. (2.14)

$$\begin{aligned} G_{1j}^0 G_{iN}^0 &= \langle 1 | G^0 | j \rangle \langle i | G^0 | N \rangle \\ &= \langle 1 | O_R^\dagger G^0 O_R | j \rangle \langle i | O_R^\dagger G^0 O_R | N \rangle \\ &= \langle N | G^0 | j' \rangle \langle i' | G^0 | 1 \rangle \\ &= G_{i'j'}^0 G_{1N}^0. \end{aligned} \quad (2.18)$$

By doing this on both terms in Equation (2.14), we get $\gamma_{ij} = -\gamma_{i'j'}$ and consequently

$$I_{ij} = -I_{i'j'}, \quad (2.19)$$

where I_{ij} is the local current in Eq. (2.9). This fact can be used to graphically predict the current pattern in a molecular junction with a symmetry: Draw a current between all the connected sites in the molecule, rotate one contact point into the other and reverse the currents. According to Eq. (2.19), the current pattern before and after the operations has to be the same. This is illustrated for a naphthalene junction in Fig. 2.3. Notice that the result $I_{ij} = -I_{i'j'}$ is true for any applied bias or temperature difference and can therefore also be used to qualitatively predict the through-current. This symmetry argument can e.g. be used to predict the current patterns in the symmetric junctions in Refs. [57, 73].

We also tried another approach to understand and predict the current pattern. One could naively think that the current patterns can be understood by looking at the highest occupied molecular orbital (HOMO) and the lowest unoccupied molecular orbital (LUMO), since these are closest to the chemical potentials of the contacts. We have examined this by decomposing the molecular part of the scattering states into the molecular orbitals, but we found that not only the HOMO and LUMO contribute to the currents. The weights of the molecular orbitals were found to be distributed in an unsystematic manner.

2.3.2 Alternant molecules

Many of the molecules studied in e.g. Ref. [57] and in Chapter 3 are so-called alternant hydrocarbons. An alternant hydrocarbon is a conjugated molecule in which the carbon atoms can be divided into two sub-lattices (historically called the starred and unstarred atoms) in such a way that starred atoms only connect to unstarred atoms and vice versa [74, 75]. Examples of alternant molecules are benzene, naphthalene, and anthracene. These molecules follow the Coulson-Rushbrooke pairing theorem which e.g. states that the molecular orbital energies are symmetrically spread around a zero-energy level and that there is a sign change of the molecular orbitals in one

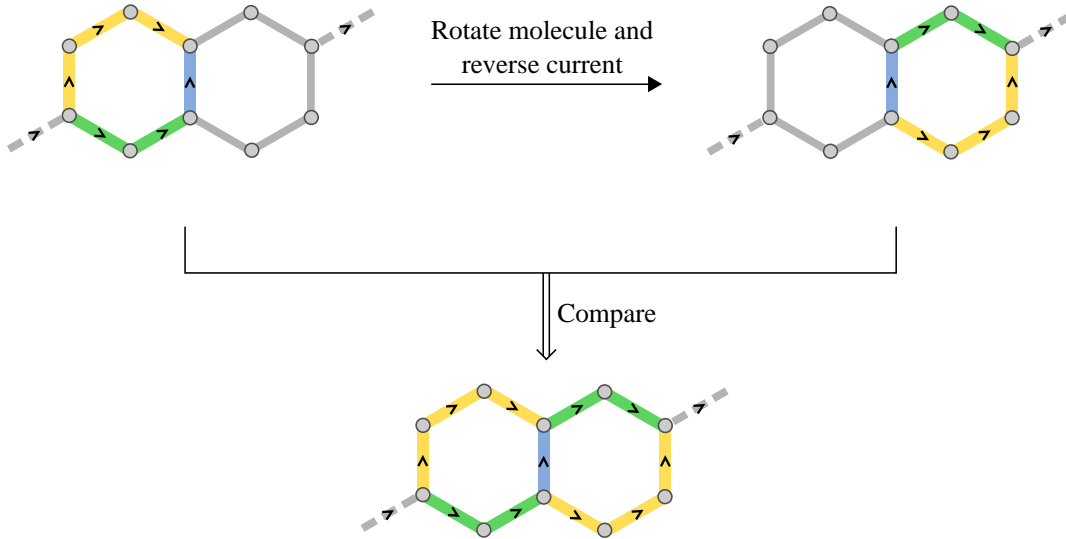


FIGURE 2.3: Graphical procedure to predict the local current patterns in symmetric junctions. Initially guessed currents are marked with different colors in the top left of the figure. After rotating one contact point into the other and reversing the currents, the local currents are unchanged. We can therefore compare the currents before and after the operations in order to obtain the local current pattern. Notice that the initially drawn arrows could as well point in the opposite directions.

of the sublattices when comparing a symmetry pair such as the HOMO and LUMO [74, 75]. Using the Coulson-Rushbrooke pairing theorem, we show in Appendix A.4 that

$$G_{ij}^0(-E) = \mp G_{ij}^0(E), \quad (2.20)$$

where the upper (lower) sign is when i and j are on the same (different) sub-lattice. By using this symmetry in Eq. (2.14), we get that γ is an even function in energy for alternant hydrocarbons

$$\gamma_{ij}(E) = \gamma_{ij}(-E). \quad (2.21)$$

This is exactly what we observed in Fig. 2.2 for anthracene and biphenyl, which are both alternant molecules.

2.3.3 Interference and local currents

As described in the introduction, the connection between local currents and interference has been studied in the literature. Both Ernzerhof et al. and Solomon et al. have observed that the local transmissions can have opposite signs when comparing energies slightly below and above the an energy of destructive interference [51, 58]. In this section, we will use Eqs. (2.13) and (2.14) to build some understanding about this observation. We will start by considering the total transmission through a junction. For the self-energies in Eq. (2.12), the transmission is

$$\mathcal{T}(E) = |G_{1N}|^2 k_L k_R, \quad (2.22)$$

where $k_\alpha = -2\text{Im} a_\alpha$ and $G_{1N} = \langle 1|G_M|N \rangle$. We can write the Greens function of the molecule as a Dyson equation (omitting again the subscript M on all G 's)

$$\begin{aligned} G &= G^0 + G^0 (\Sigma_L + \Sigma_R) G \\ &= G^0 + a_L G^0 |1\rangle\langle 1| G + a_R G^0 |N\rangle\langle N| G. \end{aligned} \quad (2.23)$$

Consider now the element that appears in Eq. (2.22). We can rewrite it as

$$G_{1N} = G_{1N}^0 \frac{1 + a_R G_{NN}^0}{1 - a_L G_{11}^0}. \quad (2.24)$$

Destructive interference occurs at the energy E_0 when $\mathcal{T}(E_0) = 0$ and consequently $G_{1N} = 0$. The interesting destructive interference points are the ones that are related to the structure of the molecule. Since the fraction in the above equation depends on the leads, we are only interested in interferences at which $G_{1N}^0 = 0$. Inserting Eqs. (2.14), (2.22), and (2.24) into Eq. (2.13), we arrive at

$$\mathcal{T}_{ij} \propto t_{ij} (G_{1i}^0 G_{jN}^0 - G_{1j}^0 G_{iN}^0) G_{1N}^0 \quad (2.25)$$

where the proportionality factor depends on the leads.⁷ With this expression, we can calculate whether there is a sign change in the bond transmission or not by analyzing the elements of $G_M^0 = (E - H_M)^{-1}$. We will now go through a few examples that have been studied in the literature.

Benzene has only four different Greens function elements: G_{11}^0 , G_{12}^0 , G_{13}^0 , and G_{14}^0 . An ortho-coupled benzene junction has been investigated in Ref. [58], in which it was shown that the local currents have different signs slightly below and above the LUMO energy, $\varepsilon_{\text{LUMO}} = -t_M$, where t_M is the hopping amplitude on the molecule. By plotting the the four different Greens function elements, it is seen that they all have opposite signs below and above $\varepsilon_{\text{LUMO}}$. From Eq. (2.25) it is therefore clear that the bond transmissions have a sign change.

Meta coupled benzene has destructive interference at $E = 0$.⁸ Around this energy, the Greens function elements G_{11}^0 and G_{13}^0 change sign. If we index the atoms with increasing numbers around the ring and consider the leads to couple to sites 1 and 5, the bond transmission from site 1 to 2 is for example

$$\begin{aligned} \mathcal{T}_{12} &\propto t_M (G_{11}^0 G_{25}^0 - G_{12}^0 G_{15}^0) G_{15}^0 \\ &= t_M (G_{11}^0 G_{14}^0 - G_{12}^0 G_{13}^0) G_{13}^0, \end{aligned} \quad (2.26)$$

where $G_{15}^0 = G_{13}^0$ and $G_{25}^0 = G_{14}^0$ for symmetry reasons, and where t_M is again the hopping amplitude in the molecule. Since only G_{11}^0 and G_{13}^0 change sign, there is no sign change in \mathcal{T}_{12} around $E = 0$. This was also observed by Solomon et al. (see Fig. S4 in Ref. [51]). However, by introducing next-nearest (NN) neighbor coupling in the meta-coupled benzene junction, they found that the transmission between some of the NN sites reversed (See Figs. 3 and S4 in Ref. [51]). This can again be explained by Eq. (2.25): A lot of new Greens function elements are introduced by the NN neighbor coupling. For the bond transmissions that reverse, the G_{1N}^0 in Eq. (2.25) has a sign change, while the parenthesis factors do not.

⁷The proportionality factor is

$$\left| \frac{1 + a_R G_{NN}^0}{1 - a_L G_{11}^0} \right|^2 k_L k_R,$$

⁸ $E = 0$ is the energy right between the HOMO and LUMO.

The above two examples demonstrate that the derived analytic tool in Eqs. (2.13)-(2.14) can be used to analyze the reversal of the local currents around a point of destructive interference. One can probably get a better understanding of the current reversals by looking deeper into the connection between the Greens function elements in Eq. (2.25).

2.4 Conclusions

In this chapter, we have described the theory to calculate local currents in the NEGF formalism. In the case of single molecule junctions, we have shown in Sec. 2.2.1 that the bond transmission can be written as a product between the transmission function and a function γ_{ij} , which only depends on the properties of the isolated molecule. The analytic expression for γ_{ij} in Eq. (2.14) is a useful tool when we want to analyze the local currents in a junction: In Sec. 2.3.1, we used it to develop a graphical procedure to predict current patterns in rotationally symmetric molecules (including the marked contact points). In Sec. 2.3.2, we described mathematically why the bond transmission is symmetric in energy in alternant molecules. Finally, we used the analytic tool to build some understanding about the connection between local currents and interferences in Sec. 2.3.3. We showed that the reversion of local currents when passing through a point of destructive interference can be described by sign changes in the elements of the Greens function of the isolated molecule, G_M .

Chapter 3

Thermoelectrically driven ring currents

*This chapter is based on the paper 'J. Phys. Chem. C 2019, **123**, 6, 3817-3822' and its supporting information written by the author and Per Hedegård. The paper is referred to as Ref. [40]. This chapter builds on the results from the previous chapter and considers the special case in which temperature and electric potential differences are applied so that the net current cancels. Thermoelectrically driven ring currents in single molecules were initially discovered during the author's master's project [1].*

With the theory described in Chapter 2, we will now calculate and analyze the thermoelectrically driven ring currents introduced in Sec. 1.2. First, we will go through the single molecule results from Ref. [40]. We will then move on to the low temperature approximation of the currents and describe mathematically why the local currents change direction twice close to some interference points. Finally, in Sec. 3.2, the existence of ring currents in a quantum mechanical calculation of gated graphene nanoribbons is presented.

3.1 Thermoelectrically driven ring currents in single molecules

We will use tight-binding Hamiltonians to describe the single molecule junctions as illustrated for para-coupled benzene in Fig. 3.1. Here t_M is the hopping element in the molecule, t_c is the coupling between the leads and the molecule, and t_L (t_R) is the hopping element in the left (right) lead. The model parameters are chosen as shown in Table 3.1. Especially the coupling, t_c , and the position of μ relative to the molecular orbitals are difficult to estimate and they vary from junction to junction. Our choice of parameters results in a conductance $G \approx 10^{-3}G_0$ for para-connected benzene at $\mu = 0.7 \epsilon_{\text{LUMO}}$.

The local currents are calculated using Eqs. (2.9) and (2.10),¹ in which the self-energies of the leads are needed. As illustrated in Fig. 3.1, we use semi-infinite chains to model the leads. For these leads, analytic expressions for the self-energies can be derived by following the procedure in Ref. [66]. The derivation is shown in Appendix A.5.1. In this chapter, we are interested in local currents in Seebeck-type experiments, where the electric currents through the junctions cancel. For a temperature difference $\Delta T = T_L - T_R$ and a fixed μ_L , we therefore use the condition $I = 0$ in the Landauer equation in Eq. (1.4) to obtain μ_R . Inserting these ΔT and $\Delta V = -(\mu_L - \mu_R)/e$ into Eq. (2.9), we can obtain the thermoelectrically driven currents.

¹We can as well use Eqs. (2.13) and (2.14), which give the same results.

TABLE 3.1: The tight-binding parameters used in the single molecule calculations.

Parameter	Value
t_M	2.5 eV
$t_L = t_R$	5 eV
t_c	0.6 eV
$\varepsilon_M = \varepsilon_L = \varepsilon_R$	0
T_L	295 K
T_R	300 K

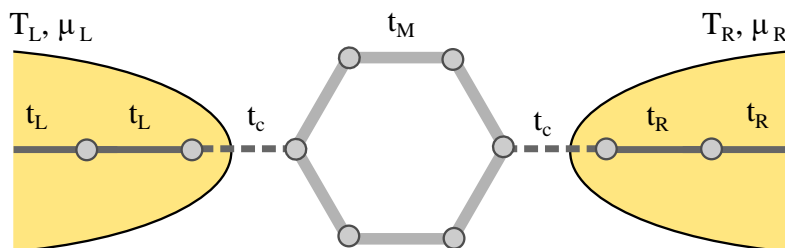


FIGURE 3.1: Illustration of the tight-binding model for a para-connected benzene junction. The leads are modeled as semi-infinite 1D chains.

The results for different benzene, naphthalene, and anthracene junctions are shown in Figure 3.2. We see that very different current patterns can be obtained depending on how the molecules are connected to the leads. The benzene results demonstrate that the paths of the ring have to differ for a current to exist. In naphthalene, ring currents of either opposite or same directions can be generated depending on how the molecule is connected to the contacts. In the case of two adjacent ring currents with same direction and intensity, the current pattern is a single current along the perimeter of the naphthalene molecule. In anthracene, we see that two separated ring currents of opposite directions can be generated and that ring currents of different intensities can exist. The thermoelectrically driven local currents are small, but they are very sensitive to the choice of parameters. As an example, if we set $t_c = 0.5 t_M$, the resulting ring current in meta-coupled benzene is 0.34 nA for $\mu_L = 0.8 \varepsilon_{\text{LUMO}}$.

Due to the symmetries of the junctions in Fig. 3.2, the current patterns can be predicted by using the rules developed in Sec. 2.3.1.² Since no current flows through the junction, the initial guess in the graphical procedure is simpler and it is shown for one of the anthracene junctions in Fig. 3.3. Remember that the procedure does not say anything about the direction and strength of the current; it just predicts the pattern.

Suppose now that we can gate the molecule in the junction and thereby shift the molecular orbital energies relative to the chemical potential. In Fig. 3.4, the ring currents are plotted as a function of the chemical potential for six different molecular junction. The clockwise currents are plotted as solid lines, while the counterclockwise currents are represented by dashed lines. The three molecules to the left are alternant, and we observe that the ring currents are odd as a function of μ . We will explained

²The rules apply to all the junctions in Fig. 3.2 except for the substituted benzene in the upper right of the figure, which is not symmetric.

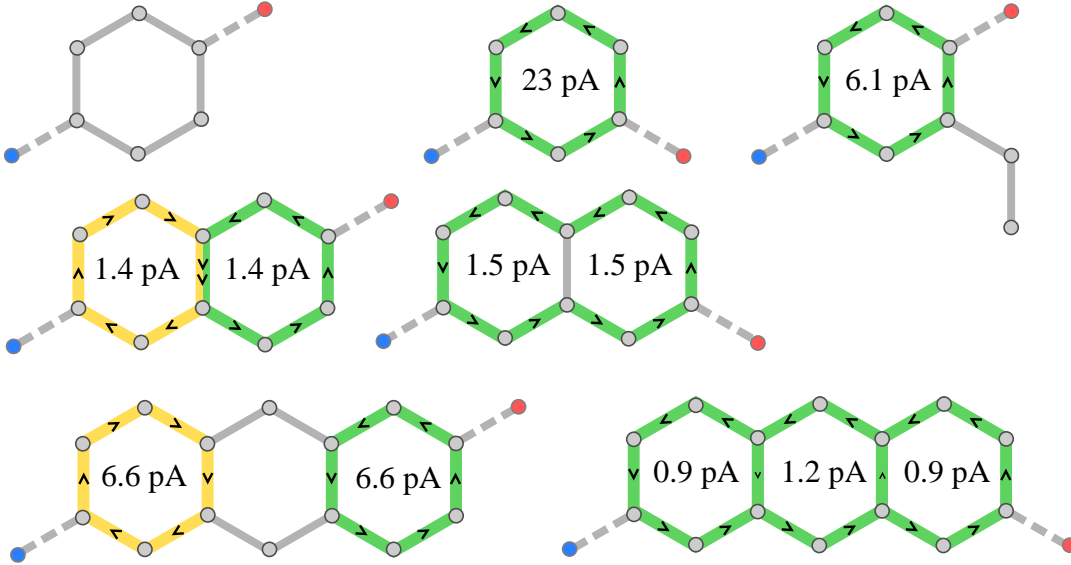


FIGURE 3.2: Electric bond currents for different single molecular junctions at $\mu_L = 0.8 \epsilon_{\text{LUMO}}$. The arrows together with the colors indicate the directions of the ring currents, while the blue and red dots indicate the cold and hot contacts, respectively.

this feature in the following section. The naphthalene junction (the middle left in Fig. 3.4) has destructive interference at $\pm 1.27 \text{ eV}$ around which the ring currents change sign twice. This interesting behavior is different from the currents discussed in Sec. 2.3.3, which only change sign once close to some destructive interference points. We will return to this observation in Sec. 3.1.2. The three junctions to the right in Fig. 3.4 show how the currents can behave in non-alternant molecules. One interesting observation here is that the azulene junction in the bottom right of Fig. 3.4 has no destructive interference between the HOMO and LUMO, but one of the ring currents turns off at $\mu = 0$.

Thermoelectrically driven ring currents can be observed by measuring the induced magnetic field just as Thomas J. Seebeck did 200 years ago. As the system gets smaller, this becomes more difficult. If we approximate a benzene unit as a ring with radius $r = 1.4 \text{ \AA}$, a ring current of 1 pA would induce a magnetic field of $B = 4.5 \text{ nT}$ in the center of the ring according to the Biot-Savart law.

3.1.1 Low temperature approximations

Under the zero-net-current condition, local currents are related to the slope of γ_{ij} . To show this, we expand the Fermi functions in Eq. (2.9) to linear order in the temperatures and potentials, $n_F^L(E) - n_F^R(E) \approx -n_F'(E)[-e\Delta V + \beta(E - \mu)k_B\Delta T]$. With this, we can express the total current as

$$I = \frac{2e}{h} [-e\Delta V \langle \mathcal{T} \rangle + k_B\Delta T \langle \mathcal{T}x \rangle] = 0, \quad (3.1)$$

where we have introduced $x = \beta(E - \mu)$ and the notation

$$\langle g(E) \rangle = \int dE [-n_F'(E)]g(E). \quad (3.2)$$

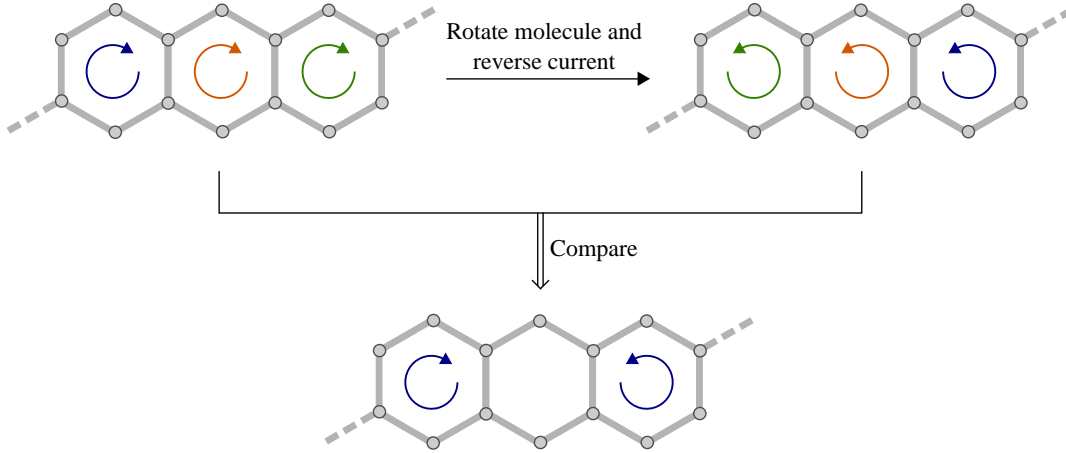


FIGURE 3.3: For the anthracene junction, we draw an initial guess for the ring currents. The colors indicate that the currents can have different amplitudes and directions. After a rotation, which brings site 1 into site N and a reversal of the currents, the currents have to be unchanged. The symmetry argument predicts the results in Fig. 3.2.

By rearranging Eq. (3.1), we get the connection between the potential difference and the temperature difference, $e\Delta V = k_B\Delta T \frac{\langle \mathcal{T}x \rangle}{\langle \mathcal{T} \rangle}$. Here $-\frac{k_B}{e} \frac{\langle \mathcal{T}x \rangle}{\langle \mathcal{T} \rangle}$ is just the Seebeck coefficient shown in Eq. (1.6). Using the introduced notation for the local currents in Eq. (2.9) (omitting the subscripts of γ)

$$\begin{aligned} \tilde{I}_{ij} &= \frac{2e}{h} [-e\Delta V \langle \gamma \mathcal{T} \rangle + k_B\Delta T \langle \gamma \mathcal{T} x \rangle] \\ &= \frac{2e}{h} k_B\Delta T \left[\langle \gamma \mathcal{T} x \rangle - \frac{\langle \mathcal{T} x \rangle}{\langle \mathcal{T} \rangle} \langle \gamma \mathcal{T} \rangle \right], \end{aligned} \quad (3.3)$$

where the tilde in \tilde{I}_{ij} indicates that it is a local current under the zero-net-current condition. We can now do a Sommerfeld expansion to evaluate the brackets. For a general function $g(E)$, which is smooth on the scale of $k_B T$,

$$\begin{aligned} \langle g(E) \rangle &\approx g(\mu) + cg''(\mu) \\ \langle g(E)x \rangle &\approx 2\beta cg'(\mu), \end{aligned} \quad (3.4)$$

where $c = \pi^2/(6\beta^2)$ [6]. Including only the lowest order terms, we get the low temperature approximation

$$\tilde{I}_{ij}(\mu) \approx \frac{2e}{h} \frac{\pi^2}{3} (k_B T)(k_B \Delta T) \gamma'_{ij}(\mu) \mathcal{T}(\mu). \quad (3.5)$$

The above approximation is good at low temperatures away from interference points and resonances. To obtain strong local currents, Eq. (3.5) indicates that $\gamma_{ij}(E)$ has to be steep at the chemical potential and that the transmission through the molecule has to be large. For alternant molecules, we found in Sec. 2.3.2 that the γ_{ij} 's are even in energy. Consequently, $\tilde{I}_{ij}(-\mu) = -\tilde{I}_{ij}(\mu)$ for alternant molecules.

Close to destructive interferences (about $10 k_B T$), we need to include more terms

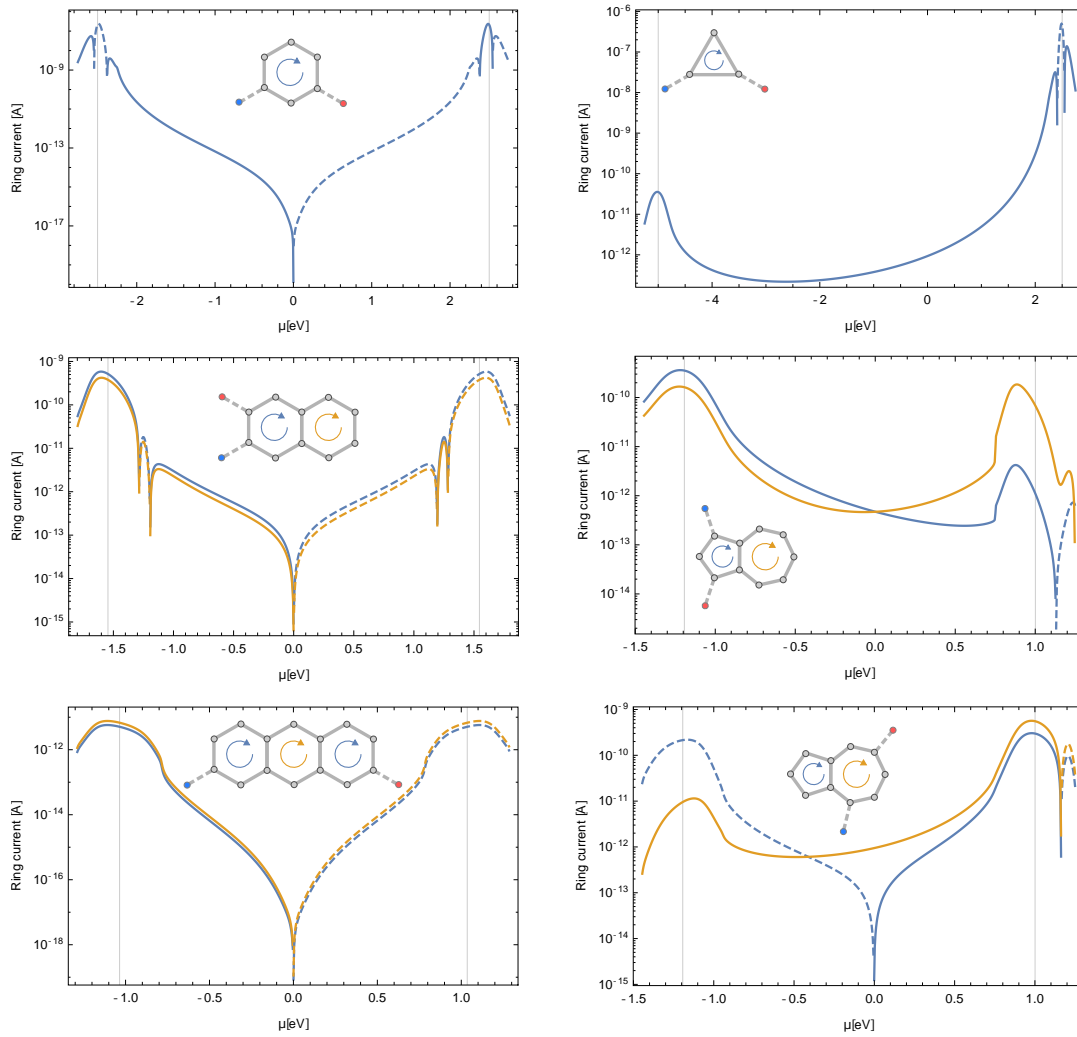


FIGURE 3.4: Ring currents plotted as a function of the chemical potential of the left lead relative to the molecular orbital energies. The chemical potential of the right lead is calculated so that there is no through current. The currents are calculated using Eq. (2.9) with the parameters in Table 3.1. Solid lines represent clockwise currents while dashed lines represent counterclockwise currents. The HOMO and LUMO are shown as vertical lines.

in the Sommerfeld expansion, which give a correction to Eq. (3.5). We will do this in the following section.

3.1.2 Thermoelectrically driven currents close to destructive interferences

Close to destructive interference, we have to be a bit more careful. At an energy of destructive interference E_0 , the transmission function is zero, $\mathcal{T}(E_0) = 0$, and we need to include the second order derivative term in the expansion of $\langle \mathcal{T} \rangle$. Combining

Eqs. (3.3) and (3.4), we get (all the functions below are evaluated at $E = \mu$)

$$\tilde{I}_{ij} \approx \frac{2e}{h} 2\beta c k_B \Delta T \left[(\gamma \mathcal{T})' - \frac{\mathcal{T}'}{\mathcal{T} + c\mathcal{T}''} (\gamma \mathcal{T} + c(\gamma \mathcal{T})'') \right] \quad (3.6)$$

$$= \frac{2e}{h} \frac{\pi^2}{3} (k_B T)(k_B \Delta T) \left[\gamma' \mathcal{T} - c\mathcal{T}' \frac{\gamma'' \mathcal{T} + 2\gamma' \mathcal{T}'}{\mathcal{T} + c\mathcal{T}''} \right]. \quad (3.7)$$

At low temperatures, the second term in the brackets is small. Even at room temperature, $c \approx 10^{-3}(\text{eV})^2$. However, as we will see in the following, the term plays an important role close to some destructive interference points.

As explained in Sec. 2.3.3, the interesting destructive interferences occur at energies E_0 where $G_{1N}^0(E_0) = 0$. Since G_{1N}^0 appears in the denominator of γ_{ij} ,³ γ_{ij} has a pole at E_0 unless the numerator cancels as well. An example in which the numerator does cancel is meta-coupled benzene as plotted in the upper left of Fig. 3.4. Meta-coupled benzene has destructive interference at $E = 0$, $\mathcal{T}(0) = 0$, but γ_{ij} is continuous in the domain around this energy, since its numerator cancels. The reason is that benzene is an alternant molecule so that γ_{ij} is an even function in energy as explained in Sec. 2.3.2. When the interference occurs at such a symmetry point,⁴ the ring currents are well described by the approximation in Eq. (3.5), which is demonstrated for meta-coupled benzene in Fig. 3.5a. Here the blue curve is calculated using Eq. (2.9) and (2.10), while the dashed is obtained from Eq. (3.5). Notice that the currents are extremely small, but this is just an example to show the consequence of the symmetry in alternant molecules.

If we modify one of the onsite energies in the meta-coupled benzene, it is no longer alternant and the interference point is shifted. As a consequence, the ring current will now get a peak on top of the low-temperature approximation as shown in Fig. 3.5b. This can be understood in the following way: For the modified benzene junction, γ_{ij} has a pole at $E_0 = -0.025 \text{ eV}$. Close to a E_0 , we can write the most dominant terms of the transmission function and γ_{ij} as

$$\begin{aligned} \mathcal{T}(E) &\approx t_0 \beta^2 (E - E_0)^2, \\ \gamma(E) &\approx \frac{1}{\beta} \frac{\gamma_0}{E - E_0}, \end{aligned} \quad (3.8)$$

where we have included the β 's to keep the coefficients, t_0 and γ_0 , unitless. Inserting these into Eq. (3.7), we get

$$\begin{aligned} \gamma' \mathcal{T} - c\mathcal{T}' \frac{\gamma'' \mathcal{T} + 2\gamma' \mathcal{T}'}{\mathcal{T} + c\mathcal{T}''} &= \beta t_0 \gamma_0 \left[-1 + \frac{4c}{(\mu - E_0)^2 + 2c} \right] \\ &= -\beta t_0 \gamma_0 \frac{(\mu - E_0)^2 - 2c}{(\mu - E_0)^2 + 2c}. \end{aligned} \quad (3.9)$$

Consequently, the thermoelectrically driven ring currents can be expressed as

$$\tilde{I}_{ij} \approx \frac{2e}{h} \frac{\pi^2}{3} (k_B T)(k_B \Delta T) \gamma'(\mu) \mathcal{T}(\mu) \left[\frac{(\mu - E_0)^2 - \frac{\pi^2}{3} (k_B T)^2}{(\mu - E_0)^2 + \frac{\pi^2}{3} (k_B T)^2} \right], \quad (3.10)$$

where we used that $\gamma'(\mu) \mathcal{T}(\mu) = -\beta t_0 \gamma_0$. We recognize the first part as the low

³See Eq. (2.14).

⁴By symmetry point, we mean the energy exactly between the HOMO and LUMO. According to the Coulson-Rushbrooke pairing theorem, the molecular orbitals are distributed symmetrically around this energy [74].

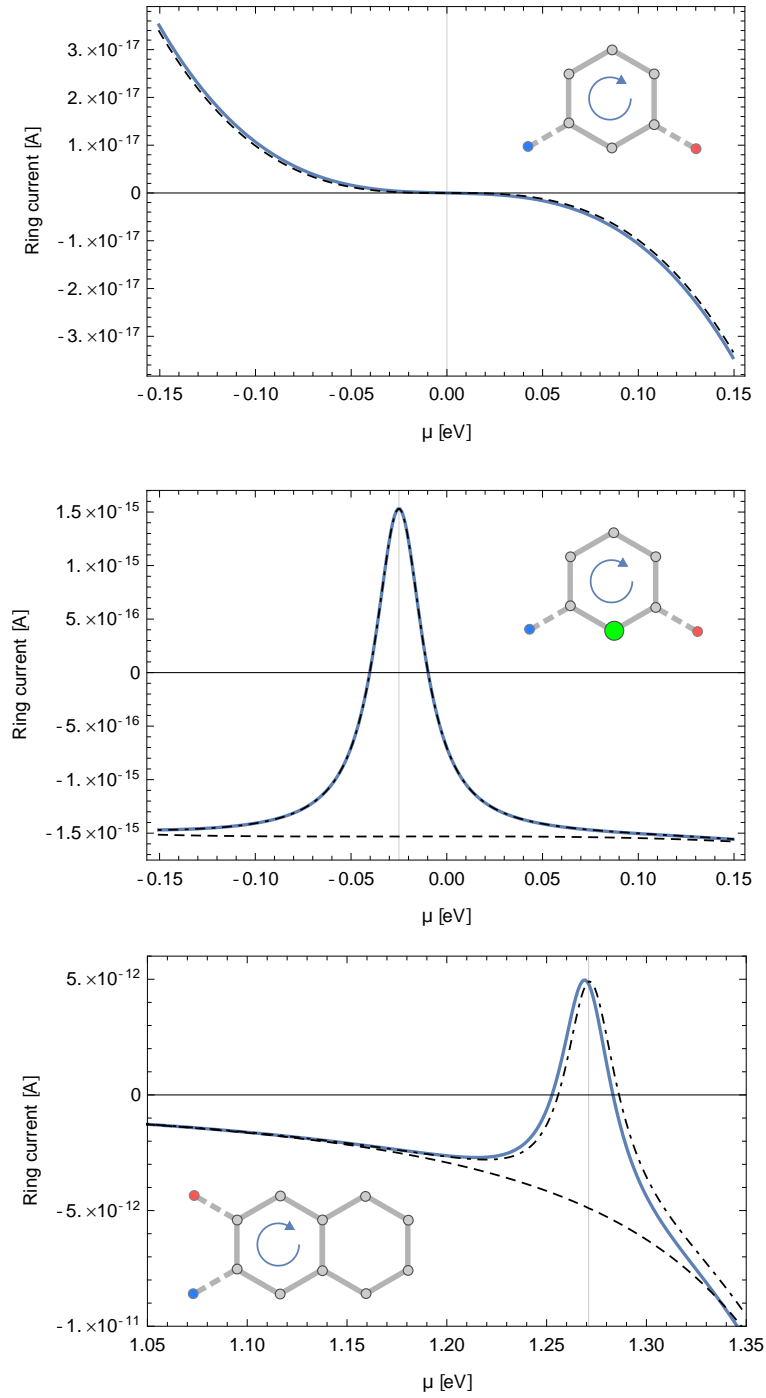


FIGURE 3.5: Thermoelectrically driven ring currents close to interference points, E_0 , marked with vertical grey lines for the temperatures $T_L = 95$ K and $T_R = 100$ K. The blue curves are calculated using Eqs. (2.9) and (2.10), the dashed lines are calculated using Eq. (3.5), and the dot-dashed lines are calculated using Eq. (3.10). a) Meta-coupled benzene for which $E_0 = 0$. b) Meta-coupled benzene with a modified onsite energy, $\varepsilon = 0.01 t_M$, at the site marked with a larger green circle. Here $E_0 = -0.025$ eV. c) A naphthalene junction for which $E_0 \approx 1.27$ eV. The currents for the naphthalene junction are also plotted in Fig. 3.4.

temperature approximation in Eq. (3.5). The function in the square brackets is $+1$ when the chemical potential is far away from E_0 , it is -1 when $\mu = E_0$, and it is zero when $\mu = E_0 \pm \frac{\pi}{\sqrt{3}}k_B T$. Consequently, the local currents cancel twice around a destructive interference point with no special symmetry. The approximation in Eq. (3.10) is plotted as a dot-dashed line in Fig. 3.5b, and we see that it is just on top of the exactly calculated curve. The two approximations in Eqs. (3.7) and (3.10) are also plotted for a naphthalene junction in Fig. 3.5c.⁵ Again, we see a good agreement between Eq. (3.10) and the correct calculation (except for a slight shift).

3.2 Ring currents in graphene nanoribbons

Gated graphene ribbons is another example of nanoscopic junctions in which we expect internal electric currents to exist [1]. Consider the system shown in Fig. 3.6, where a zigzag graphene ribbon is gated at roughly one half of the ribbon width in a short region. The gating modifies the charge density and therefore the Seebeck coefficient [76], and classical field theory indicates that local currents have to exist in a zero-net-current measurement since $\nabla \times \left(\frac{\mathbf{j}}{\sigma}\right) = \nabla T \times \nabla S \neq 0$. We model the junction by assuming that the ungated regions to the left and right are semi-infinite ribbons. We use a tight-binding Hamiltonian and again consider only nearest neighbor hopping since this is sufficient to show the effect. The gated region is modeled by modifying the onsite energies. The self-energies are calculated from an iterative procedure [77, 78], which is shown in Appendix A.5.2, and the currents then follow from Eq. (2.9).

We use the same hopping amplitude, t_M , and temperatures as shown in Table 3.1. The chemical potential for the left lead is set to $\mu_L = 0.5$ eV, while the chemical potential for the right lead is set so that no current flows through the junction. The onsite energies in the gated region are set to $\varepsilon_G = 0.6$ eV, while those in the ungated region have $\varepsilon = 0$. The resulting bond currents are shown in Fig. 3.6, where the large black arrows are averages of the six bond currents in each honeycomb unit. The bond currents are shown with small arrows on top of the bonds, the longest of which has the current intensity $\tilde{I}_{\max} = 0.6$ nA. Currents smaller than the cutoff $0.02 \tilde{I}_{\max}$ are not shown. To get a rough estimate of the generated magnetic field in the graphene ribbon, we consider a current of 1 nA that flows in a ring with radius 5 Å. This generates a magnetic field of 1 μ T in the center of the ring. A larger temperature difference would of cause lead to stronger currents and therefore increase the resulting magnetic field.

3.3 Conclusions

In this chapter, we have calculated and analyzed thermoelectrically driven ring currents in single molecule junctions. By using the theory developed in Chapter 2, we have shown that the ring currents are related to the slope of the function γ_{ij} . In Sec. 3.1.2, we showed that the ring currents change direction twice when the chemical potential is passed through an energy of destructive interference. Finally, we demonstrated the existence of ring currents in gated graphene nanoribbons.

⁵This is the same junction as the one plotted in the middle left of Fig. 3.4.

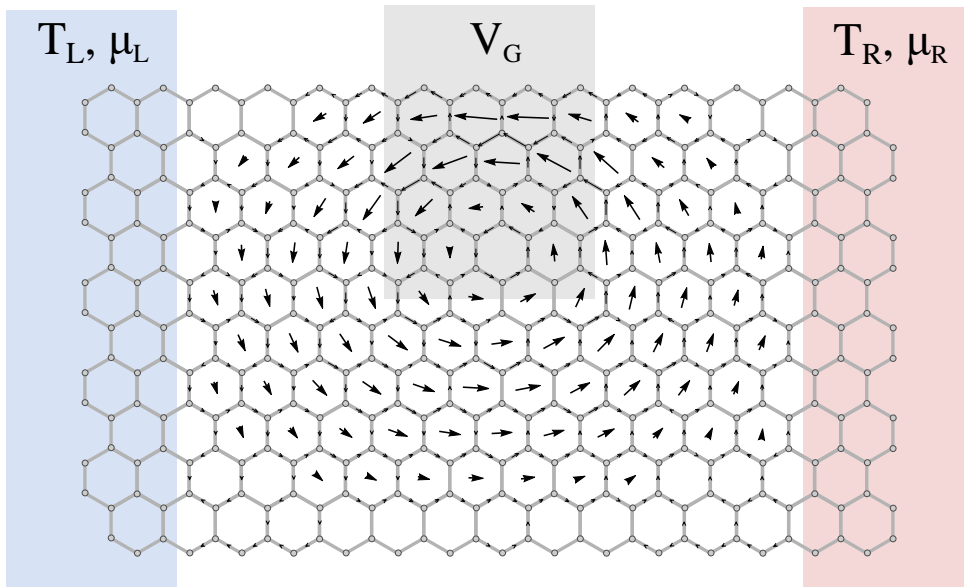


FIGURE 3.6: Local electric currents in graphene under a zero-net-current Seebeck measurement. The gate is modeled by the onsite-energies $\varepsilon_G = 0.6\text{ eV}$ in the grey region and the chemical potential of the left lead is chosen as $\mu_L = 0.5\text{ eV}$. The small arrows in the bonds are obtained from calculation and the longest of these has the current intensity 0.6 nA . The big black arrows show the average of the six currents in the particular benzene unit. The leads are modeled as semi-infinite graphene nanoribbons with the same width as the main region.

Chapter 4

Thickness dependent Seebeck coefficient in BDT crystals

The results in this chapter are collected in the paper draft in Appendix C. The paper is not published yet, which is mainly due to the challenges described in Sec. 4.3. The experimental results in this chapter were obtained by our collaborating group lead by professor Xiaohui Qiu at the National Center for Nanoscience and Technology at University of Chinese Academy of Sciences, Beijing.

As mentioned in Sec. 1.1.1, organic single molecule junctions typically have Seebeck coefficients of a few tens of $\mu\text{V}/\text{K}$. When the organic molecules are put together to form organic solids, the Seebeck coefficient can reach values higher $1000 \mu\text{V}/\text{K}$ [38, 79–81]. These differences are well understood, and they demonstrate that the transport mechanisms are different in the two cases. However, the crossover from single (or few) molecules to the microscopic regime is not well understood. This was one of the motivations for the research project described in this chapter.

The reason for the large Seebeck coefficients in some organic solids is that they are organic semiconductors. Organic semiconductors can have different structures, but large Seebeck coefficients can be obtained in both polycrystalline [81], amorphous [79], and single crystal structured organics [38, 80]. While inorganic semiconductors have continuous energy bands, organic semiconductors have discrete levels from the molecular orbitals [82]. For single crystal organics, which we will study in this chapter, it is still under debate whether the transport is band-like or not [83]. However, the Seebeck coefficient can be described by Eq. (1.10) in either case [33], and we will use the terms valence band and HOMO levels interchangeably.

Thickness dependence of the Seebeck coefficient has been studied in different systems. In single molecule junctions where the length can be altered by e.g. using a longer chain, several studies have been done [22, 23, 84–86]. As the length increases, the Seebeck coefficient can either increase or decrease, and it can even change sign. The Seebeck coefficient can be described by Eq. (1.7) in these cases and the observations are therefore due to the fact that (the slope of) the transmission function changes with the length of the molecule. The thickness dependence has also been studied in layered structures such as SnTe thin films [87], few-layered MoS₂ [88], and bismuth telluride nanoplates [89]. In these studies, the samples are mainly in the degenerate limit, so that the Seebeck coefficient is explained by Mott’s formula.¹ Common for Refs. [87–89] is that the thermoelectric properties are studied in the in-plane direction.

In this chapter, we will study the thickness dependent Seebeck coefficient of an organic single crystal semiconductor. In contrast to the mentioned studies of layered structures, we will investigate the out-of-plane Seebeck coefficient. We will start by

¹See the text below Eq. (1.9).

describing the setup and the experimental results in Sec. 4.1. In Sec. 4.2, we will study the connection between band bending and the Seebeck coefficient, and we will set up two models to describe the experimental results. Finally, the challenge of knowing the temperature difference in our setup is explained in Sec. 4.3.

4.1 BDT and experiments

We will work with experimental results obtained from crystals of the molecule α, α -bis(dithieno[3,2-b:2,3-d]thiophene), which we will refer to as BDT. The structure of BDT is shown to the left in Fig. 4.1a. The energy gap between the HOMO and LUMO of BDT has been determined experimentally to be 2.8 eV [90], while density functional theory predicts 3.2–3.6 eV [91]. From the BDT molecules, single crystals can be grown with the packing structure shown in Fig. 4.1a [90, 92], and the formed crystals are p-type semiconductor [90–92]. The samples were handled in atmospheric conditions and the crystals can therefore be contaminated by e.g. oxygen. Oxygen acts as a p-dopant in organic semiconductors, but different studies indicate that the doping is uniform [93, 94], which is important here.

To study the thickness dependence of the Seebeck coefficient, Seebeck measurements were done on samples with thicknesses ranging from 8 nm to 220 nm (the experiments were done by our collaborators at UCAS, Beijing). The BDT crystals were placed on a gold substrate and the setup was heated from underneath. A self-modified atomic force microscope (AFM) tip was brought into contact with the sample as shown in Fig. 4.1b, and the potential difference generated by the temperature difference across the sample was measured

$$S_{\text{measured}} = -\frac{\Delta V}{\Delta T}. \quad (4.1)$$

Due to the small size of the setup, it was not possible to measure the temperature difference across the sample directly. Instead, the temperature of the Au substrate was measured using a thermocouple, while the temperature of the cantilever was measured in the neighboring air. It would be ideal if we knew the temperature of the tip. This could in principle be achieved by using a thermocouple tip [95, 96]. Our experimental group put a lot of effort into obtaining the Seebeck coefficients in such a setup, but with no success, and we therefore have to treat the data at hand. The challenge of knowing the temperature drop across the sample was addressed in the author's master's thesis [1], where the modeling indicated that the temperature mainly drops across the sample. For now, we will therefore assume that the measured Seebeck coefficients are indeed the Seebeck coefficients of the samples, and we will return to the challenge of the temperature in Sec. 4.3.

The measured Seebeck coefficients are shown in Fig. 4.1c. For thin samples, $S \approx 100 \mu\text{V}/\text{K}$, and the Seebeck coefficient then increases with thickness until it saturates at $S \approx 400 \mu\text{V}/\text{K}$ for thick samples. The characteristic length of the saturation curve is $b \approx 30 \text{ nm}$ at which the values are half-way between the initial and saturation values. The large values for thick samples puzzled our group for quite some time, but with the knowledge that BDT crystals are semiconductors and the fact that semiconductors have large Seebeck coefficients, this is now easy to understand. The positive values of S_{measured} show that BDT is a p-type semiconductor as expected [90–92].

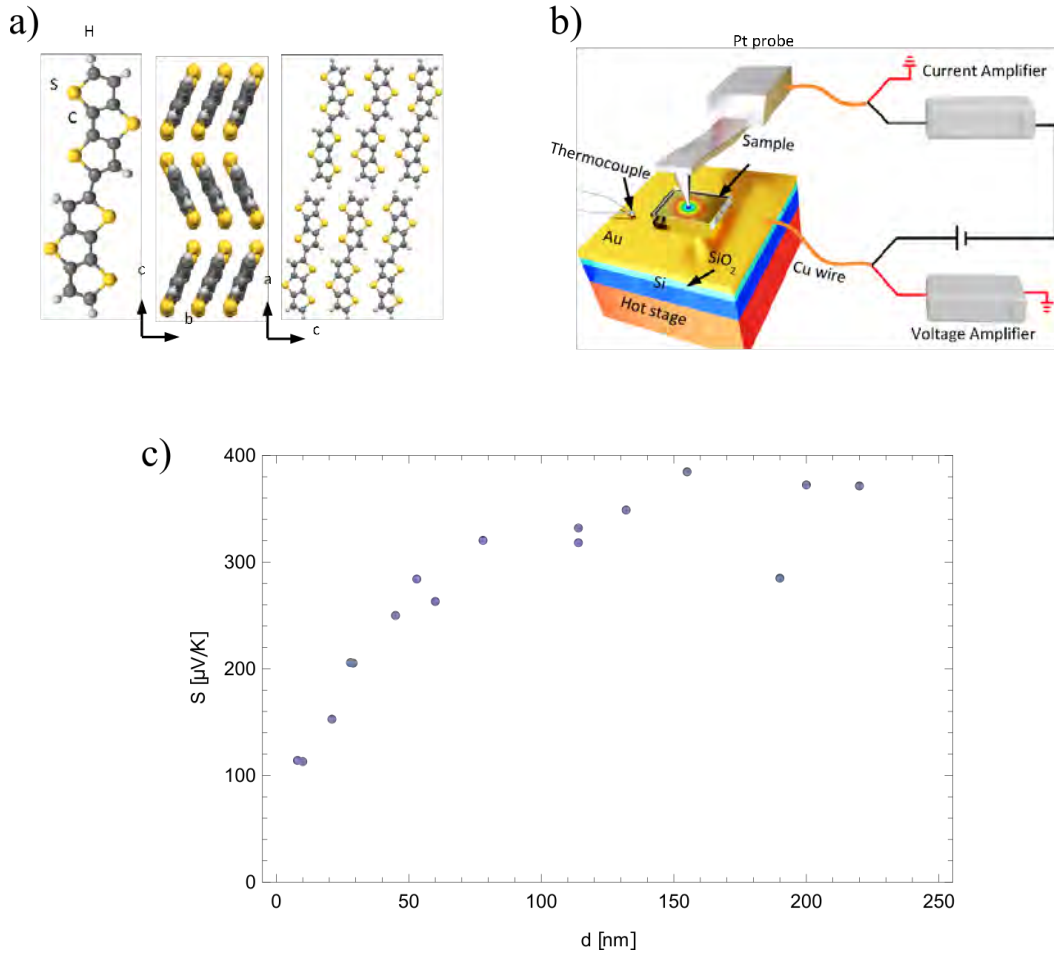


FIGURE 4.1: a) The BDT molecule to the left and the packing structure in BDT crystals to the right. b) Illustration of the experimental setup used to obtain the Seebeck coefficients in (c) for different sample thicknesses. All experiments were done by our collaborators at UCAS, Beijing. Figures (a) and (b) were produced by our collaborators.

4.1.1 Band bending

When two materials are brought into contact with each other, charges will move from one material to the other if the materials have different chemical potentials (relative to the vacuum energy) [97]. The transferred charges will stay close to the junction forming a charged region. Consider a metal in contact with a p-type semiconductor: Since the electric field has to be zero in the metal, the charges on the metal side are located at the junction. However, on the semiconductor side, the charges can spread into the material with a characteristic length known as the Debye length, λ_D . The electric potential from the accumulated charges will cause the energy bands of the semiconductor to bend. The bands can bend in different directions depending on the chemical potentials of the materials. If electrons are injected from the metal into the p-type semiconductor, the bend bands will act as a barrier for the holes. This is known as a Schottky barrier. On the other hand, if holes are injected from the metal into the p-type semiconductor, the formed layer is known as an accumulation layer, which does not have the effect as a barrier. We will return to the mathematical description of band bending in Secs. 4.2.1 and 4.2.2.

To study the band bending in BDT crystals, Kelvin probe force microscopy (KPFM)

was used to measure the surface work function. The surface work function is the energy required to remove an electron from the surface of the material to the vacuum close to the surface. We will here give a short description of the KPFM technique; a more thorough description can be found elsewhere [98, 99]. In KPFM, a conducting AFM tip is brought into electric contact with the sample. Depending on the surface work function of the sample relative to the work function of the AFM tip, charges will be exchanged. When the AFM tip is brought close to the sample after contact, an attractive electrostatic force between the sample and the tip is present due to the exchanged charges. When an external bias is applied with the same magnitude as the difference in work functions, the force cancels. KPFM can therefore be used to measure the surface work function [99].

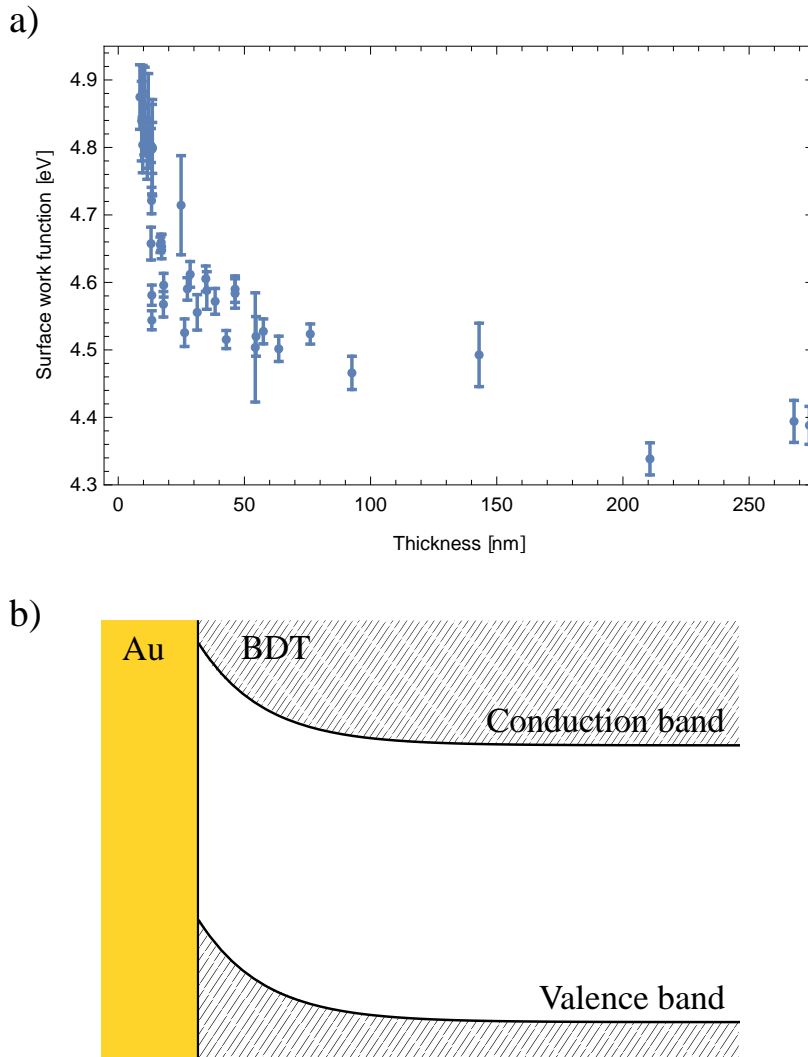


FIGURE 4.2: a) KPFM measurement of BDT samples of different thicknesses. The experiment was done by our collaborators at UCAS, Beijing. b) Schematic illustration of the band bending.

The results of the KPFM measurements are shown in Fig. 4.2a (the experiments were done by our collaborators). We see that the surface work function decreases for thicker samples and the results seem to follow a typical band bending curve. However, KPFM is not a direct measure of band bending since the surface work function can be affected by e.g. surface dipoles created by adsorbents [99]. Additionally, while we

are interested in the band bending profile inside a sample, the results in Fig. 4.2a only show what goes on at the surface of multiple individual samples [100]. However, the KPFM results give us the direction of the band bending, as shown schematically in Fig. 4.2b, which shows that holes are injected into the BDT crystals forming an accumulation layer at the interface. It also gives a rough estimate of the Debye length, which is comparable to the characteristic length of the Seebeck coefficients in Fig. 4.1c. This observation indicates that the saturation curve of $S_{\text{measured}}(d)$ could be due to the band bending: a connection that we will study in the following sections.

To get an additional independent measurement of the band bending in BDT, we tried to use Raman spectroscopy on the different sample thicknesses. The author build a model to extract information about the band bending, but the result was not realistic. We will here give a short description of the model: The accumulated charges close to the substrate give rise to an electric field. This field can affect the vibrational modes of the BDT molecules close to the surface via the so-called vibrational Stark effect [101]. Since the Raman signal is the sum of signals from all the BDT molecules in a crystal, one can expect the band bending to introduce an asymmetry in the peaks. This was indeed observed in the experimental data, which showed an increasing asymmetry with increasing sample thickness (for some of the Raman peaks). The author build a simple model and fitted it to one of the experimentally obtained Raman peaks (for all thickness simultaneously). The best fit was obtained for $\lambda_D = 3$ nm and a difference dipole of 3 Debye. According to the literature, compounds similar to BDT have difference dipoles of around 0.03–0.12 Debye [101, 102]. The obtained value is therefore unrealistically high, while the Debye length is small compared to the one indicated by the data in Fig. 4.2a. Possible explanations are that the electric field is too small for the band bending to play a role and that the observed asymmetry of the peaks is due to lattice deformations close to the substrate. We therefore continued with the KPFM measurements as the only indicator for the band bending.

4.2 Band bending and Seebeck coefficient

Since charges are injected into the semiconductor in a metal/semiconductor junction, one can expect that the band bending affects the transport properties of the semiconductor. It has been shown theoretically [103] as well as experimentally [104, 105] that the inclusion of metallic nanoparticles in semiconductors can increase the Seebeck coefficient. These observations are described by the band bending at the metal/semiconductor interfaces, which gives rise to an energy-filter effect: the scattering time of the charge carriers is strongly energy dependent. Another study measured the in-plane Seebeck coefficient of bismuth telluride nanoplates of different thicknesses [89]. Due to oxygen and nitrogen exposure from the air, the energy bands bend at the surfaces of the nanoplates. In their analysis, they show that band bending is essential in order to describe the thickness dependence of the transport properties [89].

We will now follow a similar procedure as in Ref. [89] and show that the observations in the Seebeck measurements in Fig. 4.1c can be described by band bending. In contrast to the work in Ref. [89], the BDT measurements are done in the direction perpendicular to the band bending interface. To the knowledge of the author, this has not been done before.

Since the transport direction is along the crystal c-axis shown in Fig. 4.1a, each of the molecular layers in the BDT crystals have a thickness of around 5 Å. Even the thinnest BDT sample ($d = 8$ nm) therefore has around 16 layers of molecules. The thinnest sample consequently has thousands of BDT molecules in the volume close to

the AFM tip. Because of this large number of molecules, it is reasonable to assume the material to be continuous with locally defined transport properties, and we will use the classical transport equations to treat the problem. We will start out by using a 1D model to demonstrate the connection between band bending and thermopower. In Sec. 4.2.2, we will move on to a more sophisticated 3D model, which takes into account the geometry of the setup.

4.2.1 Theoretical explanation: 1D model

We will start by neglecting the 3D geometry of the setup in Fig. 4.1b and consider the transport to be one-dimensional. In order to build a model that includes both the band bending and the Seebeck coefficient, we will consider the following three steps: (1) Given a position dependent Seebeck coefficient, calculate the effective Seebeck coefficient.² (2) For a band bending profile, determine the position dependent Seebeck coefficient. Finally, (3) determine the band bending profile. The model will eventually be fitted to the experimentally obtained Seebeck coefficients.

The electric field generated by the Seebeck effect is $E = S_{\text{local}}(x) \frac{dT}{dx}$, where $S_{\text{local}}(x)$ is the position dependent Seebeck coefficient. The potential difference across the sample is $\Delta V = -\int_0^d dx S_{\text{local}}(x) \frac{dT}{dx}$ and since phonons dominate the heat transport in organic crystals, we can consider the temperature gradient to be constant.³ With this, the effective Seebeck coefficient, $S = -\Delta V/\Delta T$, is

$$S(d) = \frac{1}{d} \int_0^d dx S_{\text{local}}(x), \quad (4.2)$$

which is the continuous analogue to S_{series} in Eq. (1.13) with identical thermal resistances. If the BDT crystal is a non-degenerate semiconductor at all positions, we can model the local Seebeck coefficient by Eq. (1.10). We assume that the transport levels around the HOMO energy are narrowly distributed so that the constant A_v in Eq. (1.10) can be neglected⁴

$$S_{\text{local}}(x) = \frac{k_B}{e} \left(\frac{\mu - \varepsilon_H(x)}{k_B T} \right), \quad (4.3)$$

where $\varepsilon_H(x)$ is the HOMO energy level (or valence band edge) at position x . With these two equations, we can calculate the effective Seebeck coefficient when the band bending profile is known.

To model the band bending, we use Poisson's equation $\nabla^2 V(\mathbf{r}) = -\frac{\rho(\mathbf{r})}{\epsilon}$. We will keep it in the 3D form so that we can reuse the expressions in the proceeding section. The charge density is $\rho(\mathbf{r}) = e[p(\mathbf{r}) - n_d]$, where $p(\mathbf{r})$ is the density of holes, while n_d is the density of dopants. Oxygen is an example of a dopant and as described earlier, we expect its concentration to be uniform [93, 94]. Using the standard equations for semiconductors (see e.g. Ref. [97]), we can rewrite Poisson's equation as

$$\nabla^2 V(\mathbf{r}) = \frac{en_d}{\epsilon} \left(1 - \exp \left[\frac{eV_{\text{bulk}} - eV(\mathbf{r})}{k_B T} \right] \right), \quad (4.4)$$

where V_{bulk} is the bulk potential in thick samples. We will now follow the text books and linearize the above differential equation. The reason is that the above is very

²By effective Seebeck coefficient we mean the one that would be measured.

³Phonons are not affected by the band bending.

⁴This is equivalent to the narrow band approximation, which is good in the case of a polaronic transport model. See e.g. Sec. 1.5.4 in Ref. [33].

difficult to solve in the 3D case. The linearization is a good approximation when $e(V_{\text{bulk}} - eV(\mathbf{r})) \ll k_B T$, which is unfortunately not the case for BDT. As the KPFM results in Fig. 4.2a indicate, the bands bend more than the thermal energy ($k_B T \approx 25$ meV). However, the linearized equation captures the shape of the band bending, and we will therefore use it as a model,

$$\nabla^2 V(\mathbf{r}) \approx \frac{1}{\lambda_D^2} [V(\mathbf{r}) - V_{\text{bulk}}], \quad (4.5)$$

where we defined the Debye length $\lambda_D = \sqrt{\frac{e^2 n_d}{\epsilon k_B T}}$, which will be used as a fitting parameter. In the 1D case, we can write the solution to the above equation as $V(x) = V_{\text{bulk}} + V_1 e^{x/\lambda_D} + V_2 e^{-x/\lambda_D}$. The position dependent valence band edge is $\varepsilon_H(x) = \varepsilon_0 - eV(x)$, where ε_0 is the band edge energy of BDT before contact. If we assume the work functions of the two contacts connecting BDT to be equal, $\varepsilon_H(0) = \varepsilon_H(d) = \varepsilon_0$, we get the solution

$$\varepsilon_H(x) = \varepsilon_0 + (\varepsilon_{\text{bulk}} - \varepsilon_0) \left[1 - \frac{1}{1 + \exp(-d/\lambda_d)} \left(e^{-x/\lambda_d} + e^{(x-d)/\lambda_d} \right) \right], \quad (4.6)$$

where $\varepsilon_{\text{bulk}} - \varepsilon_0 = -eV_{\text{bulk}}$. Here $\varepsilon_{\text{bulk}}$ is the valence band edge in the bulk of a thick sample and d is again the sample thickness. By combining Eqs. (4.2), (4.3), and (4.6) and performing the integral, we get an expression for the effective Seebeck coefficient

$$S(d) = \frac{k_B}{e} \left[\frac{\mu - \varepsilon_{\text{bulk}}}{k_B T} + \frac{2\lambda_d}{d} \frac{\varepsilon_{\text{bulk}} - \varepsilon_0}{k_B T} \tanh\left(\frac{d}{2\lambda_d}\right) \right]. \quad (4.7)$$

With Eq. (4.7), we now have an analytic model, which can be fitted to the experimentally obtained Seebeck coefficients in Fig. 4.1c. The best fit curve is shown together with the experimental data in Fig. 4.3a, where we see that the model fits the data very well. The values for this curve are (the energies are relative to $\mu = 0$)

$$\begin{aligned} \lambda_{D,1D} &= 10.4 \text{ nm} \\ \varepsilon_{0,1D} &= -0.029 \text{ eV} \\ \varepsilon_{\text{bulk},1D} &= -0.115 \text{ eV}. \end{aligned} \quad (4.8)$$

The valence band edge for a $d = 200$ nm sample is shown in Fig. 4.3b, where we have set $\mu = 0$. This band bending profile is comparable to the experimentally obtained surface work functions shown in Fig. 4.2a.

The above analysis is an evidence that the observed thickness dependence of the Seebeck coefficient is due to band bending. As mentioned, the analysis is similar to the one done by Pettes et al. [89], but our experiment is done perpendicular to the band bending interface. Since we used a tip as one of the metal contacts, there are several three-dimensional effects that can play a role. There is for example a thermal constriction resistance associated with the heat transfer into the small BDT-tip interface, heat can be transported through the surrounding air, and so on. We will therefore do a similar analysis as the above, but with the 3D geometry of the setup taken into account. This also gives rise to a theoretical finding: the existence of internal electric currents.

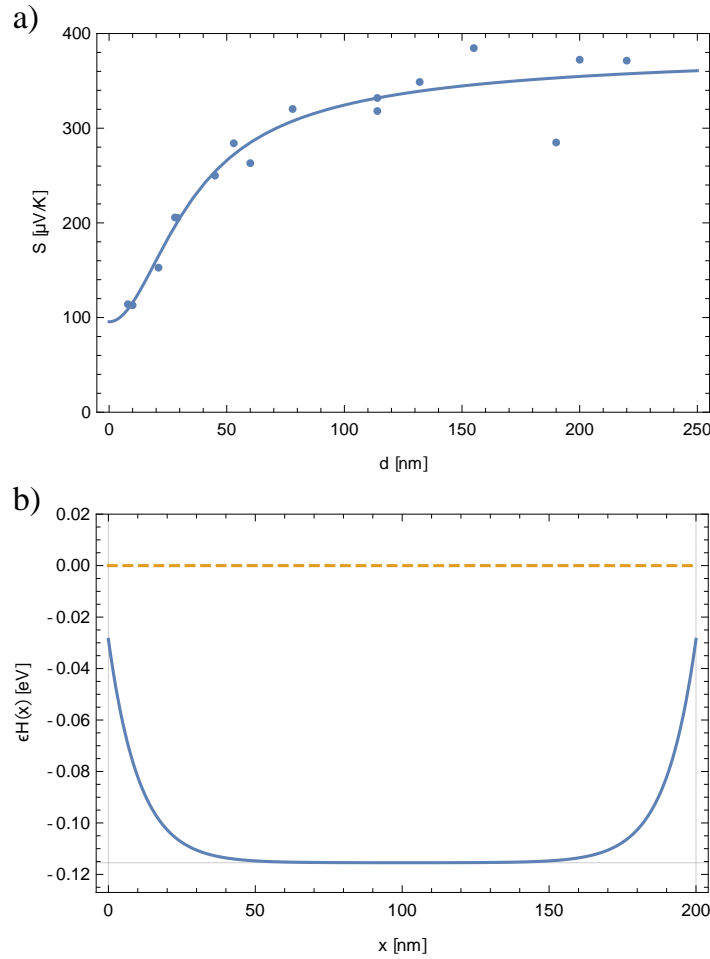


FIGURE 4.3: a) The best fit of the 1D model together with the experimental data. b) The band bending in a 200 nm thick sample for the best fit parameters of the 1D model.

4.2.2 Theoretical explanation: 3D calculations

As motivated above, we will now do a more thorough calculation in which the 3D geometry is included. Due to the complicated geometry, we will solve the differential equations numerically and we need to specify the dimensions and transport properties of the setup. The calculation region will include the sample, the Au substrate, a small part of the tip (100 nm), and the air surrounding the tip. A tip-sample contact radius of 10 nm is used. The sample is anisotropic since it e.g. conducts electricity easier in the π - π stacking direction. However, to make the calculation easier, we will ignore the anisotropy so that the calculation region becomes cylindrically symmetric, which reduces the problem to 2D. As a side note, the author tried to include an anisotropic electrical conductivity in the calculation, which did not affect the result significantly.

Just as the Seebeck coefficient is affected by the band bending, so is the electrical conductivity. The conductivity is proportional to the number of charge carriers, which increases in the BDT experiments due to hole injection from the substrate. The number of holes is $p(r) \propto \exp\left[-\frac{\mu - \epsilon_H(\mathbf{r})}{k_B T}\right]$ where $\epsilon_H(\mathbf{r})$ is again the position dependent

TABLE 4.1: Electrical conductivities, thermal conductivities, and Seebeck coefficients at room temperature. The transport properties of the metals are from Refs. [6, 106]. *) σ_0 is the prefactor used in Eq. (4.9). **) The thermal conductivity of BDT is not known, but typical values of organic films are 0.2–0.7 W m⁻¹ K⁻¹ [107]. ***) From Ref [108].

Material	σ [S/m]	κ [W m ⁻¹ K ⁻¹]	S [μ VK ⁻¹]
Au	4.6×10^7	317	1.9
Pt	9.6×10^6	72	-5.3
BDT	$\sigma_0 = 10^{2*}$	0.3**	
Air	0	0.026***	0

valence band edge, and we can therefore write the position dependent conductivity as

$$\sigma(\mathbf{r}) = \sigma_0 \exp\left[-\frac{\mu - \varepsilon_H(\mathbf{r})}{k_B T}\right]. \quad (4.9)$$

The conductivity of the BDT crystals have been measured to be around 10 S/m (see Appendix C) and we use $\sigma_0 = 10^2$ S/m, which leads to local conductivities of around 1–30 S/m for the band bending profile in Fig. 4.3b. The rest of the transport parameters are independent of the band bending, and they are listed in Tab. 4.1.

In order to calculate the effective Seebeck coefficient, we will follow a procedure similar to the one used in Sec. 4.2.1. For each sample thickness, the following steps are performed

1. Band bending profile: The differential equation in Eq. (4.5) is solved with the fixed boundary condition $V(\mathbf{r}_{\text{boundary}}) = 0$ at both the Au and tip contact regions. λ_D and V_{bulk} are inputs in this step. The valence band edge is $\varepsilon_H(\mathbf{r}) = \varepsilon_0 - eV(\mathbf{r})$.
2. Local Seebeck coefficient: The local Seebeck coefficient is calculated using Eq. (4.3).
3. Effective Seebeck coefficient: By solving the coupled differential equations $\nabla \cdot \mathbf{j}_e = 0$ and $\nabla \cdot \mathbf{j}_q = 0$ simultaneously under the zero-net-current condition as described in Sec 1.2, the effective Seebeck coefficient can be obtained.

With the input parameters λ_D , V_{bulk} , and ε_0 , the effective Seebeck coefficient is calculated for all thicknesses. An optimization procedure is run in order to obtain the parameters that describe the experimental data in Fig. 4.1c best. The best-fit parameters are (the energies are again relative to $\mu = 0$)

$$\begin{aligned} \lambda_{D,3D} &= 25.8 \text{ nm} \\ \varepsilon_{0,3D} &= -0.029 \text{ eV} \\ \varepsilon_{\text{bulk},3D} &= -0.156 \text{ eV} \end{aligned} \quad (4.10)$$

The fitted curve is plotted together with the experimental data in Fig. 4.4a, and again, we see a good agreement. The local Seebeck coefficient in the cross section of a 45 nm thick BDT sample is plotted in Fig. 4.4b. Here the sample is in contact with the Au substrate on the lower part of the plot ($z = 30$ nm), and it is in contact with the tip in the region $-10 \text{ nm} < r < 10 \text{ nm}$ and $z = 75 \text{ nm}$.⁵ Close to the metal interfaces, the

⁵Remember that the system is considered to be cylindrically symmetric. The symmetric part to the left of $r = 0$ is shown to make the plot easier to read

Seebeck coefficient is smallest, while it takes larger values away from the interfaces. Due to the small BDT-tip contact area, there are great variations in S_{local} in the \hat{r} -direction, which illustrates the importance of the three-dimensional model.

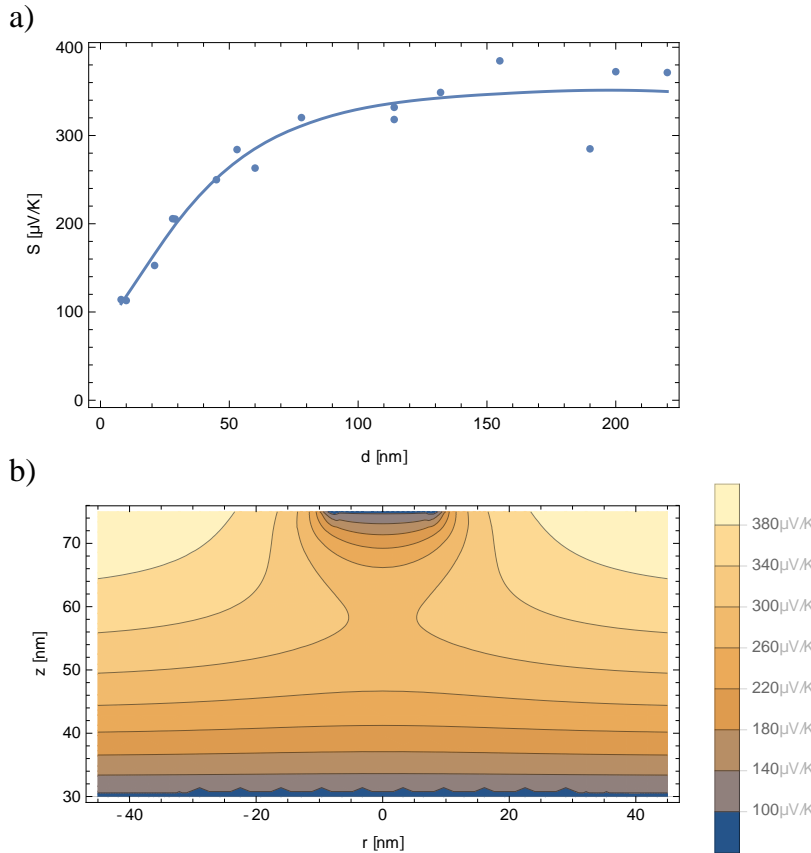


FIGURE 4.4: a) The experimental Seebeck coefficients and the effective Seebeck coefficient calculated using the 3D model with the parameters in Eq. (4.10). b) The local Seebeck coefficient for $d = 45$ nm.

The Debye length obtained with the 3D model is about 2 times larger than the one obtained in the 1D analysis. This can be explained by the thermal constriction resistance, which causes the main temperature drop to occur close to the sample-tip interface. This is seen in the temperature map of a 45 nm thick BDT sample in Fig. 4.5a. Since the electric field generated by the Seebeck effect is $\mathbf{E}(\mathbf{r}) \approx S_{\text{local}}(\mathbf{r})\nabla T$, it is therefore mainly the band bending around the BDT-tip interface that affects the measured Seebeck coefficient. Put differently, the Seebeck coefficient in the 1D model is affected by two band bending regions, while it is only affected by one in the 3D model.

As explained in the introduction in Sec. 1.2, local currents can exist in Seebeck measurements even though the through current is zero. We can calculate the local currents in the 45 nm thick BDT sample by inputting the temperature and electric potential maps in Figs. 4.5a and 4.5b into Eq. (1.1). This yields the current densities shown in Fig. 4.5c. We see that the local electric currents in the sample follow a ring pattern. Electric current enters the sample from the Au substrate far away from the tip and then exits the sample close to the tip. Remember that the in and out going currents cancel each other. The current density, j_z , in the sample close to the Au substrate ($z = 35$ nm) is plotted in Fig. 4.5d. This illustrates that the current densities are very small, but if we integrate them up, we find that a current of $I \approx 0.1$ nA flows

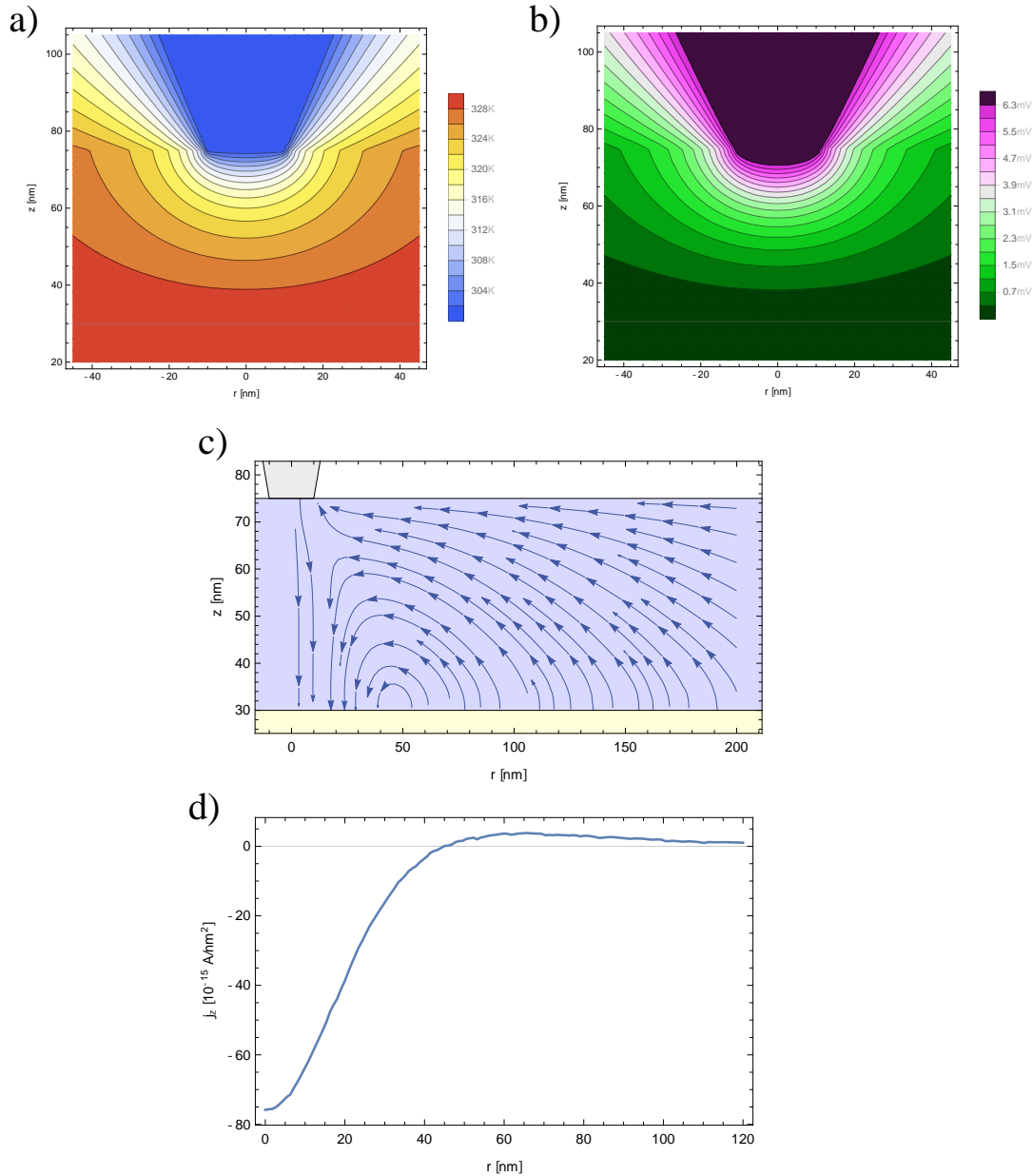


FIGURE 4.5: Calculation results for a sample of thickness $d = 45$ nm. a) and b) Temperature and electric potential maps of a cross section of the setup. c) Local electric currents in the sample. Notice that the total current through the setup is zero. d) The current density j_z plotted along the line at $z = 35$ nm.

through the disk at ($0 < r < 45$ nm, $z = 35$ nm). Even though the ring current is small, it has to be included in the calculation in order to do it correct [1], and it is interesting from a theoretical perspective.

4.3 The challenge of knowing the temperature drop

The analysis done in Sec. 4.2 demonstrates that band bending can be observed directly in a Seebeck coefficient measurement. However, as mentioned in the beginning of the chapter, the described analysis is based on the assumption that the measured Seebeck

coefficient is the same as the Seebeck coefficient of BDT crystal. Since the temperature is measured far (relative to the sample thickness) away from the sample, there can be temperature drops in other parts of the setup. This has led to different views on how to interpret the data, and it is the main reason why the paper draft in Appendix C is not finished and published. In the following, the author will argue that the analysis in Sec. 4.2 is valid and explain the opposing view on how to treat the data.

Temperature drop across the sample

It is very difficult to estimate the relation between the measured temperatures and the temperature across the sample. In a scanning thermal microscope, a thermocouple tip is used so that the temperature is known at the tip itself. Even in this case, it is difficult to know the exact temperature across the sample [96, 109, 110]. We will start by considering the simple model in Fig. 4.6, which, despite its simplicity, illustrates one of the challenges. For a more complex model, see e.g. Ref. [110]. The components in Fig. 4.6 are connected in series and the Seebeck coefficient is therefore given by Eq. (1.13). If we simplify the sample as a cylinder so that the thermal resistance is $R_{q,s} = d/(\kappa_s A_s)$, we can write

$$S = \frac{S_s R_{q,s} + S_A R_{q,A}}{R_{q,s} + R_{q,A}} \quad (4.11)$$

$$\approx \frac{S_s d + c}{d + b} \quad (4.12)$$

where $b = \kappa_s A_s R_{q,A}$ and $c = \kappa_s A_s S_A R_{q,A}$. Since the tip and substrate are metals, they have small Seebeck coefficients and we can neglect c . From the model in Eq. (4.12), it is clear that the Seebeck coefficient starts out at $S(d=0) = c/d$ and then saturates at the value S_s for thick samples. If we assume the Seebeck coefficient of BDT to be constant as a function of thickness, we can fit Eq. (4.12) to the experimental data in Fig. 4.1c. This gives a good fit with $b_{\text{fit}} \approx 32$ nm.

In the beginning of this research project, we were convinced that the observed saturation curve in the thickness dependent Seebeck coefficients was indeed due to the varying temperature drop. However, we were not able to describe the large value of $b = 32$ nm. A thorough attempt was done in the author's master's thesis, where the thermal resistance of the sample and parts of the tip were modeled using the FEM, while the remaining components were calculated by hand [1]. Inserting the obtained values into Eq. (4.11), we obtained a characteristic length of $b \approx 1$ nm (see Sec. 2.1.2 in Ref. [1]), which indicates that the temperature mainly drops across the sample. This is the reason that we have assumed the measured Seebeck coefficients to be the Seebeck coefficients of the BDT crystals in Sec. 4.2.

A proper analysis will include both the band bending and the varying temperature drop. This can be done by following the procedure in Sec. 4.2.2 and additionally calculating $R_{q,s}$ in Eq. (4.11) using the FEM, while using $R_{q,A}$ as a fitting parameter. In the paper draft in Appendix C, we used a flat prior with a minimum value for $R_{q,A}$, and the calculation ended up at this minimum limit.⁶

To add to the complication of the temperature drop, the temperature is actually measured in the surrounding air. If we take heat conduction through air into account in the Fourier/Ohm's law analysis, an additional constant shows up,

$$S \approx k \frac{S_s d}{d + \bar{b}}, \quad (4.13)$$

⁶If no prior knowledge is used, the best fit value is $R_{q,A} = 0$.

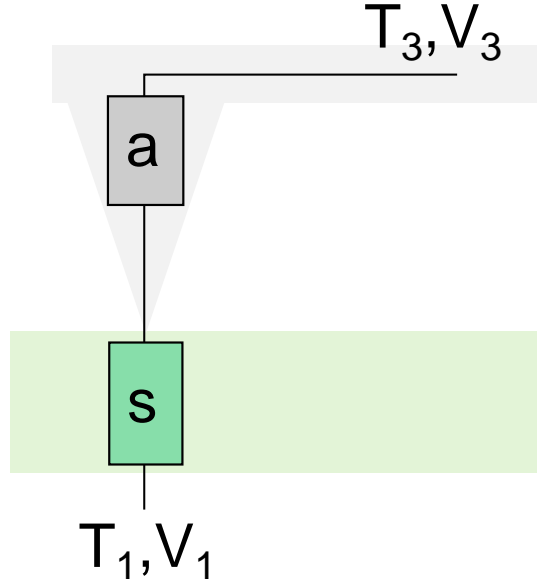


FIGURE 4.6: A simple 1D model of the setup used to illustrate the connection between the measured temperature difference and the temperature drop across the sample. 's' refers to the BDT sample, while the component 'a' includes the remaining parts of the setup.

which is derived in Appendix B.1. The length \tilde{b} depends on the heat conduction through air. The constant k is independent of the sample thickness and it was measured by our collaborators at UCAS to be $k = 0.58$, but the author does not have sufficient information to describe the measurement here. The constant was included in the paper draft in Appendix C.

Different view on the how to treat the data

The challenge of knowing exactly what is measured split our research group into two. I (the author) will here give a short description of the other view on how to treat the data and why I think the treatment is not correct.

The effective Seebeck coefficient is $S(d) = \frac{S_s(d) \cdot d}{d+b}$, just as in Eq. (4.12). It is assumed that $S_s(d)$ is constant for thick samples ($d > 20$ nm) so that $S(d)$ can be fitted to the experimental data to get rid of the temperature issue. The data is then rewritten on the form

$$S_s(d_i) = S_i \left(1 + \frac{b_{\text{fit}}}{d_i} \right), \quad (4.14)$$

where S_i is the measured Seebeck coefficient for a sample of length d_i . In this way, the Seebeck coefficient of the sample is plotted directly. The resulting representation of the data shows an almost constant S_s for thick samples. As the samples get thinner, the spread around the constant value increases. Finally, the thinnest sample of thickness $d = 8$ nm has a Seebeck coefficient about 35% larger than the other data points. This single data point indicates an enhancement of the Seebeck coefficient for thin samples, and it has been the main focus in the other part of the group.

There are several reasons that I do not agree with the above procedure. First of all, there is no good physical argument that the BDT Seebeck coefficient should be constant for thicknesses above 20 nm. In fact, the KPFM results in Fig. 4.2 indicate

that the band bending affects samples up to $d \approx 100$ nm and as described in the preceding sections, the transport properties are affected by band bending. Additionally, if the thickness dependence of the sample itself can be described by the saturation curve $S_s(d) = S_{\text{const}}d/(d + b_{\text{BDT}})$, it is not possible to separate the two effects. This is seen mathematically by inserting this $S_s(d)$ into Eq. (4.12) (neglecting the constant c)

$$\begin{aligned} S(d) &= \frac{S_{\text{const}} \cdot d}{d + b_{\text{BDT}}} \frac{d}{d + b} \\ &= \frac{S_{\text{const}} \cdot d}{d + (b + b_{\text{BDT}}) + \frac{b \cdot b_{\text{BDT}}}{d}} \end{aligned} \quad (4.15)$$

from which it is clear that b and b_{BDT} cannot be separated.

Secondly, by representing the data as in Eq. (4.14), small deviations in S_i will appear large for thin samples due to the last term in the parentheses. This is why a larger spread is observed in the data for thinner samples in this representation. Additionally, the hypothesis is based on a single data point at $d = 8$ nm.

Finally, there is no physical theory that supports the idea of an enhanced Seebeck coefficient for the thinnest sample. A possible explanation is the change in dimensionality from 3D to 2D [25, 111], but the 8 nm sample contains multiple layers of BDT molecules and it has not been possible to set up a model that supports the idea.

4.4 Discussion

In this chapter, we have studied the thickness dependence of Seebeck coefficients in BDT crystals. The experimental results showed that the Seebeck coefficient of the thinnest sample is around $100 \mu\text{V}/\text{K}$ and it then increases with thickness until it saturates at around $400 \mu\text{V}/\text{K}$ for thick samples. Additionally, KPFM measurements demonstrated the existence of energy band bending in the BDT samples close to a Au-BDT interface. We have set up two models, that connect these experimental observations and therefore indicate that the observed thickness dependence of the Seebeck coefficient is due to band bending. In the model in Sec. 4.2.1, we approximated the setup to be one-dimensional, which was sufficient to get a good fit to the data. In Sec. 4.2.2, we took into account the geometry of the setup, which e.g. revealed the existence of ring currents in the thermoelectric setup. Both models give a Debye length of a few tens of nanometers, which is consistent with the results from the KPFM measurements.

To the knowledge of the author, our study is the first in which the thickness dependence of the out-of-plane Seebeck coefficient is measured. In contrast to the work by Pettes et al. [89], which studies the in-plane Seebeck coefficient, we have demonstrated that band bending can be observed directly in a series of Seebeck coefficient measurements. However, our setup has some disadvantages. As described in Sec. 4.3, it is difficult to know the actual temperature drop across the sample. As a consequence, we can not be sure that the measured Seebeck coefficient is that of the sample. The length dependence of S_{measured} is therefore due to a combination of the band bending and the temperature effect, but as we argue in Sec. 4.3, the band bending effect dominates.

Part II

Spins out of equilibrium

Chapter 5

Introduction

In this second part of the thesis, we will stay within the topic of nonequilibrium physics, but we will move to a quite different system. We will turn off the temperature difference and instead study how an electric current influences the “motion” of localized magnetic moments. In the following chapters, we will derive the equation of motion (EOM) for a two-spin system and we will see that an electric current can drive the system into unexpected configurations.

When a quantum mechanical system is in contact with an environment (a bath), it can lose its phase and therefore its quantum mechanical character. One can think of it as if the environment is doing measurements on the quantum system, which “collapses” the system wavefunction. The system consequently turns classical. As an example, it has been shown that in the semiclassical limit, the dynamics of a quantum mechanical particle follows a Langevin equation, when it is interacting with an environment of a large number of harmonic oscillators [112, 113]. The environment gives rise to frictional and fluctuating forces, and these are connected via the fluctuation–dissipation theorem. If the system has two or more degrees of freedom, the interaction with the environment can couple these degrees of freedom. In equilibrium, the forces are symmetric in the coordinates; i.e. if the force on one mode is given by $f_x = -ky$, then there is a similar force on the other given by $f_y = -kx$.

When the environment is brought out of equilibrium, new “forces” appear in the EOMs.¹ This has been studied for atoms coupled to electronic reservoirs out of equilibrium [114–117]. The nonequilibrium conditions give rise to forces that are antisymmetric in the coordinates. I.e. if the force on one is $f_x^{nc} = -ay$, it is $f_y^{nc} = ax$ on the other, where the coefficient a vanishes when the system is brought to equilibrium. This is a non-conservative force field, which means that energy can be pumped into the system when it moves along a closed trajectory. Consequently, energy leaves the system when it follows the trajectory in the opposite direction. In the case of atoms in a nonequilibrium electronic environment, antisymmetric velocity dependent forces also appear. A simple example of such forces is $f_x^L = b\dot{y}$ and $f_y^L = -b\dot{x}$. This is the antisymmetric version of friction, but it is more like a Lorentz force; it cannot change the energy of the system.

In this thesis, we will consider a system of two localized magnetic moments which couple via a simple current-carrying metal. We will often refer to the moments as spins. In Sec. 5.1, we will start by introducing the equilibrium version in which the well-known RKKY interaction couples the two spins. In Sec. 5.2, the literature on spins coupled to a nonequilibrium electronic bath is reviewed. The calculation of the EOM for a two-spin system coupled to a nonequilibrium metal is carried out in the following chapter.

¹In the case of angular momenta, we have torques instead of forces. This is the reason for the quotation marks.

5.1 Coupled spins in equilibrium

5.1.1 The RKKY interaction

As mentioned, localized moments in a metal can couple via the conduction electrons. This was first discovered for nuclear spins that couple to conduction electrons through the hyperfine interaction [118], and later for d-electron spins [119, 120]. The indirect interaction is known as the Ruderman-Kittel-Kasuya-Yosida (RKKY) interaction after its founders. We will here briefly go through the derivation of the interaction and many of the introduced elements will be used in Chapter 6, where nonequilibrium effects are to be included.

Consider a system of two localized spins in a metal as illustrated schematically in Fig. 5.1. The system is described by the Hamiltonian

$$H = H_0 + H_{\text{int}}, \quad (5.1)$$

where the Hamiltonian for the isolated systems is

$$H_0 = \sum_{\mathbf{k}\sigma} \varepsilon_{\mathbf{k}} c_{\mathbf{k}\sigma}^\dagger c_{\mathbf{k}\sigma} - \mathbf{B} \cdot (\mathbf{S}_1 + \mathbf{S}_2). \quad (5.2)$$

Here the creation (annihilation) operator creates (removes) an electron with wave number \mathbf{k} and spin σ . We consider the conduction electrons to be free-electron-like, so that the dispersion can be written as $\varepsilon_{\mathbf{k}} = \frac{\hbar^2 k^2}{2m}$, where m is the effective mass. \mathbf{B} is the field in which direction the spins preferably want to point and we have chosen the spin operators \mathbf{S} to be dimensionless so that \mathbf{B} has units of energy. \mathbf{B} is related to the real magnetic field by $\mathbf{B} \equiv \hbar\gamma\mathbf{B}_{\text{magnetic}} = -g\mu_B\mathbf{B}_{\text{magnetic}}$, where γ is the gyromagnetic ratio, μ_B is the Bohr magneton, and g is the g-factor.

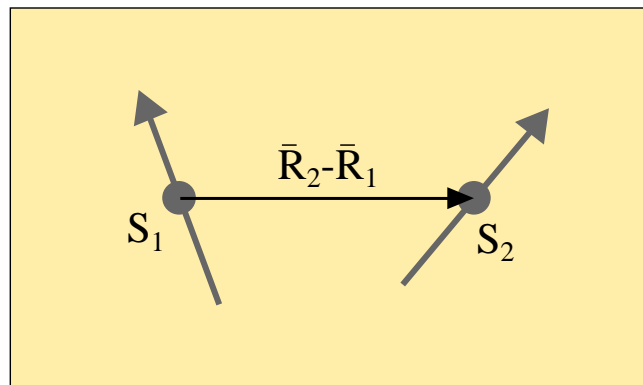


FIGURE 5.1: Illustration of two localized spins in a metal.

The conduction electrons interact with the localized spins via a direct exchange coupling. We can write the interaction as $H_{\text{int}} = -\sum_n \int d\mathbf{r} J_r(\mathbf{r} - \mathbf{R}_n) \mathbf{S}_n \cdot \mathbf{s}(\mathbf{r})$, where \mathbf{R}_n is the position of spin n , $J_r(\mathbf{r} - \mathbf{R}_n)$ is the exchange coupling, while $\mathbf{s}(\mathbf{r})$ is the spin density of the conduction electrons. The interaction is short range and can be approximated by a delta function [120, 121], $J_r(\mathbf{r} - \mathbf{R}) = J_0\delta(\mathbf{r} - \mathbf{R})$, so that

$$H_{\text{int}} = -J_0 [\mathbf{S}_1 \cdot \mathbf{s}(\mathbf{R}_1) + \mathbf{S}_2 \cdot \mathbf{s}(\mathbf{R}_2)]. \quad (5.3)$$

However, the interaction of course has a finite width, which one has to keep in mind. The spin density of the conduction electrons is

$$\begin{aligned} \mathbf{s}(\mathbf{r}) &= \frac{1}{2} \begin{pmatrix} \psi_{\uparrow}^{\dagger}(\mathbf{r}) & \psi_{\downarrow}^{\dagger}(\mathbf{r}) \end{pmatrix} \boldsymbol{\sigma} \begin{pmatrix} \psi_{\uparrow}(\mathbf{r}) \\ \psi_{\downarrow}(\mathbf{r}) \end{pmatrix} \\ &= \frac{1}{2\mathcal{V}} \sum_{\mathbf{k}\mathbf{k}'} e^{-i(\mathbf{k}-\mathbf{k}')\cdot\mathbf{r}} \sum_{\sigma\sigma'} c_{\mathbf{k}\sigma}^{\dagger} \boldsymbol{\sigma}_{\sigma\sigma'} c_{\mathbf{k}'\sigma'}, \end{aligned} \quad (5.4)$$

where we inserted the field operator, $\psi_{\sigma}(\mathbf{r}) = \frac{1}{\sqrt{\mathcal{V}}} \sum_{\mathbf{k}} e^{i\mathbf{k}\cdot\mathbf{r}} c_{\mathbf{k}\sigma}$. Notice that with the above definition of H_{int} , the exchange coupling J_0 has units of $\text{m}^3 \text{J}$.

If the interaction is considered as a perturbation, the first order process will cause the conduction electrons to spin-polarize [120] - a polarization that oscillates and decays when moving away from the localized spins. The second order processes allow the transfer of angular momentum from one localized spin to the other. One way to think about it is that the polarized conduction electrons from one localized spin interact with the other. Second order perturbation theory will therefore lead to an effective Hamiltonian for the localized spins, which are indirectly coupled via the conduction electrons

$$H_{\text{eff}} = -\mathbf{B} \cdot (\mathbf{S}_1 + \mathbf{S}_2) + J(R) \mathbf{S}_1 \cdot \mathbf{S}_2 + E_{\text{local}} \quad (5.5)$$

where $R = |\mathbf{R}_2 - \mathbf{R}_1|$ is the distance between the spins as seen in Fig. 5.1. At low temperatures, the indirect exchange coupling is [118, 120]

$$J(R) = \frac{J_0^2 k_F^6}{4\pi^3 \varepsilon_F} F(2k_F R), \quad (5.6)$$

where ε_F is the Fermi energy and k_F is the Fermi wave number. The distance dependent function is

$$F(x) = \frac{x \cos x - \sin x}{x^4}, \quad (5.7)$$

which goes as $F(x) \approx x^{-3} \cos x$ for large x . If the exchange coupling is negative (positive), the spins preferably align (anti-align) and we call the coupling ferromagnetic (antiferromagnetic). Since the coupling oscillates, the spins will be ferromagnetically coupled at some distances and antiferromagnetically coupled at others.

The term E_{local} in Eq. (5.5) includes the first and second order correction that only involves the localized spins separately. All these corrections are constants. However, with the model in Eq. (5.3), one will encounter diverging second order terms. The reason is the delta function potential, which was chosen to make the calculation easier. Giving the potential a finite width, which can be done by setting a cutoff for the Fourier components of $J_r(\mathbf{r} - \mathbf{R})$, the integrals will converge.

Magnetic dipole-dipole interactions are also present between the localized spins, but they are weak compared to the RKKY interaction [122], and they are therefore neglected in this thesis.

5.1.2 Equation of motion

Having established the mechanism for the exchange interaction of interest, we will now consider how a spin system evolves in time. To do so, we can study the time derivative

of the spin operator using the Heisenberg equation of motion, $\frac{d\hat{\mathbf{S}}_1}{dt} = \frac{i}{\hbar} [H_{\text{eff}}, \hat{\mathbf{S}}_1]$,

$$\frac{d\hat{\mathbf{S}}_1}{dt} = -\frac{1}{\hbar} \mathbf{B} \times \hat{\mathbf{S}}_1 + \frac{J}{\hbar} \hat{\mathbf{S}}_2 \times \hat{\mathbf{S}}_1, \quad (5.8)$$

where the commutation relation $[\hat{S}_i^\alpha, \hat{S}_j^\beta] = i\delta_{ij}\epsilon_{\alpha\beta\gamma}\hat{S}_i^\gamma$ was used. The same equation holds for $1 \leftrightarrow 2$. We have included hats in the above equations to stress that the $\hat{\mathbf{S}}$'s are quantum mechanical operators. If we remove the hats and consider the \mathbf{S} 's as classical angular momentum vectors, Eq. (5.8) becomes the Landau-Lifshitz equation [123]. In the classical version of Eq. (5.8), the spin vectors will precess around their local field forever. However, in real systems, the spins will relax to the ground state after some time. To ensure this, a relaxation term was suggested by Gilbert in 1956 [124],

$$\frac{d\mathbf{S}_1}{dt} = -\mathbf{B}_1 \times \mathbf{S}_1 + \eta_0 \frac{d\mathbf{S}_1}{dt} \times \mathbf{S}_1, \quad (5.9)$$

where η_0 is the Gilbert damping constant and $\mathbf{B}_1 = (\mathbf{B} - J\mathbf{S}_2)/\hbar$ is the local field felt by spin 1. The above equation is known as the Landau-Lifshitz-Gilbert (LLG) equation. Landau and Lifshitz also suggested a phenomenological relaxation term, $-\lambda \mathbf{S} \times (\mathbf{S} \times \mathbf{B})$, which is mathematically equivalent to the Gilbert term [124, 125].

Even though the phenomenological LLG equation has been known for about 60 years and is in good agreement with experiments, the microscopic origin of the relaxation is still under debate [126]. Several theories give rise to Gilbert damping, including coupling to phonons [127] and spin-orbit coupling [128]. The coupling to conduction electrons also gives rise to Gilbert damping [129–131], and it has the form²

$$\eta_0 = \frac{\pi}{8} J_0^2 \rho(\varepsilon_F)^2, \quad (5.10)$$

when the Hamiltonian is defined as in Eqs. (5.1)–(5.3). Here $\rho(\varepsilon_F) = \frac{mk_F}{\pi^2\hbar^2}$ is the density of states at the Fermi energy. In the case of two (or more) spins, the interaction in Eq. (5.3) also introduces non-local damping terms of the kind $\eta_1 \hat{\mathbf{S}}_2 \times \mathbf{S}_1$ [131, 132], which we will see in our derivation in Chapter 6 as well.

5.2 Spins in nonequilibrium conditions

Based on the previous sections, it is now interesting to ask what happens to the dynamics of a spin, when the conduction electrons are brought out of equilibrium. This has been studied for single magnetic moments [133, 134] and single magnetized regions [129]. Bode et al. did a theoretical study of a single-molecule magnet in a junction with spin-polarized leads [133]. They found that a potential difference gives rise to non-conservative torques, which can force the moment to point anti-parallel to the magnetic field. However, when the spin polarization is turned off, they are left with the standard LLG equation. The concept of spin-transfer torques has been known for quite some time [135, 136] and there has in general been a large focus on how spin-polarized currents affect magnetic systems. As Brataas et al. state in the first sentence of their Nature Materials review: “*The magnetization of a magnetic material can be reversed by using electric currents that transport spin angular momentum*” [137]. However, as we are about to demonstrate, the magnetization can also be reversed by a charge current.

² The Gilbert coefficient is stated in [130, 131], but some rewriting is required.

When two magnetic moments couple to conduction electrons, nonequilibrium conditions can modify the RKKY interaction. This has been shown in both a tunnel junction [138] and a two-dimensional electron gas [139]. However, the nonequilibrium effects on multiple magnetic moments have not been studied much in the literature. This was one reason for looking into the field, but after finishing the calculation in Chapter 6, we discovered that a similar study had already been done. Onoda et al. calculated the EOMs for multiple spins coupled via conduction electrons that carry both charge and spin currents [131]. In addition to the torques from the spin-polarized current, they found that a charge current renormalizes the exchange torques and gives a correction to the non-local damping.³ They did not calculate, or at least present, the explicit expressions for the torques generated by the charge currents. Furthermore the article by Onoda et al. focuses on the spin current, but there is some unexplored interesting physics in the EOMs induced by the charge current as well. We will take a closer look at these points in the following chapters.

³This is expressed using the words from Ref. [131]. As we will see in the following chapters, the new torques are more than just corrections to the equilibrium terms, since they appear antisymmetrically in the EOMs.

Chapter 6

Coupled spins out of equilibrium

Some of the results in this chapter are included in the paper draft in Appendix F.

In this chapter, we will calculate the equation of motion (EOM) for a two-spin system, which is in contact with a simple metal out of equilibrium. In contrast to the studies of nonequilibrium effect on atomic motion [114–117], we will calculate the effect of an electric current rather than an applied bias. The current is included by shifting the Fermi sphere as shown in Fig. 6.1 and this will be included in the density matrix in Sec. 6.2.3. As mentioned in the previous chapter, this is similar to the work done in Ref. [131].

To describe the system, we will use the Hamiltonian in Eqs. (5.1)–(5.3), which was used to derive the RKKY interaction. We will again go to second order in the local exchange in order to find how the indirect coupling affects the dynamics of the spins. The derivation in this chapter is rather technical, but our goal can be expressed as follows: as the localized spins rotate in an electronic environment, they can excite electron-hole pairs of the electron gas. These electron-hole pairs act back on the spins as torques, which are the ones we are interested in. Before doing the derivation, some important mathematical tools will be introduced.

6.1 Introduction to coherent states

Coherent states are important, when we will construct different path integrals in the following. In this section, we will briefly introduce both spin and fermionic coherent states.

6.1.1 Spin coherent states

When constructing a spin path integral, it is convenient to use spin coherent states. A spin coherent state for a single spin can be defined as [140]¹

$$|a\rangle \equiv e^{-i\phi S^z} e^{-i\theta S^y} |\uparrow\rangle, \quad (6.1)$$

where $|\uparrow\rangle = |S, m = S\rangle$, so that $S^z |\uparrow\rangle = S |\uparrow\rangle$. We have considered the spin operators to be dimensionless. The rotation operators in front rotate the state, $|\uparrow\rangle$, so that it will point 'up' along the vector with spherical polar angles θ and ϕ . A useful property of the spin coherent state is therefore that the expectation value of the vector of spin operators is

$$\langle a | \hat{\mathbf{S}} | a \rangle = S \mathbf{n} = S \begin{pmatrix} \sin \theta \cos \phi \\ \sin \theta \sin \phi \\ \cos \theta \end{pmatrix}, \quad (6.2)$$

¹It is normally defined with a phase factor $e^{-i\psi S}$, which is excluded here.

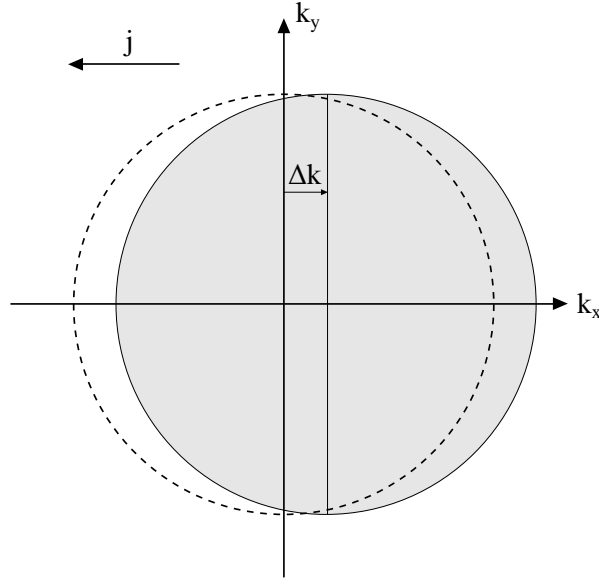


FIGURE 6.1: The electronic system is brought out of equilibrium by displacing the Fermi sphere. The figure shows a cross section of the sphere displaced by $\Delta\mathbf{k}$, which is taken to be along k_x in this figure. The electronic states are occupied in the grey region. The displacement, Δk , is small compared to the Fermi wave number, k_F , but it is exaggerated here for visualization purposes.

where \mathbf{n} is a unit vector pointing along the direction determined by the spherical polar angles θ and ϕ . This can be shown by using [140]²

$$e^{i\theta S^i} S^j e^{-i\theta S^i} = S^j \cos \theta - \epsilon_{ijk} S^k \sin \theta, \quad (6.3)$$

which is true for $i \neq j$ (for $i = j$, it is simply $e^{i\theta S^i} S^i e^{-i\theta S^i} = S^i$). We can write the identity operator for a single spin in terms of the coherent states as [141]

$$1 = \frac{2S+1}{4\pi} \int_0^\pi d\theta \sin \theta \int_0^{2\pi} d\phi |a\rangle\langle a|. \quad (6.4)$$

The identity is an important ingredient when constructing the spin path integral.

In the particular problem at hand, we consider a system with two spins. The spin coherent states are therefore

$$|a_1, a_2\rangle = \left(e^{-i\phi_1 S_1^z} e^{-i\theta_1 S_1^y} \right) \otimes \left(e^{-i\phi_2 S_2^z} e^{-i\theta_2 S_2^y} \right) |\uparrow\uparrow\rangle. \quad (6.5)$$

To keep the notation as simple as possible, we will use $|a\rangle$ to denote the two-spin coherent state unless otherwise stated. The spin identity operator in the two-spin case is $1 = 1_1 \otimes 1_2$, where the individual identities are defined as in Eq. (6.4), and we will use the short hand notation $1 = \int da |a\rangle\langle a|$.³

²This expression can be derived by writing the exponential operators as power series and then evaluating the emerging commutators.

³Written out, the identity is

$$1 = \left(\frac{2S+1}{4\pi} \right)^2 \int_0^\pi d\theta_1 \sin \theta_1 \int_0^{2\pi} d\phi_1 \int_0^\pi d\theta_2 \sin \theta_2 \int_0^{2\pi} d\phi_2 |a_1, a_2\rangle\langle a_1, a_2| \quad (6.6)$$

6.1.2 Fermionic coherent states

In this subsection, we will give a brief introduction to fermionic coherent states. For a more thorough description, see e.g. Ref. [140]. The fermionic coherent state $|\eta\rangle$ is an eigenstate of the fermionic annihilation operators

$$c_{\mathbf{k}\sigma} |\eta\rangle = \eta_{\mathbf{k}\sigma} |\eta\rangle. \quad (6.7)$$

Since the fermionic operators anti-commute, so do the eigenvalues $\eta_{\mathbf{k}\sigma}$, which are known as Grassmann numbers. We therefore have that $\eta_{\mathbf{k}\sigma}\eta_{\mathbf{k}'\sigma'} + \eta_{\mathbf{k}'\sigma'}\eta_{\mathbf{k}\sigma} = 0$ and consequently $\eta_{\mathbf{k}\sigma}^2 = 0$. The coherent states are defined as

$$|\eta\rangle = e^{-\sum_{\mathbf{k}\sigma} \eta_{\mathbf{k}\sigma} c_{\mathbf{k}\sigma}^\dagger} |0\rangle, \quad (6.8)$$

which can be written as $|\eta\rangle = \prod_{\mathbf{k}\sigma} (1 - \eta_{\mathbf{k}\sigma} c_{\mathbf{k}\sigma}^\dagger) |0\rangle$ due to the property $\eta_{\mathbf{k}\sigma}^2 = 0$. Similarly, the adjoint of the coherent state is defined as $\langle\eta| = \langle 0| e^{-\sum_{\mathbf{k}\sigma} c_{\mathbf{k}\sigma} \bar{\eta}_{\mathbf{k}\sigma}}$, where $\bar{\eta}_{\mathbf{k}\sigma}$ is a Grassmann number independent of $\eta_{\mathbf{k}\sigma}$. With these ingredients, we can write the overlap between two coherent states, the identity operator in the Fock space, and the trace of an operator O as⁴

$$\langle\eta^i|\eta^j\rangle = e^{\sum_{\mathbf{k}\sigma} \bar{\eta}_{\mathbf{k}\sigma}^i \eta_{\mathbf{k}\sigma}^j} \quad (6.9)$$

$$\mathbf{1}_{\mathcal{F}} = \int d(\bar{\eta}, \eta) e^{-\sum_{\mathbf{k}\sigma} \bar{\eta}_{\mathbf{k}\sigma} \eta_{\mathbf{k}\sigma}} |\eta\rangle\langle\eta| \quad (6.10)$$

$$\text{Tr}_e[O] = \int d(\bar{\eta}, \eta) e^{-\sum_{\mathbf{k}\sigma} \bar{\eta}_{\mathbf{k}\sigma} \eta_{\mathbf{k}\sigma}} \langle -\eta| O |\eta\rangle, \quad (6.11)$$

where $d(\bar{\eta}, \eta)$ is short hand notation for $\prod_{\mathbf{k}\sigma} d\bar{\eta}_{\mathbf{k}\sigma} d\eta_{\mathbf{k}\sigma}$ and $\langle -\eta| = \langle 0| e^{\sum_{\mathbf{k}\sigma} c_{\mathbf{k}\sigma} \bar{\eta}_{\mathbf{k}\sigma}}$. Eqs. (6.9)–(6.11) will be useful in Sec. 6.2.3, where we will construct the functional integral.

6.2 Feynman-Vernon theory

To solve the problem of two spins coupled by a nonequilibrium electronic bath, we will use the influence functional method proposed by Feynman and Vernon [142]. The Feynman-Vernon method is quite technical and for a short and comprehensible overview, see e.g. Ref. [143]. The basic idea is to trace out the electronic degrees of freedom in the density matrix. This gives the reduced density matrix of the spin system, which contains the information from the electronic bath in the so-called influence functional. By doing a perturbative expansion and some rewriting of the influence functional, the contribution from the electrons will show up in the action from which the EOMs can be read of.

The author has tried to present the derivation in a concise way with most of the technicalities collected in Appendix D. Here is an overview of what we are about to go through:

- In Sec. 6.2.1, we will trace out the electronic degrees of freedom. The resulting reduced density matrix can be written as a double path integral over spin paths, which are coupled by the influence functional.

⁴For the derivations, see e.g. Ref. [140].

- In Sec. 6.2.2, we will consider the double path integral without the influence functional. In the semiclassical approximation, we will see that the average of the two paths follows the classical EOM for uncoupled spins in a magnetic field.
- In Sec. 6.2.3, the influence functional is written as a functional integral over Grassman numbers. The integral is performed and we do an expansion to second order in the local exchange coupling, J_0 . The second order term gives a contribution which can be written in terms of the average and difference spin paths.
- In Sec. 6.2.4, the spins are assumed to be slow compared to the electrons, which leads to time-local EOMs for the spins.
- In Sec. 6.2.5, explicit expressions for the coefficients in the EOMs are derived. We arrive at the well known expressions for the RKKY coupling and the Gilbert constant. We present, for the first time, the nonequilibrium coefficients and their distance dependences. Finally, in Sec. 6.2.6, we estimate how large the nonequilibrium terms are in realistic systems.

6.2.1 The reduced density matrix

In this section, we will trace out the electronic degrees of freedom to obtain the reduced density matrix for the spins. The section is written with inspiration from Refs. [112, 113, 115, 142].

The whole system includes both the spins and the electronic bath. It can be described by the total density matrix $\hat{\rho}_{\text{tot}}(t_f) = e^{-iHt_f} \hat{\rho}_{\text{tot}}(0) e^{iHt_f}$, where the Hamiltonian is defined as in Eqs. (5.1)–(5.3), t_f is a time, and we have set $\hbar = 1$. We will assume that the spin system and the bath are initially uncorrelated so that $\hat{\rho}_{\text{tot}}(0) = \hat{\rho}_s(0) \otimes \hat{\rho}_e(0)$, where s and e refer to spins and electrons, respectively. The out-of-equilibrium condition will be included in $\hat{\rho}_e(0)$, which we will return to in Sec. 6.2.3. We are only interested in the information about the spin system, and we can therefore trace out the electronic degrees of freedom to obtain the reduced density matrix for the spins

$$\hat{\rho}_{\text{red}}(t_f) = \text{Tr}_e [e^{-iHt_f} \hat{\rho}_{\text{tot}}(0) e^{iHt_f}]. \quad (6.12)$$

Taking an element of this reduced density matrix, we get

$$\begin{aligned} \rho_{\text{red}}(a^1, b^1, t_f) &= \langle a^1 | \hat{\rho}_{\text{red}}(t_f) | b^1 \rangle \\ &= \int da^0 \int db^0 \text{Tr}_e [\langle a^1 | e^{-iHt_f} | a^0 \rangle \langle a^0 | \hat{\rho}_{\text{tot}}(0) | b^0 \rangle \langle b^0 | e^{iHt_f} | b^1 \rangle] \\ &= \int da^0 \int db^0 \mathcal{J}(a^1, b^1, t_f; a^0, b^0, 0) \rho_s(a^0, b^0, 0) \end{aligned} \quad (6.13)$$

where $1 = \int da |a\rangle\langle a|$ is short for the identity in Eq. (6.6). Both a and b refer to spin coherent states and the superscripts are used to distinguish the different states. The superscript will later be used as a time index. The introduced propagator for the reduced density is

$$\mathcal{J}(a^1, b^1, t_f; a^0, b^0, 0) = \text{Tr}_e [\hat{\rho}_e(0) \langle b^0 | e^{iHt_f} | b^1 \rangle \langle a^1 | e^{-iHt_f} | a^0 \rangle], \quad (6.14)$$

which describes the dynamics of the system. Eq. (6.14) can be written as a spin path integral by using the spin coherent states introduced in Sec. 6.1.2. To do so, we split the time evolution operator into tiny time steps, $e^{-iHt_f} = \lim_{N \rightarrow \infty} \prod_{n=1}^N e^{-iH\Delta t}$,

where $t_f = N\Delta t$. We insert identities of spin coherent states as defined in Eq. (6.4) in between all the exponential operators. Since Δt is very small, it is reasonable to expand $e^{-iH\Delta t}$ to first order in Δt , $e^{-iH\Delta t} \approx 1 - iH_{0,e}\Delta t - iH_{0,s}\Delta t - iH_{\text{int}}\Delta t$. Here $H_{0,e}$ ($H_{0,s}$) denotes the Hamiltonian of the isolated electronic (spin) system as defined in Eq. (5.2). By doing this, we can rewrite the elements as

$$\langle a^{i+1} | e^{-iH\Delta t} | a^i \rangle \approx e^{-i\Delta t [i\langle \partial_t a^i | a^i \rangle + \langle a^i | H_{0,s} | a^i \rangle]} e^{-i\Delta t [H_{0,e} + \langle a^i | H_{\text{int}} | a^i \rangle]}, \quad (6.15)$$

where we used the notation $\langle \partial_t a^i | = (\langle a^{i+1} | - \langle a^i |) / \Delta t$ and used that in the continuum limit, $N \rightarrow \infty$, $\langle a^{i+1} | H | a^i \rangle \approx \langle a^i | H | a^i \rangle$. Since the first exponential factor is just a function, we can take all these out in front and write

$$\begin{aligned} \langle a^1 | e^{-iHt_f} | a^0 \rangle &= \int \mathcal{D}a e^{i\mathcal{S}[a]} \lim_{N \rightarrow \infty} \prod_{i=1}^N e^{-i[H_{0,e} + \langle a^i | H_{\text{int}} | a^i \rangle] \Delta t} \\ &= \int \mathcal{D}a e^{i\mathcal{S}[a]} U[a], \end{aligned} \quad (6.16)$$

where $\mathcal{D}a = \prod_{n=1}^2 \prod_{i=2}^N \frac{2S+1}{4\pi} \int_0^\pi d\theta_n^i \sin \theta_n^i \int_0^{2\pi} d\phi_n^i$ and $U[a]$ is the forward time evolution operator of the electronic system, when the spins follow path a . The introduced $\mathcal{S}[a]$ denotes the action for the spin system, which we will return in the following section. Similarly, $U^\dagger(b)$ will show up in $\langle b^0 | e^{iHt_f} | b^1 \rangle$, which is the backward time evolution operator when the spins follow path b . With this notation, we can write the density matrix propagator in Eq. (6.14) as

$$\mathcal{J}(a^1, b^1, t; a^0, b^0, 0) = \int \mathcal{D}a \int \mathcal{D}b e^{i\mathcal{S}[a] - i\mathcal{S}[b]} F[a, b], \quad (6.17)$$

where

$$F[a, b] = \text{Tr}_e \left[\hat{\rho}_e(0) U^\dagger[b] U[a] \right] \quad (6.18)$$

is the influence functional. The influence functional describes the influence of the electronic environment on the spin system. One way to think about the double path integral in Eq. (6.18) is that the spins follow path a forward in time and path b backward in time. In the case where the spins do not interact with the bath, $J_0 = 0$, we get that $U^\dagger U = 1$ and consequently $F = 1$. We are therefore left with a double path integral of the spin system alone, which means that the spins propagate freely both forward and backward in time. On the other hand, when the spins interact with the electrons, $J_0 \neq 0$, the influence functional will couple the forward and backward paths. To get the contribution from the electronic bath to the spin action, we can put the influence functional on the form

$$F[a, b] = e^{i\Delta\mathcal{S}[a,b]}, \quad (6.19)$$

where $\Delta\mathcal{S}[a, b] = -i \ln F[a, b]$ is known as the influence phase [142]. It is clear that when $F[a, b] = 1$, the electronic contribution to the action vanishes, $\Delta\mathcal{S}[a, b] = 0$. Before taking a closer look at influence functional in Sec. 6.2.3, we will consider the spin action.

6.2.2 The spin action

The spin action was introduced between Eq. (6.15) and (6.16). Taking the continuum limit, we can write it as

$$\mathcal{S}[a] = - \int_0^{t_f} dt [\langle a(t) | H_{0,s} | a(t) \rangle + i \langle \partial_t a(t) | a(t) \rangle]. \quad (6.20)$$

The first term is easily evaluated by using Eq. (6.2),

$$\langle a(t) | H_{0,s} | a(t) \rangle = -S\mathbf{B} \cdot [\mathbf{n}_1^+(t) + \mathbf{n}_2^+(t)], \quad (6.21)$$

where the introduced unit vector $\mathbf{n}_n^+(t)$ describes the orientation of spin n at time t on the forward path, a . Similarly, we will later use the superscript “-” for the vectors on the backward path, b . The second term in Eq. (6.20) is (for a single spin for simplicity)⁵

$$\begin{aligned} i \langle \partial_t a | a \rangle &= i \langle \uparrow | \left(\frac{\partial}{\partial t} e^{i\theta S_y} e^{i\phi S_z} \right) e^{-i\phi S_z} e^{-i\theta S_y} | \uparrow \rangle \\ &= i \langle \uparrow | e^{i\theta S_y} \left(i\dot{\theta} S_y + i\dot{\phi} S_z \right) e^{i\phi S_z} e^{-i\phi S_z} e^{-i\theta S_y} | \uparrow \rangle \\ &= -\dot{\theta} \langle \uparrow | e^{i\theta S_y} S_y e^{-i\theta S_y} | \uparrow \rangle - \dot{\phi} \langle \uparrow | e^{i\theta S_y} S_z e^{-i\theta S_y} | \uparrow \rangle \\ &= -S\dot{\phi} \cos \theta \end{aligned} \quad (6.23)$$

where we used Eq. (6.3). This second contribution to the action is a so-called Wess-Zumino action [140]. It is a topological term, since it is invariant under any reparametrization of the time and it describes the accumulated Berry phase as the spin moves on the sphere [144].

With the above expressions, we can write the difference action in Eq. (6.17) as

$$\mathcal{S}[a] - \mathcal{S}[b] = S \sum_{n=1,2} \int_0^{t_f} dt \left\{ \mathbf{B} \cdot [\mathbf{n}_n^+ - \mathbf{n}_n^-] + \left[\dot{\phi}_n^+ \cos \theta_n^+ - \dot{\phi}_n^- \cos \theta_n^- \right] \right\} \quad (6.24)$$

where the angles $\theta_n^\pm(t)$ and $\phi_n^\pm(t)$ are the ones that describe the vector $\mathbf{n}_n^\pm(t)$.

As described in the beginning of Chapter 5, the electronic environment “collapses” the wavefunction of the spin system, so that the spins turn classical. Mathematically, this is caused by the influence functional, which will suppress contributions of histories for which the difference vectors, $\mathbf{n}_n^+ - \mathbf{n}_n^-$, are large. Because of this, it makes sense to expand the action in Eq. (6.24) to low order in the differences. In Appendix D.1, we expand the double action to first order in the difference angles, $\theta_n^+ - \theta_n^-$ and $\phi_n^+ - \phi_n^-$, and carry out the difference angle integrals. With this, we find that the unit vector \mathbf{n}_n described by the average angles $\theta_n = \frac{1}{2}(\theta_n^+ + \theta_n^-)$ and $\phi_n = \frac{1}{2}(\phi_n^+ + \phi_n^-)$ follows the classical equation of motion

$$\dot{\mathbf{n}}_n = -\mathbf{B} \times \mathbf{n}_n. \quad (6.25)$$

⁵For two spins, it is just

$$(\partial_t \langle a_1, a_2 | | a_1, a_2 \rangle = \langle \uparrow \uparrow | \left[(\partial_t R_1^\dagger) \otimes R_2^\dagger + R_1^\dagger \otimes (\partial_t R_2^\dagger) \right] (R_1 \otimes R_2) | \uparrow \uparrow \rangle \quad (6.22)$$

where $R_n = e^{-i\phi_n S_n^z} e^{-i\theta_n S_n^y}$. It is therefore the sum of the two individual contributions as in Eq. (6.23).

In other words, the unit vector pointing in the direction between the forward and backward vectors, $\mathbf{n}_n^+(t)$ and $\mathbf{n}_n^-(t)$, will precess around the magnetic field.

Say that we want to add a torque $-\mathbf{f} \times \mathbf{n}_n$ to the EOM by hand. In the introduced formalism, we could do this by adding a term $S \int dt \mathbf{f} \cdot (\mathbf{n}_n^+ - \mathbf{n}_n^-)$ to the double action in Eq. (6.24). The purpose of this chapter is to derive the torques that are caused by the interaction with the electronic system. If the influence functional therefore gives rise to contributions on this form (vectors dotted with $\mathbf{n}_n^+ - \mathbf{n}_n^-$), the torques can be read off directly from the action. As we will see in the following, a perturbative expansion of the influence phase will indeed add such contributions to the action, and these are the ones we are interested in.

6.2.3 The influence functional

We will now return to the influence functional defined in Eq. (6.18). To get on from here, we need to be more specific about the initial density matrix for the electrons. As shown in Fig. 6.1, the electrons are brought out of equilibrium by displacing the Fermi sphere. The initial density matrix for the electrons can therefore be written as

$$\hat{\rho}_e(0) = \frac{1}{Z} e^{-\beta \sum_{\mathbf{k}\sigma} (\varepsilon_{\mathbf{k}-\Delta\mathbf{k}} - \mu)} c_{\mathbf{k}\sigma}^\dagger c_{\mathbf{k}\sigma} \quad (6.26)$$

where the partition function is $Z = \prod_{\mathbf{k}\sigma} \left(1 + e^{-\beta(\varepsilon_{\mathbf{k}-\Delta\mathbf{k}} - \mu)} \right)$.

We can write Eq. (6.18) as a coherent state functional integral by splitting the time evolution operators into small time steps and inserting unit operators as defined in Eq. (6.10). This is done in detail in Appendix D.2 by following the discrete procedure in e.g. Refs. [140, 145]. In this way, the influence functional takes the form

$$F[a, b] = \frac{1}{Z} \int \mathcal{D}(\bar{\eta}, \eta) \exp \left[i \sum_{ij} \sum_{\mathbf{k}\sigma} \sum_{\mathbf{k}'\sigma'} \bar{\eta}_{\mathbf{k}\sigma}^i \left((G_{0,\mathbf{k}}^{-1})^{ij} \delta_{\mathbf{k},\mathbf{k}'} \delta_{\sigma,\sigma'} + \tilde{V}_{\mathbf{k}\sigma,\mathbf{k}'\sigma'}^{ij} \right) \eta_{\mathbf{k}'\sigma'}^j \right]. \quad (6.27)$$

Here the interaction part is $\tilde{V}_{\mathbf{k}\sigma,\mathbf{k}'\sigma'}^{ij} = \lambda_i \Delta t V_{\mathbf{k}\sigma,\mathbf{k}'\sigma'}^{\lambda_i}(t_i) \delta_{i,j+1}$, where $\lambda_i = \pm 1$ when t_i is on the forward/backward time path and

$$V_{\mathbf{k}\sigma,\mathbf{k}'\sigma'}^\pm(t) = \frac{SJ_0}{2\mathcal{V}} \sum_{n=1,2} e^{-i(\mathbf{k}-\mathbf{k}') \cdot \mathbf{R}_n} \mathbf{n}_n^\pm(t) \cdot \boldsymbol{\sigma}_{\sigma\sigma'}. \quad (6.28)$$

The vectors \mathbf{n}_n^+ and \mathbf{n}_n^- are again the orientations of spin n on the forward and backward paths, respectively (initially referred to as a and b). The inverse Greens function, $G_{0,\mathbf{k}}^{-1}$, is defined in Eq. (D.17). The Greens function itself takes the form

$$G_{0,\mathbf{k}}(t, t') = ie^{-i\varepsilon_{\mathbf{k}}(t-t')} \begin{pmatrix} n_F(\varepsilon_{\mathbf{k}-\Delta\mathbf{k}} - \mu) - \theta(t-t') & n_F(\varepsilon_{\mathbf{k}-\Delta\mathbf{k}} - \mu) \\ n_F(\varepsilon_{\mathbf{k}-\Delta\mathbf{k}} - \mu) - 1 & n_F(\varepsilon_{\mathbf{k}-\Delta\mathbf{k}} - \mu) - \theta(t' - t) \end{pmatrix} \quad (6.29)$$

in the continuum limit, where $n_F(\varepsilon)$ is the Fermi function and $\theta(t)$ is the Heaviside step function. The upper left element of the (2×2) matrix is the Greens function when both times are on the forward time contour, the upper right element is when t is on the forward and t' on the backward contour, and so on.

We can now perform the functional integral in the influence functional in Eq. (6.27)

$$\begin{aligned}
F[a, b] &= \frac{1}{Z} \det \left[iG_0^{-1} + i\tilde{V} \right] \\
&= \frac{1}{Z} \det \left[iG_0^{-1} (1 + G_0 \tilde{V}) \right] \\
&= \frac{1}{Z} \det \left[iG_0^{-1} \right] \cdot \det \left[1 + G_0 \tilde{V} \right] \\
&= e^{\text{Tr} \ln(1 + G_0 \tilde{V})},
\end{aligned} \tag{6.30}$$

where we used the properties $\det(AB) = \det(A)\det(B)$ and $\det(A) = e^{\text{Tr} \ln A}$. The determinants and traces in Eq. (6.30) are over both time, \mathbf{k} , and σ . We used that $Z = \det[iG_0^{-1}]$, which can e.g. be seen from the fact that $F[a, b] = 1$ for $J_0 = 0$ as described below Eq. (6.18). The matrix logarithm $B = \ln(A)$ means that the matrices are connected as $A = e^B$. For a small coupling J_0 , $G_0 \tilde{V}$ is small and the matrix logarithm above can be written as a power series $\ln(1 + G_0 \tilde{V}) = G_0 \tilde{V} - \frac{1}{2} G_0 \tilde{V} G_0 \tilde{V} + \dots$. To second order in the coupling, we therefore get

$$F[a, b] \approx e^{\text{Tr}[G_0 \tilde{V}] - \frac{1}{2} \text{Tr}[G_0 \tilde{V} G_0 \tilde{V}]} \tag{6.31}$$

This expansion of the matrix logarithm is our perturbative expansion. We go to second order, which means that we include processes to second order in the local exchange interaction. We therefore expect the RKKY interaction to show up in our result. With the expression in Eq. (6.31), the influence functional is on the desired form as shown in Eq. (6.19) and the next step is to evaluate the traces.

The first order term in the influence phase in Eq. (6.31) cancels because of the trace over the electron spin degrees of freedom and the fact that $\text{Tr}[\sigma_i] = 0$, where $i = (x, y, z)$. The trace in the second order term is performed in Appendix D.3 and it can be written as

$$\begin{aligned}
& -\frac{1}{2} \text{Tr} \left[G_0 \tilde{V} G_0 \tilde{V} \right] \\
&= \frac{S^2 J_0^2}{4\mathcal{V}^2} \sum_{\mathbf{k}\mathbf{k}'} \sum_{nm} e^{-i(\mathbf{k}-\mathbf{k}') \cdot (\mathbf{R}_n - \mathbf{R}_m)} \int_0^{t_f} dt \int_0^{t_f} dt' e^{-i(\varepsilon_{\mathbf{k}} - \varepsilon_{\mathbf{k}'})(t-t')} \\
&\quad \times \left\{ \begin{aligned}
& [n_F(\varepsilon_{\mathbf{k}-\Delta\mathbf{k}} - \mu) - \theta(t-t')] [n_F(\varepsilon_{\mathbf{k}'-\Delta\mathbf{k}} - \mu) - \theta(t'-t)] \mathbf{n}_n^+(t') \cdot \mathbf{n}_m^+(t) \\
& + [n_F(\varepsilon_{\mathbf{k}-\Delta\mathbf{k}} - \mu) - \theta(t'-t)] [n_F(\varepsilon_{\mathbf{k}'-\Delta\mathbf{k}} - \mu) - \theta(t-t')] \mathbf{n}_n^-(t') \cdot \mathbf{n}_m^-(t) \\
& + n_F(\varepsilon_{\mathbf{k}-\Delta\mathbf{k}} - \mu) [1 - n_F(\varepsilon_{\mathbf{k}'-\Delta\mathbf{k}} - \mu)] \mathbf{n}_n^-(t') \cdot \mathbf{n}_m^+(t) \\
& + [1 - n_F(\varepsilon_{\mathbf{k}-\Delta\mathbf{k}} - \mu)] n_F(\varepsilon_{\mathbf{k}'-\Delta\mathbf{k}} - \mu) \mathbf{n}_n^+(t') \cdot \mathbf{n}_m^-(t) \end{aligned} \right\}.
\end{aligned} \tag{6.32}$$

In the derivation, it is used that $\text{Tr}[\sigma_i \sigma_j] = 2\delta_{ij}$, which leads to the dot products. The two last terms in the curly brackets are actually the same, which can be seen by interchanging $\mathbf{k} \leftrightarrow \mathbf{k}'$, $n \leftrightarrow m$, and $t \leftrightarrow t'$. However, it is easier to arrive at the desired form when we keep them as two separate terms.

We will now introduce the average and difference vectors

$$\begin{aligned}
\mathbf{Q}_n &= \frac{\mathbf{n}_n^+ + \mathbf{n}_n^-}{2} \\
\boldsymbol{\zeta}_n &= \mathbf{n}_n^+ - \mathbf{n}_n^-
\end{aligned} \tag{6.33}$$

so that $\mathbf{n}_n^+ = \mathbf{Q}_n + \boldsymbol{\zeta}_n/2$ and $\mathbf{n}_n^- = \mathbf{Q}_n - \boldsymbol{\zeta}_n/2$. Using these, we can rewrite Eq. (6.32) as (see Appendix D.3)

$$-\frac{1}{2} \text{Tr} [G_0 \tilde{V} G_0 \tilde{V}] = i\mathcal{S}^{Q\zeta} + i\mathcal{S}^{\zeta\zeta} \quad (6.34)$$

with

$$i\mathcal{S}^{Q\zeta} = \frac{S^2 J_0^2}{2\hbar^2 \mathcal{V}^2} \sum_{nm} \int_0^{t_f} dt \int_0^{t_f} dt' \int d\omega \Lambda_{nm}(\omega, \Delta\mathbf{k}) e^{-i\omega(t-t')} \boldsymbol{\zeta}_m(t) \cdot \mathbf{Q}_n(t') \theta(t-t') \quad (6.35)$$

and

$$\begin{aligned} i\mathcal{S}^{\zeta\zeta} = & \frac{S^2 J_0^2}{8\mathcal{V}^2} \sum_{\mathbf{k}\mathbf{k}'} \sum_{nm} e^{-i(\mathbf{k}-\mathbf{k}') \cdot (\mathbf{R}_n - \mathbf{R}_m)} [n_F(\varepsilon_{\mathbf{k}-\Delta\mathbf{k}} - \mu) - n_F(\varepsilon_{\mathbf{k}'-\Delta\mathbf{k}} - \mu)] \\ & \times \coth\left(\frac{\varepsilon_{\mathbf{k}-\Delta\mathbf{k}} - \varepsilon_{\mathbf{k}'-\Delta\mathbf{k}}}{2k_B T}\right) \int_0^{t_f} dt \int_0^{t_f} dt' e^{-i(\varepsilon_{\mathbf{k}} - \varepsilon_{\mathbf{k}'})(t-t')} \boldsymbol{\zeta}_n(t') \cdot \boldsymbol{\zeta}_m(t). \end{aligned} \quad (6.36)$$

The introduced effective electron-hole pair density of states is

$$\Lambda_{nm}(\omega, \Delta\mathbf{k}) = \sum_{\mathbf{k}\mathbf{k}'} [n_F(\varepsilon_{\mathbf{k}-\Delta\mathbf{k}} - \mu) - n_F(\varepsilon_{\mathbf{k}'-\Delta\mathbf{k}} - \mu)] e^{-i(\mathbf{k}-\mathbf{k}') \cdot (\mathbf{R}_n - \mathbf{R}_m)} \delta(\omega - \varepsilon_{\mathbf{k}} + \varepsilon_{\mathbf{k}'}), \quad (6.37)$$

which has units of inverse energy. As we will see in the following, $\Lambda_{nm}(\omega, \Delta\mathbf{k})$ is an important function from which we can calculate the torques caused by the coupling to the electrons. This can already be seen in Eq. (6.35), from which time-non-local torques can be read off by following the argument stated in the end of Sec. 6.2.2. We will return to the torques shortly. The function $\Lambda_{nm}(\omega, \Delta\mathbf{k})$ has the properties

$$\Lambda_{nm}^*(\omega, \Delta\mathbf{k}) = \Lambda_{mn}(\omega, \Delta\mathbf{k}) \quad (6.38)$$

$$\Lambda_{nm}^*(\omega, \Delta\mathbf{k}) = -\Lambda_{nm}(-\omega, \Delta\mathbf{k}) \quad (6.39)$$

$$\Lambda_{nm}^*(\omega, \Delta\mathbf{k}) = \Lambda_{nm}(\omega, -\Delta\mathbf{k}), \quad (6.40)$$

which will be useful in the following discussion. One thing to notice now is that the real part of Λ describes the equilibrium effects from the electrons, while the imaginary part gives the nonequilibrium contributions. This can be seen by expanding Eq. (6.40) to first order in $\Delta\mathbf{k}$ (we only go to linear order in the electric current) and then taking either the real or imaginary part.

$\mathcal{S}^{\zeta\zeta}$ is second order in the difference vectors and it is imaginary.⁶ Contributions of this kind give rise to stochastic torques, which has been shown by e.g. Fransson and Zhu for a single spin in a tunnel junction [134]. They do a Hubbard-Stratonovich transformation, which introduces the stochastic torque and its probability distribution. In this thesis, we focus on the new torques in the two-spin system and we did therefore not study the stochastic torques any further. However, an important thing about the contribution $\mathcal{S}^{\zeta\zeta}$ is that it suppresses histories for which the difference vectors are large. We used this assumption in Sec. 6.2.2 to obtain the EOMs. As a side note, in Refs. [115, 116], which study atoms coupled via an electronic bath, the analogue of Eq. (6.36) is written by using the effective electron-hole pair density of

⁶The exchange of \mathbf{k} and \mathbf{k}' in Eq. (6.36) gives the complex conjugate and all k -values are summed over. Remember the i on the left hand side of the equality sign.

states as well. However, this can not be done in our case due to the \mathbf{k} -dependence in the hyperbolic cotangent.⁷

One way to go on from Eq. (6.35) is to Fourier transform both the step function and $\mathbf{Q}_n(t')$ [116]. In Appendix D.3.1, we show that

$$iS^{Q\zeta} = i\frac{\pi S^2 J_0^2}{2V^2} \sum_{nm} \int_0^{t_f} dt \int \frac{d\omega}{2\pi} \left\{ \mathcal{H}\{\text{Re } \Lambda_{nm}\}(\omega) + \text{Im } \Lambda_{nm}(\omega, \Delta\mathbf{k}) \right. \\ \left. + i \left[-\text{Re } \Lambda_{nm}(\omega) + \mathcal{H}\{\text{Im } \Lambda_{nm}(\omega', \Delta\mathbf{k})\}(\omega) \right] \right\} \zeta_m(t) \cdot \mathbf{Q}_n(\omega) e^{-i\omega t}, \quad (6.41)$$

where the Hilbert transform is defined as

$$\mathcal{H}\{f(\omega')\}(\omega) = \frac{1}{\pi} \mathcal{P} \int d\omega' \frac{f(\omega')}{\omega - \omega'}. \quad (6.42)$$

Here \mathcal{P} indicates the Cauchy principal value of the integral. With Eq. (6.41), we have split the influence of the electrons into four different contributions. The two terms involving the real part of Λ are equilibrium terms, while the two terms that include the imaginary part of Λ are nonequilibrium contributions (see Eq. (6.40)). From the property in Eq. (6.38), we see that the equilibrium terms are symmetric under exchange of the spin indices ($\text{Re } \Lambda_{12} = \text{Re } \Lambda_{21}$), while the nonequilibrium terms are anti-symmetric under the same exchange.

6.2.4 Slow spin approximation

The action in Eq. (6.41) gives rise to time-non-local torques in the EOMs. However, we will now assume that the spins are slow compared to the electrons, which will make the EOMs local in time. This assumption is widely used for magnetic molecules in tunnel junctions [133, 134, 144, 146], and for studies calculating the spin relaxation constant in bulk materials, Sayad et al. write: “... *these studies rely on two, partially related, assumptions: (i) the spin–electron coupling J is weak and can be treated perturbatively to lowest order ... (ii) The classical spin dynamics is slow as compared to the electron dynamics. These assumptions appear as well justified but they are also necessary to achieve a simple effective spin-only theory by eliminating the fast electron degrees of freedom*” [147]. Based on this, it seems reasonable to use the approximation here.

In our formalism, the information about the electrons is kept in the four functions in the curly bracket in Eq. (6.41). If the spins are slow compared to the electrons, the function $\mathbf{Q}_n(\omega)$ is narrow in frequency compared to the functions in the curly brackets, and we can expand these four functions to first order in the frequency.⁸ By using the property in Eq. (6.39) and that the Hilbert transform of an even/odd function $f(\omega) = \pm f(-\omega)$ is $\mathcal{H}\{f(\omega')\}(\omega) = \mp \mathcal{H}\{f(\omega')\}(-\omega)$, the slow-spin-approximation

⁷The difference between our calculation and the calculations in Refs. [115, 116] is that we use a shifted Fermi sea to incorporate the nonequilibrium conditions, while Refs. [115, 116] have two electrodes with different electrochemical potentials.

⁸As we will see in the following, this way of doing the approximation will lead to an infrared divergence in one of the terms, namely the $\frac{\partial}{\partial\omega} \mathcal{H}\{\text{Im } \Lambda_{nm}\}(\omega)|_{\omega=0}$ term in Eq. (6.43). If we expand $\Lambda_{nm}(\omega)$ instead of its Hilbert transform, the term $\mathcal{H}\{\text{Im } \Lambda_{nm}\}(\omega)$ in Eq. (6.41) will cancel and we will get an ultraviolet divergence of the $\mathcal{H}\{\text{Re } \Lambda_{nm}\}(\omega)$ term. With the expansion described in the main text, the latter term will give the equilibrium RKKY coupling, and we can deal with the infrared divergence by introducing a cutoff. We will return to this in Sec. 6.2.5.

leads to

$$i\mathcal{S}^{Q\zeta} \approx i \frac{\pi S^2 J_0^2}{2\mathcal{V}^2} \sum_{nm} \int_0^{t_f} dt \left\{ [\mathcal{H} \{ \text{Re } \Lambda_{nm} \} (0) + \text{Im } \Lambda_{nm}(0, \Delta \mathbf{k})] \zeta_m(t) \cdot \mathbf{Q}_n(t) \right. \\ \left. + \left[\frac{\partial}{\partial \omega} \text{Re } \Lambda_{nm}(\omega) \Big|_{\omega=0} - \frac{\partial}{\partial \omega} \mathcal{H} \{ \text{Im } \Lambda_{nm}(\omega', \Delta \mathbf{k}) \} (\omega) \Big|_{\omega=0} \right] \zeta_m(t) \cdot \dot{\mathbf{Q}}_n(t) \right\}, \quad (6.43)$$

where we have used that $\dot{\mathbf{Q}}_n(t) = \int d\omega (-i\omega) \mathbf{Q}_n(\omega) e^{-i\omega t}$. Inserting this action back into Eq. (6.17), we arrive at

$$\mathcal{J}(a_1, b_1, t; a_0, b_0, 0) \approx \int \mathcal{D}a \int \mathcal{D}b e^{iS \sum_n \int dt' \{ \mathbf{B}_{\text{eff},n} \cdot \zeta_n + [\dot{\phi}_n^+ \cos \theta_n^+ - \dot{\phi}_n^- \cos \theta_n^-] \}}, \quad (6.44)$$

where the influence of the electrons is included in the effective magnetic field

$$\mathbf{B}_{\text{eff},n} = \mathbf{B} + \frac{\pi S J_0^2}{2\mathcal{V}^2} \sum_m \left[\mathcal{H} \{ \text{Re } \Lambda_{mn} \} (0) \mathbf{Q}_m + \text{Im } \Lambda_{mn}(0) \mathbf{Q}_m \right. \\ \left. + \frac{\partial}{\partial \omega} \text{Re } \Lambda_{mn}(\omega) \Big|_{\omega=0} \dot{\mathbf{Q}}_m - \frac{\partial}{\partial \omega} \mathcal{H} \{ \text{Im } \Lambda_{mn} \} (\omega) \Big|_{\omega=0} \dot{\mathbf{Q}}_m \right]. \quad (6.45)$$

As explained in Sec. 6.2.2, the EOMs can be read off directly from the action in the semiclassical approximation, and the important part of the action is the vector dotted with the difference vector (see Appendix D.1). Just as in Eq. (6.25), we can therefore write out the EOMs as

$$\dot{\mathbf{n}}_1 = -\frac{1}{\hbar} \mathbf{B} \times \mathbf{n}_1 + (J + \sigma) \mathbf{n}_2 \times \mathbf{n}_1 + \eta_0 \dot{\mathbf{n}}_1 \times \mathbf{n}_1 + (\eta_1 + \chi) \dot{\mathbf{n}}_2 \times \mathbf{n}_1 \\ \dot{\mathbf{n}}_2 = -\frac{1}{\hbar} \mathbf{B} \times \mathbf{n}_2 + (J - \sigma) \mathbf{n}_1 \times \mathbf{n}_2 + \eta_0 \dot{\mathbf{n}}_2 \times \mathbf{n}_2 + (\eta_1 - \chi) \dot{\mathbf{n}}_1 \times \mathbf{n}_2, \quad (6.46)$$

where the introduced coefficients are (reintroducing \hbar)

$$J = -\frac{\pi S J_0^2}{2\hbar \mathcal{V}^2} \mathcal{H} \{ \text{Re } \Lambda_{12}(\omega', 0) \} (0) \\ \eta_0 = -\frac{\pi S J_0^2}{2\mathcal{V}^2} \frac{\partial}{\partial \hbar \omega} \text{Re } \Lambda_{11}(\omega, 0) \Big|_{\omega=0} \\ \eta_1 = -\frac{\pi S J_0^2}{2\mathcal{V}^2} \frac{\partial}{\partial \hbar \omega} \text{Re } \Lambda_{12}(\omega, 0) \Big|_{\omega=0} \\ \sigma = -\frac{\pi S J_0^2}{2\hbar \mathcal{V}^2} \text{Im } \Lambda_{21}(0, \Delta \mathbf{k}) \\ \chi = \frac{\pi S J_0^2}{2\mathcal{V}^2} \frac{\partial}{\partial \hbar \omega} \mathcal{H} \{ \text{Im } \Lambda_{21}(\omega', \Delta \mathbf{k}) \} (\omega) \Big|_{\omega=0}. \quad (6.47)$$

The first three coefficients in Eq. (6.47) are equilibrium coefficients, which can be seen from Eq. (6.40) and the text below, while the last two are nonequilibrium coefficients. The EOMs in Eq. (6.46) share the coefficients in Eq. (6.47), which can be understood from the property in Eq. (6.38). The property gives that the (non-)equilibrium terms are even (odd) under the exchange of spin indices and that $\text{Im } \Lambda_{11}(\omega) = 0$. The well-known equilibrium terms are: the standard precession due to the magnetic field, a precessional term due to the exchange coupling J , and a Gilbert damping term with the coefficient η_0 . Additionally, there is an equilibrium non-local relaxation term with

the coefficient η_1 , which has been discussed in the literature [131, 132]. The more interesting result is the nonequilibrium terms with coefficients σ and χ , which are odd under the exchange of the spin coordinates, $1 \leftrightarrow 2$. As mentioned earlier, these terms have already been presented by Onoda et al. [131]. However, Onoda et al. did not show the expressions for the coefficients, which we will do in the next section.

In our theoretical setup, we chose a simple metal to make the calculation as simple as possible. However, the derived EOMs would most likely show up in other two-spin systems coupled by a nonequilibrium electronic bath. An example could be magnetic molecules in a tunnel junction. We therefore consider the result in Eq. (6.46) to be rather general, and in Chapter 7, we will study the dynamics of a system with such EOMs. But first, we will calculate the coefficients in Eq. (6.47) for the simple model chosen in this chapter.

6.2.5 The final result

Now that we have established the nonequilibrium EOMs for the two spins in Eq. (6.46), we would like to calculate the explicit expressions for the coefficients in Eq. (6.47). To make the calculations easier, we assume that the temperature is low so that $\mu = \varepsilon_F$ and $n'_F(\varepsilon - \mu) = -\delta(\varepsilon_F)$. For the first four coefficients in Eq. (6.47), the calculations are long but straight forward, and they are presented in Appendices D.4.1–D.4.3. For the coefficient χ , the integral diverges due to the electron-hole pair excitations with small energies. The small energies mean that the excitations are slow. However, we assumed in Sec. 6.2.4 that the electrons are fast compared to the spins and we will therefore introduce a cutoff $\delta\varepsilon$ below which we shall neglect the excitations. The derivation of χ is presented in Appendix D.4.4. The results are

$$\begin{aligned}
 J(R) &= -\pi S J_0^2 \rho(\varepsilon_F)^2 \frac{\varepsilon_F}{\hbar} F(2k_F R) \\
 \eta_0 &= \frac{\pi S J_0^2}{8} \rho(\varepsilon_F)^2 \\
 \eta_1(R) &= \frac{\pi S J_0^2}{8} \rho(\varepsilon_F)^2 \left(\frac{\sin(k_F R)}{k_F R} \right)^2 \\
 \sigma(\mathbf{R}) &= -\frac{\pi S J_0^2}{2} \rho(\varepsilon_F)^2 L(k_F R) \frac{\varepsilon_F}{\hbar} \frac{\Delta \mathbf{k} \cdot \mathbf{R}}{k_F R} \\
 \chi(\mathbf{R}) &= -S J_0^2 \rho(\varepsilon_F)^2 L(k_F R) \frac{\varepsilon_F}{\delta\varepsilon} \frac{\Delta \mathbf{k} \cdot \mathbf{R}}{k_F R}.
 \end{aligned} \tag{6.48}$$

Here $\rho(\varepsilon_F) = \frac{mk_F}{\pi^2 \hbar^2}$ is the density of states at the Fermi energy, $\mathbf{R} = \mathbf{R}_2 - \mathbf{R}_1$ is the position vector between the two spins, $F(x) = \frac{x \cos(x) - \sin(x)}{x^4}$ is the function that appears in the RKKY interaction in Eq. (5.6), and

$$L(x) = \sin(x) \frac{x \cos(x) - \sin(x)}{x^3}. \tag{6.49}$$

The distance dependent functions are plotted in Fig. 6.2. All of them oscillate and decay, and obviously $\sin^2(x)/x^2$ only takes positive values. The units of the different constants in the EOMs are the following: $\rho(\varepsilon_F)$ has units of $1/(\text{m}^3 \text{J})$, J_0 has units of $\text{m}^3 \text{J}$, S is dimensionless, and \mathbf{B} has units of Joule. The η 's and χ are therefore dimensionless, while J and σ have units of s^{-1} .

The EOMs in Eq. (6.46) are obtained from a perturbative expansion to second order in the local exchange coupling. The equilibrium terms should therefore be the same as the ones obtained from standard perturbation theory. Indeed, we see that the

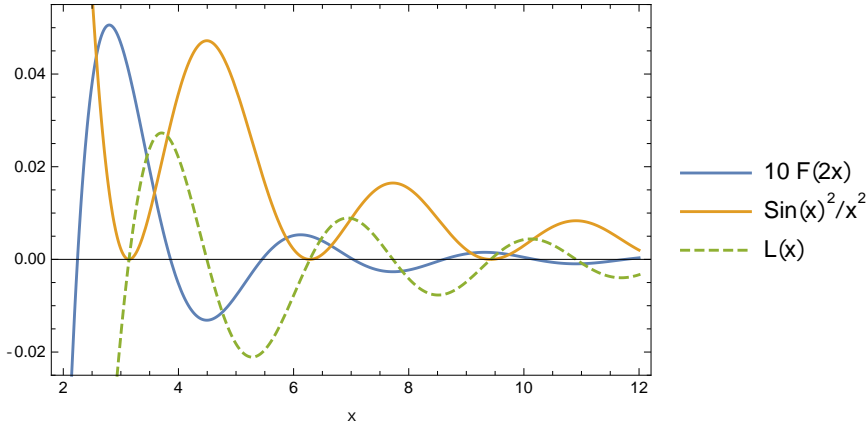


FIGURE 6.2: Plots of the distance dependent functions in Eq. (6.48). The solid lines describe equilibrium terms, while the dashed line describes the nonequilibrium coefficients. Notice that $F(2x)$ is multiplied by a factor of 10 to make it easier to compare the functions.

indirect exchange, $J(R)$, in Eq. (6.48) is the same as RKKY exchange in Eq. (5.6), while the obtained Gilbert coefficient, η_0 , is the same as in Eq. (5.10). To get the relaxation terms to take energy out of the spin system, we will see in Chapter 7 that the η 's have to be positive. This is indeed the case in Eq. (6.48). However, the sign of the indirect exchange seems to be wrong,⁹ but the author was not able to find the mistake. The nonequilibrium terms are proportional to $\Delta\mathbf{k} \cdot \mathbf{R}$ and they therefore vanish when the position vector between the spins is perpendicular to the current direction. The equilibrium terms only depends on the distance itself since the equilibrium electron gas is homogeneous.

6.2.6 Estimating the nonequilibrium coefficients

To get an idea of the magnitude of the nonequilibrium coefficients, we can compare them to the equilibrium ones. By taking taking $\Delta\mathbf{k}$ to be parallel with \mathbf{R} , we can write

$$\frac{\sigma(R)}{|J(R)|} = -\frac{1}{2} \frac{\Delta k}{k_F} \frac{L(k_F R)}{|F(2k_F R)|} \quad (6.50)$$

and

$$\frac{\chi(R)}{\eta_0} = -\frac{8}{\pi} L(k_F R) \frac{\varepsilon_F}{\delta\varepsilon} \frac{\Delta k}{k_F}. \quad (6.51)$$

To get a rough numeric estimate, consider a typical metal such as copper for which $k_F \approx 10^{10} \text{ m}^{-1}$, $\varepsilon_F \approx 4 \text{ eV}$, and $n_e \approx 10^{29} \text{ m}^{-3}$ [6]. The magnitude of the current density is given by $j = en_e v$, where the average velocity of the electrons is $v = \hbar\Delta k/m$. For a cross section area of 1 mm^2 and an electric current of $I = 1 \text{ A}$, the current density is 10^2 A/cm^2 , which gives $\Delta k = \frac{m}{\hbar} \frac{1}{en_e} j \approx 0.5 \text{ m}^{-1}$. We choose an energy cutoff which corresponds to the Larmor frequency of a free electron in a magnetic field $B_{\text{magnetic}} = 0.01 \text{ T}$. This corresponds to the field from a small bar magnet. Remember that $B \equiv \hbar\gamma B_{\text{magnetic}}$, where B_{magnetic} is the strength of the actual magnetic field.

⁹If we insert Eq. (5.6) into Eq. (5.8), we see that the sign is different from the one obtained in Eqs. (6.46) and (6.48).

The gyromagnetic ratio of a free electron is $\gamma \approx 1.8 \times 10^{11} \text{ rads}^{-1}\text{T}^{-1}$ and the cutoff energy is therefore

$$\delta\varepsilon = \hbar\gamma B_{\text{magnetic}} \approx 10^{-6} \text{ eV}. \quad (6.52)$$

Finally, we choose a distance so that $k_F R = 7$, which corresponds to a distance of $R = 7 \text{ \AA}$ in the specific case. Inserting all these numbers into Eqs. (6.50) and (6.51), we get

$$\begin{aligned} \left| \frac{\sigma}{J} \right| &\approx 10^{-8} \\ \left| \frac{\chi}{\eta_0} \right| &\approx 5 \times 10^{-6}. \end{aligned} \quad (6.53)$$

So in the specific case, the nonequilibrium coefficients are small compared to the equilibrium coefficients.

The coefficients obviously get larger if we increase the current. Consider for example a copper nanowire with radius $r = 100 \text{ nm}$ through which a current density of 10^6 A cm^{-2} can flow without destroying the wire [148].¹⁰ The wire is sufficiently large for our bulk calculation to be reasonable, and we therefore obtain coefficients that are a factor of 10^4 larger than those in Eq. (6.53). The nonequilibrium coefficients are therefore still small compared to the equilibrium ones, but they can possibly take larger values in e.g. a nanoscale junction. However, the calculation of such a system would require another theoretical setup than the one used in this chapter.

6.3 Conclusions and outlook

In this chapter, we have used the Feynman-Vernon influence functional approach to derive the EOMs for two spins that couple indirectly via an electron gas out of equilibrium. The resulting equations in Eq. (6.46) include the torques from precession, the RKKY exchange coupling, and local and non-local relaxations terms. In addition to these equilibrium terms, the nonequilibrium condition gives rise to two new torques characterized by the coefficients σ and χ . σ is “added” to the exchange coupling, while χ is “added” to the non-local relaxation coefficient, but both of them show up anti-symmetrically in the EOMs. I.e. while the exchange torque is $(J + \sigma)\mathbf{n}_2 \times \mathbf{n}_1$ in one EOM, it is $(J - \sigma)\mathbf{n}_1 \times \mathbf{n}_2$ in the other. Both σ and χ are proportional to $\Delta\mathbf{k} \cdot \mathbf{R}$, so that they vanish when the vector between the spins is perpendicular to the current direction. They have the same sign and vary as $\sin(2k_F R)/R^2$ for large distances. They therefore decay slower than the RKKY coupling, which varies as $\cos(2k_F R)/R^3$ for large distances.

The nonequilibrium coefficients are small compared to the equilibrium coefficients. In Sec. 6.2.6, we estimated them to be around four orders of magnitude smaller compared to the equilibrium coefficients in a copper nanowire. For a future project, it would be interesting to study whether larger values could be obtained in other systems.

The spins studied in this chapter are quantum angular momenta, which have a limited Hilbert space. The described theory can therefore be used to study other systems with limited Hilbert spaces. An example could be two quantum dots that couple via a current carrying wire. This would be an interesting problem for a future project.

¹⁰According to Ref. [148], the the maximum current density at room temperature is $3.9 \times 10^7 \text{ A cm}^{-2}$.

Chapter 7

Study of the spin equations of motion

Some of the results in this chapter are included in the paper draft in Appendix F.

In Chapter 6, we established the equations of motion for two spins coupled to a Fermi sphere out of equilibrium. We calculated the explicit expressions for the different torques and showed, for the first time, the distance dependence of the nonequilibrium torques. Even though the EOMs in Eq. (6.46) were calculated from a specific model, one can expect that the nonequilibrium torques show up in other systems where the spins couple to electronic degrees of freedom. That could for example be two spins placed in a nanoscopic junction or two spins connected to a two-dimensional electron gas out of equilibrium.

In this chapter, we will study the EOMs in Eq. (6.46) and assume that the nonequilibrium coefficients, σ and χ , can take larger values than estimated for the specific model in Sec. 6.2.6. We will additionally assume, that the coefficients can have different signs. This study was originally started by Kasper Bonfils and his results can be found in Ref. [149]. Here we will start in Sec. 7.1 by doing some rewritings of the EOMs, which will illustrate that the equations are quite difficult to interpret. In Sec. 7.2, we will do a linear stability analysis, which allows us to check the stability for different sets of coefficients. The stability diagrams for different regions in parameter space will be shown and discussed in Sec. 7.2.4. Finally, numerical simulations of the two spins are done in Sec. 7.3.

To keep this chapter as short and simple as possible, we will most often only consider the equation for spin 1. However, as is seen in Eq. (6.46), the equation for spin 2 is obtained by

$$\begin{aligned}
 1 &\leftrightarrow 2 \\
 \sigma &\rightarrow -\sigma \\
 \chi &\rightarrow -\chi.
 \end{aligned}
 \tag{7.1}$$

7.1 Analytic considerations

Even the standard Landau-Lifshitz-Gilbert equations for coupled spins is a hard problem to analyze [150]. Here we have additional terms which do not make it easier. However, we will start by doing some rewritings of the EOMs to see if it can give us some understanding of the different terms. As a starter, we will consider a single spin in a magnetic field. We will then move to the full two-spin equations.

Single spin in a magnetic field

As a simple start, we will consider the equation for a single spin in a magnetic field

$$\dot{\mathbf{n}} = -\mathbf{B} \times \mathbf{n} + \eta_0 \dot{\mathbf{n}} \times \mathbf{n}. \quad (7.2)$$

We know that the spin precesses about the magnetic field axis, and the Gilbert term causes the spin to relax towards the direction of the magnetic field. This relaxation can be seen mathematically by

$$\begin{aligned} \mathbf{B} \cdot \dot{\mathbf{n}} &= \eta_0 \mathbf{B} \cdot (\dot{\mathbf{n}} \times \mathbf{n}) \\ &= \eta_0 \mathbf{B} \cdot [-(\mathbf{B} \times \mathbf{n}) \times \mathbf{n} + \eta_0 (\dot{\mathbf{n}} \times \mathbf{n}) \times \mathbf{n}] \\ &= \eta_0 \mathbf{B} \cdot [\mathbf{B} - \mathbf{n}(\mathbf{n} \cdot \mathbf{B})] - \eta_0 \dot{\mathbf{n}} \cdot \mathbf{n} \\ &= \frac{\eta_0}{1 + \eta_0^2} [B^2 - (\mathbf{n} \cdot \mathbf{B})^2]. \end{aligned} \quad (7.3)$$

The fraction is a positive number smaller than 1/2, since η_0 is positive. The square bracket factor is positive until \mathbf{n} is parallel to the magnetic field, where it becomes zero. Consequently, $\mathbf{n} \cdot \mathbf{B}$ will increase until $\mathbf{n} \parallel \mathbf{B}$. If we choose $\mathbf{B} = B\hat{z}$ and use $\eta_0 \ll 1$, so that we can neglect the denominator, the solution is

$$n_z(t) = \frac{1 + n_{z0} - [1 - n_{z0}] e^{-2\eta_0 B t}}{1 + n_{z0} + [1 - n_{z0}] e^{-2\eta_0 B t}}, \quad (7.4)$$

where $n_{z0} = n_z(0)$. $n_z(t)$ is half way between $n_z(0)$ and 1 at the time $t_{1/2} = \frac{1}{2B\eta_0} \ln\left(\frac{3+n_{z0}}{1+n_{z0}}\right)$.

The full equations

If we use the full EOMs for the two spins, the rewriting similar to the above becomes quite tedious. If we neglect terms to second order in η_0 , η_1 , and χ , we show in Appendix E.1 that

$$\begin{aligned} \dot{n}_1^z &= (J + \sigma)(\mathbf{n}_2 \times \mathbf{n}_1) \cdot \hat{z} + \eta_0 B [1 - (n_1^z)^2] + (\eta_1 + \chi)B [\mathbf{n}_1 \cdot \mathbf{n}_2 - n_1^z n_2^z] \\ &\quad + [(\eta_0 - \eta_1)J + (\eta_0 + \eta_1)\sigma - J\chi] [(\mathbf{n}_1 \cdot \mathbf{n}_2)n_1^z - n_2^z]. \end{aligned} \quad (7.5)$$

All the terms, except for the standard Gilbert relaxation considered above, depend on the orientation of the other spin. Since both spins rotate and can take any configuration at a particular time, the above expression is difficult to analyze.

We can also derived an expression for the time derivative of the energy $\dot{E} = -S\mathbf{B} \cdot \sum_i \dot{\mathbf{n}}_i + JS(\dot{\mathbf{n}}_1 \cdot \mathbf{n}_2 + \dot{\mathbf{n}}_2 \cdot \mathbf{n}_1)$.¹ However, this resulted in an expression that is even more complicated than the above, and it is therefore not shown. One important to learn from the change in energy is that the terms including χ drop out. The nonequilibrium torques $+\dot{\mathbf{n}}_2 \times \mathbf{n}_1$ and $-\dot{\mathbf{n}}_1 \times \mathbf{n}_2$ in the EOMs consequently do not change the energy of the spin system. These torques are therefore reminiscent of a Lorentz force. The change in energy caused by the σ -torques is $\dot{E}_\sigma = 2\sigma(\mathbf{n}_1 \times \mathbf{n}_2) \cdot \mathbf{B}$. To build a deeper understanding of the full EOMs, we will now do a linear stability analysis.

¹The easiest way to do this is to insert Eq. (E.5) into the expression for \dot{E} .

7.2 Linear stability analysis

In this section, we will do a linear stability analysis of the EOMs. This allows us to find the stable configuration of the spins for a set of coefficients. For the rest of this chapter, we will use a scaled version of the EOMs in Eq. (6.46). By scaling the equations with $|J|$, we get

$$\begin{aligned}\partial_\tau \mathbf{n}_1 &= -\tilde{\mathbf{B}} \times \mathbf{n}_1 + (p_J + \tilde{\sigma}) \mathbf{n}_2 \times \mathbf{n}_1 + \eta_0 (\partial_\tau \mathbf{n}_1) \times \mathbf{n}_1 + (\eta_1 + \chi) (\partial_\tau \mathbf{n}_2) \times \mathbf{n}_1 \\ \partial_\tau \mathbf{n}_2 &= -\tilde{\mathbf{B}} \times \mathbf{n}_2 + (p_J - \tilde{\sigma}) \mathbf{n}_1 \times \mathbf{n}_2 + \eta_0 (\partial_\tau \mathbf{n}_2) \times \mathbf{n}_2 + (\eta_1 - \chi) (\partial_\tau \mathbf{n}_1) \times \mathbf{n}_2,\end{aligned}\quad (7.6)$$

where $p_J = J/|J|$ indicates the sign of the indirect exchange coupling, $\tau = |J|t$ is the rescaled time, and

$$\begin{aligned}\tilde{\mathbf{B}} &= \frac{\mathbf{B}}{\hbar|J|} \\ \tilde{\sigma} &= \frac{\sigma}{|J|},\end{aligned}\quad (7.7)$$

which are all dimensionless. The advantage of this rewriting is that we get rid of the units.

In the following subsections, we will go through the different steps of the linear stability analysis. In short, the different steps are

1. In Sec. 7.2.1, we will find the fixed points \mathbf{v}_0 of the EOMs for which $\dot{\mathbf{n}}_1 = \dot{\mathbf{n}}_2 = 0$. Here $\mathbf{v}_0 = (\theta_1^0, \phi_1^0, \theta_2^0, \phi_2^0)$ describes a configuration of the spins.²
2. We will linearize the EOMs around the fixed points to get equations of the form $\partial_\tau \delta \mathbf{v} = \mathbf{M} \delta \mathbf{v}$. Here $\delta \mathbf{v} = \mathbf{v} - \mathbf{v}_0$ is the deviation from the fixed point and \mathbf{M} is the stability matrix. In Sec. 7.2.2, we will do the linearization around the ferromagnetic and antiferromagnetic configurations, which is quite simple and instructive. The general linearization in Sec. 7.2.3 is more tedious.
3. The solution to the linear differential equations in the previous step is

$$\begin{aligned}\delta \mathbf{v}(\tau) &= e^{\mathbf{M}\tau} \delta \mathbf{v}(0) \\ &= \sum_i c_i e^{\lambda_i \tau} \mathbf{u}_i,\end{aligned}\quad (7.8)$$

where \mathbf{u}_i is an eigenvector of \mathbf{M} with eigenvalues λ_i , while $\delta \mathbf{v}(0) = \sum_i c_i \mathbf{u}_i$. The fixed point \mathbf{v}_0 is stable if all the real parts of the eigenvalues are negative, $\text{Re } \lambda_i < 0$ for all i .

The last point can be understood as follows: If we make a small arbitrary rotation of the spins away from a fixed point, the new state $\delta \mathbf{v}(t)$ can be decomposed into the eigenvectors of \mathbf{M} . Since the deviation is small, the linearization is a good approximation. If all the real parts of the eigenvalues are negative, the deviations will decay and the spins return to the fixed point. This is true for any small rotation. On the other hand, if just one of the eigenvalues has a positive real part, the fixed point is unstable. The reason is that these components will increase in time so that the spins rotate away from the fixed point.

²In Sec. 7.2.2, where the linearization is done around the ferromagnetic and antiferromagnetic configurations, we will use Cartesian coordinates, $\mathbf{v}_0 = (x_1^0, y_1^0, x_2^0, y_2^0)$. The stated representation of the fixed points, $\mathbf{v}_0 = (\theta_1^0, \phi_1^0, \theta_2^0, \phi_2^0)$, is used in Sec. 7.2.3.

The small rotations mentioned above can be caused by the stochastic torques from the electronic bath [133, 134]. We did not consider these torques in the derivation of the EOMs in Chapter 6. However, they are just the analogue to the fluctuating forces on atoms that couple to an environment [112].

7.2.1 Fixed points

We consider the fixed points of the coupled differential equations in Eq. (7.6) where $\dot{\mathbf{n}}_1 = \dot{\mathbf{n}}_2 = 0$. In a fixed point, Eqs. (7.6) reduce to

$$\begin{aligned}\tilde{\mathbf{B}} \times \mathbf{n}_1 &= (p_J + \tilde{\sigma})\mathbf{n}_2 \times \mathbf{n}_1 \\ \tilde{\mathbf{B}} \times \mathbf{n}_2 &= (p_J - \tilde{\sigma})\mathbf{n}_1 \times \mathbf{n}_2.\end{aligned}\tag{7.9}$$

It is easy to see that the ferromagnetic configurations (\uparrow, \uparrow) and (\downarrow, \downarrow) are solutions to the above equations, where the first (last) arrow refers to spin 1 (2) while 'up' refers to the direction of the magnetic field. When both spins point antiparallel to the magnetic field, the energy contribution $-\mathbf{B} \cdot \mathbf{S}$ is maximized and it is intuitively not an important configuration to consider. However, as we will see later, (\downarrow, \downarrow) is actually a stable configuration under some conditions. The antiferromagnetic configurations, (\uparrow, \downarrow) and (\downarrow, \uparrow) , are of course solutions to Eqs. (7.9) as well.

When the coupling is antiferromagnetic, $p_J = 1$, the spins will tend to point in opposite directions in order to minimize the energy contribution $J\mathbf{n}_1 \cdot \mathbf{n}_2$. However, it competes with the magnetic field, $-\mathbf{B} \cdot \mathbf{S}$, and the result is a canted spin configuration, which is also a fixed point of Eq. (7.9). For the magnetic field $\tilde{\mathbf{B}} = \tilde{B}\hat{z}$, we can write it as $\phi_1 - \phi_2 = \pi$ and [149]

$$\theta_1^{\text{can}} = \cos^{-1} \left(\frac{\tilde{B}^2 - 4p_J \tilde{\sigma}}{2\tilde{B}(1 - \tilde{\sigma})} \right),\tag{7.10}$$

which is a physical solution to Eq. (7.9) for $|\tilde{\sigma}| < \tilde{B}/2 < 1$ (see Appendix E.2). The canted spin configuration is plotted in Fig. 7.1, where $\phi_1 = 0$ was chosen to make it easier to visualize. However, the configuration is a fixed point for any choice of ϕ_1 as long as $\Delta\phi = \pi$. For $\tilde{\sigma} \ll 1$, we can rewrite Eq. (7.10) as

$$n_1^{z,\text{can}} = \cos \theta_1^{\text{can}} \approx \frac{\tilde{B}}{2} \left\{ 1 + \left[1 - \left(\frac{2}{\tilde{B}} \right)^2 \right] \tilde{\sigma} \right\}.\tag{7.11}$$

Under equilibrium conditions, the canted configuration is symmetric, $\theta_1^{\text{can}} = \theta_2^{\text{can}}$. $\tilde{\sigma}$ skews the configuration by forcing one spin closer to the magnetic field, while forcing the other spin away as seen in Fig. 7.1. Remember that the angle for spin 2 is obtained by the changes in Eq. (7.1).

We described the canted configuration as a result of the competition between the antiferromagnetic coupling and the magnetic field. However, as we will see later, the current can make the canted configuration stable even when the coupling is ferromagnetic.

7.2.2 Linearization of the EOM around ferromagnetic and antiferromagnetic configurations

In this section, we will linearize the EOMs around the spin configurations (\uparrow, \uparrow) , (\downarrow, \downarrow) , (\uparrow, \downarrow) , and (\downarrow, \uparrow) . The procedure cannot be used to check whether the canted

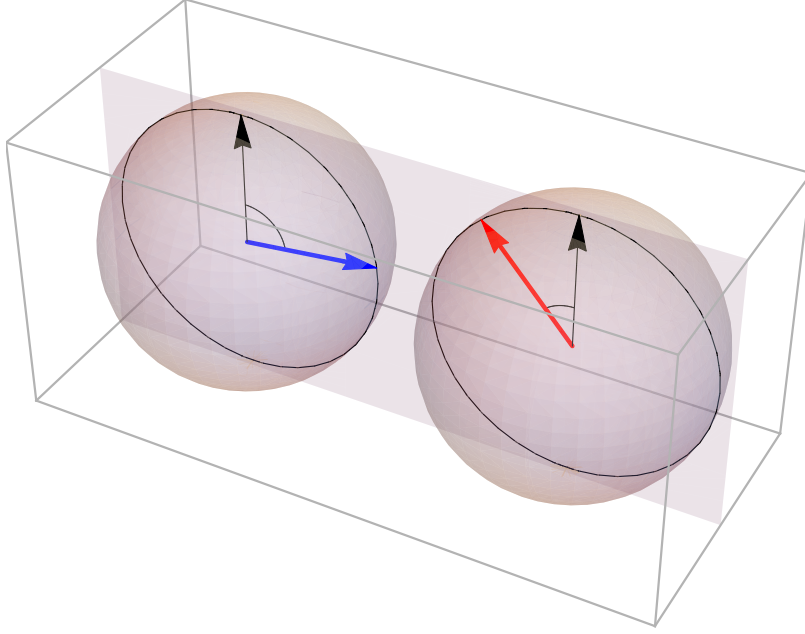


FIGURE 7.1: The canted spin configuration, which satisfies Eq. (7.9). The black arrow indicates the magnetic field direction and the blue (red) arrow is spin 1 (2). The parameters $\tilde{B} = 1$ and $\tilde{\sigma} = 0.2$ are used and the angles are calculated using Eq. (7.10). The figure is generated in Mathematica.

configuration is stable, but it is simple and instructive, and the stability matrix can be put on a compact analytic form. In Sec. 7.2.3, we will follow a more general procedure, which can be used to check the stability of all fixed points.

When the spins are close to pointing either up or down, we can write their vectors as

$$\mathbf{n}_1 \approx \begin{pmatrix} x_1 \\ y_1 \\ p_1 \end{pmatrix}, \quad \mathbf{n}_2 \approx \begin{pmatrix} x_2 \\ y_2 \\ p_2 \end{pmatrix}, \quad \dot{\mathbf{n}}_1 \approx \begin{pmatrix} \dot{x}_1 \\ \dot{y}_1 \\ 0 \end{pmatrix}, \quad \dot{\mathbf{n}}_2 \approx \begin{pmatrix} \dot{x}_2 \\ \dot{y}_2 \\ 0 \end{pmatrix}, \quad (7.12)$$

where the x 's and y 's are small and where $p_i = \pm 1$ indicates that spin i points up/down. We can work out the different cross products in Eq. (7.6) and keep only terms up to first order in the coordinates:

$$\begin{aligned} \tilde{\mathbf{B}} \times \mathbf{n}_1 &\approx \tilde{B}(-y_1 \hat{x} + x_1 \hat{y}) \\ \mathbf{n}_2 \times \mathbf{n}_1 &\approx (p_1 y_2 - p_2 y_1) \hat{x} + (p_2 x_1 - p_1 x_2) \hat{y} \\ \dot{\mathbf{n}}_1 \times \mathbf{n}_1 &\approx p_1(\dot{y}_1 \hat{x} - \dot{x}_1 \hat{y}) \\ \dot{\mathbf{n}}_2 \times \mathbf{n}_1 &\approx p_1(\dot{y}_2 \hat{x} - \dot{x}_2 \hat{y}). \end{aligned} \quad (7.13)$$

The remaining cross products are easily seen by exchanging $1 \leftrightarrow 2$ in the desired way. Collecting the terms with time derivatives on one side of the equality sign, we can write

$$A \partial_\tau \mathbf{v} = C \mathbf{v}, \quad (7.14)$$

where $\mathbf{v} = (x_1, y_1, x_2, y_2)^T$ and

$$\begin{aligned} \mathbf{A} &= \mathbf{1} - \eta_0 \begin{pmatrix} p_1 \mathbf{a} & 0 \\ 0 & p_2 \mathbf{a} \end{pmatrix} - \eta_1 \begin{pmatrix} 0 & p_1 \mathbf{a} \\ p_2 \mathbf{a} & 0 \end{pmatrix} - \chi \begin{pmatrix} 0 & p_1 \mathbf{a} \\ -p_2 \mathbf{a} & 0 \end{pmatrix} \\ \mathbf{C} &= \tilde{B} \begin{pmatrix} \mathbf{a} & 0 \\ 0 & \mathbf{a} \end{pmatrix} + p_J \begin{pmatrix} -p_2 \mathbf{a} & p_1 \mathbf{a} \\ p_2 \mathbf{a} & -p_1 \mathbf{a} \end{pmatrix} + \tilde{\sigma} \begin{pmatrix} -p_2 \mathbf{a} & p_1 \mathbf{a} \\ -p_2 \mathbf{a} & p_1 \mathbf{a} \end{pmatrix}. \end{aligned} \quad (7.15)$$

The introduced (2×2) matrix is $\mathbf{a} = i\sigma_y$, where σ_y is a Pauli matrix. We can rearrange Eq. (7.14) to get

$$\partial_\tau \mathbf{v} = \mathbf{M}_c(p_1, p_2) \mathbf{v}, \quad (7.16)$$

where $\mathbf{M}_c(p_1, p_2) = \mathbf{A}^{-1}(p_1, p_2) \mathbf{C}(p_1, p_2)$ is the stability matrix. This matrix can be used to check the stability of the different configurations (p_1, p_2) in different regions of the parameter space. The subscript is used to indicate that the stability matrix uses Cartesian coordinates. In the ferromagnetic cases, $p_2 = p_1$, we can write the above matrices in the compact form

$$\begin{aligned} \mathbf{A}(p_1, p_1) &= \mathbf{1} - p_1 [\eta_0 \boldsymbol{\tau}_0 + \eta_1 \boldsymbol{\tau}_x + \chi i \boldsymbol{\tau}_y] \otimes \mathbf{a} \\ \mathbf{C}(p_1, p_1) &= \left[\tilde{B} \boldsymbol{\tau}_0 + p_1 p_J (\boldsymbol{\tau}_x - \boldsymbol{\tau}_0) + p_1 \tilde{\sigma} (i \boldsymbol{\tau}_y - \boldsymbol{\tau}_z) \right] \otimes \mathbf{a} \end{aligned} \quad (7.17)$$

where the $\boldsymbol{\tau}$'s are Pauli matrices and “ \otimes ” denotes the Kronecker product. These matrices are easy to type into some mathematics software to calculate the eigenvalues for a desired point in parameter space and therefore check for stable points as explained in the beginning of Sec. 7.2. It would be nice to get an analytic expression for the hyperplanes in parameter space where the eigenvalues pass through zero, potentially marking a phase boundary between two different stable regions. The author attempted to do so but did not manage to reduce it to a simple expression.

Similarly, for the antiferromagnetic configuration, where $p_2 = -p_1$, we can write the matrices as

$$\begin{aligned} \mathbf{A}(p_1, -p_1) &= \mathbf{1} - p_1 [\eta_0 \boldsymbol{\tau}_z + \eta_1 i \boldsymbol{\tau}_y + \chi \boldsymbol{\tau}_x] \otimes \mathbf{a} \\ \mathbf{C}(p_1, -p_1) &= \left[\tilde{B} \boldsymbol{\tau}_0 + p_1 p_J (\boldsymbol{\tau}_z + i \boldsymbol{\tau}_y) + p_1 \tilde{\sigma} (\boldsymbol{\tau}_0 + \boldsymbol{\tau}_x) \right] \otimes \mathbf{a}. \end{aligned} \quad (7.18)$$

The presented stability matrix can only be used when the spins point either up or down. To study the canted spin configuration, we therefore have to follow a more general approach.

7.2.3 General linearization

The stability of the canted spin configuration for the EOMs in Eq. (7.6) has been investigated by Kasper Bonfils [149]. In his thesis, the EOMs were iterated by inserting the expressions for $\dot{\mathbf{n}}$ on the right hand side of the equations. Terms of second order in η_0 and χ were then neglected (η_1 was not included in his analysis) and the equations were expanded to first order in the angles around the fixed points. For Bonfils's final analytic expression, see Sec. 4.2 in Ref. [149].

Here, we will not restrict the analysis to first order in η 's and χ . We will start by rewriting the EOMs as

$$\begin{pmatrix} 1 + \eta_0 [\mathbf{n}_1]_{\times} & (\eta_1 + \chi) [\mathbf{n}_1]_{\times} \\ (\eta_1 - \chi) [\mathbf{n}_2]_{\times} & 1 + \eta_0 [\mathbf{n}_2]_{\times} \end{pmatrix} \begin{pmatrix} \partial_{\tau} \mathbf{n}_1 \\ \partial_{\tau} \mathbf{n}_2 \end{pmatrix} = \begin{pmatrix} -\tilde{\mathbf{B}} \times \mathbf{n}_1 + (p_J + \tilde{\sigma}) \mathbf{n}_2 \times \mathbf{n}_1 \\ -\tilde{\mathbf{B}} \times \mathbf{n}_1 + (p_J - \tilde{\sigma}) \mathbf{n}_1 \times \mathbf{n}_2 \end{pmatrix}$$

$$\mathbf{A} \begin{pmatrix} \partial_{\tau} \mathbf{n}_1 \\ \partial_{\tau} \mathbf{n}_2 \end{pmatrix} = \mathbf{F}, \quad (7.19)$$

where $[\mathbf{n}_i]_{\times}$ is the cross product matrix so that $[\mathbf{n}_i]_{\times} \mathbf{n}_j = \mathbf{n}_i \times \mathbf{n}_j$. With this, we can write

$$\begin{pmatrix} \partial_{\tau} \mathbf{n}_1 \\ \partial_{\tau} \mathbf{n}_2 \end{pmatrix} = \mathbf{A}^{-1} \mathbf{F}. \quad (7.20)$$

Since the lengths of the \mathbf{n} 's are constant, the above can be represented as a (4×1) vector: two dimensions for each spin just as in Sec. 7.2.2. If we use Cartesian coordinates in Eq. (7.20), we can rotate the \mathbf{n} 's into their respective spherical polar coordinate system in which the $\hat{\rho}$ components drop out. We could not start out with this choice of coordinates since the coupled differential equations in Eq. (7.19) require a shared coordinate system. The time derivative in spherical polar coordinates is $\dot{\mathbf{n}}_1 = \dot{\theta}_1 \hat{\theta}_1 + \dot{\phi}_1 \sin \theta_1 \hat{\phi}_1$, so we need to divide the $\hat{\phi}$ components by $\sin \theta$ to get $\partial_{\tau} \mathbf{v} = (\partial_{\tau} \theta_1, \partial_{\tau} \phi_1, \partial_{\tau} \theta_2, \partial_{\tau} \phi_2)^T$ on the left hand side; this step requires that $\sin \theta \neq 0$. Finally, we can expand the right hand side to first order in the angles around the fixed point to get

$$\partial_{\tau} \begin{pmatrix} \delta \theta_1 \\ \delta \phi_1 \\ \delta \theta_2 \\ \delta \phi_2 \end{pmatrix} = \mathbf{M}(\tilde{\mathbf{B}}, \mathbf{v}_0) \begin{pmatrix} \delta \theta_1 \\ \delta \phi_1 \\ \delta \theta_2 \\ \delta \phi_2 \end{pmatrix}, \quad (7.21)$$

where $\delta \theta_i = \theta_i - \theta_i^0$ is the deviation from the fixed point angle and where the stability matrix is written as a function of the magnetic field and the fixed point. The mathematical description of how to get from Eq. (7.20) to Eq. (7.21) is found in Appendix E.3 and the expression for the stability matrix is given in Eqs. (E.18)–(E.20). As mentioned, the stability matrix includes the fractions $1/\sin \theta_1^0$ and $1/\sin \theta_2^0$, and it can therefore not be used to check the stability of the ferromagnetic configuration $(\theta_1^0, \phi_1^0, \theta_2^0, \phi_2^0) = (0, 0, 0, 0)$ with $\tilde{\mathbf{B}} = \tilde{B} \hat{z}$, etc., which caused some problems in Ref. [149]. However, if we just rotate the magnetic field, we find that $\mathbf{M}(\tilde{B} \hat{x}, (\pi/2, 0, \pi/2, 0))$ has exactly the same eigenvalues as $\mathbf{M}_c(+1, +1)$ in Eq. (7.16). Consequently, the stability matrix in Eq. (7.21) can be used to check the stability of all the fixed points found in Sec. 7.2.1.

7.2.4 Stability diagrams

With the stability matrix in Eq. (7.21), we can now use the procedure described in the beginning of Sec. 7.2 to check the stability at different points in parameter space. Unless otherwise stated, we will use the following magnetic field and relaxation coefficients

$$\begin{aligned} \tilde{B} &= 1 \\ \eta_0 &= 0.01 \\ \eta_1 &= \eta_0/2. \end{aligned} \quad (7.22)$$

Here the $\eta_0 = 0.01$ is a typical value for metallic ferromagnets [151, 152].

The stability diagram in the case of antiferromagnetic coupling is shown in Fig. 7.2. As expected, the canted configuration is stable in the equilibrium case, $(\sigma, \chi) = (0, 0)$, where the exchange coupling and magnetic field compete. Remember that the spin configurations of the canted spin region in Fig. 7.2 are different for the different σ values as stated in Eq. (7.10). As σ and χ become sufficiently large and of opposite sign, the ferromagnetic configuration (\uparrow, \uparrow) becomes stable. In this region, the nonequilibrium terms therefore drive the system into a configuration where the energy contribution $J\mathbf{S}_1 \cdot \mathbf{S}_2$ is maximized. This is a quite interesting result, and we will return to the possible applications of this later.

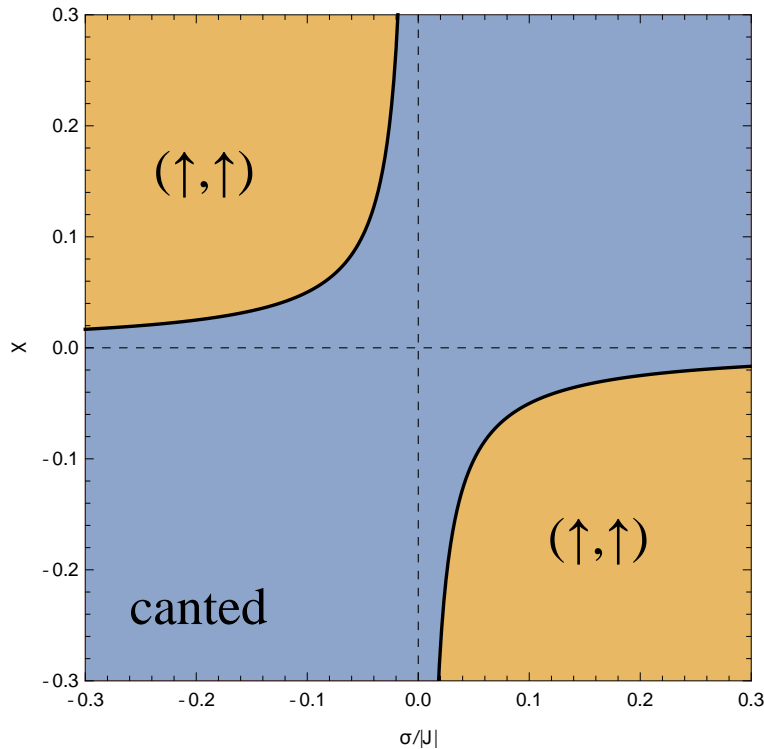


FIGURE 7.2: Stability diagram with $J > 0$ and the parameters in Eq. (7.22).

The same analysis is done in the case of ferromagnetic coupling, and the result is shown in Fig. 7.3. As expected, the equilibrium configuration is ferromagnetic pointing along the magnetic field, but as σ and χ become sufficiently large and of opposite sign, the spins will end up pointing antiparallel to the magnetic field. This is surprising since it maximizes the energy contribution from the magnetic field, $-\sum_i \mathbf{B} \cdot \mathbf{S}_i$. If σ and χ are large and of same sign, the canted configuration becomes stable, while none of the fixed points are stable in the white region in Fig. 7.3. The presented stability diagrams will be confirmed in Sec. 7.3 by running numerical simulations of the spin system.

The stability diagrams in Fig. 7.2 and 7.3 are both symmetric under the inversion $(\sigma, \chi) \rightarrow (-\sigma, -\chi)$. This can be understood from the symmetry in the EOMs in Eq. (7.6): after doing the exchange $(\sigma, \chi) \rightarrow (-\sigma, -\chi)$, spin 1 will follow the same EOM as spin 2 did before the exchange (and vice versa). Consequently, if they end up in the configuration $(\theta_1, \phi_1, \theta_2, \phi_2) = (\theta_a, \phi_a, \theta_b, \phi_b)$ for (σ, χ) , they will end up in the configuration $(\theta_b, \phi_b, \theta_a, \phi_a)$ for $(-\sigma, -\chi)$.

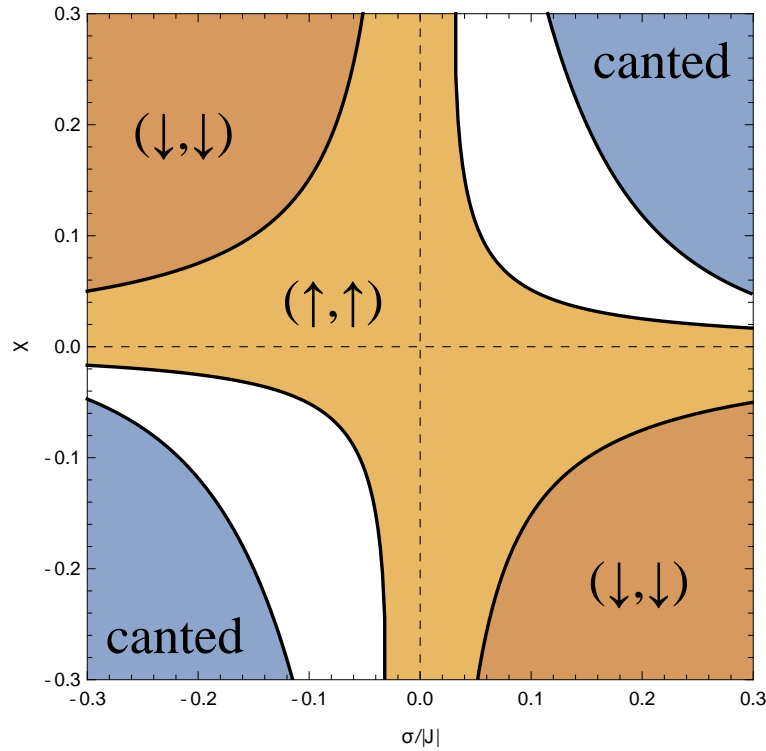


FIGURE 7.3: Stability diagram with $J < 0$ and the parameters in Eq. (7.22).

To get an idea of the effects of the different parameters, six different stability diagrams for different values of \tilde{B} and η_0 are plotted in Fig. 7.4. The diagrams in the left column have antiferromagnetic coupling, while the right diagrams have ferromagnetic coupling. Only a single parameter is changed in the diagrams when compared to the plots in Figs. 7.2 and 7.3, and the varied parameter is shown to the left of the rows.

In the upper row of Fig. 7.4, the magnetic field is small compared to the indirect exchange. This does not affect the boundaries of the (\uparrow, \uparrow) and (\downarrow, \downarrow) phases significantly when compared to the cases with $\tilde{B} = 1$. As mentioned below Eq. (7.10), the canted spin configuration is a physical solution when $|\tilde{\sigma}| < \tilde{B}/2 < 1$. This limit has become clear now that the magnetic field is smaller, and it can be understood as follows: as $\tilde{\sigma}$ increases positively from 0, spin 1 is forced downwards, while spin 2 is forced upwards and at $\tilde{\sigma} = \tilde{B}/2$, the antiferromagnetic configuration (\downarrow, \uparrow) is reached. The opposite is true when $\tilde{\sigma}$ takes negative values.

In the middle row in Fig. 7.4, the magnetic field dominates over the exchange torque, and the ferromagnetic configuration (\uparrow, \uparrow) is stable in equilibrium no matter the sign of the exchange coupling. Both diagrams show that the system turns chaotic when the nonequilibrium parameters are large. In the lower row of Fig. 7.4, the relaxation parameters, η_0 and η_1 , are lowered by a factor of 10, when compared to Figs. 7.2 and 7.3. As a consequence, the phase boundaries are drawn closer to $(\tilde{\sigma}, \chi) = (0, 0)$. The composition of phases are not affected by this change.

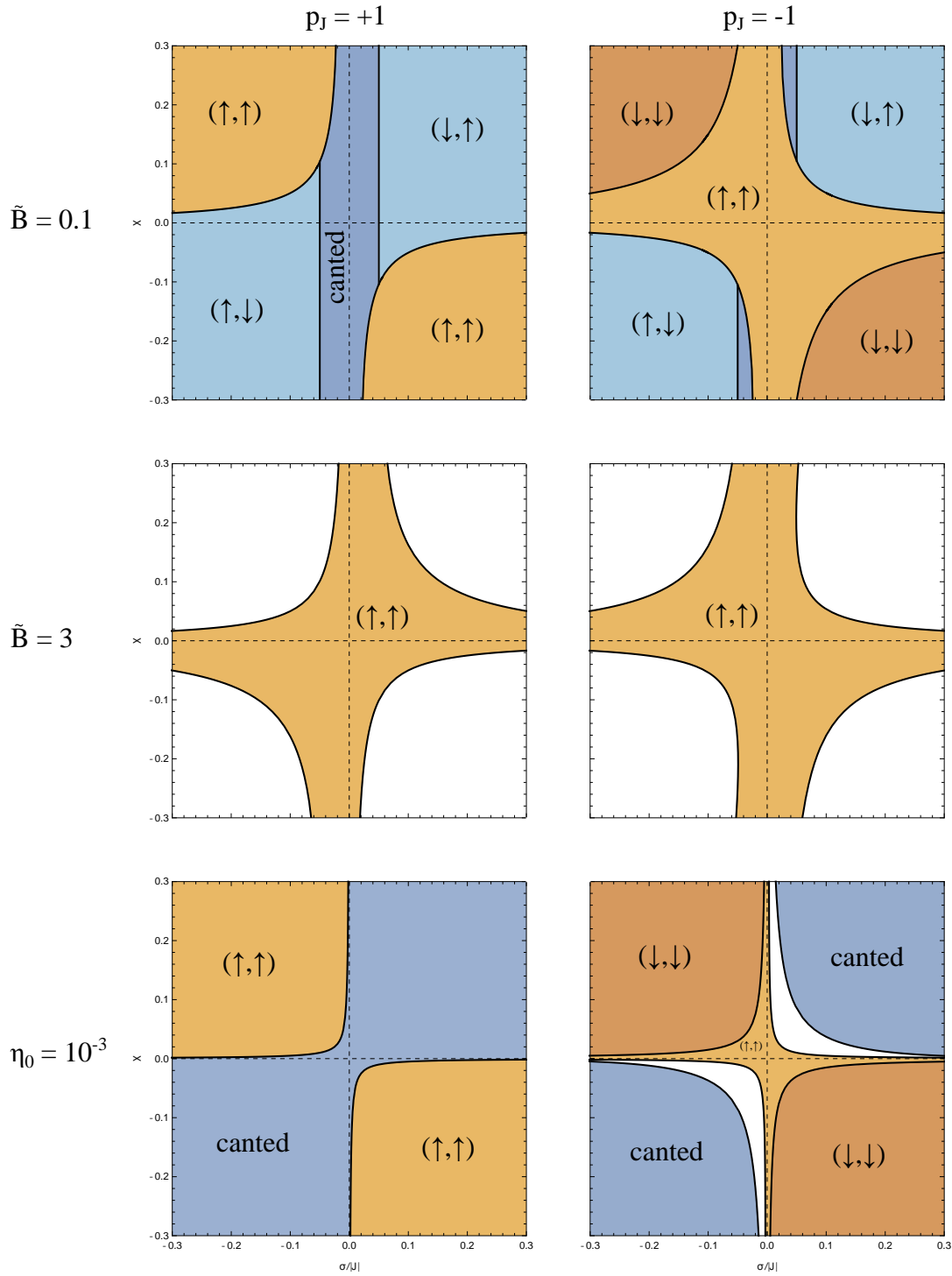


FIGURE 7.4: Stability diagrams obtained from linear stability analysis. The left (right) diagrams have antiferromagnetic (ferromagnetic) coupling. In all diagrams, a single parameter is changed when compared to the diagrams in Figs. 7.2 and 7.3. Unless stated to the left, the parameters are therefore as in Eq. (7.22).

7.3 Numerical calculations

As an additional tool, we can simulate the spin system numerically. This can be done by using Euler's method on Eq. (7.20) so that

$$\begin{pmatrix} \mathbf{n}_1(\tau) \\ \mathbf{n}_2(\tau) \end{pmatrix} = \begin{pmatrix} \mathbf{n}_1(\tau - \Delta\tau) \\ \mathbf{n}_2(\tau - \Delta\tau) \end{pmatrix} + \Delta\tau \mathbf{A}^{-1}(\tau - \Delta\tau) \mathbf{F}(\tau - \Delta\tau). \quad (7.23)$$

By choosing a set of parameters (\tilde{B} , η_0 , and so on) and the initial spin configuration $\mathbf{n}_1(0)$ and $\mathbf{n}_2(0)$, the above equation allows us to calculate the orientation of the spins at any desired time τ in the future. We use Cartesian coordinates in the above equation, which means that numerical errors can cause the length of the vectors to change. The lengths of the vectors can therefore be used as a measure of the numerical error [125].

We will start by considering a few trajectories of the spins. For three different points in parameter space, which are all included in the stability diagrams in Figs. 7.2 and 7.3, we let the spin system evolve until they stop moving. The initial state is arbitrarily chosen to be $(\theta_1^0, \phi_1^0, \theta_2^0, \phi_2^0) = (0.3\pi, 0, 0.4\pi, 0.8\pi)$. The results are shown in Fig. 7.5, where the left blue spin is spin 1, while spin 2 is red and to the right. The initial orientations are indicated with dots, while the arrows show the final orientations. In Fig. 7.5a the coupling is antiferromagnetic, but the spins end up pointing parallel to the magnetic field. In Figs. 7.5b and 7.5c, the coupling is ferromagnetic, but the spins end up in the canted configuration and (\downarrow, \downarrow) , respectively. In all three cases, the final orientations agree with the stability diagrams in Figs. 7.2 and 7.3. However, it is difficult to learn a lot from these trajectory plots.

To do a more thorough investigation of the final orientations of the spins, we can do a numerical raster scan of the parameter space. This can be thought of as a way to verify the stability diagrams obtained in Sec. 7.2.4. We will use a time step size of $\Delta\tau = 10^{-4}$ and allow the system to evolve for 10^7 steps. The system is considered to be stable when both spins are slower than $|\partial_\tau \mathbf{n}_i| < 0.05$ for 10^5 time steps. For the calculations that reach this stability criterion, it is checked whether the final configuration is close to any of the fixed points described in Sec. 7.2.1. The stable configuration $(\theta_1^{\text{final}}, \theta_2^{\text{final}})$ is identified with the fixed point $(\theta_1^{\text{fix}}, \theta_2^{\text{fix}})$ if $|\theta_i^{\text{final}} - \theta_i^{\text{fix}}| < 0.08$ for both spins.

The result is shown in Fig. 7.6 in the case of ferromagnetic coupling. Each of the 441 points represent a numerical simulation as described above and the black lines are the same as in Fig. 7.3 obtained from the linear stability analysis. If the simulation did not reach the stability criterion or if the stable point was not identified with a fixed point, the calculation was marked as 'not specified'. The result is in good agreement with the stability diagram in Fig. 7.3. However, when close to a phase boundary, the simulation times were not long enough for the system to reach stable points. Additionally, the system reached the canted spin configuration in some cases in the 1st quadrant in Fig. 7.6 in which a chaotic state was expected. Possible reasons are that the chosen stability criterion is not strong enough or that the chosen initial configurations by luck run into the canted configuration. Optimally, the calculation should therefore be done for different initial configurations. Another explanation could be that the Euler method is too simple to simulate the spin EOMs. In most of the cases in which stability is reached, the vector lengths are close to unchanged, which indicates that the numerical errors are small. In some of the stable calculations, however, the vector lengths increased with $\sim 3\%$ and in some of the chaotic calculations the errors were even larger. Despite the numerical errors, the result in Fig. 7.6 is in good

agreement the result from the stability analysis.

7.4 Conclusion

In this chapter, we have studied the behavior of a two-spin system that follows the equations of motion discovered in Chapter 6. We found that the nonequilibrium torque-dependent torques ($\chi\dot{\mathbf{n}}_2 \times \mathbf{n}_1$ and $-\chi\dot{\mathbf{n}}_1 \times \mathbf{n}_2$) do not change the energy of the spin system. A linear stability analysis showed that the nonequilibrium torques can drive the spin system into unexpected configurations. As examples, the spins can end up in the canted (and antiferromagnetic) configuration even though the coupling is ferromagnetic and they can end up pointing antiparallel to the magnetic field in the ferromagnetic case. These interesting cases are obtained when the nonequilibrium coefficients, σ and χ , are large. Compared to the equilibrium coefficients, we approximately need $|\sigma| > 0.1|J|$ and $|\chi| > 10\eta_0$.

The findings in this chapter suggest a new way to prepare a spin system. Instead of applying a magnetic field, the system can be prepared with an electric current. With the current, different configurations can be obtained; not just the ferromagnetic configuration.

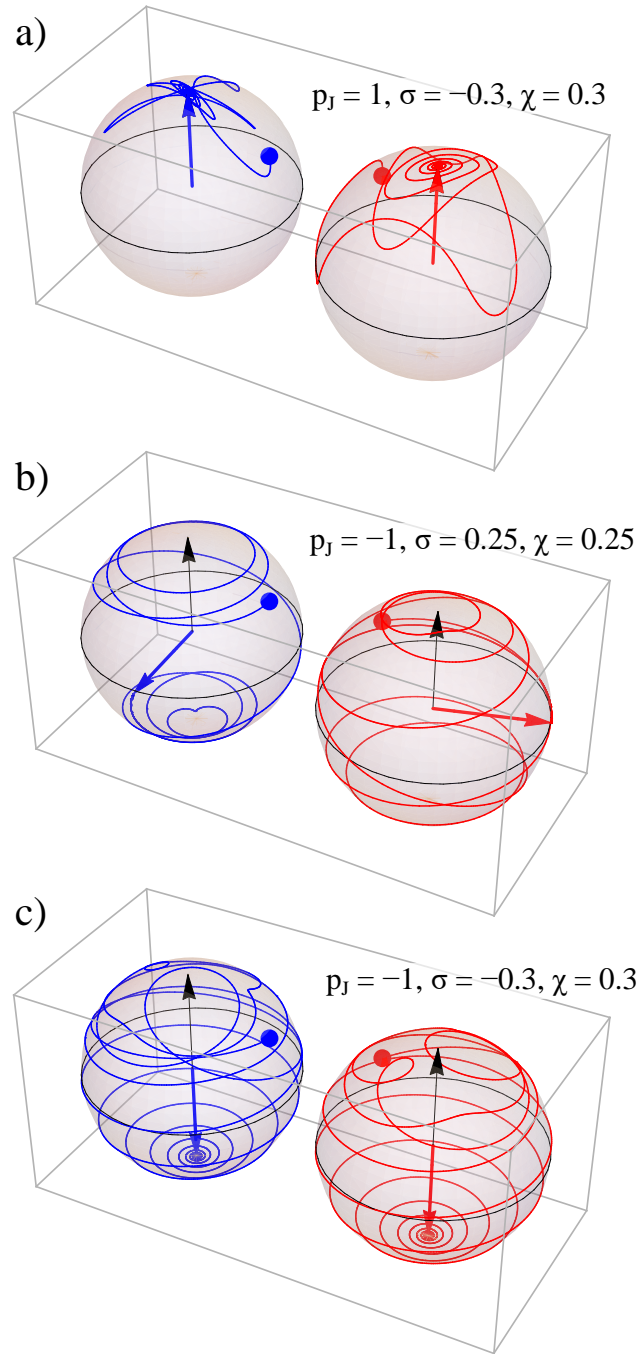


FIGURE 7.5: Spin trajectories for different choices of parameters. In all cases, the spins start in the arbitrarily chosen configuration $(\theta_1, \phi_1, \theta_2, \phi_2) = (0.3\pi, 0, 0.4\pi, 0.8\pi)$, which is represented by dots. The final configuration is shown by vectors. In (b) the spins end up in the canted spin configuration with $(n_1^z, n_2^z) = (-0.8, 0)$ and $\Delta\phi = \pi$, which agrees with Eq. (7.10). In all simulations, the parameters in Eq. (7.22) are used.

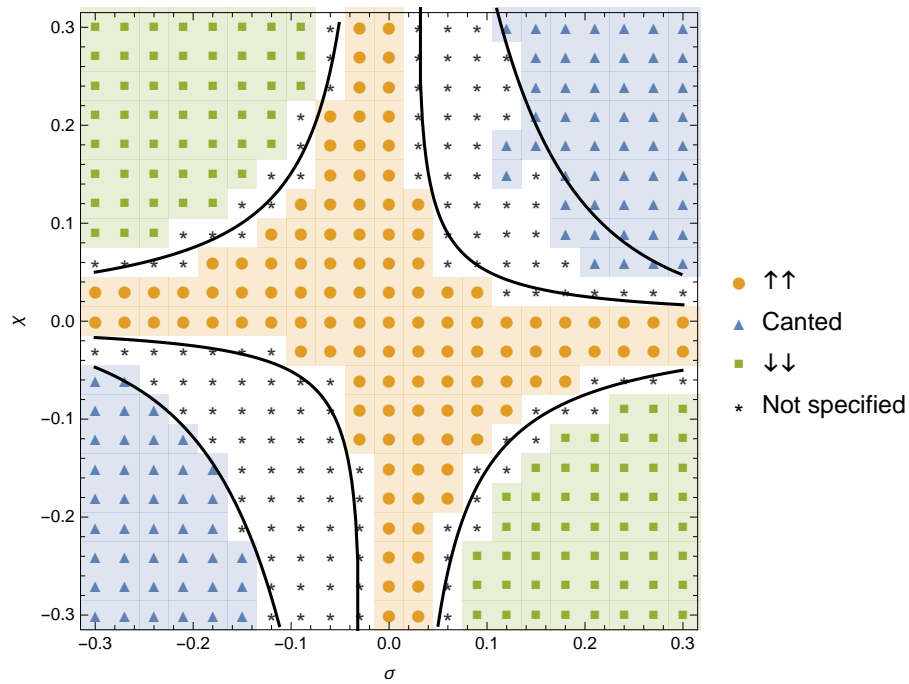


FIGURE 7.6: Numerical simulation results for $p_J = -1$, $\tilde{B} = 1$, $\eta_0 = 10^{-2}$, and $\eta_1 = \eta_0/2$. Each point represents a numerical simulation and the shape and color indicates the final configuration or the simulation. 'Not specified' means that the simulation did not reach a stable point or that the stable point could not be identified with any of the fixed point configurations. The black lines are the same as in Fig. 7.3.

Appendices

Appendix A

Appendix to Chapters 2 and 3

A.1 Nonequilibrium density matrix in the single particle picture

In the single particle picture, we can write the density matrix as

$$\begin{aligned}\rho &= 2 \sum_{\alpha,k} n_F^\alpha(E_k) |\psi_{\alpha k}\rangle\langle\psi_{\alpha k}| \\ &= 2 \int dE \sum_{\alpha,k} n_F^\alpha(E) \delta(E - E_k) |\psi_{\alpha k}\rangle\langle\psi_{\alpha k}|,\end{aligned}\tag{A.1}$$

where $|\psi_{\alpha k}\rangle$ is the scattering state for an electron incoming from lead α with the energy E_k . For an observable A , we can sum up the contributions from all electrons by using $\langle A \rangle = \text{Tr}[\rho A]$. We are interested in the local currents on the molecule, and we therefore consider the density matrix in the molecular subspace

$$\begin{aligned}\rho_M &= M\rho M \\ &= 2 \int dE \sum_{\alpha,k} n_F^\alpha(E) \delta(E - E_k) G_M H_{M\alpha} |\phi_{\alpha k}\rangle\langle\phi_{\alpha k}| H_{\alpha M} G_M^\dagger \\ &= 2 \sum_{\alpha} \int dE n_F^\alpha(E) G_M H_{M\alpha} \left(\sum_k \delta(E - E_k) |\phi_{\alpha k}\rangle\langle\phi_{\alpha k}| \right) H_{\alpha M} G_M^\dagger \\ &= \frac{1}{\pi} \sum_{\alpha} \int dE n_F^\alpha(E) G_M \Gamma_{\alpha} G_M^\dagger.\end{aligned}\tag{A.2}$$

Here we have used that the molecular part of the scattering state is $|\psi_{\alpha k}^M\rangle = G_M H_{M\alpha} |\phi_{\alpha k}\rangle$, where $|\phi_{\alpha k}\rangle$ is the incoming wave in lead α (see e.g. Ref. [59]). We have also used that

$$\begin{aligned}\Gamma_{\alpha} &= i \left(\Sigma_{\alpha} - \Sigma_{\alpha}^\dagger \right) \\ &= i \left(H_{M\alpha} G_{\alpha}^0 H_{\alpha M} - H_{M\alpha} G_{\alpha}^{0\dagger} H_{\alpha M} \right) \\ &= i H_{M\alpha} \left(\frac{1}{E - H_{\alpha} + i\eta} - \frac{1}{E - H_{\alpha} - i\eta} \right) H_{\alpha M} \\ &= i H_{M\alpha} \frac{-2i\eta}{(E - H_{\alpha})^2 + \eta^2} H_{\alpha M} \\ &= 2\pi H_{M\alpha} \delta(E - H_{\alpha}) H_{\alpha M} \\ &= 2\pi H_{M\alpha} \left[\sum_k |\phi_{\alpha k}\rangle\langle\phi_{\alpha k}| \delta(E - E_k) \right] H_{\alpha M}.\end{aligned}\tag{A.3}$$

A.2 Derivation of $\text{Tr} \left[G_M \Gamma G_M^\dagger A \right] = 0$

In this section, we will show that

$$\text{Tr} \left[G_M \Gamma_L G_M^\dagger A \right] = - \text{Tr} \left[G_M \Gamma_R G_M^\dagger A \right] \quad (\text{A.4})$$

for a Hermitian operator A in the molecular subspace that reverses under time-reversal, $TAT^{-1} = -A$. Here $T = i\sigma_y K$ is the time-reversal operator, where K is the complex conjugation operator. To show this, we first write $\Gamma = \Gamma_L + \Gamma_R$ as

$$\begin{aligned} \Gamma &= i \left(\Sigma - \Sigma^\dagger \right) \\ &= i \left((G_M^\dagger)^{-1} - G_M^{-1} \right), \end{aligned} \quad (\text{A.5})$$

where we used that $G_M^{-1} = (G_M^0)^{-1} - \Sigma_L + \Sigma_R = (G_M^0)^{-1} - \Sigma$. We can use this property to write $\text{Tr} \left[(\Gamma_L + \Gamma_R) G_M^\dagger A G_M \right]$ as

$$\text{Tr} \left[\Gamma G_M^\dagger A G_M \right] = i \left(\text{Tr} [AG] - \text{Tr} \left[G_M^\dagger A \right] \right). \quad (\text{A.6})$$

For an arbitrary matrix B , one can show that $\text{Tr} [TBT^{-1}] = \text{Tr} [B]^*$.¹ If A reverses under time-reversal, $TAT^{-1} = -A$, we get

$$\begin{aligned} \text{Tr} [AG_M] &= \text{Tr} [TAT^{-1} T G_M T^{-1}]^* \\ &= - \text{Tr} [A^* G_M] \\ &= - \text{Tr} [A^T G_M^T] \end{aligned} \quad (\text{A.11})$$

where we have used that $T G_M T^{-1} = G_M^*$, $G_M = G_M^T$, and $A = A^\dagger$. Consequently, $\text{Tr} [AG_M] = 0$ and the same goes for $\text{Tr} \left[G_M^\dagger A \right] = 0$, and Eq. (A.4) follows.

A.3 Derivation of single channel expression

When the self-energies can be written as in Eq. (2.12), the bond transmission in Eq. (2.10) can be put on the simpler form in Eq. (2.13). In this section, we will go

¹An arbitrary matrix can be written on the form

$$B = M_0 \otimes I_{2 \times 2} + \sum_i M_i \otimes \sigma_i, \quad (\text{A.7})$$

where the σ 's are Pauli spin matrices and the M 's can be any matrices. If we now use the time reversal operator

$$T = i\sigma_y K, \quad (\text{A.8})$$

where K is the complex conjugate operator, we can write

$$TBT^{-1} = M_0^* \otimes I_{2 \times 2} - \sum_i M_i^* \otimes \sigma_i. \quad (\text{A.9})$$

Taking the trace gives

$$\begin{aligned} \text{Tr} [TBT^{-1}] &= \text{Tr} [M_0^*] \text{Tr} [I_{2 \times 2}] - \sum_i \text{Tr} [M_i^*] \text{Tr} [\sigma_i] \\ &= \text{Tr} [M_0]^* \\ &= \text{Tr} [B]^*. \end{aligned} \quad (\text{A.10})$$

through the derivation hereof.

For the self-energies in Eq. (2.12), the transmission function in Eq. (2.4) can be written as

$$\mathcal{T} = k_L k_R |G_{N1}|^2, \quad (\text{A.12})$$

where $k_\alpha = -2 \text{Im} a_\alpha$ so that $\Gamma_L = k_L |1\rangle\langle 1|$. Consider now the bond transmission by inserting the local current operator, $\hat{I}_{ij} = \frac{ie}{\hbar} t_{ij} (|i\rangle\langle j| - |j\rangle\langle i|)$, into the Eq. (2.10)

$$\begin{aligned} \mathcal{T}_{ij} &= \frac{\hbar}{e} \text{Tr} \left[G_M \Gamma_L G_M^\dagger \hat{I}_{ij} \right] \\ &= it_{ij} k_L (G_{j1} G_{i1}^* - G_{i1} G_{j1}^*) \\ &= 2t_{ij} k_L \text{Im}(G_{i1} G_{j1}^*), \end{aligned} \quad (\text{A.13})$$

where the elements are $G_{ij} = \langle i | G_M | j \rangle$. In the following, we will rewrite $\text{Im}(G_{i1} G_{j1}^*)$ step by step: The full Greens function can be written as $G = G^0 + G^0(\Sigma_L + \Sigma_R)G$ and an element is

$$G_{ij} = G_{ij}^0 + a_L G_{i1}^0 G_{1j} + a_R G_{iN}^0 G_{Nj}. \quad (\text{A.14})$$

Remember that H_M is symmetric so that $G_{ij}^0 = G_{ji}^0$. We will consider energies away from resonances so that G^0 is real. Since we integrate up all energies, we of course have to remember the resonances. However, they do not make a significant contribution to the integral in I_{ij} . The product between two Greens function elements is

$$\begin{aligned} G_{i1} G_{j1}^* &= (G_{i1}^0 + a_L G_{i1}^0 G_{11} + a_R G_{iN}^0 G_{N1}) (G_{j1}^0 + a_L^* G_{j1}^{0*} G_{11}^* + a_R^* G_{jN}^0 G_{N1}^*) \\ &= \color{red}{G_{i1}^0 G_{j1}^0} + \color{blue}{a_L^* G_{i1}^0 G_{j1}^0 G_{11}^*} + \color{blue}{a_R^* G_{i1}^0 G_{jN}^0 G_{N1}^*} \\ &\quad + a_L \color{red}{G_{i1}^0 G_{j1}^0 G_{11}} + |a_L|^2 \color{red}{G_{i1}^0 G_{j1}^0 G_{11} G_{11}^*} + a_L a_R^* \color{red}{G_{i1}^0 G_{jN}^0 G_{11} G_{N1}^*} \\ &\quad + a_R \color{red}{G_{iN}^0 G_{j1}^0 G_{N1}} + a_R a_L^* \color{red}{G_{iN}^0 G_{j1}^0 G_{N1} G_{11}^*} + |a_R|^2 \color{red}{G_{iN}^0 G_{jN}^0 G_{N1} G_{N1}^*}, \end{aligned} \quad (\text{A.15})$$

where the red terms are real, while the two blue terms are each others complex conjugate. Taking the imaginary part,

$$\begin{aligned} \text{Im}(G_{i1} G_{j1}^*) &= \text{Im} \left[a_R^* G_{i1}^0 G_{jN}^0 (1 + a_L G_{11}) G_{N1}^* + a_R G_{iN}^0 G_{j1}^0 (1 + a_L^* G_{11}^*) G_{N1} \right] \\ &= (G_{i1}^0 G_{jN}^0 - G_{j1}^0 G_{iN}^0) \text{Im} \left[a_R^* (1 + a_L G_{11}) G_{N1}^* \right] \\ &= (G_{1i}^0 G_{jN}^0 - G_{1j}^0 G_{iN}^0) \text{Im} \left[\frac{a_R^*}{G_{N1}} (1 + a_L G_{11}) \right] |G_{N1}|^2 \\ &= (G_{1i}^0 G_{jN}^0 - G_{1j}^0 G_{iN}^0) \text{Im} \left[\frac{a_R^*}{G_{N1}} \left(1 + \frac{1}{G_{N1}^0} (G_{N1} - G_{N1}^0 - a_R G_{NN}^0 G_{N1}) \right) \right] |G_{N1}|^2 \\ &= (G_{1i}^0 G_{jN}^0 - G_{1j}^0 G_{iN}^0) \frac{k_R}{2G_{N1}^0} |G_{N1}|^2, \end{aligned} \quad (\text{A.16})$$

where we have rewritten the expression for the element G_{N1} as $a_L = \frac{1}{G_{N1}^0 G_{11}} (G_{N1} - G_{N1}^0 - a_R G_{NN}^0 G_{N1})$. Inserting the above expression into Eq. (A.13) and using Eq. (A.12),

we get

$$\begin{aligned} \mathcal{T}_{ij} &= t_{ij} \frac{G_{1i}^0 G_{jN}^0 - G_{1j}^0 G_{iN}^0}{G_{N1}^0} k_L k_R |G_{N1}|^2 \\ &= t_{ij} \frac{G_{1i}^0 G_{jN}^0 - G_{1j}^0 G_{iN}^0}{G_{1N}^0} \mathcal{T}, \end{aligned} \quad (\text{A.17})$$

which is the expression stated in Eqs. (2.13) and (2.14).

A.4 Symmetry of γ for Alternant Molecules

In this section, we show that for an arbitrary alternant molecule, $\gamma_{ij}(-E) = \gamma_{ij}(E)$. To do this, we use the Coulson-Rushbrooke pairing theorem, which states that for alternant molecules, the molecular orbitals are symmetrically distributed about a zero energy level [74]. Additionally, for a symmetry pair (e.g. HOMO and LUMO), we can go from one orbital to the other by changing the sign at every other site. We divide the sites into two sub-lattices, the ones at which there is a sign change and the ones at which there is not.

Consider an arbitrary element of the Greens function for the isolated molecule

$$\begin{aligned} G_{ij}^0 &= \langle i | \frac{1}{E - H_M} | j \rangle \\ &= \sum_n \frac{\psi_i^n \psi_j^n}{E - \varepsilon_n}, \end{aligned} \quad (\text{A.18})$$

where i and j are site indices, n refers to the molecular orbital, and $\psi_i^n = \langle i | n \rangle$. We will use \tilde{n} to denote the symmetry partner of n . We have two different scenarios for the Greens function element. The sites i and j can either be on the same sub-lattice or on different sub-lattices

$$\begin{aligned} \psi_i^n \psi_j^n &= \pm \psi_i^{\tilde{n}} \psi_j^{\tilde{n}} \\ \varepsilon_n &= -\varepsilon_{\tilde{n}} \end{aligned} \quad (\text{A.19})$$

where the upper (lower) sign is when i and j are on the same (different) sub-lattice. We then have

$$\begin{aligned} G_{ij}^0(-|E|) &= \sum_n \frac{\psi_i^n \psi_j^n}{-|E| - \varepsilon_n} \\ &= \pm \sum_n \frac{\psi_i^{\tilde{n}} \psi_j^{\tilde{n}}}{-|E| + \varepsilon_{\tilde{n}}} \\ &= \mp G_{ij}^0(|E|) \end{aligned} \quad (\text{A.20})$$

since the sums over n and \tilde{n} both include all orbitals. We can choose the sites 1 and i to be on the same sub-lattice, so that $G_{1i}^0(-E) = -G_{1i}^0(E)$, $G_{1j}^0(-E) = G_{1j}^0(E)$, and $G_{jN}^0(-E) = \pm G_{jN}^0(E)$ where the upper (lower) sign refers to 1 and N on the same

(different) sub-lattice. Using these in the expression for γ in Eq. (2.14), we get

$$\begin{aligned} \frac{G_{1i}^0(-E)G_{jN}^0(-E) - G_{1j}^0(-E)G_{iN}^0(-E)}{G_{1N}^0(-E)} &= \frac{\mp G_{1i}^0(E)G_{jN}^0(E) \pm G_{1j}^0(E)G_{iN}^0(E)}{\mp G_{1N}^0(E)} \\ &= \frac{G_{1i}^0(E)G_{jN}^0(E) - G_{1j}^0(E)G_{iN}^0(E)}{G_{1N}^0(E)}. \end{aligned} \quad (\text{A.21})$$

We have therefore proved that for alternant molecules

$$\gamma_{ij}(-E) = \gamma_{ij}(E). \quad (\text{A.22})$$

A.5 Self-energy for semi-infinite leads

In this section, we will see how to calculate self-energies for two different types of semi-infinite leads.

A.5.1 1D chain

In the single molecule junctions, we model the leads as semi-infinite linear chains of atoms as illustrated in Fig. 3.1. In this case, the self-energy for the left lead can be written as

$$\begin{aligned} \Sigma_L &= H_{ML}g_L H_{LM} \\ &= t_c^2 g_{L,11} |in_L\rangle\langle in_L|, \end{aligned} \quad (\text{A.23})$$

where $g_L = (E - H_L + i\eta)^{-1}$,² and where the index 1 is the outermost site of the chain. We use that the left lead couples to the orbital $|in_L\rangle$ on the molecule. $g_{L,11}$ is known as the surface Greens function and in this case it is just a number. To calculate $g_{L,11}$, we will follow the procedure described in Sec. (3.2.1) in Ref. [66]: We can write the inverse Greens function of the left lead as

$$\begin{aligned} g_L^{-1} &= E - H_L + i\eta \\ &= E - H_L^0 - V + i\eta \\ &= (g_L^0)^{-1} - V, \end{aligned} \quad (\text{A.24})$$

where V is the matrix including the coupling between the two outermost sites, H_L^0 is the Hamiltonian without V , and $g_L^0 = (E - H_L^0 + i\eta)^{-1}$. Multiplying from the left with g_L^0 and from the right with g_L , we get

$$g_L = g_L^0 + g_L^0 V g_L. \quad (\text{A.25})$$

The Greens function element for the outermost site is (dropping the subscript L)

$$\begin{aligned} g_{11} &= \langle 1|g|1\rangle \\ &= g_{11}^0 + g_{11}^0 V_{12} g_{21} \end{aligned} \quad (\text{A.26})$$

²In Chapter 2, we used G_L^0 to describe this Greens function. To make the derivation more readable, we have dropped the superscript and used lowercase g in this section.

where site 2 is the next-outermost site. Similarly, we can write

$$g_{21} = g_{22}^0 V_{21} g_{11}. \quad (\text{A.27})$$

But $g_{22}^0 = g_{11}$, $V_{12} = V_{21} = -t_L$, and $g_{11}^0 = \frac{1}{E - \varepsilon_L + i\eta}$. We therefore end up with $g_{11} = \frac{1}{E - \varepsilon_L + i\eta} (1 + t_L^2 g_{11}^2)$, which can be rewritten as

$$0 = t_L^2 g_{11}^2 - (E - \varepsilon_L + i\eta) g_{11} + 1. \quad (\text{A.28})$$

This second order equation has the solutions

$$g_{L,11} = \frac{E - \varepsilon_L}{2t_L^2} \pm \frac{1}{2t_L^2} \sqrt{(E - \varepsilon_L)^2 - 4t_L^2}. \quad (\text{A.29})$$

We will only consider energies $(E - \varepsilon_L)^2 < 4t_L^2$ for which propagating modes are allowed in the chain [1]. From the representation in Eq. (A.3), we see that the imaginary part of the self-energy is negative.³ We will therefore use the lower sign in Eq. (A.29). With Eqs. (A.23) and (A.29), we have derived the self-energy for the semi-infinite chain. The $\Gamma_L = -2 \text{Im} \Sigma_L$ that appears in the expressions for the transmission and bond transmission is then

$$\Gamma_L = \frac{t_c^2}{t_L^2} \sqrt{4t_L^2 - (E - \varepsilon_L)^2} |\text{in}_L \rangle \langle \text{in}_L|. \quad (\text{A.30})$$

The derivation for the right lead is of course the same as described above, but with R instead of L .

A.5.2 Graphene nanoribbons

For graphene nanoribbons, we cannot simply write down an analytic expression for the self-energy as we did for the chain in Appendix A.5.1. Instead, we can follow an iterative procedure [77], and we will follow the description in Appendix B in Ref. [78] closely.

We consider a semi-infinite zigzag-edge graphene ribbon as shown in Fig. A.1. The ribbon is described by the Hamiltonian H_L and we are interested in the self-energy $\Sigma_L = H_{ML} g_L H_{LM}$, where the Greens function is $g_L = (E + i\eta - H_L)^{-1}$. The ribbon can be separated into unit cells with N atoms as shown in the figure, and the only part of g_L that appears in the self-energy is the surface Greens functions, $g_L^{\text{surface}} = g_{L,11}$, i.e. the part of the Greens function that belongs to the outermost unit cell 1. To obtain this, we can start by writing [78]

$$(E + i\eta - H_L) = \begin{pmatrix} d & -A & 0 & 0 & \\ -B & D & -A & 0 & \cdots \\ 0 & -B & D & -A & \\ & & \vdots & & \ddots \end{pmatrix} \quad (\text{A.31})$$

³In Eq. (A.3), we see that $\Gamma_L = -2 \text{Im} \Sigma_L = 2\pi H_{ML} \delta(E - H_L) H_{LM}$.

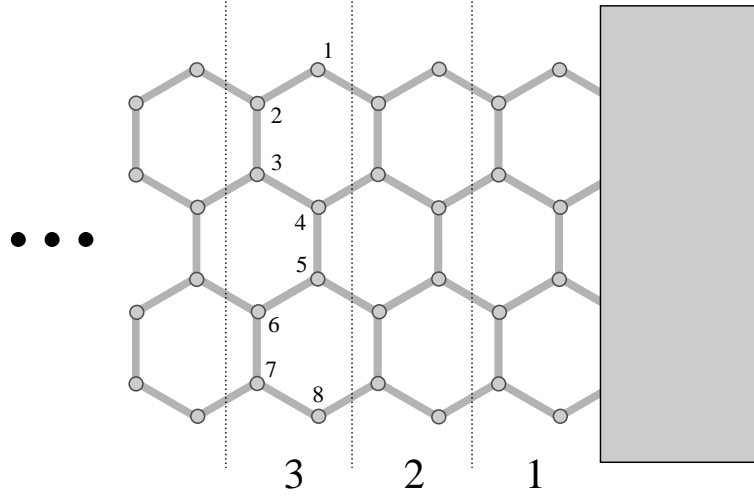


FIGURE A.1: Illustration of the semi-infinite graphene ribbon. The grey region represents the device/molecule described by H_M , while the ribbon continues infinitely to the left. The unit cells are numbered as shown below the ribbon.

where

$$B = -t \begin{pmatrix} 0 & 1 & 0 & 0 \\ 0 & 0 & 0 & 0 & \cdots \\ 0 & 0 & 0 & 0 \\ 0 & 0 & 1 & 0 \\ & \vdots & & \ddots \end{pmatrix} \quad (\text{A.32})$$

with the displayed block repeated down the diagonal and

$$D = \begin{pmatrix} E + i\eta & -t & 0 & & \\ -t & E + i\eta & -t & \cdots & \\ 0 & -t & E + i\eta & & \\ & & & \vdots & \ddots \end{pmatrix}. \quad (\text{A.33})$$

Additionally, $d = D$ and $A = B^T$. The introduced matrices have dimensions $(N \times N)$. For the right lead, $A_R = A_L^T$ and $B_R = B_L^T$. By considering the first column of

$$(E + i\eta - H_L)g_L = 1, \quad (\text{A.34})$$

we get

$$d g_{11} = 1 + A g_{21} \quad (\text{A.35})$$

$$D g_{n1} = B g_{n-1,1} + A g_{n+1,1}. \quad (\text{A.36})$$

These equations describe the connection between the Greens function from unit cell 1 to n and the Greens functions from 1 to neighbors of n . We can now eliminate all the Greens functions involving even n . By inserting g_{21} from Eq. (A.36) into Eq. (A.35), we get

$$d g_{11} = 1 + AD^{-1}(B g_{11} + A g_{31}), \quad (\text{A.37})$$

which can be rearranged to

$$(d - AD^{-1}B)g_{11} = 1 + AD^{-1}A g_{31}. \quad (\text{A.38})$$

We now have the connection between g_{11} and g_{31} . We can do the same to eliminate all the even n 's in Eq. (A.36)

$$\begin{aligned} D g_{2m+1,1} &= B g_{2m,1} + A g_{(2m+2),1} \\ &= BD^{-1} (B g_{2m-1,1} + A g_{2m+1,1}) + AD^{-1} (B g_{2m+1,1} + A g_{2m+3,1}) \end{aligned} \quad (\text{A.39})$$

and after rearranging

$$(D - BD^{-1}A - AD^{-1}B) g_{2m+1,1} = BD^{-1}B g_{2m-1,1} + AD^{-1}A g_{2m+3,1}. \quad (\text{A.40})$$

We therefore have

$$\begin{aligned} d_1 g_{11} &= 1 + A_1 g_{31} \\ D_1 g_{2m+1,1} &= B_1 g_{2m-1,1} + A_1 g_{2m+3,1} \end{aligned} \quad (\text{A.41})$$

with

$$\begin{aligned} d_1 &= d - AD^{-1}B \\ A_1 &= AD^{-1}A \\ B_1 &= BD^{-1}B \\ D_1 &= D - BD^{-1}A - AD^{-1}B \end{aligned} \quad (\text{A.42})$$

where the subscript 1 indicates that we have eliminated once. We can do it again to get $d_2 g_{11} = 1 + A_2 g_{51}$. If we continue iterating, we find that $A_n \approx 0$ for large n . After the iteration has converged, we have obtained the surface Greens function

$$g_{11} \approx d_n^{-1} \quad (\text{A.43})$$

for large n . To check whether the solution is correct, we can verify that

$$g_{11} = \frac{1}{E - H_{L,1} - A g_{11} B} \quad (\text{A.44})$$

where $H_{L,1}$ is the unit cell Hamiltonian.

Appendix B

Appendix to Chapter 4

B.1 BDT experiment: Heat conduction through air

We consider the model shown in Fig. B.1, where all the boxes are components characterized by Seebeck coefficients, thermal conductivities, and electric conductivities. The letter 's' refers to the sample, 'a' is the series connected parts, while 'b' and 'c' are air-components. The model includes the fact that the temperature and potential differences are not measured at the same points: The temperature is measured in the air which is marked by point 4 in Fig. B.1. We can write the measured Seebeck

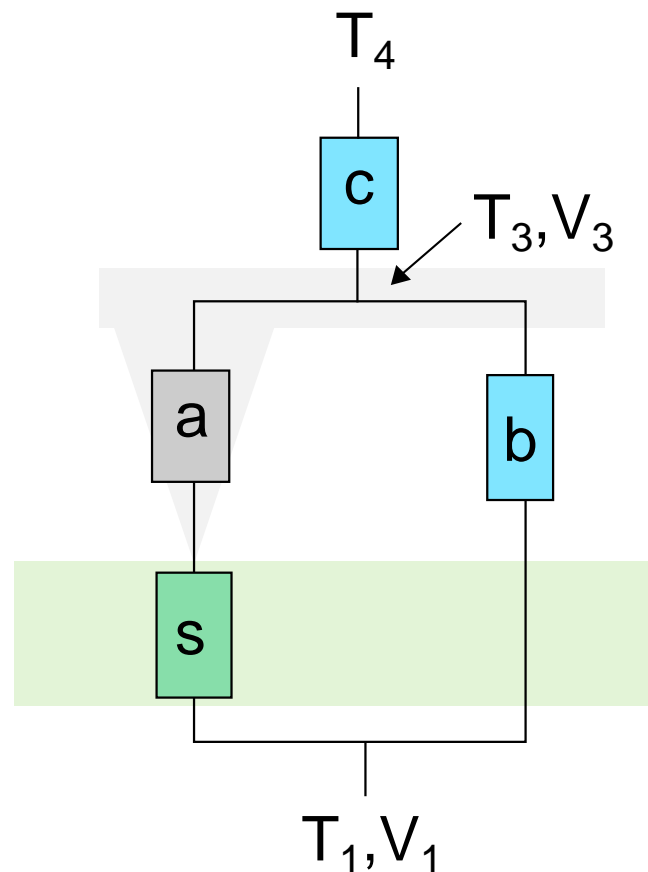


FIGURE B.1: A components model which takes into account the heat conduction by air. All the components have an associated R^q , S , and R . 's' refers to the sample, 'a' to the tip and cantilever, while 'b' and 'c' are air components.

coefficient as

$$\begin{aligned} S_{\text{measured}} &= -\frac{V_3 - V_1}{T_4 - T_1} \\ &= \frac{S_s \Delta T_s + S_a \Delta T_a}{T_4 - T_1}, \end{aligned} \quad (\text{B.1})$$

where ΔT_i is the temperature difference across component i . We used that the electric current is $I = G_i \Delta V_i + G_i S_i \Delta T_i = 0$ for $i = \{a, s\}$ so that $\Delta V_i = -S_i \Delta T_i$. Assuming that the heat current is mainly driven by the temperature gradient, the denominator of the above expression is

$$\begin{aligned} T_4 - T_1 &= I^q \left(R_{\text{parallel}}^q + R_c^q \right) \\ &= I^q \left(\frac{1}{\frac{1}{R_s^q + R_a^q} + \frac{1}{R_b^q}} + R_c^q \right) \\ &= I^q \left(\frac{(R_s^q + R_a^q) R_b^q}{R_s^q + R_a^q + R_b^q} + R_c^q \right), \end{aligned} \quad (\text{B.2})$$

where the R^q 's are thermal resistances and I^q is the heat current. In the numerator in Eq. (B.1), we will use $\Delta T_s = R_s^q I_a^q$ and $\Delta T_a = R_a^q I_a^q$

$$\begin{aligned} S_{\text{measured}} &= \frac{(S_s R_s^q + S_a R_a^q) I_a^q}{I^q \left(\frac{(R_s^q + R_a^q) R_b^q}{R_s^q + R_a^q + R_b^q} + R_c^q \right)} \\ &= \frac{S_s R_s^q + S_a R_a^q}{\frac{(R_s^q + R_a^q) R_b^q}{R_s^q + R_a^q + R_b^q} + R_c^q} \frac{R_b^q}{R_s^q + R_a^q + R_b^q} \\ &= \frac{S_s R_s^q + S_a R_a^q}{(R_s^q + R_a^q) R_b^q + (R_s^q + R_a^q + R_b^q) R_c^q} R_b^q \\ &= w_s S_s + w_a S_a, \end{aligned} \quad (\text{B.3})$$

where we used that $I_a^q = \frac{1}{R_s^q + R_a^q} \Delta T_b$ and $I_b^q = \frac{1}{R_b^q} \Delta T_b$ so that $I_a^q / I^q = \frac{I_a^q}{I_a^q + I_b^q} = \frac{R_b^q}{R_s^q + R_a^q + R_b^q}$. We have written the measured Seebeck coefficient as a weighed sum of the Seebeck components. Since metals have small Seebeck coefficients, the last term in Eq. (B.3) is small, and we are therefore mainly interested in the weight of the sample

$$w_s = \frac{R_b^q}{(R_s^q + R_a^q)(R_b^q + R_c^q) + R_b^q R_c^q} R_s^q. \quad (\text{B.4})$$

Using the simplification $R_s^q = \frac{d}{A_s \kappa_s}$, where d is the sample thickness, A_s is the sample area, and κ_s is the thermal conductivity of the sample, we can rewrite the weight as

$$\begin{aligned} w_s &= \frac{R_b^q}{R_b^q + R_c^q} \cdot \frac{R_s^q}{R_s^q + R_a^q + R_c^q \frac{R_b^q}{R_b^q + R_c^q}} \\ &= k \cdot \frac{R_s^q}{R_s^q + R_a^q + R_c^q k} \\ &\approx k \cdot \frac{d}{d + A_s \kappa_s (R_a^q + R_c^q k)}. \end{aligned} \quad (\text{B.5})$$

We therefore have

$$\boxed{w_s \approx k \frac{d}{d + \tilde{b}}} \quad (\text{B.6})$$

with

$$k = \frac{R_b^q}{R_b^q + R_c^q} = \frac{1}{1 + \frac{R_c^q}{R_b^q}} \quad (\text{B.7})$$

$$\tilde{b} = A_s \kappa_s (R_a^q + R_c^q k).$$

For $R_b^q \rightarrow \infty$, we arrive at our series result in Eq. (4.12), since $k \rightarrow 1$ and $\tilde{b} \rightarrow b$.

By putting together Eqs. (B.3) and (B.6), we get (neglecting the small Seebeck coefficient of the metallic connecting parts, $S_a \approx 0$)

$$S_{\text{measured}} = S_s \frac{k \cdot d}{d + \tilde{b}}. \quad (\text{B.8})$$

From the definition in Eq. (B.7), we see that $0 < k < 1$ so that the fraction in Eq. (B.8) is smaller than 1. Consequently, the actual Seebeck coefficient of the sample S_s can be larger than the measured one. k only depends on thermal transport through the air, which is independent of the thickness of the sample. In the specific BDT experiment, it has been measured by our collaborators at the UCAS in Beijing to be $k \approx 0.5$. We do not have enough knowledge about the specific experiment to describe it here, but the factor is used in the paper draft in Appendix C.

Appendix C

BDT paper draft

This appendix presents a paper draft, which includes the results from Chapter 4. The draft is written by Kasper Nørgaard and the author of this thesis. A lot of people contributed to the work described herein, most of whom work/studied at the Chinese Academy of Sciences in Beijing.

In this draft, the measured Seebeck coefficients are a factor of ≈ 2 larger than the ones presented in Chapter 4. The factor was experimentally obtained and it is due to the heat conduction through air as described in Sec. B.1. The paper is not published due to the challenges described in Sec. 4.3.

Thermopower of SAMS

...,[†] Jens Broe Rix,^{‡,¶} Kasper Nørgaard,[‡] Per Hedegård,^{*,‡} and ...[†]

[†]*Nano-Science Center, Chinese Academy of Sciences, Beijing, China*

[‡]*Nano-Science Center, University of Copenhagen, Universitetsparken 5, 2100 Copenhagen
Ø, Denmark*

[¶]*Sino-Danish Center for Education and Research, Beijing, China*

E-mail: hedegard@nbi.ku.dk

Phone: +45 3532 0435

Abstract

What has been done...

Ever since Thomas Seebeck's discovery of the thermoelectric effect almost 200 years ago, the electric response of a material to an applied temperature difference has captured the attention of scientist. The thermopower (or Seebeck coefficient) is the ratio of a measured induced voltage difference to an applied temperature difference, $S = -\Delta V/\Delta T = -(k_B/e)(e\Delta V)/(k_B\Delta T)$, and it has a scale given by $k_B/e = 86\mu\text{V}/\text{K}$. The Seebeck coefficient varies strongly for different materials: for metals S is typically a few $\mu\text{V}/\text{K}$, while for semiconductors the Seebeck coefficient is several hundred $\mu\text{V}/\text{K}$. These facts have been understood for a long time.

In recent time, experiments have been performed on nanoscale systems. Organic single molecule junctions typically show Seebeck coefficients of few tens of $\mu\text{V}/\text{K}$,¹⁻³ a value which is closer to that of metals, even though a molecule with its discrete electron spectrum is reminiscent of a semiconductor. This behavior is understood theoretically because electrons

have the possibility to tunnel across the molecule and the Seebeck coefficient is given by the variation of the tunnelling probability with energy: $S/(k_B/e) = \pi^2/3(k_B T) d \ln(\mathcal{T})/dE$. I.e. the same expression as that of a metal with the conductivity replaced by the tunnelling probability \mathcal{T} .⁴ When these molecules are put together into organic crystals, a valence band will be formed from the HOMOs (highest occupied molecular orbitals), a conduction band originates from the LUMOs, and so on. Similar to conventional semiconductors, these organic semiconductors show Seebeck coefficients of hundreds of $\mu\text{V}/\text{K}$.^{5,6} For a p-type semiconductor the Seebeck coefficient is given by⁷

$$S_{\text{sc}} = \frac{k_B}{e} \left(\frac{\mu - E_v}{k_B T} + A_v \right) \quad (1)$$

where μ is the chemical potential, E_v is the energy maximum of the valence band while A_v is a constant that depends on the density of states and the energy dependent mobility. For a n-type semiconductor where the chemical potential is closer to the conduction band, we would have E_c and A_c instead of E_v and A_v .

The crossover between small Seebeck coefficients in single molecules and large Seebeck coefficients in organic crystals is yet to be understood. The change in dimensionality is one effect that can influence the thermopower.⁸ In the transition from a 2D monolayer (or a few layers) to multi layered structures, band bending can affect the Seebeck coefficient which has been studied in different inorganic semiconductors.⁹⁻¹¹ In this work we study the thickness dependent Seebeck coefficient in organic semiconductors in the crossover from a few layers of SAMs (self assembled monolayers) to organic crystals.

We investigated the thermoelectric properties of a p-type single-crystal organic semiconductor, α,α -bis(dithieno[3,2-b:2,3-d]thiophene) (BDT),^{12,13} with thicknesses varying between 8 nm and 220 nm. This molecule, belonging to the large family of π -conjugated molecules, forms high-quality molecular crystals, which can be described as "stacks" of self-assembled monolayers (SAMs). This basic structure, combined with our ability to grow thin crystal

plates with different thicknesses d (see methods), makes BDT an ideal model system for studying the thickness dependence of the Seebeck coefficient $S(d)$ down to a thickness of 4-5 monolayers. The crystal structure of BDT (Figure 1a) reveals a completely coplanar conformation of the molecules with a unique π - π stacking along the b -axis. Single crystals of BDT were grown on a SiO_2/Si substrate via physical vapor deposition (PVD) and then mechanically transferred to a 70 nm thick Au substrate, which was deposited on a SiO_2/Si wafer. Transmission electron microscopy (TEM) was used to verify that the samples were indeed single crystals (See SI). The thin crystals could be visualized in an optical microscope and their thicknesses were established by atomic-force microscopy (AFM). The crystals were oriented with the c -axis perpendicular to the substrate.

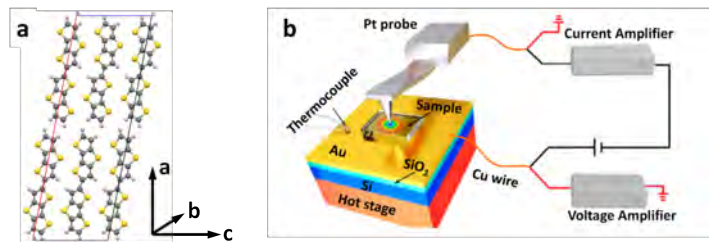


Figure 1: Lattice structure of BDT single crystals and experimental setup. a) Lattice structure of the BDT single crystal. The thermoelectric measurements are performed along the crystal c -axis. b) Schematic illustration of the experimental setup. The AFM was modified by connecting a current amplifier and a voltage amplifier between the Pt probe and the Au substrate using Cu wires. The sample located on the ~ 70 nm thick Au substrate was heated by the hot stage to a set temperature above ambient temperature during the thermoelectric measurements. I-V characteristics were also measured at the same sample location in contact mode.

We used a Scanning Thermoelectric Microscope (SThEM)^{14,15} to study the thermopower (S) and resistance (R) of the individual submicron thick BDT crystals. The experimental setup is illustrated in Figure 1b. This approach enabled a direct measurement of the nanoscale thermoelectric properties by measuring the thermoelectric voltage induced by contact between a room-temperature tip and a heated sample. We connected a current amplifier and a voltage amplifier to an atomic force microscope between the AFM tip (Pt) and

the Au substrate. The AFM worked in contact mode under ambient conditions. At each point of the measurement, the tip was brought into contact with the sample and reached thermal equilibrium. The current amplifier loop was connected to measure the I-V curve, and then disconnected while the thermoelectric voltage measurement loop was connected. The sample was heated by a thermostatic hot stage to 5K (10K, 15K, 20K) above room temperature, and a micro thermocouple (Omega[®] type-K) was mounted on the Au substrate by silver paste to monitor its temperature. As the room-temperature tip made contact with the heated sample, a temperature difference was created in the sample near the contact point. The thermoelectric voltage generated by the temperature difference was measured by the voltage amplifier.

The measured Seebeck coefficients are shown in Figure 2b. The positive values confirm that the BDT crystal is a p-type semiconductor¹² and we see a strong thickness dependence with values ranging from about $250\mu\text{V}/\text{K}$ for thin samples to about $800\mu\text{V}/\text{K}$ for thick ones. The Seebeck coefficient saturates for thick samples and the half-maximum is reached at around 40 nm. To understand this thickness dependence we consider two possible explanations: Thickness dependence of the temperature drop and band bending.

When the Seebeck coefficient of a setup is measured, the result is a weighted average of the components in the setup. How the components are weighted depends on the geometry of the setup. Consider for simplicity two components with different Seebeck coefficients S_1 and S_2 and thermal resistances $R_{q,1}$ and $R_{q,2}$. If these components are coupled in series the resulting Seebeck coefficient is

$$S_{\text{series}} = \frac{R_{q,1}S_1 + R_{q,2}S_2}{R_{q,1} + R_{q,2}} \quad (2)$$

We see that the Seebeck coefficient is a weighted average of the involved S 's with weight factors given by the materials' thermal resistances. If the components were instead parallel-coupled the weight factors would be given by the electrical conductances. In our experimental

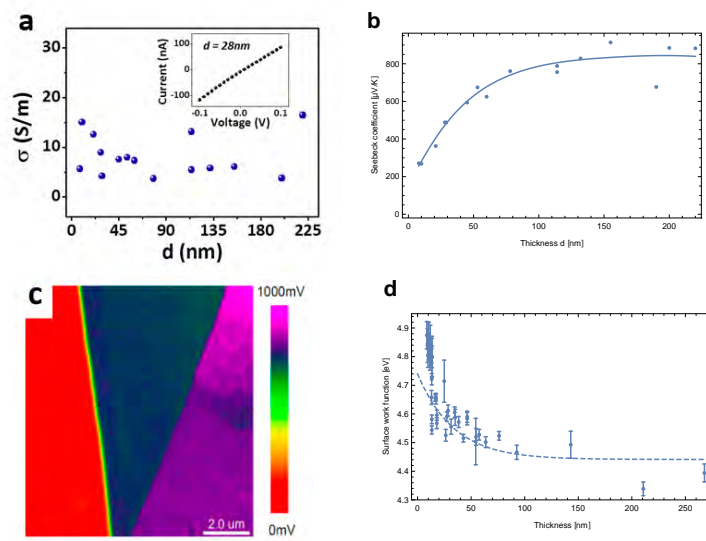


Figure 2: I-V characterizations and thermoelectric measurements. a) Electrical conductivity for each BDT single crystal with different thickness. Inset: I-V curve of the 28nm thick BDT crystal obtained by scanning the voltage between the Au substrate and the Pt probe. b) The measured Seebeck coefficients as a function of the BDT crystal thickness. The solid curve represents the best fit to a model including the band bending in the metal-semiconductor interface. c) Surface potential of a BDT single crystal on Au, measured by KPFM. d) The measured surface work function of BDT crystals as a function of sample thickness obtained from KPFM measurements. The dashed line uses the fitted Debye length from Figure 2b and represents the position dependent band bending in a thick sample.

setup (see Figure 1b) the measured Seebeck coefficient includes both the sample, the tip and the probe, and we can approximate it as a series connection between the sample and the Pt components. When the sample thickness goes to zero, the thermal resistance of the sample vanishes and according to eq. (2) the thermoelectric response will be from platinum only. For thick samples, the thermal resistance of the sample will dominate and the measured Seebeck coefficient will be that of the sample. Consequently this effect will give a thickness dependent Seebeck coefficient that starts out at a few $\mu\text{V}/\text{K}$ (the value for Pt) and then increases until it saturates at the Seebeck coefficient of the organic semiconductor in a similar fashion as observed in the experimental results in Figure 2b. However, due to the high thermal conductivity of Pt compared to that of an organic crystal, the characteristic length of this saturation curve is only expected to be around a few nanometers (see supporting information) and the effect can therefore not explain the experimental results. The effect is included when the data is fitted.

When the organic semiconductor is put into contact with the Au substrate there will be a transfer of charges between the materials. The accumulated charges will bend the bands of the semiconductor and consequently change its transport properties. The change in the Seebeck coefficient is readily seen from equation (1) where the edge of the valence band $E_v(\mathbf{r})$ now depends on the distance to the substrate. The surface work function in the vicinity of the Au-sample interface was measured using Kelvin Probe Force Microscopy (KPFM) and the results are shown in Figure 2c and 2d. This indicates that the bands bend with an energy shift around 0.3 eV and with the Debye length $\lambda_D \approx 50$ nm.

Consider for a moment the problem to be one-dimensional. If we take eq. (2) to the continuum limit and use that the thermal conductivity is not affected significantly by the band bending (the thermal transport in organic crystals is dominated by phonons), the Seebeck coefficient of the sample is $S_{\text{sample}} = \frac{1}{d} \int_0^d S(x) dx$. When the sample thickness d is comparable to the thickness of the space charge layer λ_D the measured Seebeck coefficient is affected by the band bending. For thick samples $d \gg \lambda_D$ the bulk value will dominate.

Consequently, this simple consideration illustrates that the measured Seebeck coefficient will vary for small thickness but saturate at some value larger than λ_D . However, in the actual experimental setup the variation is not 1-dimensional as stipulated in the above simple physical model. The STM tip defines a small nanosized contact around which the bands bend and we expect the electric potential and therefore the transport coefficients to vary in all 3 dimensions. Instead of using equation (2) we therefore have to use the finite element method (FEM) to calculate the electric potential and Seebeck coefficient.

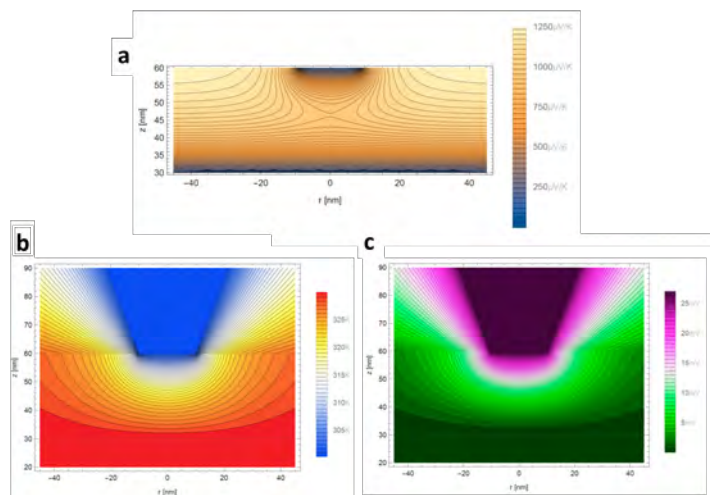


Figure 3: a) The calculated local Seebeck coefficient in a cross section of a 30 nm thick BDT sample. (b) and (c) show the calculated temperature and electric potential maps, respectively, when the setup is subject to a temperature difference $\Delta T = 30$ K and the condition that no net current passes through the setup. It is obtained by solving the coupled continuity equations as described in the text. Notice the grey lines that separates the Au substrate and the sample.

To model the band bending we use Poisson's equation. We assume that dopants such as oxygen are distributed uniformly as in other organic semiconductors^{16,17} and we end up with the differential equation $\nabla^2 f(\mathbf{r}) = \frac{e^2 n_d}{\epsilon k_B T} [e^{f(\mathbf{r})} - 1]$ where $f(\mathbf{r}) = (e\phi_{\text{bulk}} - e\phi(\mathbf{r})) / (k_B T)$. This equation is difficult to solve for the particular geometry and we therefore use the

$f(\mathbf{r}) \ll 1$ limit to model our system:

$$\nabla^2 \phi(\mathbf{r}) = \frac{1}{\lambda_D^2} [\phi(\mathbf{r}) - \phi_{\text{bulk}}] \quad (3)$$

where we have introduced the Debye length $\lambda_D = \sqrt{\epsilon k_B T / (e^2 n_d)}$. The system at hand is not in this limit, but the model will capture the correct behavior of the potential. We assume the work functions of Au and Pt to be equal so that the electric potential at the sample-tip and sample-substrate interfaces are the same $\phi_0 = \phi(\mathbf{r}_{\text{boundary}})$. The parameter ϕ_0 defines the boundary condition to eq. (3) and we solve the boundary value problem using the FEM. To simplify the calculation we have taken the setup to be cylindrically symmetric around the center of the tip. The spatial dependence of the valence band edge is

$$E_v(\mathbf{r}) = \varepsilon_v - e\phi(\mathbf{r}) \quad (4)$$

The local Seebeck coefficient is obtained from eq. (1) and it is shown for a 30 nm thick sample in Figure 3. Similarly the electric conductivity is $\sigma(\mathbf{r}) = \sigma_0 \exp[(\mu - E_v(\mathbf{r})) / (k_B T)]$. Using the FEM method again, we can obtain the total Seebeck coefficient by solving the coupled continuity equations $\nabla \cdot \mathbf{j}_e(\mathbf{r}) = 0$ and $\nabla \cdot \mathbf{j}_q(\mathbf{r}) = 0$ with the boundary conditions of a temperature difference and with the condition of zero electric through current (See supporting material). For the local Seebeck coefficients in Figure 3a we obtain the temperature and electric potential maps shown in Figures 3b and 3c. Similarly we can obtain the resistance by applying only a potential difference and calculating the responsive current.

The described procedure was done for all sample thicknesses and we ran an optimization to find the parameters $\mu - \varepsilon_v$, $\phi_{\text{bulk}} - \phi_0$, λ_D , and $R_{q,\text{Pt}}$ that fit the measured Seebeck coefficients in Figure 2b best. We obtained a Debye length of $\lambda_D \approx 33$ nm, $\phi_{\text{bulk}} - \phi_0 = 0.3$ V, while $R_{q,\text{Pt}}$ hit the minimum of our prior. In Figure 2b we see that the model fits the Seebeck measurements well. Additionally we have used the best-fit-parameters to plot the band bending profile of thick BDT sample. The result is shown as a dashed line in Figure

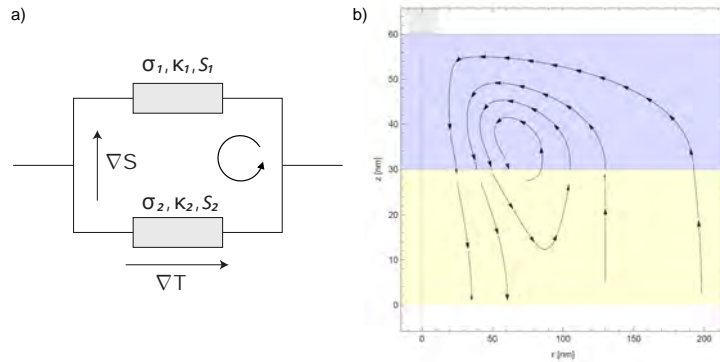


Figure 4: Current loops. Calculated electric current densities inside a 30 nm thick BDT crystal, in contact with a metallic substrate (bottom) and AFM tip (top left corner).

2d together with the KPFM data and we see an agreement in the length dependence and the energy shift. This strongly indicates that the characteristic length dependence of the Seebeck coefficient is due to the band bending.

The 3D geometry of the setup and the inhomogeneity caused by the band bending give rise to an interesting effect of internal electric current loops. The existence of circulating currents can be understood from the parallel coupled device shown in Figure 4a where temperature and potential differences are present so that no electric current flows through the setup. A resulting circulating current then exists¹⁸

$$I_c = \frac{S_1 - S_2}{R_1 + R_2} \Delta T. \quad (5)$$

This may seem surprising, but it was actually such currents Thomas Seebeck observed (using a compass needle) in 1821 when he first discovered the effect. Circulating currents have also been studied more recently.^{18,19} For an inhomogeneous material with varying transport parameters it can be shown that local circulating currents exist if $\nabla S \times \nabla T \neq 0$. Here, ∇S is the direction in which S varies locally and ∇T is the direction along which the temperature varies. A requirement for local currents is thus that these directions must not be parallel and this is, schematically, what happens for the parallel coupled materials in Figure 4a. For

the potential and temperature maps shown in Figures 3b and 3c we have calculated the local current densities using $\mathbf{j}_e = -\sigma\nabla V - \sigma S\nabla T$. The result in Figure 4b shows the circulating electric currents in a 30 nm thick sample. Notice that current enters and leaves the sample but just as in the experiment there is no total current flowing through the setup.

In conclusion, we measured significant variations in the thermopower of thin single crystals of a *p*-type organic semiconductor using an AFM-based method. The observed Seebeck coefficients ranged between $250\mu\text{V}/\text{K}$ for very thin crystals and $800\mu\text{V}/\text{K}$ for thicker crystals. The variations were observed at the same length scale as that of the band bending, and we demonstrated that the thickness dependent Seebeck coefficient is in fact caused by the band bending. Additionally we noticed theoretically that electric circulating currents exist in the setup when measuring the Seebeck coefficient. This is contrary to the usual assumption of zero currents and it is due to the 3D geometry and inhomogeneity of the setup.

Methods

Organic single crystals of α,α -bis(dithieno[3,2-b:2,3-d]thiophene) (BDT) were fabricated by physical vapour deposition on a SiO_2/Si substrate. The BDT single crystal was grown at 180°C for 5-7 hours, under an argon flow (0.04 L/min), yielding thin BDT crystal plates with a thicknesses ranging from about 8nm to 220nm. The molecular crystals were chemically stable at room temperature. For electric and thermopower measurements, the thin BDT plates were mechanically transferred from the silicon wafer to the target Au/Si substrate. Au thin films (about 320 nm) were prepared by electron vapour deposition on Si substrates, using the template stripping approach.²⁰ The Au films were cut freshly as needed.

The experimental setup is shown schematically in Figure 1b. To acquire the current-voltage (I-V) characteristics and thermoelectric voltage, we modified a commercially available atomic force microscope (AFM, Bruker Dimension Icon) by connecting a current amplifier (Keithley 6430 Sourcemeter) and a voltage amplifier (a home-made 1000 times voltage pre-amplifier and Keithley 2182A Nanovoltmeter) between the pure Pt tip (Bruker RMN-

12PT400B) and Au substrate. In an ambient environment, the AFM worked in contact mode. At each point of the measurement, the tip was brought into contact with the sample and reached thermal equilibrium. The current amplifier loop was connected to measure the I-V curve, and then disconnected while the thermoelectric voltage measurement loop was connected. The sample was heated by a thermostatic hot stage to 5K (10K, 15K, 20K) above room temperature, and a micro thermocouple (Omega type-K) was mounted on the Au substrate by silver paste to monitor its temperature. The thermoelectric voltage generated by the temperature difference was measured by the voltage amplifier.

References

- (1) Reddy, P.; Jang, S.-Y.; Segalman, R. a.; Majumdar, A. *Science (New York, N.Y.)* **2007**, *315*, 1568–1571.
- (2) Baheti, K.; Malen, J. A.; Doak, P.; Reddy, P.; Jang, S. Y.; Tilley, T. D.; Majumdar, A.; Segalman, R. A. *Nano Letters* **2008**, *8*, 715–719.
- (3) Widawsky, J. R.; Darancet, P.; Neaton, J. B.; Venkataraman, L. *Nano Letters* **2012**, *12*, 354–358.
- (4) Cutler, M.; Mott, N. F. *Physical Review* **1969**, *181*, 1336–1340.
- (5) Pernstich, K. P.; Rössner, B.; Batlogg, B. *Nature materials* **2008**, *7*, 321–5.
- (6) Zhang, F.; Zang, Y.; Huang, D.; Di, C.-a.; Gao, X.; Sirringhaus, H.; Zhu, D. *Advanced Functional Materials* **2015**, n/a–n/a.
- (7) Fritzsche, H. *Solid State Communications* **1971**, *9*, 1813–1815.
- (8) Kim, R.; Datta, S.; Lundstrom, M. S. *Journal of Applied Physics* **2009**, *105*.
- (9) Rogacheva, E. I.; Nashchekina, O. N.; Vekhov, Y. O.; Dresselhaus, M. S. *International Conference on Thermoelectrics, ICT, Proceedings* **2005**, *2003-Janua*, 346–349.

-
- (10) Pettes, M. T.; Maassen, J.; Jo, I.; Lundstrom, M. S.; Shi, L. *Nano Letters* **2013**, *13*, 5316–5322.
- (11) Kayyalha, M.; Maassen, J.; Lundstrom, M.; Shi, L.; Chen, Y. P. *Journal of Applied Physics* **2016**, *120*.
- (12) Siringhaus, H.; Friend, R. H.; Li, X. C.; Moratti, S. C.; Holmes, A. B.; Feeder, N. *Applied Physics Letters* **1997**, *71*, 3871.
- (13) Zhang, L.; Tan, L.; Hu, W.; Wang, Z. *J. Mater. Chem.* **2009**, *19*, 8216–8222.
- (14) Lyeo, H.-K.; Khajetoorians, A. A.; Shi, L.; Pipe, K. P.; Ram, R. J.; Shakouri, A.; Shih, C. K. *Science* **2004**, *303*, 816–818.
- (15) Walrath, J. C.; Lin, Y. H.; Pipe, K. P.; Goldman, R. S. *Applied Physics Letters* **2013**, *103*, 212101.
- (16) Van Faassen, E.; Kerp, H. *Sensors and Actuators, B: Chemical* **2003**, *88*, 329–333.
- (17) Nayak, P. K.; Rosenberg, R.; Barnea-Nehoshtan, L.; Cahen, D. *Organic Electronics: physics, materials, applications* **2013**, *14*, 966–972.
- (18) Apertet, Y.; Ouerdane, H.; Goupil, C.; Lecoeur, P. *Physical Review B - Condensed Matter and Materials Physics* **2012**, *85*, 1–3.
- (19) Fu, D.; Levander, A. X.; Zhang, R.; Ager, J. W.; Wu, J. *Physical Review B - Condensed Matter and Materials Physics* **2011**, *84*, 1–6.
- (20) Weiss, E. A.; Kaufman, G. K.; Kriebel, J. K.; Li, Z.; Schalek, R.; Whitesides, G. M. *Langmuir* **2007**, *23*, 9686–9694.

Appendix D

Appendix to Chapter 6

D.1 Equations of motion

The spin action was found in Eq. (6.24) to be

$$\mathcal{S}[a] - \mathcal{S}[b] + \Delta\mathcal{S} = S \sum_{n=1,2} \int_0^{t_f} dt \left\{ \mathbf{B}_{\text{eff},n} \cdot \boldsymbol{\zeta}_n + \dot{\phi}_n^+ \cos \theta_n^+ - \dot{\phi}_n^- \cos \theta_n^- \right\} \quad (\text{D.1})$$

where $\boldsymbol{\zeta}_n = \mathbf{n}_n^+ - \mathbf{n}_n^-$ and where we introduced the effective magnetic field, which can include contributions from the electrons as shown in Eq. (6.45). The subscript n is the spin index, while the superscripts $+$ and $-$ indicate the forward and backward path, a and b , respectively. Let us introduce the average and difference angles

$$\begin{aligned} \theta_n &= \frac{1}{2} [\theta_n^+ + \theta_n^-] \\ \xi_{n\theta} &= \theta_n^+ - \theta_n^-, \end{aligned} \quad (\text{D.2})$$

so that $\theta_n^\pm = \theta_n \pm \frac{1}{2} \xi_{n\theta}$ and the same for ϕ . We will now assume that the most dominant contributions to $e^{i(\mathcal{S}[a] - \mathcal{S}[b] + \Delta\mathcal{S}[a,b])/\hbar}$ come from the histories where the paths a and b are close. As explained in Sec. 6.2.3, this is ensured by the influence functional, which couples the forward and backward paths and suppresses large differences between the two. The difference angles are therefore small, and we can expand the actions to first order in $\xi_{n\theta}$ and $\xi_{n\phi}$. We get

$$\begin{aligned} \boldsymbol{\zeta}_n &\approx \left. \frac{\partial(\mathbf{n}_n^+ - \mathbf{n}_n^-)}{\partial \xi_{n\theta}} \right|_{\xi=0} \xi_{n\theta} + \left. \frac{\partial(\mathbf{n}_n^+ - \mathbf{n}_n^-)}{\partial \xi_{n\phi}} \right|_{\xi=0} \xi_{n\phi} \\ &= \frac{\partial \mathbf{n}_n}{\partial \theta_n} \xi_{n\theta} + \frac{\partial \mathbf{n}_n}{\partial \phi_n} \xi_{n\phi} \\ &= \hat{\theta}_n \xi_{n\theta} + \hat{\phi}_n \sin(\theta_n) \xi_{n\phi}, \end{aligned} \quad (\text{D.3})$$

where it was used that in spherical polar coordinates $d\boldsymbol{\rho} = d\rho \hat{\rho} + \rho d\theta \hat{\theta} + \rho \sin \theta d\phi \hat{\phi}$. The introduced \mathbf{n}_n is described by the average angles θ_n and ϕ_n . The effective magnetic field in Eq. (6.45) depends on $\mathbf{Q}_n = (\mathbf{n}_n^+ + \mathbf{n}_n^-)/2$, which, to first order in the difference angles, is

$$\mathbf{Q}_n \approx \mathbf{n}_n. \quad (\text{D.4})$$

Finally, the last two terms in Eq. (D.1) are

$$\begin{aligned} & \left[\dot{\phi}_n \pm \frac{1}{2} \dot{\xi}_{n\phi} \right] \cos \left(\theta_n \pm \frac{1}{2} \xi_{n\theta} \right) \\ & \approx \left[\dot{\phi}_n \pm \frac{1}{2} \dot{\xi}_{n\phi} \right] \left[\cos \theta_n \mp \frac{1}{2} \sin(\theta_n) \xi_{n\theta} \right] \\ & = \dot{\phi}_n \cos \theta_n \pm \frac{1}{2} \left[\cos(\theta_n) \dot{\xi}_{n\phi} - \dot{\phi}_n \sin(\theta_n) \xi_{n\theta} \right] - \frac{1}{4} \dot{\xi}_{n\phi} \sin(\theta_n) \xi_{n\theta}. \end{aligned} \quad (\text{D.5})$$

Putting this together, we can write Eq. (D.1) as

$$\begin{aligned} & \mathcal{S}[a] - \mathcal{S}[b] \\ & = S \int_0^{t_f} dt \left\{ \sum_n [B_{\text{eff},n\theta} \xi_{n\theta} + B_{\text{eff},n\phi} \sin(\theta_n) \xi_{n\phi}] + \sum_n \left[\cos \theta_n \dot{\xi}_{n\phi} - \dot{\phi}_n \sin(\theta_n) \xi_{n\theta} \right] \right\} \\ & = S \int_0^{t_f} dt \sum_n \left\{ [B_{\text{eff},n\theta} - \dot{\phi}_n \sin \theta_n] \xi_{n\theta} + \sin \theta_n [B_{\text{eff},n\phi} + \dot{\theta}_n] \xi_{n\phi} \right\} + S \sum_n [\cos(\theta_n) \xi_{n\phi}]_0^{t_f}, \end{aligned} \quad (\text{D.6})$$

where integration by parts was used from the first to second line. The boundary terms, $[\cos(\theta_n) \xi_{n\phi}]_0^{t_f}$, are not important and mathematically they can be taken out in front of Eq. (6.17) and included in the normalization factor [143]. A more physical argument is that we are looking for an equation of motion for the spins. There can be some time-non-local torques in this equation, i.e. the spins are affected by the spin trajectories in the near past, but the spin orientations in the far past or future should not affect the motion. The boundary terms in the above equations can therefore not play an important role.

When integrating $e^{i(\mathcal{S}[a]-\mathcal{S}[b])/h}$ over the phase space, we can choose to integrate over the average and difference angles. Integration over the difference angles only give contributions when the square brackets in front of $\xi_{n\theta}$ and $\xi_{n\phi}$ in Eq. (D.6) are zero. Consequently,

$$\begin{aligned} \dot{\theta}_n & = -B_{\text{eff},n\phi} \\ \dot{\phi}_n \sin(\theta_n) & = B_{\text{eff},n\theta} \end{aligned} \quad (\text{D.7})$$

for both $n = 1$ and $n = 2$. This is just the angle components of the Bloch equation

$$\dot{\mathbf{n}}_n = -\mathbf{B}_{\text{eff},n} \times \mathbf{n}_n, \quad (\text{D.8})$$

which can be seen from the fact that $\mathbf{n} = \hat{\rho}$ and that the time derivative of an arbitrary vector \mathbf{A} in spherical polar coordinates is

$$\begin{aligned} \dot{\mathbf{A}} & = \hat{\rho} \left(\dot{A}_\rho - A_\theta \dot{\theta} - A_\phi \dot{\phi} \sin \theta \right) + \hat{\theta} \left(\dot{A}_\theta + A_\rho \dot{\theta} - A_\phi \dot{\phi} \cos \theta \right) \\ & \quad + \hat{\phi} \left(\dot{A}_\phi + A_\rho \dot{\phi} \sin \theta + A_\theta \dot{\phi} \cos \theta \right). \end{aligned} \quad (\text{D.9})$$

With this, we have shown that the average vectors, \mathbf{n}_n , follow the classical path.

D.2 Constructing the functional integral

We can write Eq. (6.18) as a coherent state functional integral by splitting the time evolution operators into small time steps and inserting unit operators as defined in

Eq. (6.10). To illustrate the procedure, we split it into 6 steps (with inspiration from Refs. [140, 145])

$$\begin{aligned}
& \text{Tr}_e \left[U^\dagger(b)U(a) \hat{\rho}_e(0) \right] \\
&= \int d(\bar{\eta}, \eta) e^{-\sum_{i=1}^6 \sum_{\mathbf{k}\sigma} \bar{\eta}_{\mathbf{k}\sigma}^i \eta_{\mathbf{k}\sigma}^i} \langle \eta^6 | e^{iH_e(b(t_6))\Delta t} | \eta^5 \rangle \langle \eta^5 | e^{iH_e(b(t_5))\Delta t} | \eta^4 \rangle \\
&\quad \times \langle \eta^4 | 1 | \eta^3 \rangle \langle \eta^3 | e^{-iH_e(a(t_3))\Delta t} | \eta^2 \rangle \langle \eta^2 | e^{-iH_e(a(t_2))\Delta t} | \eta^1 \rangle \langle \eta^1 | \rho_e(0) | -\eta^6 \rangle,
\end{aligned} \tag{D.10}$$

where we used that the trace can be written as in Eq. (6.11). Just as for the spin coherent states, the superscripts are time indices. All the Grassmann numbers are integrated over, i.e. $d(\bar{\eta}, \eta) = \prod_i \prod_{\mathbf{k}\sigma} d\bar{\eta}_{\mathbf{k}\sigma}^i d\eta_{\mathbf{k}\sigma}^i$. The different elements in Eq. (D.10) can be rewritten by using the properties of the coherent states. We will start with an element of the time evolution operator

$$\begin{aligned}
& \langle \eta^i | e^{-iH_e(t_i - t_{i-1})} | \eta^{i-1} \rangle \\
&\approx \langle \eta^i | \eta^{i-1} \rangle - i(t_i - t_{i-1}) \langle \eta^i | H_e(c^\dagger, c) | \eta^{i-1} \rangle \\
&= e^{\sum_{\mathbf{k}\sigma} \bar{\eta}_{\mathbf{k}\sigma}^i \eta_{\mathbf{k}\sigma}^{i-1}} (1 - i(t_i - t_{i-1}) H_e(\bar{\eta}^i, \eta^{i-1})) \\
&\approx \exp \left(\sum_{\mathbf{k}\sigma} \bar{\eta}_{\mathbf{k}\sigma}^i \eta_{\mathbf{k}\sigma}^{i-1} - i(t_i - t_{i-1}) H_e(\bar{\eta}^i, \eta^{i-1}) \right) \\
&= \exp \left(\sum_{\mathbf{k}\sigma} \bar{\eta}_{\mathbf{k}\sigma}^i \eta_{\mathbf{k}\sigma}^{i-1} - i(t_i - t_{i-1}) \sum_{\mathbf{k}\sigma} \sum_{\mathbf{k}'\sigma'} \bar{\eta}_{\mathbf{k}\sigma}^i \left[\varepsilon_{\mathbf{k}} \delta_{\mathbf{k},\mathbf{k}'} \delta_{\sigma,\sigma'} - V_{\mathbf{k}\sigma,\mathbf{k}'\sigma'}^{\lambda_i} \right] \eta_{\mathbf{k}'\sigma'}^{i-1} \right)
\end{aligned} \tag{D.11}$$

where Eq. (6.9) was used in the first step and where $\lambda_i = +1$ ($\lambda_i = -1$) when t_i is on the forward (backward) time path. We have used the notation

$$\begin{aligned}
\langle a(t) | H_{\text{int}} | a(t) \rangle &= -sJ_0 \sum_n \mathbf{n}_n^+(t) \cdot \mathbf{s}(\mathbf{R}_n) \\
&= -\frac{sJ_0}{2\mathcal{V}} \sum_{\mathbf{k}\sigma} \sum_{\mathbf{k}'\sigma'} \sum_{n=1,2} e^{-i(\mathbf{k}-\mathbf{k}') \cdot \mathbf{R}_n} \mathbf{n}_n^+(t) \cdot \boldsymbol{\sigma}_{\sigma\sigma'} c_{\mathbf{k}\sigma}^\dagger c_{\mathbf{k}'\sigma'} \\
&= -\sum_{\mathbf{k}\sigma} \sum_{\mathbf{k}'\sigma'} c_{\mathbf{k}\sigma}^\dagger V_{\mathbf{k}\sigma,\mathbf{k}'\sigma'}^+(t) c_{\mathbf{k}'\sigma'}
\end{aligned} \tag{D.12}$$

and the same for b and “ $-$ ” (minus superscript). The introduced V is therefore

$$V_{\mathbf{k}\sigma,\mathbf{k}'\sigma'}^\pm(t) = \frac{sJ_0}{2\mathcal{V}} \sum_{n=1,2} e^{-i(\mathbf{k}-\mathbf{k}') \cdot \mathbf{R}_n} \mathbf{n}_n^\pm(t) \cdot \boldsymbol{\sigma}_{\sigma\sigma'}. \tag{D.13}$$

The density matrix of the electronic system is defined in Eq. (6.26). The element of $\rho_e(0)$ is

$$\begin{aligned}
\langle \eta^1 | \rho_e(0) | -\eta^N \rangle &= \frac{1}{Z} \langle \eta^1 | e^{-\beta \sum_{\mathbf{k}\sigma} (\varepsilon_{\mathbf{k}-\Delta\mathbf{k}-\mu}) c_{\mathbf{k}\sigma}^\dagger c_{\mathbf{k}\sigma}} | -\eta^N \rangle \\
&= \frac{1}{Z} \prod_{\mathbf{k}\sigma} \prod_{\mathbf{k}'\sigma'} \prod_{\mathbf{k}''\sigma''} \langle 0 | (1 - c_{\mathbf{k}\sigma} \bar{\eta}_{\mathbf{k}\sigma}^1) e^{-\beta (\varepsilon_{\mathbf{k}'-\Delta\mathbf{k}-\mu}) c_{\mathbf{k}'\sigma'}^\dagger c_{\mathbf{k}'\sigma'}} (1 + \eta_{\mathbf{k}''\sigma''}^N c_{\mathbf{k}''\sigma''}^\dagger) | 0 \rangle \\
&= \frac{1}{Z} \prod_{\mathbf{k}\sigma} \langle 0 | (1 - c_{\mathbf{k}\sigma} \bar{\eta}_{\mathbf{k}\sigma}^1) e^{-\beta (\varepsilon_{\mathbf{k}-\Delta\mathbf{k}-\mu}) c_{\mathbf{k}\sigma}^\dagger c_{\mathbf{k}\sigma}} (1 + \eta_{\mathbf{k}\sigma}^N c_{\mathbf{k}\sigma}^\dagger) | 0 \rangle \\
&= \frac{1}{Z} \prod_{\mathbf{k}\sigma} \left[\langle 0 | e^{-\beta (\varepsilon_{\mathbf{k}-\Delta\mathbf{k}-\mu}) c_{\mathbf{k}\sigma}^\dagger c_{\mathbf{k}\sigma}} | 0 \rangle - \bar{\eta}_{\mathbf{k}\sigma}^1 \eta_{\mathbf{k}\sigma}^N \langle 0 | c_{\mathbf{k}\sigma} e^{-\beta (\varepsilon_{\mathbf{k}-\Delta\mathbf{k}-\mu}) c_{\mathbf{k}\sigma}^\dagger c_{\mathbf{k}\sigma}} c_{\mathbf{k}\sigma}^\dagger | 0 \rangle \right] \\
&= \frac{1}{Z} \prod_{\mathbf{k}\sigma} \left[1 - \bar{\eta}_{\mathbf{k}\sigma}^1 \eta_{\mathbf{k}\sigma}^N e^{-\beta (\varepsilon_{\mathbf{k}-\Delta\mathbf{k}-\mu})} \right] \\
&= \frac{1}{Z} \exp \left\{ - \sum_{\mathbf{k}\sigma} \bar{\eta}_{\mathbf{k}\sigma}^1 \eta_{\mathbf{k}\sigma}^N e^{-\beta (\varepsilon_{\mathbf{k}-\Delta\mathbf{k}-\mu})} \right\},
\end{aligned} \tag{D.14}$$

where we used the definitions of the coherent states, $|\eta\rangle = \prod_{\mathbf{k}\sigma} (1 - \eta_{\mathbf{k}\sigma} c_{\mathbf{k}\sigma}^\dagger) |0\rangle$ and $\langle \eta| = \prod_{\mathbf{k}\sigma} \langle 0| (1 - c_{\mathbf{k}\sigma} \bar{\eta}_{\mathbf{k}\sigma})$. Inserting Eqs. (D.11) and (D.14) into Eq. (D.10), we can write the influence functional as

$$F[a, b] = \frac{1}{Z} \int \mathcal{D}(\bar{\eta}, \eta) \exp \left[i \sum_{ij} \sum_{\mathbf{k}\sigma} \sum_{\mathbf{k}'\sigma'} \bar{\eta}_{\mathbf{k}\sigma}^i \left((G_{0,\mathbf{k}}^{-1})^{ij} \delta_{\mathbf{k},\mathbf{k}'} \delta_{\sigma,\sigma'} + \tilde{V}_{\mathbf{k}\sigma,\mathbf{k}'\sigma'}^{ij} \right) \eta_{\mathbf{k}'\sigma'}^j \right]. \tag{D.15}$$

Here the interaction part is

$$\tilde{V}_{\mathbf{k}\sigma,\mathbf{k}'\sigma'}^{ij} = \lambda_i \Delta t V_{\mathbf{k}\sigma,\mathbf{k}'\sigma'}^{\lambda_i}(t_i) \delta_{i,j+1} \tag{D.16}$$

where λ_i is defined below Eq. (D.11), while $V_{\mathbf{k}\sigma,\mathbf{k}'\sigma'}^{\lambda_i}$ is defined in Eq. (D.13). The reason for the λ_i in front of the above expression is that $(t_i - t_{i-1})$ in Eq. (D.11) takes different signs on the forward and backward paths. The introduced inverse Greens function is diagonal in \mathbf{k} and independent of σ

$$iG_{0,\mathbf{k}}^{-1} = \left(\begin{array}{ccc|ccc} & -1 & & & & -e^{-\beta(\varepsilon_{\mathbf{k}-\Delta\mathbf{k}-\mu})} \\ & 1 - i\varepsilon_{\mathbf{k}}\Delta t & -1 & & & \\ & & 1 - i\varepsilon_{\mathbf{k}}\Delta t & -1 & & \\ & & & \ddots & \ddots & \\ & & & & 1 & \\ \hline & & & & \ddots & \\ & & & & \ddots & \\ & & & & -1 & \\ & & & & 1 + i\varepsilon_{\mathbf{k}}\Delta t & -1 \\ & & & & & 1 + i\varepsilon_{\mathbf{k}}\Delta t & -1 \\ & & & & & & -1 \end{array} \right). \tag{D.17}$$

Taking the inverse of the above matrix and taking it to the continuum limit, one gets (see Ref. [145])

$$G_{0,\mathbf{k}}(t, t') = ie^{-i\varepsilon_{\mathbf{k}}(t-t')} \begin{pmatrix} n_F(\varepsilon_{\mathbf{k}-\Delta\mathbf{k}} - \mu) - \theta(t-t') & n_F(\varepsilon_{\mathbf{k}-\Delta\mathbf{k}} - \mu) \\ n_F(\varepsilon_{\mathbf{k}-\Delta\mathbf{k}} - \mu) - 1 & n_F(\varepsilon_{\mathbf{k}-\Delta\mathbf{k}} - \mu) - \theta(t' - t), \end{pmatrix} \quad (\text{D.18})$$

where $n_F(\varepsilon)$ is the Fermi function and $\theta(t)$ is the Heaviside step function. The upper left element in Eq. (D.18) is the Greens function on the forward time path, the upper right is the Greens function when t' (t) is on the backward (forward) time path and so on.

D.3 Rewriting $\text{Tr}[G_0 \tilde{V} G_0 \tilde{V}]$

We will start by performing the trace in Eq. (6.32). The Greens function is defined in Eq. (6.29) and \tilde{V} is defined above Eq. (6.28). We get

$$\begin{aligned} -\frac{1}{2} \text{Tr}[G_0 \tilde{V} G_0 \tilde{V}] &= -\frac{\Delta t^2}{2} \sum_{\mathbf{k}\sigma} \sum_{\mathbf{k}'\sigma'} \sum_{ij} \lambda_i \lambda_j G_{0,\mathbf{k}}^{i-1,j} \tilde{V}_{\mathbf{k}\sigma,\mathbf{k}'\sigma'}^{\lambda_j}(t_j) G_{0,\mathbf{k}'}^{j-1,i} \tilde{V}_{\mathbf{k}'\sigma',\mathbf{k}\sigma}^{\lambda_i}(t_i) \\ &\approx -\frac{1}{2} \sum_{\mathbf{k}\sigma} \sum_{\mathbf{k}'\sigma'} \sum_{\lambda\lambda'} (-1)^{\lambda-\lambda'} \int_0^{t_f} dt \int_0^{t_f} dt' G_{0,\mathbf{k}}^{\lambda\lambda'}(t, t') V_{\mathbf{k}\sigma,\mathbf{k}'\sigma'}^{\lambda'}(t') G_{0,\mathbf{k}'}^{\lambda'\lambda}(t', t) V_{\mathbf{k}'\sigma',\mathbf{k}\sigma}^{\lambda}(t) \\ &= -\frac{S^2 J_0^2}{8\mathcal{V}^2} \sum_{\mathbf{k}\sigma} \sum_{\mathbf{k}'\sigma'} \sum_{nm} e^{-i(\mathbf{k}-\mathbf{k}')\cdot(\mathbf{R}_n-\mathbf{R}_m)} \sum_{\lambda\lambda'} (-1)^{\lambda-\lambda'} \\ &\quad \times \int_0^{t_f} dt \int_0^{t_f} dt' G_{0,\mathbf{k}}^{\lambda\lambda'}(t, t') \mathbf{n}_n^{\lambda'}(t') \cdot \boldsymbol{\sigma}_{\sigma\sigma'} G_{0,\mathbf{k}'}^{\lambda'\lambda}(t', t) \mathbf{n}_m^{\lambda}(t) \cdot \boldsymbol{\sigma}_{\sigma'\sigma} \\ &= -\frac{S^2 J_0^2}{4\mathcal{V}^2} \sum_{\mathbf{k}\mathbf{k}'} \sum_{nm} e^{-i(\mathbf{k}-\mathbf{k}')\cdot(\mathbf{R}_n-\mathbf{R}_m)} \sum_{\lambda\lambda'} (-1)^{\lambda-\lambda'} \\ &\quad \times \int_0^{t_f} dt \int_0^{t_f} dt' G_{0,\mathbf{k}}^{\lambda\lambda'}(t, t') G_{0,\mathbf{k}'}^{\lambda'\lambda}(t', t) \mathbf{n}_n^{\lambda'}(t') \cdot \mathbf{n}_m^{\lambda}(t) \\ &= -\frac{S^2 J_0^2}{4\mathcal{V}^2} \sum_{\mathbf{k}\mathbf{k}'} \sum_{nm} e^{-i(\mathbf{k}-\mathbf{k}')\cdot(\mathbf{R}_n-\mathbf{R}_m)} \int_0^{t_f} dt \int_0^{t_f} dt' \left\{ G_{0,\mathbf{k}}^{++}(t, t') G_{0,\mathbf{k}'}^{++}(t', t) \mathbf{n}_n^+(t') \cdot \mathbf{n}_m^+(t) \right. \\ &\quad \left. + G_{0,\mathbf{k}}^{--}(t, t') G_{0,\mathbf{k}'}^{--}(t', t) \mathbf{n}_n^-(t') \cdot \mathbf{n}_m^-(t) - G_{0,\mathbf{k}}^{+-}(t, t') G_{0,\mathbf{k}'}^{-+}(t', t) \mathbf{n}_n^-(t') \cdot \mathbf{n}_m^+(t) \right. \\ &\quad \left. - G_{0,\mathbf{k}}^{-+}(t, t') G_{0,\mathbf{k}'}^{+-}(t', t) \mathbf{n}_n^+(t') \cdot \mathbf{n}_m^-(t) \right\} \\ &= \frac{S^2 J_0^2}{4\mathcal{V}^2} \sum_{\mathbf{k}\mathbf{k}'} \sum_{nm} e^{-i(\mathbf{k}-\mathbf{k}')\cdot(\mathbf{R}_n-\mathbf{R}_m)} \int_0^{t_f} dt \int_0^{t_f} dt' e^{-i(\varepsilon_{\mathbf{k}}-\varepsilon_{\mathbf{k}'})(t-t')} \\ &\quad \times \left\{ [n_F(\varepsilon_{\mathbf{k}-\Delta\mathbf{k}} - \mu) - \theta(t-t')] [n_F(\varepsilon_{\mathbf{k}'-\Delta\mathbf{k}} - \mu) - \theta(t'-t)] \mathbf{n}_n^+(t') \cdot \mathbf{n}_m^+(t) \right. \\ &\quad \left. + [n_F(\varepsilon_{\mathbf{k}-\Delta\mathbf{k}} - \mu) - \theta(t'-t)] [n_F(\varepsilon_{\mathbf{k}'-\Delta\mathbf{k}} - \mu) - \theta(t-t')] \mathbf{n}_n^-(t') \cdot \mathbf{n}_m^-(t) \right. \\ &\quad \left. + n_F(\varepsilon_{\mathbf{k}-\Delta\mathbf{k}} - \mu) [1 - n_F(\varepsilon_{\mathbf{k}'-\Delta\mathbf{k}} - \mu)] \mathbf{n}_n^-(t') \cdot \mathbf{n}_m^+(t) \right. \\ &\quad \left. + [1 - n_F(\varepsilon_{\mathbf{k}-\Delta\mathbf{k}} - \mu)] n_F(\varepsilon_{\mathbf{k}'-\Delta\mathbf{k}} - \mu) \mathbf{n}_n^+(t') \cdot \mathbf{n}_m^-(t) \right\}, \end{aligned} \quad (\text{D.19})$$

where we used the notation $G_{0,\mathbf{k}}^{ij} = G_{0,\mathbf{k}}^{\lambda\lambda'}(t, t')$ in which the λ 's indicate the four elements in Eq. (D.18). The factor $(-1)^{\lambda-\lambda'}$ is negative when the t 's are on different contours. It was used that for Pauli matrices, $\text{Tr}[\sigma_i\sigma_j] = 2\delta_{ij}$, so that we obtain the dot products. The two last terms in the curly brackets are actually the same, but we keep them as two terms since it will make it easier to arrive at the desired result.

We can write the spins as $\mathbf{n}^+ = \mathbf{Q} + \boldsymbol{\zeta}/2$ and $\mathbf{n}^- = \mathbf{Q} - \boldsymbol{\zeta}/2$ where $\mathbf{Q} = \frac{\mathbf{n}^+ + \mathbf{n}^-}{2}$ and $\boldsymbol{\zeta} = \mathbf{n}^+ - \mathbf{n}^-$. With this, the four different dot products in Eq. (D.19) can be written as

$$\begin{aligned} \mathbf{n}_n^\pm(t') \cdot \mathbf{n}_m^\pm(t) &= \mathbf{Q}_n(t') \cdot \mathbf{Q}_m(t) \pm \frac{1}{2}\mathbf{Q}_n(t') \cdot \boldsymbol{\zeta}_m(t) \pm \frac{1}{2}\mathbf{Q}_m(t) \cdot \boldsymbol{\zeta}_n(t') + \frac{1}{4}\boldsymbol{\zeta}_n(t') \cdot \boldsymbol{\zeta}_m(t) \\ \mathbf{n}_n^\mp(t') \cdot \mathbf{n}_m^\pm(t) &= \mathbf{Q}_n(t') \cdot \mathbf{Q}_m(t) \pm \frac{1}{2}\mathbf{Q}_n(t') \cdot \boldsymbol{\zeta}_m(t) \mp \frac{1}{2}\mathbf{Q}_m(t) \cdot \boldsymbol{\zeta}_n(t') - \frac{1}{4}\boldsymbol{\zeta}_n(t') \cdot \boldsymbol{\zeta}_m(t). \end{aligned} \quad (\text{D.20})$$

Inserting these into Eq. (D.19), we get 16 different terms. The functions in front of the four new dot products can be collected. To make the rewriting easier, we will use notation $\theta = \theta(t - t')$, $\tilde{\theta} = \theta(t' - t)$ and $f_{\mathbf{k}} = n_F(\varepsilon_{\mathbf{k}-\Delta\mathbf{k}} - \mu)$. Let us first consider the functions in front of the QQ and $\xi\xi$ terms (upper and lower sign, respectively)

$$\begin{aligned} &(f_{\mathbf{k}} - \theta)(f_{\mathbf{k}'} - \tilde{\theta}) + (f_{\mathbf{k}} - \tilde{\theta})(f_{\mathbf{k}'} - \theta) \pm [f_{\mathbf{k}}(1 - f_{\mathbf{k}'} + f_{\mathbf{k}'}(1 - f_{\mathbf{k}}))] \\ &= 2f_{\mathbf{k}}f_{\mathbf{k}'} - f_{\mathbf{k}} - f_{\mathbf{k}'} \mp [2f_{\mathbf{k}}f_{\mathbf{k}'} - f_{\mathbf{k}} - f_{\mathbf{k}'}] \\ &= \begin{cases} 0 \\ 4f_{\mathbf{k}}f_{\mathbf{k}'} - 2f_{\mathbf{k}} - 2f_{\mathbf{k}'} \end{cases} \quad (\text{D.21}) \\ &= \begin{cases} 0 \\ 2 \coth\left(\frac{\varepsilon_{\mathbf{k}-\Delta\mathbf{k}} - \varepsilon_{\mathbf{k}'-\Delta\mathbf{k}}}{2k_B T}\right) [n_F(\varepsilon_{\mathbf{k}-\Delta\mathbf{k}} - \mu) - n_F(\varepsilon_{\mathbf{k}'-\Delta\mathbf{k}} - \mu)] \end{cases}, \end{aligned}$$

where $\coth(x)$ is the hyperbolic cotangent. We see that the QQ terms have dropped out. For the functions in front of the $\mathbf{Q}_m(t) \cdot \boldsymbol{\zeta}_n(t')$ and $\mathbf{Q}_n(t') \cdot \boldsymbol{\zeta}_m(t)$ terms (upper and lower sign, respectively)

$$\begin{aligned} &(f_{\mathbf{k}} - \theta)(f_{\mathbf{k}'} - \tilde{\theta}) - (f_{\mathbf{k}} - \tilde{\theta})(f_{\mathbf{k}'} - \theta) \mp f_{\mathbf{k}}(1 - f_{\mathbf{k}'} + f_{\mathbf{k}'}(1 - f_{\mathbf{k}})) \\ &= -\theta f_{\mathbf{k}'} - \tilde{\theta} f_{\mathbf{k}} + \theta f_{\mathbf{k}} + \tilde{\theta} f_{\mathbf{k}'} \mp (f_{\mathbf{k}} - f_{\mathbf{k}'}) \\ &= (f_{\mathbf{k}} - f_{\mathbf{k}'}) (\theta - \tilde{\theta}) \mp (f_{\mathbf{k}} - f_{\mathbf{k}'}) (\theta + \tilde{\theta}) \\ &= (f_{\mathbf{k}} - f_{\mathbf{k}'} \mp (f_{\mathbf{k}} - f_{\mathbf{k}'})) \theta - (f_{\mathbf{k}} - f_{\mathbf{k}'} \pm (f_{\mathbf{k}} - f_{\mathbf{k}'})) \tilde{\theta} \\ &= \begin{cases} -2(f_{\mathbf{k}} - f_{\mathbf{k}'}) \tilde{\theta} \\ 2(f_{\mathbf{k}} - f_{\mathbf{k}'}) \theta \end{cases}. \end{aligned} \quad (\text{D.22})$$

Inserting these back into Eq. (D.3) and remembering the factors in Eq. (D.20), we arrive at

$$\begin{aligned}
& -\frac{1}{2} \text{Tr}[G_0 V G_0 V] \\
&= \frac{S^2 J_0^2}{4\mathcal{V}^2} \sum_{\mathbf{k}\mathbf{k}'} \sum_{nm} e^{-i(\mathbf{k}-\mathbf{k}')\cdot(\mathbf{R}_n-\mathbf{R}_m)} [n_F(\varepsilon_{\mathbf{k}-\Delta\mathbf{k}} - \mu) - n_F(\varepsilon_{\mathbf{k}'-\Delta\mathbf{k}} - \mu)] \\
&\quad \times \int_0^{t_f} dt \int_0^{t_f} dt' e^{-i(\varepsilon_{\mathbf{k}}-\varepsilon_{\mathbf{k}'})(t-t')} \left\{ \theta(t-t') \boldsymbol{\zeta}_m(t) \cdot \mathbf{Q}_n(t') - \theta(t'-t) \boldsymbol{\zeta}_n(t') \cdot \mathbf{Q}_m(t) \right. \\
&\quad \quad \quad \left. + \frac{1}{2} \coth\left(\frac{\varepsilon_{\mathbf{k}-\Delta\mathbf{k}} - \varepsilon_{\mathbf{k}'-\Delta\mathbf{k}}}{2k_B T}\right) \boldsymbol{\zeta}_n(t') \cdot \boldsymbol{\zeta}_m(t) \right\} \\
&= i\mathcal{S}^{Q\zeta} + i\mathcal{S}^{\zeta\zeta}.
\end{aligned} \tag{D.23}$$

The first introduced contribution to the action is¹

$$\begin{aligned}
i\mathcal{S}^{Q\zeta} &= \frac{S^2 J_0^2}{2\mathcal{V}^2} \sum_{\mathbf{k}\mathbf{k}'} \sum_{nm} e^{-i(\mathbf{k}-\mathbf{k}')\cdot(\mathbf{R}_n-\mathbf{R}_m)} [n_F(\varepsilon_{\mathbf{k}-\Delta\mathbf{k}} - \mu) - n_F(\varepsilon_{\mathbf{k}'-\Delta\mathbf{k}} - \mu)] \\
&\quad \times \int_0^{t_f} dt \int_0^{t_f} dt' e^{-i(\varepsilon_{\mathbf{k}}-\varepsilon_{\mathbf{k}'})(t-t')} \theta(t-t') \boldsymbol{\zeta}_m(t) \cdot \mathbf{Q}_n(t') \\
&= \frac{S^2 J_0^2}{2\mathcal{V}^2} \sum_{nm} \int_0^{t_f} dt \int_0^{t_f} dt' \int d\omega \Lambda_{nm}(\omega, \Delta\mathbf{k}) e^{-i\omega(t-t')} \boldsymbol{\zeta}_m(t) \cdot \mathbf{Q}_n(t') \theta(t-t'),
\end{aligned} \tag{D.24}$$

where the effective electron-hole pair density of states is

$$\Lambda_{nm}(\omega, \Delta\mathbf{k}) = \sum_{\mathbf{k}\mathbf{k}'} [n_F(\varepsilon_{\mathbf{k}-\Delta\mathbf{k}} - \mu) - n_F(\varepsilon_{\mathbf{k}'-\Delta\mathbf{k}} - \mu)] e^{-i(\mathbf{k}-\mathbf{k}')\cdot(\mathbf{R}_n-\mathbf{R}_m)} \delta(\omega - \varepsilon_{\mathbf{k}} + \varepsilon_{\mathbf{k}'}) \tag{D.25}$$

which has units of Joule⁻¹.

The term $\mathcal{S}^{\zeta\zeta}$ can be read off directly from Eq. (D.23) and it is shown in Eq. (6.36). We cannot rewrite it in terms of $\Lambda_{nm}(\omega, \Delta\mathbf{k})$ due to the k -dependence in the hyperbolic cotangent.

D.3.1 Fourier transforming

Inspired by Ref. [116], we will rewrite parts of Eq. (6.35) by Fourier transforming. To make the following easier to read, we have omitted subscripts and $\Delta\mathbf{k}$ dependences.

¹Alternatively, we can reformulate parts of the integrand in Eq. (D.24) as

$$(f_{\mathbf{k}} - f_{\mathbf{k}'})\theta(t-t') \boldsymbol{\zeta}_m(t) \cdot \mathbf{Q}_n(t') \rightarrow f_{\mathbf{k}}(1 - f_{\mathbf{k}'}) [\theta(t-t') \boldsymbol{\zeta}_m(t) \cdot \mathbf{Q}_n(t') - \theta(t'-t) \boldsymbol{\zeta}_n(t') \cdot \mathbf{Q}_m(t)],$$

where $f_{\mathbf{k}} = n_F(\varepsilon_{\mathbf{k}-\Delta\mathbf{k}} - \mu)$. This can be seen by doing the rewriting $f_{\mathbf{k}} - f_{\mathbf{k}'} = f_{\mathbf{k}}(1 - f_{\mathbf{k}'}) - f_{\mathbf{k}'}(1 - f_{\mathbf{k}})$ and interchanging $\mathbf{k} \leftrightarrow \mathbf{k}'$, $n \leftrightarrow m$, and $t \leftrightarrow t'$ in the second term.

Consider the integral

$$\begin{aligned}
I &= \int dt' \int d\omega \Lambda(\omega) \theta(t-t') Q(t') e^{-i\omega(t-t')} \\
&= 2\pi \int dt' \int \frac{d\omega}{2\pi} \int \frac{d\omega'}{2\pi} \int \frac{d\omega''}{2\pi} \Lambda(\omega) \theta(\omega') Q(\omega'') e^{-i(\omega+\omega')(t-t')} e^{-i\omega''t'} \quad (\text{D.26}) \\
&= 2\pi \int \frac{d\omega}{2\pi} \int \frac{d\omega'}{2\pi} \Lambda(\omega) \theta(\omega') Q(\omega + \omega') e^{-i(\omega+\omega')t}
\end{aligned}$$

where it was used that $\int dt' e^{i(\omega+\omega'-\omega'')t'} = 2\pi\delta(\omega + \omega' - \omega'')$ in the last step. We can now insert the Fourier transform of the step function $\theta(\omega') = \pi\delta(\omega') + \mathcal{P}\frac{i}{\omega'}$, where \mathcal{P} denotes the Cauchy principal value

$$\begin{aligned}
I &= \pi \int \frac{d\omega}{2\pi} \Lambda(\omega) Q(\omega) e^{-i\omega t} + 2\pi i \int \frac{d\omega}{2\pi} \mathcal{P} \int \frac{d\omega'}{2\pi} \frac{\Lambda(\omega)}{\omega'} Q(\omega + \omega') e^{-i(\omega+\omega')t} \\
&= \pi \int \frac{d\omega}{2\pi} \Lambda(\omega) Q(\omega) e^{-i\omega t} + 2\pi i \mathcal{P} \int \frac{d\omega}{2\pi} \int \frac{d\omega'}{2\pi} \frac{\Lambda(\omega)}{\omega' - \omega} Q(\omega') e^{-i\omega't} \\
&= \pi \int \frac{d\omega}{2\pi} \Lambda(\omega) Q(\omega) e^{-i\omega t} + i\pi \int \frac{d\omega'}{2\pi} \left[\frac{1}{\pi} \mathcal{P} \int d\omega \frac{\Lambda(\omega)}{\omega' - \omega} \right] Q(\omega') e^{-i\omega't} \\
&= i\pi \int \frac{d\omega}{2\pi} [-i\Lambda(\omega) + \mathcal{H}\{\Lambda(\omega')\}(\omega)] Q(\omega) e^{-i\omega t} \\
&= i\pi \int \frac{d\omega}{2\pi} \left[-i \operatorname{Re} \Lambda(\omega) + \operatorname{Im} \Lambda(\omega) + \mathcal{H}\{\operatorname{Re} \Lambda\}(\omega) + i\mathcal{H}\{\operatorname{Im} \Lambda\}(\omega) \right] Q(\omega) e^{-i\omega t} \quad (\text{D.27})
\end{aligned}$$

where the Hilbert transform is defined as in Eq. (6.42).

D.4 Integrals

In this section, we will perform the integrals in Eq. (6.47). These are rather long, and they can probably be done in a shorter way, but the procedure works. We will start with some useful rewriting and integrals before we turn to the individual coefficient calculations in Secs. D.4.1–D.4.4.

First of all, we will emphasize that the real part of Λ gives the equilibrium contributions, while the imaginary part leads to the non-equilibrium contributions. To first order in $\Delta\mathbf{k}$, the Fermi function is $n_F(\varepsilon_{\mathbf{k}-\Delta\mathbf{k}} - \mu) \approx n_F(\varepsilon_{\mathbf{k}} - \mu) - n'_F(\varepsilon_{\mathbf{k}} - \mu) \frac{\hbar^2}{m} \mathbf{k} \cdot \Delta\mathbf{k}$. With this, we can write Λ in Eq. (6.37) as

$$\begin{aligned}
\Lambda_{nm}(\omega, \Delta\mathbf{k}) &\approx \Lambda_{nm}(\omega, 0) - \sum_{\mathbf{k}\mathbf{k}'} \frac{\hbar^2}{m} \left[n'_F(\varepsilon_{\mathbf{k}} - \mu) \mathbf{k} - n'_F(\varepsilon_{\mathbf{k}'} - \mu) \mathbf{k}' \right] \cdot \Delta\mathbf{k} \\
&\quad \times e^{-i(\mathbf{k}-\mathbf{k}') \cdot (\mathbf{R}_n - \mathbf{R}_m)} \delta(\omega - \varepsilon_{\mathbf{k}} + \varepsilon_{\mathbf{k}'}). \quad (\text{D.28})
\end{aligned}$$

From the property in Eq. (6.40), it is clear that the first term is real while the second term is imaginary.

Rewriting $\Lambda_{nm}(\omega, \Delta \mathbf{k})$

We will start by rewriting Λ , which will be useful in Secs. D.4.2 and D.4.3. First, we turn the sums into integrals, $\sum_{\mathbf{k}} \rightarrow \frac{\mathcal{V}}{(2\pi)^3} \int d\mathbf{k}$, and rewrite as follows

$$\begin{aligned} \Lambda_{nm}(\omega, \Delta \mathbf{k}) &= \sum_{\mathbf{k}\mathbf{k}'} [n_F(\varepsilon_{\mathbf{k}-\Delta \mathbf{k}} - \mu) - n_F(\varepsilon_{\mathbf{k}'-\Delta \mathbf{k}} - \mu)] e^{-i(\mathbf{k}-\mathbf{k}') \cdot (\mathbf{R}_n - \mathbf{R}_m)} \delta(\omega - \varepsilon_{\mathbf{k}} + \varepsilon_{\mathbf{k}'}) \\ &= \frac{\mathcal{V}^2}{(2\pi)^6} \int d\mathbf{k} n_F(\varepsilon_{\mathbf{k}-\Delta \mathbf{k}} - \mu) \int d\mathbf{k}' \left[e^{-i(\mathbf{k}-\mathbf{k}') \cdot (\mathbf{R}_n - \mathbf{R}_m)} \delta(\omega - \varepsilon_{\mathbf{k}} + \varepsilon_{\mathbf{k}'}) \right. \\ &\quad \left. - e^{i(\mathbf{k}-\mathbf{k}') \cdot (\mathbf{R}_n - \mathbf{R}_m)} \delta(\omega - \varepsilon_{\mathbf{k}'} + \varepsilon_{\mathbf{k}}) \right]. \end{aligned} \quad (\text{D.29})$$

We can rewrite the delta function as $\delta(\varepsilon - \varepsilon_{\mathbf{k}}) = \sqrt{\frac{m}{2\hbar^2\varepsilon}} \delta\left(k - \sqrt{\frac{2m\varepsilon}{\hbar^2}}\right)$, where $k = |\mathbf{k}|$. For $n \neq m$, the \mathbf{k}' integrals are

$$\begin{aligned} &\int d\mathbf{k}' e^{\pm i\mathbf{k}' \cdot (\mathbf{R}_n - \mathbf{R}_m)} \delta(\hbar\omega \mp \varepsilon_{\mathbf{k}} \pm \varepsilon_{\mathbf{k}'}) \\ &= \frac{m}{\hbar^2} \frac{1}{\sqrt{k^2 \mp q^2}} 2\pi \int dk' k'^2 \delta\left(k' - \sqrt{k^2 \mp q^2}\right) \int_{-1}^1 dx e^{\pm i x k' R} \\ &= \frac{2\pi m}{\hbar^2} \sqrt{k^2 \mp q^2} \int_{-1}^1 dx e^{\pm i x R \sqrt{k^2 \mp q^2}} \\ &= \frac{2\pi m}{\hbar^2} \sqrt{k^2 \mp q^2} \frac{2 \sin\left(R \sqrt{k^2 \mp q^2}\right)}{R \sqrt{k^2 \mp q^2}} \\ &= \frac{4\pi m}{\hbar^2} \frac{1}{R} \sin\left(R \sqrt{k^2 \mp q^2}\right) \end{aligned} \quad (\text{D.30})$$

where we have introduced $\hbar\omega = \hbar^2 q^2 / (2m)$ and used the notation $x = \cos \theta$. Putting this back into Eq. (D.29), we get

$$\begin{aligned} \Lambda_{nm}(\omega, \Delta \mathbf{k}) &= \frac{\mathcal{V}^2}{(2\pi)^5} \frac{2m}{\hbar^2} \frac{1}{R} \int d\mathbf{k} n_F(\varepsilon_{\mathbf{k}-\Delta \mathbf{k}} - \mu) \left[e^{-i\mathbf{k} \cdot (\mathbf{R}_n - \mathbf{R}_m)} \sin\left(R \sqrt{k^2 - q^2}\right) \right. \\ &\quad \left. - e^{\mathbf{k} \cdot (\mathbf{R}_n - \mathbf{R}_m)} \sin\left(R \sqrt{k^2 + q^2}\right) \right]. \end{aligned} \quad (\text{D.31})$$

The Hilbert transform, $\mathcal{H}\{\text{Im} \Lambda_{nm}(\omega', \Delta \mathbf{k})\}(\omega)$

The Hilbert transform of Λ is (insert Eq. (6.37) into Eq. (6.42))

$$\mathcal{H}\{\Lambda_{nm}(\omega', \Delta \mathbf{k})\}(\omega) = \frac{1}{\pi} \mathcal{P} \sum_{\mathbf{k}\mathbf{k}'} \frac{n_F(\varepsilon_{\mathbf{k}-\Delta \mathbf{k}} - \mu) - n_F(\varepsilon_{\mathbf{k}'-\Delta \mathbf{k}} - \mu)}{\hbar\omega + \varepsilon_{\mathbf{k}} - \varepsilon_{\mathbf{k}'}} e^{-i(\mathbf{k}-\mathbf{k}') \cdot (\mathbf{R}_n - \mathbf{R}_m)}, \quad (\text{D.32})$$

which will be the starting point in Secs. D.4.1 and D.4.4.

Useful integrals

We will now state two integrals, which will be useful in the following sections. Both of them are derived in Sec. D.4.5. One is

$$\mathcal{P} \sum_{\mathbf{k}'} \frac{e^{i\mathbf{k}' \cdot \mathbf{R}}}{\varepsilon_{\mathbf{k}} - \varepsilon_{\mathbf{k}'}} = -\frac{m\mathcal{V}}{2\hbar^2\pi} \frac{\cos(kR)}{R} \quad (\text{D.33})$$

and the other is (at low temperatures)

$$\begin{aligned} & \int d\mathbf{k} n'_F(\varepsilon_{\mathbf{k}} - \mu) \mathbf{k} \cdot \Delta\mathbf{k} \sin(\mathbf{k} \cdot \mathbf{R}) g(k) \\ & \approx \frac{4\pi m}{\hbar^2} \frac{1}{R^3} \Delta\mathbf{k} \cdot \mathbf{R} [k_F R \cos(k_F R) - \sin(k_F R)] g(k_F), \end{aligned} \quad (\text{D.34})$$

where $g(k)$ is any function of k .

D.4.1 \mathbf{J} , $\mathcal{H}\{\text{Re}\Lambda\}(0)$

We will start with the equilibrium coefficients. Starting from Eq. (D.32), the integral in J in Eq. (6.47) is

$$\begin{aligned} \mathcal{H}\{\Lambda_{12}(\omega', 0)\}(0) &= \frac{1}{\pi} \text{Re} \sum_{\mathbf{k}\mathbf{k}'} \mathcal{P} \frac{n_F(\varepsilon_{\mathbf{k}} - \mu) - n_F(\varepsilon_{\mathbf{k}'} - \mu)}{\varepsilon_{\mathbf{k}} - \varepsilon_{\mathbf{k}'}} e^{-i(\mathbf{k}-\mathbf{k}') \cdot (\mathbf{R}_1 - \mathbf{R}_2)} \\ &= \frac{2}{\pi} \text{Re} \sum_{\mathbf{k}\mathbf{k}'} \mathcal{P} \frac{n_F(\varepsilon_{\mathbf{k}} - \mu)}{\varepsilon_{\mathbf{k}} - \varepsilon_{\mathbf{k}'}} e^{i(\mathbf{k}-\mathbf{k}') \cdot \mathbf{R}} \\ &= \frac{2}{\pi} \text{Re} \sum_{\mathbf{k}} n_F(\varepsilon_{\mathbf{k}} - \mu) e^{i\mathbf{k} \cdot \mathbf{R}} \mathcal{P} \sum_{\mathbf{k}'} \frac{e^{-i\mathbf{k}' \cdot \mathbf{R}}}{\varepsilon_{\mathbf{k}} - \varepsilon_{\mathbf{k}'}} \\ &= -\frac{2}{\pi} \frac{m\mathcal{V}}{2\hbar^2\pi R} \text{Re} \sum_{\mathbf{k}} n_F(\varepsilon_{\mathbf{k}} - \mu) e^{i\mathbf{k} \cdot \mathbf{R}} \cos(kR) \\ &\approx -\frac{m\mathcal{V}}{\pi^2\hbar^2} \frac{1}{R} \frac{\mathcal{V}}{(2\pi)^2} \int_0^{k_F} dk k^2 \cos(kR) \int_{-1}^1 dx \cos(xkR) \\ &= -\frac{m\mathcal{V}}{\pi^2\hbar^2} \frac{1}{R} \frac{\mathcal{V}}{(2\pi)^2} \int_0^{k_F} dk k^2 \cos(kR) \frac{2 \sin(kR)}{kR} \\ &= -\frac{2m\mathcal{V}}{\pi^2\hbar^2} \frac{1}{R^2} \frac{\mathcal{V}}{(2\pi)^2} \int_0^{k_F} dk k \cos(kR) \sin(kR) \\ &= \frac{2m\mathcal{V}}{\pi^2\hbar^2} \frac{1}{R^2} \frac{\mathcal{V}}{(2\pi)^2} \frac{1}{8R^2} [2k_F R \cos(2k_F R) - \sin(2k_F R)] \\ &= \frac{2m\mathcal{V}}{\pi^2\hbar^2} \frac{\mathcal{V}}{(2\pi)^2} \frac{1}{8} 2^4 k_F^4 F(2k_F R) \\ &= \mathcal{V}^2 \frac{mk_F}{\pi^2\hbar^2} \frac{k_F^3}{2\pi^2\varepsilon_F} 2\varepsilon_F F(2k_F R) \\ &= 2\mathcal{V}^2 \varepsilon_F \rho(\varepsilon_F)^2 F(2k_F R), \end{aligned} \quad (\text{D.35})$$

where the sum in Eq. (D.33) was used in the third step and $\int_0^{k_F} dk k \cos(k\Delta R) \sin(k\Delta R) = \frac{\sin(2k_F\Delta R) - 2k_F\Delta R \cos(2k_F\Delta R)}{8\Delta R^2}$ was used further down. The density of states was introduced in the last step,

$$\rho(\varepsilon_F) = \frac{k_F^3}{2\pi^2\varepsilon_F} = \frac{mk_F}{\pi^2\hbar^2}. \quad (\text{D.36})$$

D.4.2 $\eta, \frac{\partial}{\partial \omega} \Lambda_{nm}(\omega, 0)|_{\omega=0}$

To get the non-local relaxation coefficient, we consider the real part of Eq. (D.31) at $T = 0$

$$\begin{aligned}
\Lambda_{12}(\omega, 0) &\approx \frac{\mathcal{V}^2}{(2\pi)^5} \frac{2m}{\hbar^2} \frac{1}{R} \int d\mathbf{k} n_F(\varepsilon_{\mathbf{k}} - \varepsilon_F) \cos(\mathbf{k} \cdot \mathbf{R}) \left[\sin\left(R\sqrt{k^2 - q^2}\right) - \sin\left(R\sqrt{k^2 + q^2}\right) \right] \\
&\approx \frac{\mathcal{V}^2}{(2\pi)^4} \frac{2m}{\hbar^2} \frac{1}{R} \int_0^{k_F} dk k^2 \left[\sin\left(R\sqrt{k^2 - q^2}\right) - \sin\left(R\sqrt{k^2 + q^2}\right) \right] \int_{-1}^1 dx \cos(xkR) \\
&= \frac{\mathcal{V}^2}{(2\pi)^4} \frac{4m}{\hbar^2} \frac{1}{R^2} \int_0^{k_F} dk k \sin(kR) \left[\sin\left(R\sqrt{k^2 - q^2}\right) - \sin\left(R\sqrt{k^2 + q^2}\right) \right].
\end{aligned} \tag{D.37}$$

We are interested in the derivative with respect to ω

$$\begin{aligned}
\frac{\partial}{\partial \omega} \Lambda_{12}(\omega, 0)|_{\omega=0} &= \left(\frac{\partial \omega}{\partial q} \right)^{-1} \frac{\partial}{\partial q} \Lambda_{12}(\omega, 0)|_{q=0} \\
&= -\frac{m}{\hbar} \frac{\mathcal{V}^2}{(2\pi)^4} \frac{4m}{\hbar^2} \frac{1}{R^2} \int_0^{k_F} dk k \sin(kR) \cos(kR) \frac{2R}{k} \\
&= -\mathcal{V}^2 \frac{m^2}{2\hbar^3 \pi^4} \frac{1}{R} \int_0^{k_F} dk \sin(kR) \cos(kR) \\
&= -\mathcal{V}^2 \frac{\hbar}{2k_F^2} \left(\frac{k_F m}{\pi^2 \hbar^2} \right)^2 \frac{1}{R} \frac{\sin^2(k_F R)}{2R} \\
&= -\hbar \mathcal{V}^2 \frac{\rho(\varepsilon_F)^2}{4} \left(\frac{\sin(k_F R)}{k_F R} \right)^2.
\end{aligned} \tag{D.38}$$

The local relaxation is obtained by setting $R = 0$ in the above expression,

$$\frac{\partial}{\partial \omega} \Lambda_{nm}(\omega, 0)|_{\omega=0} = -\hbar \mathcal{V}^2 \frac{\rho(\varepsilon_F)^2}{4}, \tag{D.39}$$

for both $n = 1$ and $n = 2$.

D.4.3 $\sigma, \text{Im} \Lambda(0, \Delta \mathbf{k})$

We will now look at the non-equilibrium terms. By taking the imaginary part of Eq. (D.31) and setting $q = 0$, we have

$$\begin{aligned}
\text{Im} \Lambda_{21}(0, \Delta \mathbf{k}) &= -\frac{\mathcal{V}^2}{(2\pi)^5} \frac{4m}{\hbar^2} \frac{1}{R} \int d\mathbf{k} n_F(\varepsilon_{\mathbf{k} - \Delta \mathbf{k}} - \mu) \sin(kR) \sin(\mathbf{k} \cdot \mathbf{R}) \\
&\approx \frac{\mathcal{V}^2}{(2\pi)^5} \frac{4m}{\hbar^2} \frac{1}{R} \frac{\hbar^2}{m} \int d\mathbf{k} n'_F(\varepsilon_{\mathbf{k}} - \mu) \mathbf{k} \cdot \Delta \mathbf{k} \sin(kR) \sin(\mathbf{k} \cdot \mathbf{R}) \\
&\approx \frac{4\mathcal{V}^2}{(2\pi)^5} \frac{1}{R} \frac{4\pi m}{\hbar^2} \frac{1}{R^3} \Delta \mathbf{k} \cdot \mathbf{R} [k_F R \cos(k_F R) - \sin(k_F R)] \sin(k_F R) \\
&= \mathcal{V}^2 \frac{k_F^3}{2\pi^2 \varepsilon_F} \frac{m k_F}{\pi^2 \hbar^2} \varepsilon_F \sin(k_F R) \frac{k_F R \cos(k_F R) - \sin(k_F R)}{(k_F R)^3} \frac{\Delta \mathbf{k} \cdot \mathbf{R}}{k_F R} \\
&= \mathcal{V}^2 \rho(\varepsilon_F)^2 \varepsilon_F L(k_F R) \frac{\Delta \mathbf{k} \cdot \mathbf{R}}{k_F R},
\end{aligned} \tag{D.40}$$

where the \mathbf{k} integral is found in Eq. (D.34) and where the introduced function is defined as

$$L(x) = \sin(x) \frac{x \cos(x) - \sin(x)}{x^3}. \quad (\text{D.41})$$

D.4.4 $\chi, \frac{\partial}{\partial \omega} \mathcal{H} \{ \text{Im} \Lambda_{21} \} (\omega) \big|_{\omega=0}$

We start by taking the ω derivative of Eq. (D.32)

$$\begin{aligned} & \frac{\partial}{\partial \omega} \mathcal{H} \{ \text{Im} \Lambda_{21} \} (\omega) \big|_{\omega=0} \\ &= -\frac{1}{\pi} \text{Im} \mathcal{P} \sum_{\mathbf{k}\mathbf{k}'} \frac{n_F(\varepsilon_{\mathbf{k}-\Delta\mathbf{k}} - \mu) - n_F(\varepsilon_{\mathbf{k}'-\Delta\mathbf{k}} - \mu)}{(\varepsilon_{\mathbf{k}} - \varepsilon_{\mathbf{k}'})^2} e^{-i(\mathbf{k}-\mathbf{k}') \cdot \mathbf{R}} \\ &\approx -\frac{\hbar^2}{\pi m} \mathcal{P} \sum_{\mathbf{k}\mathbf{k}'} \frac{n'_F(\varepsilon_{\mathbf{k}} - \mu) \mathbf{k} \cdot \Delta\mathbf{k} - n'_F(\varepsilon_{\mathbf{k}'} - \mu) \mathbf{k}' \cdot \Delta\mathbf{k}}{(\varepsilon_{\mathbf{k}} - \varepsilon_{\mathbf{k}'})^2} \sin((\mathbf{k} - \mathbf{k}') \cdot \mathbf{R}) \\ &= -\frac{2\hbar^2}{\pi m} \mathcal{P} \sum_{\mathbf{k}\mathbf{k}'} \frac{n'_F(\varepsilon_{\mathbf{k}} - \mu) \mathbf{k} \cdot \Delta\mathbf{k}}{(\varepsilon_{\mathbf{k}} - \varepsilon_{\mathbf{k}'})^2} \sin((\mathbf{k} - \mathbf{k}') \cdot \mathbf{R}) \\ &= -\frac{2\hbar^2}{\pi m} \frac{\mathcal{V}}{(2\pi)^2} \sum_{\mathbf{k}} n'_F(\varepsilon_{\mathbf{k}} - \mu) \mathbf{k} \cdot \Delta\mathbf{k} \mathcal{P} \int_0^\infty dk' \frac{k'^2}{(\varepsilon_{\mathbf{k}} - \varepsilon_{\mathbf{k}'})^2} \int_{-1}^1 dy' \sin(\mathbf{k} \cdot \mathbf{R} - y' k' R) \\ &= -\frac{2\hbar^2}{\pi m} \frac{\mathcal{V}}{(2\pi)^2} \sum_{\mathbf{k}} n'_F(\varepsilon_{\mathbf{k}} - \mu) \mathbf{k} \cdot \Delta\mathbf{k} \mathcal{P} \int_0^\infty dk' \frac{k'^2}{(\varepsilon_{\mathbf{k}} - \varepsilon_{\mathbf{k}'})^2} \frac{2 \sin(\mathbf{k} \cdot \mathbf{R}) \sin(k' R)}{k' R} \\ &= -\frac{4\hbar^2}{\pi m} \frac{\mathcal{V}^2}{(2\pi)^5} \frac{1}{R} \int d\mathbf{k} n'_F(\varepsilon_{\mathbf{k}} - \mu) \sin(\mathbf{k} \cdot \mathbf{R}) \mathbf{k} \cdot \Delta\mathbf{k} I(\varepsilon_{\mathbf{k}}, R) \\ &\approx -\frac{4\hbar^2}{\pi m} \frac{\mathcal{V}^2}{(2\pi)^5} \frac{4\pi m}{\hbar^2} \frac{1}{R^4} \Delta\mathbf{k} \cdot \mathbf{R} [k_F R \cos(k_F R) - \sin(k_F R)] I(\varepsilon_F, R) \\ &= -\frac{\mathcal{V}^2}{2\pi^5} \frac{1}{R^4} \Delta\mathbf{k} \cdot \mathbf{R} [k_F R \cos(k_F R) - \sin(k_F R)] I(\varepsilon_F, R), \end{aligned} \quad (\text{D.42})$$

where $y' = \cos \theta'$ and where the second last step is done using Eq. (D.34). We are now left with solving the integral

$$\begin{aligned} I(\varepsilon_F, R) &= \mathcal{P} \int_0^\infty dk \frac{k \sin(kR)}{(\varepsilon_F - \varepsilon_{\mathbf{k}})^2} \\ &= R^2 \left(\frac{2m}{\hbar^2} \right)^2 \mathcal{P} \int_0^\infty dx \frac{x \sin(x)}{(x_F^2 - x^2)^2} \\ &= R^2 \left(\frac{2m}{\hbar^2} \right)^2 \lim_{\delta x \rightarrow 0} \left[\int_0^{x_F - \delta x} dx \frac{x \sin(x)}{(x_F^2 - x^2)^2} + \int_{x_F + \delta x}^\infty dx \frac{x \sin(x)}{(x_F^2 - x^2)^2} \right], \end{aligned} \quad (\text{D.43})$$

where $x_F = k_F R$ and $x = kR$. This integral diverges for $\delta x \rightarrow 0$. Small δx means that the excitation energy of the electron hole pair is small. Such a pair is slow, but as described in Sec. 6.2.4, we assume that the electrons are fast compared to the spins. Using this assumption, we can therefore introduce a cutoff so that the slow electrons are ignored, and the integral consequently converges. A reasonable cutoff is the Larmor frequency, which is small compared to the Fermi energy so that $\delta x \ll \delta x_F$. By linearizing the dispersion around the Fermi energy, $\varepsilon_{\mathbf{k}} \approx \varepsilon_F + \frac{\hbar^2}{m} k_F (k - k_F)$, we see that the cutoff can be rewritten as $\delta x = \delta k R \approx \frac{1}{2} k_F R \frac{\delta \varepsilon}{\varepsilon_F}$, where $\delta \varepsilon$ is the cutoff

energy. With this, we can simplify the integral as

$$\begin{aligned}
I_{\text{cutoff}} &= R^2 \left(\frac{2m}{\hbar^2} \right)^2 \left[\int_0^{x_F - \delta x} dx \frac{x \sin(x)}{(x_F^2 - x^2)^2} + \int_{x_F + \delta x}^{\infty} dx \frac{x \sin(x)}{(x_F^2 - x^2)^2} \right] \\
&= R^2 \left(\frac{2m}{\hbar^2} \right)^2 \frac{1}{4x_F^2 \delta x - \delta x^3} \left\{ x_F \delta x \cos x_F [\text{Ci}(2x_F + \delta x) - \text{Ci}(2x_F - \delta x)] \right. \\
&\quad + x_F \delta x \sin x_F [\text{Si}(2x_F + \delta x) - \text{Si}(2x_F - \delta x) + 2\text{Si}(\delta x) - \pi] \\
&\quad \left. + 2x_F \cos \delta x \sin x_F - \delta x \cos x_F \sin \delta x + \mathcal{O}(\delta x^3 x_F^{-1}) \right\} \\
&\approx R^2 \left(\frac{2m}{\hbar^2} \right)^2 \frac{\sin x_F \cos \delta x}{2x_F \delta x} \\
&\approx \frac{2m^2 \sin(k_F R)}{\hbar^4 k_F \delta k} \\
&\approx \frac{2m \sin(k_F R)}{\hbar^2 \delta \varepsilon},
\end{aligned} \tag{D.44}$$

where the first step was done in Mathematica, while $\delta k \approx \frac{k_F \delta \varepsilon}{2 \varepsilon_F}$ was used in the last step. In the second line in Eq. (D.44), $\text{Si}(x)$ and $\text{Ci}(x)$ are the sine and cosine integral functions, respectively. Inserting the result in Eq. (D.44) back into Eq. (D.42), we arrive at our final result,

$$\begin{aligned}
\frac{\partial}{\partial \omega} \mathcal{H} \{ \text{Im} \Lambda_{21} \} (\omega) \Big|_{\omega=0} &\approx -\frac{\mathcal{V}^2}{2\pi^5} \frac{2m}{\hbar^2} k_F^4 \frac{[k_F R \cos(k_F R) - \sin(k_F R)] \sin(k_F R)}{(k_F R)^3} \frac{1}{\delta \varepsilon} \frac{\Delta \mathbf{k} \cdot \mathbf{R}}{k_F R} \\
&= -\frac{2\mathcal{V}^2}{\pi} \rho(\varepsilon_F)^2 L(k_F R) \frac{\varepsilon_F}{\delta \varepsilon} \frac{\Delta \mathbf{k} \cdot \mathbf{R}}{k_F R},
\end{aligned} \tag{D.45}$$

where $L(x)$ is defined in Eq. (D.41) and $\rho(\varepsilon_F)$ is found in Eq. (D.36).

D.4.5 Additional integrals

The sum in Eq. (D.33) can be solved as follows

$$\begin{aligned}
\mathcal{P} \sum_{\mathbf{k}'} \frac{e^{-i\mathbf{k}' \cdot \mathbf{R}}}{\varepsilon_{\mathbf{k}} - \varepsilon_{\mathbf{k}'}} &= \frac{\mathcal{V}}{(2\pi)^2} \mathcal{P} \int_0^{\infty} dk' k'^2 \frac{1}{\varepsilon_{\mathbf{k}} - \varepsilon_{\mathbf{k}'}} \int_{-1}^1 dx e^{-ixk'R} \\
&= \frac{\mathcal{V}}{(2\pi)^2} \mathcal{P} \int_0^{\infty} dk' k'^2 \frac{1}{\varepsilon_{\mathbf{k}} - \varepsilon_{\mathbf{k}'}} \frac{2 \sin(k'R)}{k'R} \\
&= \frac{\mathcal{V}}{(2\pi)^2} \frac{2}{R} \frac{2m}{\hbar^2} \mathcal{P} \int_0^{\infty} dk' \frac{k' \sin(k'R)}{k^2 - k'^2} \\
&= \frac{m\mathcal{V}}{\pi^2 \hbar^2} \frac{1}{R} \lim_{\delta k \rightarrow 0} \left[\int_0^{k-\delta k} dk' \frac{k' \sin(k'R)}{k^2 - k'^2} + \int_{k+\delta k}^{\infty} dk' \frac{k' \sin(k'R)}{k^2 - k'^2} \right] \\
&= \frac{m\mathcal{V}}{\pi^2 \hbar^2} \frac{1}{R} \left[-\frac{\pi \cos(kR)}{2} \right] \\
&= -\frac{m\mathcal{V}}{2\pi \hbar^2} \frac{\cos(kR)}{R}.
\end{aligned} \tag{D.46}$$

The integral in Eq. (D.34) is

$$\begin{aligned}
& \int d\mathbf{k} n'_F(\varepsilon_{\mathbf{k}} - \mu) \mathbf{k} \cdot \Delta\mathbf{k} \sin(\mathbf{k} \cdot \mathbf{R}) g(k) \\
&= \int_0^\infty dk k^2 n'_F(\varepsilon_k - \mu) g(k) \int_0^{2\pi} d\phi \int_0^\pi d\theta \sin\theta \mathbf{k} \cdot \Delta\mathbf{k} \sin(\mathbf{k} \cdot \mathbf{R}) \quad (\text{D.47}) \\
&= \frac{4\pi m}{\hbar^2} \frac{1}{R^3} \Delta\mathbf{k} \cdot \mathbf{R} [k_F R \cos(k_F R) - \sin(k_F R)] g(k_F),
\end{aligned}$$

where we chose $\mathbf{R} = R\hat{\mathbf{z}}$ so that

$$\begin{aligned}
& \int_0^{2\pi} d\phi \int_0^\pi d\theta \sin\theta \mathbf{k} \cdot \Delta\mathbf{k} \sin(\mathbf{k} \cdot \mathbf{R}) \\
&= k \int_0^{2\pi} d\phi \int_0^\pi d\theta \sin\theta (\Delta k_x \sin\theta \cos\phi + \Delta k_y \sin\theta \sin\phi + \Delta k_z \cos\theta) \sin(kR \cos\theta) \\
&= 2\pi k \Delta k_z \int_0^\pi d\theta \sin\theta \cos\theta \sin(kR \cos\theta) \\
&= 2\pi k \Delta k_z \int_{-1}^1 dx x \sin(xkR) \\
&= -2\pi k \Delta k_z \frac{2kR \cos(kR) - 2 \sin(kR)}{(kR)^2} \\
&= -4\pi \frac{\Delta\mathbf{k} \cdot \mathbf{R}}{R} \frac{kR \cos(kR) - \sin(kR)}{kR^2} \quad (\text{D.48})
\end{aligned}$$

and used

$$\begin{aligned}
\int_0^\infty dk n'_F(\varepsilon_k - \mu) f(k) &= \int_0^\infty d\varepsilon \left(\frac{d\varepsilon_k}{dk} \right)^{-1} n'_F(\varepsilon - \mu) f(k(\varepsilon)) \\
&= \frac{m}{\hbar^2} \int_0^\infty n'_F(\varepsilon - \mu) \frac{f(k(\varepsilon))}{k(\varepsilon)} \quad (\text{D.49}) \\
&\approx -\frac{m}{\hbar^2} \frac{f(k_F)}{k_F}.
\end{aligned}$$

Appendix E

Appendix to Chapter 7

E.1 Analytic considerations

In this part, we will derive an expression for \dot{n}_1^z in the case where terms including $\eta_0\eta_1$, $\eta_0\chi$, $\sigma\chi$ can be neglected. To do so, we will iterate the EOMs by inserting the $\dot{\mathbf{n}}$'s on the right hand sides of the equations. This will generate a lot of terms, so to keep it as simple as possible, we use the notation

$$\dot{\mathbf{n}}_i = -\mathbf{B} \times \mathbf{n}_i + A_{\bar{i}i} \mathbf{n}_{\bar{i}} \times \mathbf{n}_i + \sum_j C_{ji} \dot{\mathbf{n}}_j \times \mathbf{n}_i, \quad (\text{E.1})$$

where \bar{i} is the opposite of i (i.e. if $i = 1$, $\bar{i} = 2$ and vice versa). The matrices \mathbf{A} and \mathbf{C} are

$$\begin{aligned} \mathbf{A} &= \begin{pmatrix} 0 & J - \sigma \\ J + \sigma & 0 \end{pmatrix} \\ \mathbf{C} &= \begin{pmatrix} \eta_0 & \eta_1 - \chi \\ \eta_1 + \chi & \eta_0 \end{pmatrix}. \end{aligned} \quad (\text{E.2})$$

Let's consider the last term in the expression above

$$\begin{aligned} \sum_j C_{ji} \dot{\mathbf{n}}_j \times \mathbf{n}_i &= \sum_j C_{ji} \left[-\mathbf{B} \times \mathbf{n}_j + A_{\bar{j}j} \mathbf{n}_{\bar{j}} \times \mathbf{n}_j + \sum_l C_{lj} \dot{\mathbf{n}}_l \times \mathbf{n}_j \right] \times \mathbf{n}_i \\ &= \sum_j C_{ji} \left\{ -[(\mathbf{n}_i \cdot \mathbf{B})\mathbf{n}_j - \mathbf{B}(\mathbf{n}_i \cdot \mathbf{n}_j)] + A_{\bar{j}j} [(\mathbf{n}_{\bar{j}} \cdot \mathbf{n}_i)\mathbf{n}_j - (\mathbf{n}_i \cdot \mathbf{n}_j)\mathbf{n}_{\bar{j}}] \right. \\ &\quad \left. + \sum_l C_{lj} [(\dot{\mathbf{n}}_l \cdot \mathbf{n}_i)\mathbf{n}_j - (\mathbf{n}_i \cdot \mathbf{n}_j)\dot{\mathbf{n}}_l] \right\} \\ &= \sum_j C_{ji} \left\{ -[(\mathbf{n}_i \cdot \mathbf{B})\mathbf{n}_j - \mathbf{B}(\mathbf{n}_i \cdot \mathbf{n}_j)] + A_{\bar{j}j} [(\mathbf{n}_{\bar{j}} \cdot \mathbf{n}_i)\mathbf{n}_j - (\mathbf{n}_i \cdot \mathbf{n}_j)\mathbf{n}_{\bar{j}}] \right. \\ &\quad \left. + C_{ij} [(\dot{\mathbf{n}}_i \cdot \mathbf{n}_i)\mathbf{n}_j - (\mathbf{n}_i \cdot \mathbf{n}_j)\dot{\mathbf{n}}_i] + C_{\bar{i}j} [(\dot{\mathbf{n}}_{\bar{i}} \cdot \mathbf{n}_i)\mathbf{n}_j - (\mathbf{n}_i \cdot \mathbf{n}_j)\dot{\mathbf{n}}_{\bar{i}}] \right\}. \end{aligned} \quad (\text{E.3})$$

Putting this back into Eq. (E.1), we get

$$\begin{aligned} \dot{\mathbf{n}}_i = \frac{1}{1 + \sum_j C_{ji} C_{ij} (\mathbf{n}_i \cdot \mathbf{n}_j)} & \left\{ -\mathbf{B} \times \mathbf{n}_i + A_{ii} \mathbf{n}_i \times \mathbf{n}_i \right. \\ & + \sum_j C_{ji} \left[-[(\mathbf{n}_i \cdot \mathbf{B}) \mathbf{n}_j - \mathbf{B}(\mathbf{n}_i \cdot \mathbf{n}_j)] + A_{jj} [(\mathbf{n}_j \cdot \mathbf{n}_i) \mathbf{n}_j - (\mathbf{n}_i \cdot \mathbf{n}_j) \mathbf{n}_j] \right. \\ & \left. \left. + C_{ij} [(\dot{\mathbf{n}}_i \cdot \mathbf{n}_i) \mathbf{n}_j - (\mathbf{n}_i \cdot \mathbf{n}_j) \dot{\mathbf{n}}_i] \right] \right\}. \end{aligned} \quad (\text{E.4})$$

If we now do the sum and insert the elements of the matrices in Eq. (E.2), we get

$$\begin{aligned} \dot{\mathbf{n}}_1 = \frac{1}{1 + \eta_0^2 + (\eta_1^2 - \chi^2)(\mathbf{n}_1 \cdot \mathbf{n}_2)} & \left\{ -\mathbf{B} \times \mathbf{n}_1 + (J + \sigma) \mathbf{n}_2 \times \mathbf{n}_1 + \eta_0 [\mathbf{B} - (\mathbf{n}_1 \cdot \mathbf{B}) \mathbf{n}_1] \right. \\ & + \eta_0 (J + \sigma) [(\mathbf{n}_2 \cdot \mathbf{n}_1) \mathbf{n}_1 - \mathbf{n}_2] + \eta_0 (\eta_1 + \chi) [(\dot{\mathbf{n}}_2 \cdot \mathbf{n}_1) \mathbf{n}_1 - \dot{\mathbf{n}}_2] \\ & - (\eta_1 + \chi) [(\mathbf{n}_1 \cdot \mathbf{B}) \mathbf{n}_2 - \mathbf{B}(\mathbf{n}_1 \cdot \mathbf{n}_2)] + (\eta_1 + \chi)(J - \sigma) [\mathbf{n}_2 - (\mathbf{n}_1 \cdot \mathbf{n}_2) \mathbf{n}_1] \\ & \left. + \eta_0 (\eta_1 + \chi) [(\dot{\mathbf{n}}_2 \cdot \mathbf{n}_1) \mathbf{n}_2 - (\mathbf{n}_1 \cdot \mathbf{n}_2) \dot{\mathbf{n}}_2] \right\} \\ \approx \frac{1}{1 + \eta_0^2 + (\eta_1^2 - \chi^2)(\mathbf{n}_1 \cdot \mathbf{n}_2)} & \left\{ -\mathbf{B} \times \mathbf{n}_1 + (J + \sigma) \mathbf{n}_2 \times \mathbf{n}_1 + \eta_0 [\mathbf{B} - (\mathbf{n}_1 \cdot \mathbf{B}) \mathbf{n}_1] \right. \\ & + [\eta_0 (J + \sigma) - (\eta_1 + \chi)(J - \sigma)] [(\mathbf{n}_2 \cdot \mathbf{n}_1) \mathbf{n}_1 - \mathbf{n}_2] \\ & \left. + (\eta_1 + \chi) [\mathbf{B}(\mathbf{n}_1 \cdot \mathbf{n}_2) - (\mathbf{n}_1 \cdot \mathbf{B}) \mathbf{n}_2] \right\} \\ \approx \frac{1}{1 + \eta_0^2 + (\eta_1^2 - \chi^2)(\mathbf{n}_1 \cdot \mathbf{n}_2)} & \left\{ -\mathbf{B} \times \mathbf{n}_1 + (J + \sigma) \mathbf{n}_2 \times \mathbf{n}_1 + \eta_0 [\mathbf{B} - (\mathbf{n}_1 \cdot \mathbf{B}) \mathbf{n}_1] \right. \\ & + [(\eta_0 - \eta_1)J + (\eta_0 + \eta_1)\sigma - J\chi] [(\mathbf{n}_2 \cdot \mathbf{n}_1) \mathbf{n}_1 - \mathbf{n}_2] \\ & \left. + (\eta_1 + \chi) [\mathbf{B}(\mathbf{n}_1 \cdot \mathbf{n}_2) - (\mathbf{n}_1 \cdot \mathbf{B}) \mathbf{n}_2] \right\}, \end{aligned} \quad (\text{E.5})$$

where we neglected terms of order $\eta_0 \eta_1$ and $\eta_0 \chi$ in the first step and neglected $\sigma \chi$ in the second. The rewriting $\eta_0 (J + \sigma) - (\eta_1 + \chi)(J - \sigma) = (\eta_0 - \eta_1 - \chi)J + (\eta_0 + \eta_1 + \chi)\sigma \approx (\eta_0 - \eta_1)J + (\eta_0 + \eta_1)\sigma - J\chi$ was used in the last step. We now want to see how the component parallel to the magnetic field evolves. Setting $\mathbf{B} = B \hat{z}$, we get

$$\begin{aligned} \dot{n}_1^z = \frac{1}{1 + \eta_0^2 + (\eta_1^2 - \chi^2)(\mathbf{n}_1 \cdot \mathbf{n}_2)} & \left\{ (J + \sigma) (\mathbf{n}_2 \times \mathbf{n}_1) \cdot \hat{z} + \eta_0 B [1 - (n_1^z)^2] \right. \\ & + [(\eta_0 - \eta_1)J + (\eta_0 + \eta_1)\sigma - J\chi] [(\mathbf{n}_1 \cdot \mathbf{n}_2) n_1^z - n_2^z] \\ & \left. + (\eta_1 + \chi) B [\mathbf{n}_1 \cdot \mathbf{n}_2 - n_1^z n_2^z] \right\} \end{aligned} \quad (\text{E.6})$$

E.2 Canted spin configuration

The canted spin configuration is derived in Sec. 3.2.1 in Ref. [149]. It has the angles $\Delta\phi = \pi$ and

$$\theta_1^{\text{can}} = \cos^{-1} \left(\frac{\tilde{B}^2 - 4p_J \tilde{\sigma}}{2\tilde{B}(1 - \tilde{\sigma})} \right), \quad (\text{E.7})$$

which are also given in Eq. (7.10). The canted configuration is a physical solution when

$$-1 < \frac{\tilde{B}^2 - 4p_J \tilde{\sigma}}{2\tilde{B}(1 - \tilde{\sigma})} < 1. \quad (\text{E.8})$$

The inequality for spin 2 is obtained by $\tilde{\sigma} \rightarrow -\tilde{\sigma}$, and this one should also be fulfilled. In the antiferromagnetic case, $p_J = +1$, the right inequality¹ in Eq. (E.8) is

$$\begin{aligned} \frac{\tilde{B}^2 - 4\tilde{\sigma}}{2\tilde{B}(1 - \tilde{\sigma})} &< 1 \\ \tilde{B}^2 - 4\tilde{\sigma} &< 2\tilde{B} - 2\tilde{B}\tilde{\sigma} \\ -\tilde{B}(2 - \tilde{B}) &< 2\tilde{\sigma}(2 - \tilde{B}), \end{aligned} \quad (\text{E.9})$$

where we used that $|\tilde{\sigma}| < 1$ in the first step. If $\tilde{B} > 2$, we will end up with $\tilde{B} < \mp 2\tilde{\sigma}$ (the upper and lower sign refers to spin 1 and 2, respectively), which cannot be fulfilled since \tilde{B} is positive. This therefore sets the upper limit for \tilde{B} . For $\tilde{B} < 2$

$$\tilde{B} > \mp 2\tilde{\sigma}, \quad (\text{E.10})$$

which sets the lower limit for \tilde{B} . Putting these findings together, we have shown that the canted spin configuration is a physical solution when

$$|\tilde{\sigma}| < \tilde{B}/2 < 1. \quad (\text{E.11})$$

If we work out the inequalities in the case of ferromagnetic coupling, $p_J = -1$, we end up with the same limits.

E.3 General linearization of the EOMs

As described in Sec. 7.2.3, the EOMs in Eq. (7.6) can be rewritten as

$$\begin{pmatrix} \partial_\tau \mathbf{n}_1 \\ \partial_\tau \mathbf{n}_2 \end{pmatrix} = \mathbf{A}^{-1} \mathbf{F} \quad (\text{E.12})$$

with

$$\begin{aligned} \mathbf{A} &= \begin{pmatrix} 1 + \eta_0 [\mathbf{n}_1]_\times & (\eta_1 + \chi) [\mathbf{n}_1]_\times \\ (\eta_1 - \chi) [\mathbf{n}_2]_\times & 1 + \eta_0 [\mathbf{n}_2]_\times \end{pmatrix} \\ \mathbf{F} &= \begin{pmatrix} -\tilde{\mathbf{B}} \times \mathbf{n}_1 + (p_J + \tilde{\sigma}) \mathbf{n}_2 \times \mathbf{n}_1 \\ -\tilde{\mathbf{B}} \times \mathbf{n}_1 + (p_J - \tilde{\sigma}) \mathbf{n}_1 \times \mathbf{n}_2 \end{pmatrix}, \end{aligned} \quad (\text{E.13})$$

where \mathbf{A} is a (6×6) matrix while \mathbf{F} is a (6×1) vector. It is convenient to describe the EOM for the individual spin in Eq. (7.6) in their local spherical polar coordinate system since the $\hat{\rho}$ components drop out. However, when treating the coupled EOMs simultaneously, we need to choose a common coordinate system, and we choose to use Cartesian coordinates. The cross product matrix $[\mathbf{n}_i]_\times$ is therefore

$$[\mathbf{n}_i]_\times = \begin{pmatrix} 0 & -n_i^z & n_i^y \\ n_i^z & 0 & -n_i^x \\ -n_i^y & n_i^x & 0 \end{pmatrix} \quad (\text{E.14})$$

¹The left inequality in Eq. (E.8) gives the same limits on \tilde{B} as we find in this section.

so that $[\mathbf{n}_i]_{\times} \mathbf{n}_j = \mathbf{n}_i \times \mathbf{n}_j$. To get the angles on the left hand side of Eq. (E.12), we can rotate the individual vector into its spherical polar coordinate system. Remember that the time derivative in spherical polar coordinates is $\dot{\mathbf{n}}_1 = \dot{\theta}_1 \hat{\theta}_1 + \dot{\phi}_1 \sin \theta_1 \hat{\phi}_1$ so that

$$\begin{pmatrix} 0 \\ \partial_{\tau} \theta_1 \\ \sin \theta_1 \partial_{\tau} \phi_1 \\ 0 \\ \partial_{\tau} \theta_2 \\ \sin \theta_2 \partial_{\tau} \phi_2 \end{pmatrix} = \begin{pmatrix} \mathbf{R}_1 & \mathbf{0} \\ \mathbf{0} & \mathbf{R}_2 \end{pmatrix} \begin{pmatrix} \partial_{\tau} \mathbf{n}_1 \\ \partial_{\tau} \mathbf{n}_2 \end{pmatrix}, \quad (\text{E.15})$$

where \mathbf{R}_i is the rotation matrix that rotates from Cartesian coordinates to the spherical polar coordinates of spin i

$$\mathbf{R}_i = \begin{pmatrix} \sin \theta_i \cos \phi_i & \sin \theta_i \sin \phi_i & \cos \theta_i \\ \cos \theta_i \cos \phi_i & \cos \theta_i \sin \phi_i & -\sin \theta_i \\ -\sin \phi_i & \cos \phi_i & 0 \end{pmatrix}. \quad (\text{E.16})$$

By filtering out $\hat{\rho}$ components (which are zero) in Eq. (E.12), we can get the time derivatives of the angles on the left hand side

$$\partial_{\tau} \begin{pmatrix} \theta_1 \\ \phi_1 \\ \theta_2 \\ \phi_2 \end{pmatrix} = \mathbf{D} \mathbf{F}, \quad (\text{E.17})$$

where \mathbf{D} is the (4×6) matrix

$$\mathbf{D} = \text{diag} \left(1, \frac{1}{\sin \theta_1}, 1, \frac{1}{\sin \theta_2} \right) \begin{pmatrix} 0 & 1 & 0 & 0 & 0 & 0 \\ 0 & 0 & 1 & 0 & 0 & 0 \\ 0 & 0 & 0 & 0 & 1 & 0 \\ 0 & 0 & 0 & 0 & 0 & 1 \end{pmatrix} \begin{pmatrix} \mathbf{R}_1 & \mathbf{0} \\ \mathbf{0} & \mathbf{R}_2 \end{pmatrix} \mathbf{A}^{-1}. \quad (\text{E.18})$$

We have to be a bit careful here, since we divide by $\sin \theta$. We will return to this point shortly. The matrix 'diag' is a diagonal matrix with its inputs on the diagonal.

We will now expand the right hand side to first order in the angles around the fixed points. At first sight, this seems quite messy, but \mathbf{F} vanishes at the fixed point, $\mathbf{F}(\mathbf{v}_0) = 0$. We can therefore write the linear stability equation as

$$\begin{pmatrix} \partial_{\tau} \delta \theta_1 \\ \partial_{\tau} \delta \phi_1 \\ \partial_{\tau} \delta \theta_2 \\ \partial_{\tau} \delta \phi_2 \end{pmatrix} = \mathbf{M} \begin{pmatrix} \delta \theta_1 \\ \delta \phi_1 \\ \delta \theta_2 \\ \delta \phi_2 \end{pmatrix}, \quad (\text{E.19})$$

where

$$\mathbf{M}_{ij} = \sum_k \mathbf{D}_{ik}(\mathbf{v}_0) \left. \frac{\partial \mathbf{F}_k(\mathbf{v})}{\partial v_j} \right|_{\mathbf{v}=\mathbf{v}_0}. \quad (\text{E.20})$$

This stability matrix is used to calculate the phase diagrams in Sec. 7.2.4. \mathbf{D} is evaluated at the fixed point and since it includes the fractions $1/\sin \theta_1^0$ and $1/\sin \theta_2^0$, we have to ensure that the fixed point vectors do not point along the poles. However, as explained in the main text, we can just rotate both $\tilde{\mathbf{B}}$ and the \mathbf{n} 's away from the poles. In this way, Eq. (E.20) can also be used to check the stability of the ferromagnetic and antiferromagnetic configurations.

We could work out the Jacobian matrix in Eq. (E.20) to get an explicit analytic form of the stability matrix, but this is basically what is done in Ref. [149] for the canted spin configuration. If the reader is interested, see e.g. Sec. 4.2 in Ref. [149].

Appendix F

Spin paper draft

This appendix presents a paper draft, which includes the results from Chapters 6 and 7. The introduction to the draft was written by Per Hedegård, while the rest was written by the author of this thesis.

Spins in rough weather

Jens B. Rix^{1,2} and Per Hedegård¹

¹*Nano-Science Center, Niels Bohr Institute,*

University of Copenhagen, 2100 Copenhagen, Denmark

²*Sino-Danish Center for Education and Research (SDC),*

University of Chinese Academy of Sciences, 101408 Beijing, China

(Dated: August 17, 2019)

Abstract

I. INTRODUCTION

The dynamics of a physical system with few degrees of freedom in contact with a large quantum system out of equilibrium is quite general and often complicated. It certainly depends on the degree to which the large system is out of equilibrium. A much studied situation is where the large quantum system is the electrons of a metal brought out of equilibrium such that it carries an electronic current. The physical system in focus could be an atom or a molecule, whose dynamics will change as the environment carries current. It is well known, that a quantum system in contact with some environment will turn classical. This is due to the “collapse” of the system wavefunction that results from the measurements constantly carried out by the environment. The resulting classical dynamics was first studied extensively by Caldeira and Leggett.¹ Their focus was to study to what extent quantum behavior of the system (like e.g. the Josephson current in a Josephson junction) the coupling to the electronic excitations of the superconducting metal.

A byproduct of such studies was the realization, that the resulting effective classical dynamics is of the Langevin equation type. This is Newton’s equation supplemented by extra “forces” due to the coupling to the environment. If the environment is in thermal equilibrium, the forces are friction and random fluctuating forces. The fluctuation-dissipation theorem ensures that those forces are related, such that the resulting dynamics will take the system into a thermal state at the same temperature as that of the environment.

More importantly, if the environment is out of equilibrium, new hitherto less studied forces will emerge. In particular if the system has two or more degrees of freedom, those new forces will couple the system degrees of freedom. Some aspects of this is in fact old news. A vibrating molecule in contact with a large electronic system will have the restoring forces changed due to the presence of the electrons. Vibrational modes will couple, and new normal modes will emerge. If the small system in focus are the magnetic moments of a couple of impurity atoms, the coupling to the electrons will result in an effective RKKY-coupling between the moments. More recently, it was discovered that when brought out of equilibrium, e.g. when a current is present, vibrational modes couple in an entirely new way. The well-known coupling is symmetrical in the mode coordinates, i.e. if the force on one mode x , due to the presence of another y , is $f_x = -ky$, then the force on y is $f_y = -kx$. The new coupling resulting from the non-equilibrium nature of the environment, on the

other hand, is anti-symmetric: $f_x^{nc} = ay$ and $f_y^{nc} = -ax$. Here a is a function of the current which satisfy $a(I = 0) = 0$. This is a non-conservative force field, much like the wind force of a tornado. If the particle is moving with the wind, energy is pumped into the system, while energy is lost if the system moves against the wind. Typically, friction forces are proportional to the velocity. Out of equilibrium environments also produce asymmetric velocity dependent forces: $f_x^B = by$ and $f_y^B = -bx$. This new force is not of the friction type, since it cannot do any work. It is more like a Lorentz force. The origin of such a force is related to the Berry phase of the electrons.² Since the electrons are experiencing a time dependent environment (the physical system we focus on), they will have the phases of their wave function changed a.la. Berry. Since such a phase change does not change the energy of the electron, no energy is being transferred, and hence the resulting force on the system is not changing, i.e. the force cannot do any work.

In the original study of those new forces, the system was described as a set of vibrational modes in the harmonic approximation. I.e. there was no limit to how large the amplitude of the vibrations were. This quickly becomes unphysical. As energy is being pumped into the system, the vibrational amplitudes grow and anharmonic effects will take over and some uncontrollable breakdown of the system will take place. In the case where the system is a molecule, it will either break apart or maybe jump to some other position.

The purpose of this paper is to study a physical system, where the configuration space is limited. A natural candidate is the angular momentum of e.g. an impurity atom. This is much more robust. To change L^2 , a large energy of the order of 1 eV is required. Hence, a model with a fixed L^2 is warranted. Further, we want to study the dynamics of two such angular momenta. They will be coupled through the Ruderman-Kittel-Kasuya-Yosida (RKKY) coupling, but here the focus is on couplings generated through the non-equilibrium nature of the electronic environment. Such a system was studied by von Oppen et al. using the philosophy outlined above.³ These authors, however, only considered one angular moment. As such, the new forces (non-conservative, Berry) which emerge, when we have more than one degree of freedom will be missed. We shall generalized the description of vibrational modes² to a system of angular momenta coupled via an electronic environment in which there is a current. In the original work the current is implemented through an applied bias. Here we will do a much simpler calculation, since we will build a net flow of particles into the density matrix.

A model of coupled angular momenta is interesting to study in its own right, but it can also work as a model for a system with a limited Hilbert space, which is coupled to a current carrying environment of electrons. An example is a system of coupled quantum dots, which has a limited number of bound states in each dot. Such a system can be monitored by a current carrying channel of electrons, which will generate a dynamics of the state of the quantum dot, which can be classified using the concepts developed for the angular momenta system.

In Sec. II, we will derive the equations of motion (EOMs) for two spins coupled to a current carrying simple metal. The explicit expression for the non-equilibrium torques are presented for the first time and we see that they decay slower than the RKKY interaction as a function of distance. In Sec. III, we will do a more general study of the derived EOMs and show that the non-equilibrium torques can drive the spin system into unexpected configurations.

II. THEORY

We will consider two spins in an electronic environment as illustrated in Fig. 1a. The whole system is described by the Hamiltonian

$$H = H_0 + H_{\text{int}}, \quad (1)$$

where the non-interacting part is

$$H_0 = \sum_{\mathbf{k}\sigma} \varepsilon_{\mathbf{k}} c_{\mathbf{k}\sigma}^\dagger c_{\mathbf{k}\sigma} - \mathbf{B} \cdot (\mathbf{S}_1 + \mathbf{S}_2). \quad (2)$$

Here \mathbf{S}_n is a vector of spin operators for the localized spin n , and we consider the electrons to be free, $\varepsilon_{\mathbf{k}} = \hbar^2 k^2 / (2m)$. The localized spins interact with the itinerant electrons via local exchange,

$$H_{\text{int}} = -J_0 [\mathbf{S}_1 \cdot \mathbf{s}(\mathbf{R}_1) + \mathbf{S}_2 \cdot \mathbf{s}(\mathbf{R}_2)], \quad (3)$$

where $\mathbf{s}(\mathbf{r}) = \frac{1}{2V} \sum_{\mathbf{k}\mathbf{k}'} e^{i(\mathbf{k}'-\mathbf{k})\cdot\mathbf{r}} \sum_{\sigma\sigma'} c_{\mathbf{k}\sigma}^\dagger \boldsymbol{\sigma}_{\sigma\sigma'} c_{\mathbf{k}'\sigma'}$ is the spin density of the itinerant electrons. We want to study the dynamics of the localized spins alone. To do so, we use the Feynman-Vernon influence functional method⁴ in which the itinerant electrons are traced out. The propagator for the reduced density matrix can be written as^{1,5}

$$\mathcal{J}(a^1, b^1, t; a^0, b^0, 0) = \int \mathcal{D}a \int \mathcal{D}b e^{i\mathcal{S}[a] - i\mathcal{S}[b]} F[a, b], \quad (4)$$

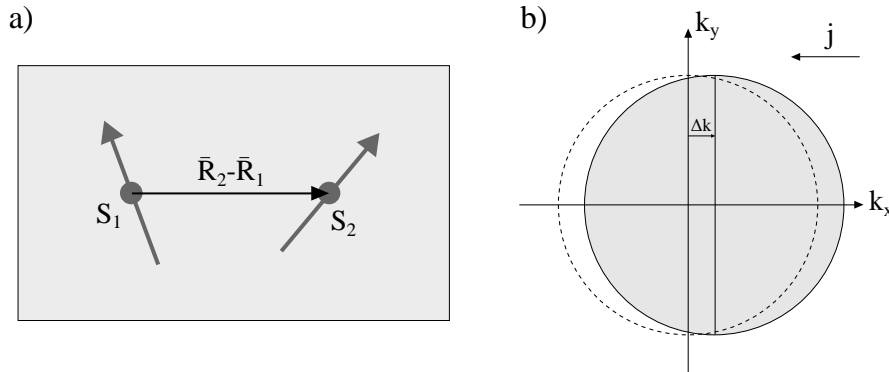


FIG. 1. a) Illustration of two localized spins in an electronic environment. b) The electronic environment is brought out of equilibrium by displacing the Fermi sphere. The figure shows a cross section of the sphere displaced by $\Delta\mathbf{k}$, which is taken to be along k_x in this figure. The displacement, Δk , is small compared to the Fermi wave number, k_F , but it is exaggerated here for visualization purposes.

where $\mathcal{S}[a]$ is the action for the spin. The path integral was constructed using the spin coherent states, $|a\rangle \equiv e^{-i\phi S^z} e^{-i\theta S^y} |\uparrow\rangle$, where $|\uparrow\rangle = |S, m = S\rangle$.[?] The influence functional is

$$F[a, b] = \text{Tr}_e [\hat{\rho}_e(0) U^\dagger[b] U[a]], \quad (5)$$

where $U[a]$ ($U^\dagger[b]$) is the forward (backward) time evolution operator of the electronic system, when the spins follow path a (b). The metal carries a current, which is included in the density operator for the electrons, $\rho_e(0) = Z^{-1} \exp\left[-\beta \sum_{\mathbf{k}\sigma} (\varepsilon_{\mathbf{k}-\Delta\mathbf{k}} - \mu) c_{\mathbf{k}\sigma}^\dagger c_{\mathbf{k}\sigma}\right]$, as illustrated in Fig. 1b.

To obtain the influence of the electrons on the localized spins, we want to get the influence functional on the form $F[a, b] = e^{i\Delta\mathcal{S}[a, b]}$. To do so, a functional integral is constructed from Eq. (5) by using fermionic coherent states. The integral is performed, which yields $F[a, b] = e^{\text{Tr} \ln(1 + G_0 \tilde{V})}$. To second order in the local exchange coupling, J_0 , we get

$$F[a, b] \approx e^{\text{Tr}[G_0 \tilde{V}] - \frac{1}{2} \text{Tr}[G_0 \tilde{V} G_0 \tilde{V}]}, \quad (6)$$

where

$$G_{0,\mathbf{k}}(t, t') = ie^{-i\varepsilon_{\mathbf{k}}(t-t')} \begin{pmatrix} n_F(\varepsilon_{\mathbf{k}-\Delta\mathbf{k}} - \mu) - \theta(t-t') & n_F(\varepsilon_{\mathbf{k}-\Delta\mathbf{k}} - \mu) \\ n_F(\varepsilon_{\mathbf{k}-\Delta\mathbf{k}} - \mu) - 1 & n_F(\varepsilon_{\mathbf{k}-\Delta\mathbf{k}} - \mu) - \theta(t' - t) \end{pmatrix} \quad (7)$$

and

$$\tilde{V}_{\mathbf{k}\sigma,\mathbf{k}'\sigma'}(t) = \begin{pmatrix} V_{\mathbf{k}\sigma,\mathbf{k}'\sigma'}^+(t) & 0 \\ 0 & V_{\mathbf{k}\sigma,\mathbf{k}'\sigma'}^-(t) \end{pmatrix} \quad (8)$$

where $V_{\mathbf{k}\sigma,\mathbf{k}'\sigma'}^\pm(t) = \frac{SJ_0}{2\mathcal{V}} \sum_{n=1,2} e^{-i(\mathbf{k}-\mathbf{k}')\cdot\mathbf{R}_n} \mathbf{n}_n^\pm(t) \cdot \boldsymbol{\sigma}_{\sigma\sigma'}$. For more details, see Supporting information. The first order term in Eq. (6) vanishes due to the trace over the spin indices and the fact that $\text{Tr}[\sigma_i] = 0$ for the Pauli spin matrices σ_i . The second order term in Eq. (6) can be written as $i\Delta\mathcal{S} = -\frac{1}{2} \text{Tr}[G_0\tilde{V}G_0\tilde{V}] = i\mathcal{S}^{\mathcal{Q}\zeta} + i\mathcal{S}^{\zeta\zeta}$, where

$$i\mathcal{S}^{\mathcal{Q}\zeta} = \frac{S^2J_0^2}{2\hbar^2\mathcal{V}^2} \sum_{nm} \int_0^{t_f} dt \int_0^{t'} dt' \int d\omega \Lambda_{nm}(\omega, \Delta\mathbf{k}) e^{-i\omega(t-t')} \boldsymbol{\zeta}_m(t) \cdot \mathbf{Q}_n(t') \theta(t-t') \quad (9)$$

where we introduced the average and difference vectors, $\mathbf{Q} = (n^a + n^b)/2$ and $\boldsymbol{\zeta} = n^a - n^b$, respectively. The introduced effective electron-hole pair density of states is

$$\Lambda_{nm}(\omega, \Delta\mathbf{k}) = \sum_{\mathbf{k}\mathbf{k}'} [n_F(\varepsilon_{\mathbf{k}-\Delta\mathbf{k}} - \mu) - n_F(\varepsilon_{\mathbf{k}'-\Delta\mathbf{k}} - \mu)] e^{-i(\mathbf{k}-\mathbf{k}')\cdot(\mathbf{R}_n-\mathbf{R}_m)} \delta(\omega - \varepsilon_{\mathbf{k}} + \varepsilon_{\mathbf{k}'}). \quad (10)$$

From Eq. (9), we see that the coupling to the electrons give rise to time non-local torques. In Sec. II A, we will assume the electrons to be fast compared to the spins, which will make the EOMs local in time. The effective electron-hole pair density of states has the important properties

$$\Lambda_{nm}^*(\omega, \Delta\mathbf{k}) = \Lambda_{mn}(\omega, \Delta\mathbf{k}), \quad (11)$$

$$\Lambda_{nm}^*(\omega, \Delta\mathbf{k}) = -\Lambda_{nm}(-\omega, \Delta\mathbf{k}), \quad (12)$$

$$\Lambda_{nm}^*(\omega, \Delta\mathbf{k}) = \Lambda_{nm}(\omega, -\Delta\mathbf{k}). \quad (13)$$

To first order in $\Delta\mathbf{k}$, it is clear from Eq. (13) that the real part of Λ gives the equilibrium contributions, while the imaginary part of Λ gives nonequilibrium contributions. Additionally, we see from Eq. (11) that the equilibrium contributions are even under exchange of spin indices, while the nonequilibrium contributions are odd. $\mathcal{S}^{\zeta\zeta}$ is imaginary and suppresses the histories for which the difference vectors, $\boldsymbol{\zeta}$, are large. It is responsible for stochastic torques,^{3,6} which we do not study any further here. The expression for $\mathcal{S}^{\zeta\zeta}$ is found in supporting information.

By Fourier transforming, the contribution to the action in Eq. (9) can be written as

$$iS^{Q\zeta} = i \frac{\pi S^2 J_0^2}{2\mathcal{V}^2} \sum_{nm} \int_0^{t_f} dt \int \frac{d\omega}{2\pi} \left\{ \mathcal{H} \{ \text{Re } \Lambda_{nm} \} (\omega) + \text{Im } \Lambda_{nm}(\omega, \Delta \mathbf{k}) \right. \\ \left. + i [- \text{Re } \Lambda_{nm}(\omega) + \mathcal{H} \{ \text{Im } \Lambda_{nm}(\omega', \Delta \mathbf{k}) \} (\omega)] \right\} \zeta_m(t) \cdot \mathbf{Q}_n(\omega) e^{-i\omega t}, \quad (14)$$

where the Hilbert transform is $\mathcal{H}\{f(\omega')\}(\omega) = \frac{1}{\pi} \mathcal{P} \int d\omega' \frac{f(\omega')}{\omega - \omega'}$.

A. Slow spin approximation

We will now assume that the spins are slow compared to the electrons. This assumption is widely used for magnetic molecules in tunnel junctions.^{3,6-8} In our formalism, the information about the electrons is kept in the four functions in the curly bracket in Eq. (14). If the spins are slow compared to the electrons, the function $\mathbf{Q}_n(\omega)$ is narrow in frequency compared to the functions in the curly brackets, and we can expand these four functions to first order in frequency. By using the property in Eq. (12), the influence of the electrons appear in the action as the effective magnetic field,

$$\mathbf{B}_{\text{eff},n} = \mathbf{B} + \frac{\pi S J_0^2}{2\mathcal{V}^2} \sum_m \left[\mathcal{H} \{ \text{Re } \Lambda_{mn} \} (0) \mathbf{Q}_m + \text{Im } \Lambda_{mn}(0) \mathbf{Q}_m \right. \\ \left. + \frac{\partial}{\partial \omega} \text{Re } \Lambda_{mn}(\omega) \Big|_{\omega=0} \dot{\mathbf{Q}}_m - \frac{\partial}{\partial \omega} \mathcal{H} \{ \text{Im } \Lambda_{mn} \} (\omega) \Big|_{\omega=0} \dot{\mathbf{Q}}_m \right], \quad (15)$$

and in the semi-classical approximation, spin n will precess about this field. By performing the integrals, we arrive at the EOMs

$$\dot{\mathbf{n}}_1 = -\hbar^{-1} \mathbf{B} \times \mathbf{n}_1 + (J + \sigma) \mathbf{n}_2 \times \mathbf{n}_1 + \eta_0 \dot{\mathbf{n}}_1 \times \mathbf{n}_1 + (\eta + \chi) \dot{\mathbf{n}}_2 \times \mathbf{n}_1 \\ \dot{\mathbf{n}}_2 = -\hbar^{-1} \mathbf{B} \times \mathbf{n}_2 + (J - \sigma) \mathbf{n}_1 \times \mathbf{n}_2 + \eta_0 \dot{\mathbf{n}}_2 \times \mathbf{n}_2 + (\eta - \chi) \dot{\mathbf{n}}_1 \times \mathbf{n}_2 \quad (16)$$

where \mathbf{n}_1 is the vector described by the average angles, $\theta = (\theta^a + \theta^b)$ and $\phi = (\phi^a + \phi^b)$, and where the distance dependent coefficients are

$$J(R) = -8\eta_0 \frac{\varepsilon_F}{\hbar} F(2k_F R) \\ \eta_1(R) = \eta_0 \left(\frac{\sin(k_F R)}{k_F R} \right)^2 \\ \sigma(\mathbf{R}) = -4\eta_0 L(k_F R) \frac{\varepsilon_F}{\hbar} \frac{\Delta \mathbf{k} \cdot \mathbf{R}}{k_F R} \\ \chi(\mathbf{R}) = -\frac{8\eta_0}{\pi} L(k_F R) \frac{\varepsilon_F}{\delta \varepsilon} \frac{\Delta \mathbf{k} \cdot \mathbf{R}}{k_F R}. \quad (17)$$

Here $\eta_0 = \frac{\pi S J_0^2}{8} \rho(\varepsilon_F)^2$, where the density of states at the Fermi energy is $\rho(\varepsilon_F) = k_F^3 / (2\pi^2 \varepsilon_F)$ and the distance dependent functions are $F(x) = \frac{x \cos(x) - \sin(x)}{x^4}$ and $L(x) = \sin(x) \frac{x \cos(x) - \sin(x)}{x^3}$. In the derivation of $\chi(\mathbf{R})$, slow electron-hole pairs with energies lower than the cutoff $\delta\varepsilon$ were neglected. The non-equilibrium terms are proportional to $\Delta\mathbf{k} \cdot \mathbf{R}$ and they therefore vanish when the position vector between the spins is perpendicular to the current direction. The EOMs in Eq. (16) have been derived by Onoda et al.⁹ However, this is the first time that the explicit expressions for the non-equilibrium coefficients, σ and χ , have been presented.

For the specific model, one can estimate the magnitudes of these new coefficients. For a current density of 10^6 A cm^{-2} in a copper nanowire and the distance $R = 7 \text{ \AA}$ between the spins, the coefficients are $|\sigma/J| \approx 10^{-4}$ and $|\chi/\eta_0| \approx 10^{-2}$. Here, a cutoff equivalent to an electron in a 0.01 T magnetic field was used.

III. ANALYSIS OF EQUATIONS OF MOTION

Having established the EOMs for a specific model, we will now do a more general study of the EOMs. We will assume that the non-equilibrium coefficients, σ and χ , can take larger values than estimated for the specific model above. The coupled differential equations have fixed points, $\dot{\mathbf{n}}_1 = \dot{\mathbf{n}}_2 = 0$, when $\mathbf{B} \times \mathbf{n}_1 = (J + \sigma)\mathbf{n}_2 \times \mathbf{n}_1$ and $\mathbf{B} \times \mathbf{n}_2 = (J - \sigma)\mathbf{n}_1 \times \mathbf{n}_2$ are fulfilled. It is easy to see that the ferromagnetic (FM) configurations (\uparrow, \uparrow) and (\downarrow, \downarrow) as well as the antiferromagnetic (AFM) configurations (\uparrow, \downarrow) and (\downarrow, \uparrow) are fixed points. Here the first (second) arrow refers to spin 1 (2) and up refers to the direction of the magnetic field. Additionally, it can be derived that a canted spin configuration with $\phi_2 - \phi_1 = \pi$ and

$$\theta_{1/2}^{\text{canted}} = \cos^{-1} \left(\frac{B^2 \mp 4J\sigma}{2B(J \mp \sigma)} \right), \quad (18)$$

is a fixed point when $2|\sigma| < B < 2|J|$. From Eq. (18), we see that the θ -angles in the canted spin are equal in equilibrium, but the introduction of σ skews the configuration.

The nonequilibrium terms in the EOMs can drive the spin system into unexpected configurations. When the coupling is AFM, $J > 0$, the equilibrium system would reach either the canted or antiferromagnetic configuration depending on the size of B/J . However, the presence of the nonequilibrium terms can drive the system into the ferromagnetic configuration. This is shown in Fig. 2a, where the trajectories of two spins are plotted for the indicated choice of parameters. The dots in the figure indicate the initial spin orientations,

while the arrows show where the spins end up. Similarly, in Fig. 2b and Fig. 2c the coupling is ferromagnetic and we would expect the spins to reach a point where they both point up along the B-field. However, in Fig. 2b the spins end up in the canted configuration with the angles shown in Eq. (18), while both spins reach a point where they point antiparallel to the magnetic field in Fig. 2c.

To get a more complete picture of the parameter space, we do a linear stability analysis around the fixed points. For the FM and AFM configurations this is most easily done by linearizing the vectors $(n_i^x, n_i^y, n_i^z) \approx (x_i, y_i, \pm 1)$, where the upper (lower) sign refers to the spin pointing (anti-)parallel to the magnetic field. Inserting these into the EOMs and keeping only first order terms, we can write $(\delta\dot{x}_1, \delta\dot{y}_1, \delta\dot{x}_2, \delta\dot{y}_2)^T = \mathbf{M}_{z_1, z_2} (\delta x_1, \delta y_1, \delta x_2, \delta y_2)^T$, where $\delta x_1 = x_1 - x_1^0$ is the deviation from the fixed point coordinate x_1^0 and where the subfixes of the matrix indicate the fixed point, $z_i = \pm 1$. For the canted spin configuration, we can rewrite the EOMs as $(\dot{\mathbf{n}}_1^T, \dot{\mathbf{n}}_2^T)^T = [\mathbf{F}(\mathbf{n}_1, \mathbf{n}_2)]^T$, where $\mathbf{F}(\mathbf{n}_1, \mathbf{n}_2)$ is a vector. Linearization and rotation lead to $(\delta\dot{\theta}_1, \delta\dot{\phi}_1, \delta\dot{\theta}_2, \delta\dot{\phi}_2)^T = \mathbf{M}_{\text{canted}} (\delta\theta_1, \delta\phi_1, \delta\theta_2, \delta\phi_2)^T$, where $\mathbf{M}_{\text{canted}}$ contains the Jacobian matrix. A fixed point is stable, when all the real parts of the eigenvalues of the corresponding matrix are negative, and we therefore have the tool to scan the parameter space for stabilities.

The stability diagram in the case of AFM coupling is shown in Fig. 3a. As expected, the canted configuration is stable in the equilibrium case, $(\sigma, \chi) = (0, 0)$, where the exchange coupling and magnetic field compete. As σ and χ become sufficiently large and of opposite sign, we see that the ferromagnetic configuration (\uparrow, \uparrow) becomes stable. This means that the non-equilibrium terms have driven the system into a configuration where the exchange energy is maximized. Remember that the spin configurations in the canted spin region in Fig. 3 are different for the different σ values as stated in Eq. (18).

The same analysis is done in the case of FM coupling, and the result is shown in Fig. 3b. As expected, the equilibrium configuration is FM pointing along the magnetic field, but as the σ and χ become sufficiently large and of opposite sign, both spins will end up pointing antiparallel to the magnetic field. This is surprising since it maximizes the energy contribution from the magnetic field. If σ and χ are large and of same sign, the canted configuration becomes stable, while none of the fixed points are stable in the white region in Fig. 3b. The diagrams agree with the end points of the trajectories in Fig. 2, and a raster scan of numerical simulations has been done to confirm the stability diagrams in Fig. 3.

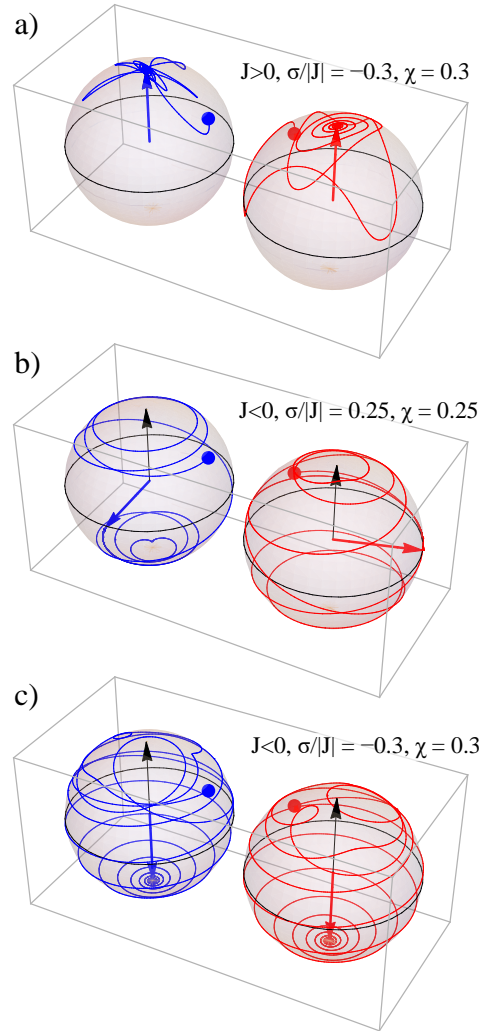


FIG. 2. Spin trajectories obtained from Euler method simulations of the equations of motion. In all cases, the spins start in the arbitrarily chosen configuration $(\theta_1, \phi_1, \theta_2, \phi_2) = (0.3\pi, 0, 0.4\pi, 0.8\pi)$, which is represented by a dots. The simulations ran until the spins stopped moving, and the final directions are shown by arrows. In (b) the spins end up in the canted spin configuration with $(n_1^z, n_2^z) = (-0.8, 0)$ and $\Delta\phi = \pi$, which agrees with Eq. (18). In all simulations, the parameters $B/|J| = 1$, $\eta_0 = 0.01$, and $\eta_0 = 0.5\eta_0$ are used.

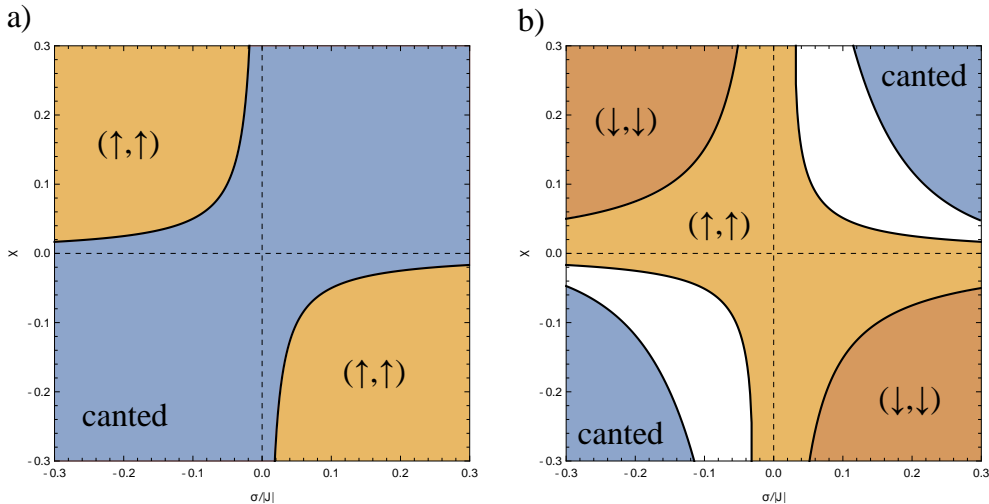


FIG. 3. Phase diagrams obtained from a linear stability analysis with parameters $B/|J| = 1$, $\eta_0 = 0.01$, and $\eta_1 = 0.5\eta_0$. In (a), the coupling is FM, $J > 0$, while it is AFM in (b), $J < 0$. In the white region, none of the fixed points are stable.

The stability diagrams in Fig. 3 are symmetric under the inversion $(\sigma, \chi) \rightarrow (-\sigma, -\chi)$. The reason is that the EOMs in Eq. (16) are left unchanged by the exchanges $(\sigma, \chi) \rightarrow (-\sigma, -\chi)$ and $(1, 2) \rightarrow (2, 1)$.

Since σ and χ originate from an electric current, the findings in Fig. 3 suggest that an electric current can drive two magnetic moments into a variety of configurations. A possible application is that an electric current can be used to prepare a system with magnetic moments in a desired configuration.

IV. CONCLUSION

We have used the Feynman-Vernon influence functional approach to derive the EOMs for two spins that couple to a current carrying metal. The non-equilibrium torques were calculated for a specific model and the explicit expressions were presented. A general study of the EOMs showed that the non-equilibrium torques can drive the spin system into unexpected configurations. With this discovered property, a current can maybe be used to prepare a

spin system in different desired configurations.

-
- ¹ A. O. Caldeira and A. J. Leggett, “*Path integral approach to quantum Brownian motion*,” *Physica A: Statistical Mechanics and its Applications* **121**, 587 (1983).
 - ² J. T. Lü, M. Brandbyge, and P. Hedegård, “*Blowing the Fuse: Berry’s Phase and Runaway Vibrations in Molecular Conductors*,” *Nano Letters* **10**, 1657 (2010).
 - ³ N. Bode, L. Arrachea, G. S. Lozano, T. S. Nunner, and F. von Oppen, “*Current-induced switching in transport through anisotropic magnetic molecules*,” *Phys. Rev. B* **85**, 115440 (2012).
 - ⁴ R. P. Feynman and F. L. Vernon, “*The theory of a general quantum system interacting with a linear dissipative system*,” *Annals of Physics* **24**, 118 (1963).
 - ⁵ A. Schmid, “*On a quasiclassical Langevin equation*,” *Journal of Low Temperature Physics* **49**, 609 (1982).
 - ⁶ J. Fransson and J.-X. Zhu, “*Spin dynamics in a tunnel junction between ferromagnets*,” *New Journal of Physics* **10**, 013017 (2008).
 - ⁷ J.-X. Zhu, Z. Nussinov, A. Shnirman, and A. V. Balatsky, “*Novel Spin Dynamics in a Josephson Junction*,” *Phys. Rev. Lett.* **92**, 107001 (2004).
 - ⁸ J.-X. Zhu and J. Fransson, “*Electric field control of spin dynamics in a magnetically active tunnel junction*,” *Journal of Physics: Condensed Matter* **18**, 9929 (2006).
 - ⁹ M. Onoda and N. Nagaosa, “*Dynamics of Localized Spins Coupled to the Conduction Electrons with Charge and Spin Currents*,” *Phys. Rev. Lett.* **96**, 66603 (2006).

Bibliography

- [1] J. B. Rix, *Thermoelectrically Driven Current Loops*, Master's thesis, University of Copenhagen (2015).
- [2] H. D. Young, R. A. Freedman, and F. Lewis, *University Physics with Modern Physics*, 13th ed. (Pearson Addison Wesley, 2012) p. 885.
- [3] T. J. Seebeck, "Ueber die Magnetische Polarisation der Metalle und Erze durch Temperatur-Differenz (*On the magnetic polarization of metals and minerals by temperature differences*)," *Annalen der Physik und Chemie* **6**, 1 (1826).
- [4] E. Velmre, "Thomas Johann Seebeck (1770–1831)," *Proc. Estonian Acad. Sci. Eng.* **13**, 276 (2007).
- [5] K. L. Caneva, *The Form and Function of Scientific Discoveries* (Smithsonian Institution Libraries., Washington, DC, 2001) pp. 1–10.
- [6] J. Solyom, in *Fundamentals of the Physics of Solids* (Springer, 2007) Chap. 16.
- [7] J. C. A. Peltier, "Nouvelles expériences sur la caloricité des courants électrique (*New experiments on the heat effects of electric currents*)," *Annales de Chimie et de Physique* **56**, 371 (1834).
- [8] L. Onsager, "Reciprocal Relations in Irreversible Processes," *Physical Review* **37**, 405 (1931).
- [9] H. B. Callen, "The application of Onsager's reciprocal relations to thermoelectric, thermomagnetic, and galvanomagnetic effects," *Physical Review* **73**, 1349 (1948).
- [10] G. Pennelli, "Review of nanostructured devices for thermoelectric applications," *Beilstein Journal of Nanotechnology* **5**, 1268 (2014).
- [11] Caltech Thermoelectrics group, "Brief History of Thermoelectrics," <http://www.thermoelectrics.caltech.edu/thermoelectrics/history.html> .
- [12] G. Joshi, H. Lee, Y. Lan, X. Wang, G. Zhu, D. Wang, R. W. Gould, D. C. Cuff, M. Y. Tang, M. S. Dresselhaus, G. Chen, and Z. Ren, "Enhanced Thermoelectric Figure-of-Merit in Nanostructured p-type Silicon Germanium Bulk Alloys," *Nano Letters* **8**, 4670 (2008).
- [13] Y. Lan, A. J. Minnich, G. Chen, and Z. Ren, "Enhancement of Thermoelectric Figure-of-Merit by a Bulk Nanostructuring Approach," *Advanced Functional Materials* **20**, 357 (2010).
- [14] R. Venkatasubramanian, E. Siivola, T. Colpitts, and B. O'Quinn, "Thin-film thermoelectric devices with high room-temperature figures of merit," *Nature* **413**, 597 (2001).

- [15] A. I. Boukai, Y. Bunimovich, J. Tahir-Kheli, J.-K. Yu, W. A. Goddard III, and J. R. Heath, “*Silicon nanowires as efficient thermoelectric materials*,” *Nature* **451**, 168 (2008).
- [16] J. L. Blackburn, A. J. Ferguson, C. Cho, and J. C. Grunlan, “*Carbon-Nanotube-Based Thermoelectric Materials and Devices*,” *Advanced Materials* **30**, 1704386 (2018).
- [17] C. M. Finch, V. M. García-Suárez, and C. J. Lambert, “*Giant thermopower and figure of merit in single-molecule devices*,” *Phys. Rev. B* **79**, 33405 (2009).
- [18] L.-D. Zhao, S.-H. Lo, Y. Zhang, H. Sun, G. Tan, C. Uher, C. Wolverton, V. P. Dravid, and M. G. Kanatzidis, “*Ultralow thermal conductivity and high thermoelectric figure of merit in SnSe crystals*,” *Nature* **508**, 373 (2014).
- [19] C. Goupil, *Continuum Theory and Modeling of Thermoelectric Elements* (John Wiley and Sons, 2015) p. 7.
- [20] H. Bruus and K. Flensberg, *Many-Body Quantum Theory in Condensed Matter Physics* (Oxford University Press, 2004) pp. 103–111.
- [21] S. Datta, *Quantum Transport: Atom to Transistor* (Cambridge University Press, Cambridge, 2005).
- [22] O. Karlström, M. Strange, and G. C. Solomon, “*Understanding the length dependence of molecular junction thermopower*,” *The Journal of Chemical Physics* **140**, 044315 (2014).
- [23] F. Hüser and G. C. Solomon, “*From Chemistry to Functionality: Trends for the Length Dependence of the Thermopower in Molecular Junctions*,” *The Journal of Physical Chemistry C* **119**, 14056 (2015).
- [24] G. D. Mahan and J. O. Sofo, “*The best thermoelectric*,” *Proceedings of the National Academy of Sciences* **93**, 7436 (1996).
- [25] R. Kim, S. Datta, and M. S. Lundstrom, “*Influence of dimensionality on thermoelectric device performance*,” *Journal of Applied Physics* **105**, 034506 (2009).
- [26] C. Jeong, R. Kim, and M. S. Lundstrom, “*On the best bandstructure for thermoelectric performance: A Landauer perspective*,” *Journal of Applied Physics* **111**, 113707 (2012).
- [27] P. Reddy, S.-Y. Jang, R. A. Segalman, and A. Majumdar, “*Thermoelectricity in Molecular Junctions*,” *Science* **315**, 1568 (2007).
- [28] J. R. Widawsky, P. Darancet, J. B. Neaton, and L. Venkataraman, “*Simultaneous determination of conductance and thermopower of single molecule junctions*,” *Nano Letters* **12**, 354 (2012).
- [29] J. A. Malen, P. Doak, K. Baheti, T. D. Tilley, R. A. Segalman, and A. Majumdar, “*Identifying the Length Dependence of Orbital Alignment and Contact Coupling in Molecular Heterojunctions*,” *Nano Letters* **9**, 1164 (2009).
- [30] C. Jeong, R. Kim, M. Luisier, S. Datta, and M. Lundstrom, “*On Landauer versus Boltzmann and full band versus effective mass evaluation of thermoelectric transport coefficients*,” *Journal of Applied Physics* **107**, 023707 (2010).

- [31] J. Solyom, in *Fundamentals of the Physics of Solids* (Springer, 2007) Chap. 26.
- [32] N. F. Mott and H. Jones, *The theory of the properties of metals and alloys* (Oxford: The Clarendon Press, 1936).
- [33] D. Venkateshvaran, *Seebeck coefficient in organic semiconductors*, **Phd thesis**, University of Cambridge (2014).
- [34] H. Fritzsche, “A general expression for the thermoelectric power,” *Solid State Communications* **9**, 1813 (1971).
- [35] C. Herring, “Theory of the Thermoelectric Power of Semiconductors,” *Phys. Rev.* **96**, 1163 (1954).
- [36] M. Lundstrom, “Lecture 4: Thermoelectric Effects - Physical Approach,” (2011).
- [37] M. Lundstrom, “Lecture 5: Thermoelectric Effects - Mathematics,” (2011).
- [38] K. P. Pernstich, B. Rössner, and B. Batlogg, “Field-effect-modulated Seebeck coefficient in organic semiconductors,” *Nature Materials* **7**, 321 (2008).
- [39] Y. Apertet, H. Ouerdane, C. Goupil, and P. Lecoeur, “Thermoelectric internal current loops inside inhomogeneous systems,” *Phys. Rev. B* **85**, 33201 (2012).
- [40] J. B. Rix and P. Hedegård, “Thermoelectric Driven Ring Currents in Single Molecules and Graphene Nanoribbons,” *The Journal of Physical Chemistry C* **123**, 3817 (2019).
- [41] L. I. Anatyshuk and A. V. Prybyla, “On the Theory of the Anisotropic Thermoelement,” *Journal of Electronic Materials* **40**, 1304 (2011).
- [42] T. W. Silk and A. J. Schofield, “Thermoelectric Effects in Anisotropic Systems: Measurement and Applications,” (2008), [arXiv:0808.3526](https://arxiv.org/abs/0808.3526) .
- [43] L. I. Anatyshuk and O. Y. Luste, “Thermoelectric eddy currents and transverse thermal emf in zonally inhomogeneous plates,” *Soviet Physics Journal* **12**, 801 (1969).
- [44] D. Fu, A. X. Levander, R. Zhang, J. W. Ager, and J. Wu, “Electrothermally driven current vortices in inhomogeneous bipolar semiconductors,” *Phys. Rev. B* **84**, 45205 (2011).
- [45] L. I. Anatyshuk and O. J. Luste, in *XVI ICT '97. Proceedings ICT'97. 16th International Conference on Thermoelectrics (Cat. No.97TH8291)* (1997) pp. 595–598.
- [46] M. A. Reed, C. Zhou, C. J. Muller, T. P. Burgin, and J. M. Tour, “Conductance of a Molecular Junction,” *Science* **278**, 252 (1997).
- [47] B. Xu and N. J. Tao, “Measurement of Single-Molecule Resistance by Repeated Formation of Molecular Junctions,” *Science* **301**, 1221 (2003).
- [48] S. V. Aradhya and L. Venkataraman, “Single-molecule junctions beyond electronic transport,” *Nature Nanotechnology* **8**, 399 (2013).
- [49] M. Ratner, “A brief history of molecular electronics,” *Nature Nanotechnology* **8**, 378 (2013).

- [50] D. Xiang, X. Wang, C. Jia, T. Lee, and X. Guo, “*Molecular-Scale Electronics: From Concept to Function*,” *Chemical Reviews* **116**, 4318 (2016).
- [51] G. C. Solomon, C. Herrmann, T. Hansen, V. Mujica, and M. A. Ratner, “*Exploring local currents in molecular junctions*,” *Nature Chemistry* **2**, 223 (2010).
- [52] C. Herrmann, G. C. Solomon, and M. A. Ratner, “*Local Pathways in Coherent Electron Transport through Iron Porphyrin Complexes: A Challenge for First-Principles Transport Calculations*,” *The Journal of Physical Chemistry C* **114**, 20813 (2010).
- [53] D. Nozaki and W. G. Schmidt, “*Current density analysis of electron transport through molecular wires in open quantum systems*,” *Journal of Computational Chemistry* **38**, 1685 (2017).
- [54] G. Cabra, A. Jensen, and M. Galperin, “*On simulation of local fluxes in molecular junctions*,” *The Journal of Chemical Physics* **148**, 204103 (2018).
- [55] Y. Tsuji, R. Movassagh, S. Datta, and R. Hoffmann, “*Exponential Attenuation of Through-Bond Transmission in a Polyene: Theory and Potential Realizations*,” *ACS Nano* **9**, 11109 (2015).
- [56] T. Stuyver, N. Blotwijk, S. Fias, P. Geerlings, and F. De Proft, “*Exploring Electrical Currents through Nanographenes: Visualization and Tuning of the through-Bond Transmission Paths*,” *ChemPhysChem* **18**, 3012 (2017).
- [57] D. Rai, O. Hod, and A. Nitzan, “*Circular currents in molecular wires*,” *Journal of Physical Chemistry C* **114**, 20583 (2010).
- [58] M. Ernzerhof, H. Bahmann, F. Goyer, M. Zhuang, and P. Rocheleau, “*Electron Transmission through Aromatic Molecules*,” *Journal of Chemical Theory and Computation* **2**, 1291 (2006).
- [59] M. Paulsson, “*Non Equilibrium Green’s Functions for Dummies: Introduction to the One Particle NEGF equations*,” (2002), arXiv:0210519 [cond-mat] .
- [60] C. Caroli, R. Combescot, P. Nozieres, and D. Saint-James, “*Direct calculation of the tunneling current*,” *Journal of Physics C: Solid State Physics* **4**, 916 (1971).
- [61] Y. Meir and N. S. Wingreen, “*Landauer formula for the current through an interacting electron region*,” *Phys. Rev. Lett.* **68**, 2512 (1992).
- [62] T. N. Todorov, “*Tight-binding simulation of current-carrying nanostructures*,” *Journal of Physics: Condensed Matter* **14**, 3049 (2002).
- [63] A. Pecchia and A. D. Carlo, “*Atomistic theory of transport in organic and inorganic nanostructures*,” *Reports on Progress in Physics* **67**, 1497 (2004).
- [64] T. Markussen, R. Stadler, and K. S. Thygesen, “*The Relation between Structure and Quantum Interference in Single Molecule Junctions*,” *Nano Letters* **10**, 4260 (2010).
- [65] K. G. L. Pedersen, M. Strange, M. Leijnse, P. Hedegård, G. C. Solomon, and J. Paaske, “*Quantum interference in off-resonant transport through single molecules*,” *Phys. Rev. B* **90**, 125413 (2014).

- [66] M. Zilly, *Electronic conduction in linear quantum systems: Coherent transport and the effects of decoherence*, *Phd thesis*, Universität Duisburg-Essen (2010).
- [67] T.-W. Tsai, Q.-R. Huang, S.-M. Peng, and B.-Y. Jin, “Smallest Electrical Wire Based on Extended Metal-Atom Chains,” *The Journal of Physical Chemistry C* **114**, 3641 (2010).
- [68] D. Rai, O. Hod, and A. Nitzan, “Magnetic fields effects on the electronic conduction properties of molecular ring structures,” *Phys. Rev. B* **85**, 155440 (2012).
- [69] H. K. Yadalam and U. Harbola, “Controlling local currents in molecular junctions,” *Phys. Rev. B* **94**, 115424 (2016).
- [70] M. Brandbyge, M. R. Sørensen, and K. W. Jacobsen, “Conductance eigenchannels in nanocontacts,” *Phys. Rev. B* **56**, 14956 (1997).
- [71] M. Paulsson and M. Brandbyge, “Transmission eigenchannels from nonequilibrium Green’s functions,” *Phys. Rev. B* **76**, 115117 (2007).
- [72] M. G. Reuter and T. Hansen, “Communication: Finding destructive interference features in molecular transport junctions,” *The Journal of Chemical Physics* **141**, 181103 (2014).
- [73] S. K. Maiti, “Conformation-dependent electron transport through a biphenyl molecule: circular current and related issues,” *The European Physical Journal B* **86**, 296 (2013).
- [74] C. A. Coulson and G. S. Rushbrooke, “Note on the method of molecular orbitals,” *Mathematical Proceedings of the Cambridge Philosophical Society* **36**, 193 (1940).
- [75] R. B. Mallion and D. H. Rouvray, “The golden jubilee of the Coulson-Rushbrooke pairing theorem,” *Journal of Mathematical Chemistry* **5**, 1 (1990).
- [76] Y. M. Zuev, W. Chang, and P. Kim, “Thermoelectric and Magnetothermoelectric Transport Measurements of Graphene,” *Phys. Rev. Lett.* **102**, 96807 (2009).
- [77] M. P. L. Sancho, J. M. L. Sancho, J. M. L. Sancho, and J. Rubio, “Highly convergent schemes for the calculation of bulk and surface Green functions,” *Journal of Physics F: Metal Physics* **15**, 851 (1985).
- [78] G. Metalidis, *Electronic Transport in Mesoscopic Systems*, *Phd thesis*, Martin-Luther-Universität Halle-Wittenberg (2007).
- [79] B. Maennig, M. Pfeiffer, A. Nollau, X. Zhou, K. Leo, and P. Simon, “Controlled p-type doping of polycrystalline and amorphous organic layers: Self-consistent description of conductivity and field-effect mobility by a microscopic percolation model,” *Phys. Rev. B* **64**, 195208 (2001).
- [80] D. Wang, L. Tang, M. Long, and Z. Shuai, “First-principles investigation of organic semiconductors for thermoelectric applications,” *The Journal of Chemical Physics* **131**, 224704 (2009).
- [81] W. C. Germs, K. Guo, R. A. J. Janssen, and M. Kemerink, “Unusual Thermoelectric Behavior Indicating a Hopping to Bandlike Transport Transition in Pentacene,” *Phys. Rev. Lett.* **109**, 16601 (2012).

- [82] C. Wang, H. Dong, L. Jiang, and W. Hu, "Organic semiconductor crystals," *Chem. Soc. Rev.* **47**, 422 (2018).
- [83] H. Klauk, R. Noriega, and A. Salleo, in *Organic Electronics II: More Materials and Applications* (2012) Chap. 3, pp. 68–73.
- [84] J. R. Widawsky, W. Chen, H. Vázquez, T. Kim, R. Breslow, M. S. Hybertsen, and L. Venkataraman, "Length-Dependent Thermopower of Highly Conducting Au–C Bonded Single Molecule Junctions," *Nano Letters* **13**, 2889 (2013).
- [85] D. Kim, P. S. Yoo, and T. Kim, "Length-dependent thermopower determination of amine-terminated oligophenyl single molecular junctions formed with Ag electrodes," *Journal of the Korean Physical Society* **66**, 602 (2015).
- [86] E. J. Dell, B. Capozzi, J. Xia, L. Venkataraman, and L. M. Campos, "Molecular length dictates the nature of charge carriers in single-molecule junctions of oxidized oligothiophenes," *Nature Chemistry* **7**, 209 (2015).
- [87] E. I. Rogacheva, O. N. Nashchekina, Y. O. Vekhov, and M. S. Dresselhaus, "Oscillations in the thickness dependences of the Seebeck coefficient in SnTe thin films," *International Conference on Thermoelectrics, ICT, Proceedings 2003-Janua*, 346 (2003).
- [88] M. Kayyalha, J. Maassen, M. Lundstrom, L. Shi, and Y. P. Chen, "Gate-tunable and thickness-dependent electronic and thermoelectric transport in few-layer MoS₂," *Journal of Applied Physics* **120**, 134305 (2016).
- [89] M. T. Pettes, J. Maassen, I. Jo, M. S. Lundstrom, and L. Shi, "Effects of surface band bending and scattering on thermoelectric transport in suspended bismuth telluride nanoplates," *Nano Letters* **13**, 5316 (2013).
- [90] X. C. Li, H. Sirringhaus, F. Garnier, A. B. Holmes, S. C. Moratti, N. Feeder, W. Clegg, S. J. Teat, and R. H. Friend, "A highly π -stacked organic semiconductor for thin film transistors based on fused thiophenes," *Journal of the American Chemical Society* **120**, 2206 (1998).
- [91] A. Irfan, M. Nadeem, M. Athar, F. Kanwal, and J. Zhang, "Electronic, optical and charge transfer properties of α,α' -bis(dithieno[3,2-b:2',3'-d]thiophene) (BDT) and its heteroatom-substituted analogues," *Computational and Theoretical Chemistry* **968**, 8 (2011).
- [92] H. Sirringhaus, R. H. Friend, X. C. Li, S. C. Moratti, A. B. Holmes, and N. Feeder, "Bis(dithienothiophene) organic field-effect transistors with a high ON/OFF ratio," *Applied Physics Letters* **71**, 3871 (1997).
- [93] E. van Faassen and H. Kerp, "Explanation of the low oxygen sensitivity of thin film phthalocyanine gas sensors," *Sensors and Actuators B: Chemical* **88**, 329 (2003).
- [94] P. K. Nayak, R. Rosenberg, L. Barnea-Nehoshtan, and D. Cahen, "O₂ and organic semiconductors: Electronic effects," *Organic Electronics* **14**, 966 (2013).
- [95] A. Majumdar, "Scanning Thermal Microscopy," *Annual Review of Materials Science* **29**, 505 (1999).

- [96] L. Shi and A. Majumdar, “*Thermal Transport Mechanisms at Nanoscale Point Contacts*,” *Journal of Heat Transfer* **124**, 329 (2002).
- [97] J. Solyom, in *Fundamentals of the Physics of Solids* (Springer, 2007) Chap. 27.
- [98] V. Palermo, M. Palma, and P. Samori, “*Electronic characterization of organic thin films by Kelvin probe force microscopy*,” *Advanced Materials* **18**, 145 (2006).
- [99] W. Melitz, J. Shen, A. C. Kummel, and S. Lee, “*Kelvin probe force microscopy and its application*,” *Surface Science Reports* **66**, 1 (2011).
- [100] M. Oehzelt, N. Koch, and G. Heimel, “*Organic semiconductor density of states controls the energy level alignment at electrode interfaces*,” *Nature Communications* **5**, 4174 (2014).
- [101] S. D. Fried and S. G. Boxer, “*Measuring Electric Fields and Noncovalent Interactions Using the Vibrational Stark Effect*,” *Accounts of Chemical Research* **48**, 998 (2015).
- [102] S. H. Brewer and S. Franzen, “*A quantitative theory and computational approach for the vibrational Stark effect*,” *The Journal of Chemical Physics* **119**, 851 (2003).
- [103] S. V. Faleev and F. Léonard, “*Theory of enhancement of thermoelectric properties of materials with nanoinclusions*,” *Phys. Rev. B* **77**, 214304 (2008).
- [104] D.-K. Ko, Y. Kang, and C. B. Murray, “*Enhanced Thermopower via Carrier Energy Filtering in Solution-Processable Pt-Sb₂Te₃ Nanocomposites*,” *Nano Letters* **11**, 2841 (2011).
- [105] S. I. Kim, S. Hwang, J. W. Roh, K. Ahn, D.-H. Yeon, K. H. Lee, and S. W. Kim, “*Experimental evidence of enhancement of thermoelectric properties in tellurium nanoparticle-embedded bismuth antimony telluride*,” *Journal of Materials Research* **27**, 2449 (2012).
- [106] C. Kittel, *Introduction to Solid State Physics*, 8th ed. (Wiley, 2005).
- [107] N. Kim, B. Domercq, S. Yoo, A. Christensen, B. Kippelen, and S. Graham, “*Thermal transport properties of thin films of small molecule organic semiconductors*,” *Applied Physics Letters* **87**, 1 (2005).
- [108] E. W. Lemmon and R. T. Jacobsen, “*Viscosity and Thermal Conductivity Equations for Nitrogen, Oxygen, Argon, and Air*,” *International Journal of Thermophysics* **25**, 21 (2004).
- [109] K. Kim, J. Chung, G. Hwang, O. Kwon, and J. Sik Lee, “*Quantitative Measurement with Scanning Thermal Microscope by Preventing the Distortion Due to the Heat Transfer through the Air*,” *ACS Nano* **5**, 8700 (2011).
- [110] S. Gomès, A. Assy, and P.-O. Chapuis, “*Scanning thermal microscopy: A review*,” *Physica Status Solidi (a)* **212**, 477 (2015).
- [111] H. K. Ng, D. Chi, and K. Hippalgaonkar, “*Effect of dimensionality on thermoelectric powerfactor of molybdenum disulfide*,” *Journal of Applied Physics* **121**, 204303 (2017).

- [112] A. Schmid, “*On a quasiclassical Langevin equation,*” *Journal of Low Temperature Physics* **49**, 609 (1982).
- [113] A. O. Caldeira and A. J. Leggett, “*Path integral approach to quantum Brownian motion,*” *Physica A: Statistical Mechanics and its Applications* **121**, 587 (1983).
- [114] D. Dundas, E. J. McEniry, and T. N. Todorov, “*Current-driven atomic water-wheels,*” *Nature Nanotechnology* **4**, 99 (2009).
- [115] J. T. Lü, M. Brandbyge, and P. Hedegård, “*Blowing the Fuse: Berry’s Phase and Runaway Vibrations in Molecular Conductors,*” *Nano Letters* **10**, 1657 (2010).
- [116] J.-T. Lü, M. Brandbyge, P. Hedegård, T. N. Todorov, and D. Dundas, “*Current-induced atomic dynamics, instabilities, and Raman signals: Quasiclassical Langevin equation approach,*” *Phys. Rev. B* **85**, 245444 (2012).
- [117] T. N. Todorov, D. Dundas, J.-T. Lü, M. Brandbyge, and P. Hedegård, “*Current-induced forces: a simple derivation,*” *European Journal of Physics* **35**, 065004 (2014).
- [118] M. A. Ruderman and C. Kittel, “*Indirect exchange coupling of nuclear magnetic moments by conduction electrons,*” *Physical Review* **96**, 99 (1954).
- [119] T. Kasuya, “*A Theory of Metallic Ferro- and Antiferromagnetism on Zener’s Model,*” *Progress of Theoretical Physics* **16**, 45 (1956).
- [120] K. Yosida, “*Magnetic Properties of Cu-Mn Alloys,*” *Physical Review* **106**, 893 (1957).
- [121] J. Solyom, in *Fundamentals of the Physics of Solids* (Springer, 2007) Chap. 14.
- [122] D. C. Johnston, “*Magnetic dipole interactions in crystals,*” *Phys. Rev. B* **93**, 14421 (2016).
- [123] L. Landau and E. Lifshitz, “*On the theory of the dispersion of magnetic permeability in ferromagnetic bodies,*” *Phys. Zeitsch. der Sow* **8**, 153 (1935).
- [124] T. L. Gilbert, “*A phenomenological theory of damping in ferromagnetic materials,*” *IEEE Transactions on Magnetics* **40**, 3443 (2004).
- [125] D. Bauer, *Atomistic Spin-Dynamics in Confined Magnetic Nano-Structures*, Diplomarbeit in physik, Rheinisch-Westfälischen Technischen Hochschule Aachen (2008).
- [126] R. A. Lukaszew, *Handbook of Nanomagnetism: Applications and Tools*, 1st ed. (Pan Stanford, 2015) pp. 71–80.
- [127] H. Suhl, “*Theory of the magnetic damping constant,*” *IEEE Transactions on Magnetics* **34**, 1834 (1998).
- [128] V. Kamberský, “*Spin-orbital Gilbert damping in common magnetic metals,*” *Phys. Rev. B* **76**, 134416 (2007).
- [129] S. Zhang and Z. Li, “*Roles of Nonequilibrium Conduction Electrons on the Magnetization Dynamics of Ferromagnets,*” *Phys. Rev. Lett.* **93**, 127204 (2004).
- [130] A. Sakuma, “*Microscopic description of Landau-Lifshitz-Gilbert type equation based on the s-d model,*” (2006), arXiv:0602075 [cond-mat] .

- [131] M. Onoda and N. Nagaosa, “*Dynamics of Localized Spins Coupled to the Conduction Electrons with Charge and Spin Currents*,” *Phys. Rev. Lett.* **96**, 66603 (2006).
- [132] F. Delgado and J. Fernández-Rossier, “*RKKY oscillations in the spin relaxation rates of atomic-scale nanomagnets*,” *Phys. Rev. B* **95**, 75413 (2017).
- [133] N. Bode, L. Arrachea, G. S. Lozano, T. S. Nunner, and F. von Oppen, “*Current-induced switching in transport through anisotropic magnetic molecules*,” *Phys. Rev. B* **85**, 115440 (2012).
- [134] J. Fransson and J.-X. Zhu, “*Spin dynamics in a tunnel junction between ferromagnets*,” *New Journal of Physics* **10**, 013017 (2008).
- [135] L. Berger, “*Emission of spin waves by a magnetic multilayer traversed by a current*,” *Phys. Rev. B* **54**, 9353 (1996).
- [136] J. Slonczewski, “*Current-driven excitation of magnetic multilayers*,” *Journal of Magnetism and Magnetic Materials* **159**, L1 (1996).
- [137] A. Brataas, A. D. Kent, and H. Ohno, “*Current-induced torques in magnetic materials*,” *Nature Materials* **11**, 372 (2012).
- [138] N. F. Schwabe, R. J. Elliott, and N. S. Wingreen, “*Ruderman-Kittel-Kasuya-Yosida interaction across a tunneling junction out of equilibrium*,” *Phys. Rev. B* **54**, 12953 (1996).
- [139] J. Fransson, “*Dynamical exchange interaction between localized spins out of equilibrium*,” *Phys. Rev. B* **82**, 180411 (2010).
- [140] A. Altland and B. D. Simons, *Condensed Matter Field Theory*, 2nd ed. (Cambridge University Press, 2010) pp. 129–132, 136–142, 160–164, 703–706.
- [141] J. R. Klauder and B.-S. Skagerstam (World Scientific Publishing Co. Pte. Ltd., Singapore, 1985) Chap. I.4.
- [142] R. P. Feynman and F. L. Vernon, “*The theory of a general quantum system interacting with a linear dissipative system*,” *Annals of Physics* **24**, 118 (1963).
- [143] J.-T. Lü, B.-Z. Hu, P. Hedegård, and M. Brandbyge, “*Semi-classical generalized Langevin equation for equilibrium and nonequilibrium molecular dynamics simulation*,” *Progress in Surface Science* **94**, 21 (2019).
- [144] J.-X. Zhu and J. Fransson, “*Electric field control of spin dynamics in a magnetically active tunnel junction*,” *Journal of Physics: Condensed Matter* **18**, 9929 (2006).
- [145] A. Kamenev, *Field Theory of Non-Equilibrium Systems*, 1st ed. (Cambridge University Press, 2011) pp. 12–19, 183–188.
- [146] J.-X. Zhu, Z. Nussinov, A. Shnirman, and A. V. Balatsky, “*Novel Spin Dynamics in a Josephson Junction*,” *Phys. Rev. Lett.* **92**, 107001 (2004).
- [147] M. Sayad and M. Potthoff, “*Spin dynamics and relaxation in the classical-spin Kondo-impurity model beyond the Landau-Lifschitz-Gilbert equation*,” *New Journal of Physics* **17**, 113058 (2015).

-
- [148] A. Aziz, T. Zhang, Y.-H. Lin, F. Daneshvar, H.-J. Sue, and M. E. Welland, “1D copper nanowires for flexible printable electronics and high ampacity wires,” *Nanoscale* **9**, 13104 (2017).
- [149] K. Bonfils, *Spin Dynamics out of Equilibrium*, Master’s thesis, University of Copenhagen (2017).
- [150] M. Lakshmanan, “The fascinating world of the Landau–Lifshitz–Gilbert equation: an overview,” *Philosophical Transactions of the Royal Society A: Mathematical, Physical and Engineering Sciences* **369**, 1280 (2011).
- [151] K. Gilmore, Y. U. Idzerda, and M. D. Stiles, “Identification of the Dominant Precession-Damping Mechanism in Fe, Co, and Ni by First-Principles Calculations,” *Phys. Rev. Lett.* **99**, 27204 (2007).
- [152] E. Barati, M. Cinal, D. M. Edwards, and A. Umerski, “Calculation of Gilbert damping in ferromagnetic films,” *EPJ Web of Conferences* **40**, 18003 (2013).